



Universiteit
Leiden
The Netherlands

Molecular and Nano-engineering with iron, ruthenium and carbon: Hybrid structures for sensing

Geest, E.P. van

Citation

Geest, E. P. van. (2021, January 14). *Molecular and Nano-engineering with iron, ruthenium and carbon: Hybrid structures for sensing*. Retrieved from <https://hdl.handle.net/1887/139187>

Version: Publisher's Version

License: [Licence agreement concerning inclusion of doctoral thesis in the Institutional Repository of the University of Leiden](#)

Downloaded from: <https://hdl.handle.net/1887/139187>

Note: To cite this publication please use the final published version (if applicable).

Cover Page



Universiteit Leiden



The handle <http://hdl.handle.net/1887/139187> holds various files of this Leiden University dissertation.

Author: Geest, E.P. van

Title: Molecular and Nano-engineering with iron, ruthenium and carbon: Hybrid structures for sensing

Issue Date: 2021-01-14

Molecular and Nano-Engineering with Iron, Ruthenium and Carbon: Hybrid Structures for Sensing

Proefschrift

ter verkrijging van de graad van Doctor aan de Universiteit Leiden,
op gezag van Rector Magnificus Prof. Mr. C.J.J.M. Stolker,
volgens besluit van het College voor Promoties

te verdedigen op 14 januari 2021

klokke 10:00

Erik Pieter van Geest

Geboren te Naaldwijk, Nederland

Samenstelling Promotiecomissie

Promotores

Prof. dr. S. Bonnet

Dr. G.F. Schneider

Overige leden

Prof. dr. H.S. Overkleeft

Prof. dr. J. Brouwer

Dr. I.M.N. Groot

Prof. dr. J.M. van Ruitenbeek

Dr. G. Molnar (*Laboratoire de Chimie de Coordination, Toulouse, France*)

Prof. dr. H.S.J. van der Zant (*TU Delft*)

The studies described in this thesis were performed at the Leiden Institute of Chemistry at Leiden University, the Netherlands.

ISBN: 978-94-6332-720-6

Printing: GVO Drukkers & Vormgevers

"Questions are like fire / they need feeding to survive"

Them Crooked Vultures

"Man muß die Dinge so einfach wie möglich machen. Aber nicht einfacher."

Albert Einstein

*To my parents,
and all who supported me*

Table of Contents

List of Abbreviations	6
1. Introduction	9
1.1. Graphene and metal complexes: tools for engineers	10
1.2. Engineering with carbon – graphene based sensors	11
1.3. Iron complexes as molecular switches: spin crossover	18
1.4. Ruthenium complexes – a matter of light and dark	26
1.5. Aim of this thesis	30
1.6. References	31
2. Contactless spin switch sensing by chemo-electric gating of graphene	37
2.1. Introduction	38
2.1. Results and Discussion	40
2.2. Conclusions & Outlook	51
2.3. References and Notes	52
3. Large-area thin films of the spin crossover complex [Fe(bapbpy)(NCS) ₂] grown selectively on graphene	55
3.1. Introduction	56
3.2. Results and Discussion	57
3.3. Conclusions & Outlook	66
3.4. Acknowledgements	67
3.5. References and Notes	67
4. Polymer-coated graphene-based gas sensors: chemical fingerprinting by simultaneous sensing	69
4.1. Introduction	70
4.2. Results and Discussion	72
4.3. Chemical fingerprint (CF) vapor sensors	80
4.4. Conclusions & Outlook	87
4.5. References and Notes	88
5. Monitoring a ruthenium-based photoreaction with graphene on paper	89
5.1. Introduction	90
5.2. Results and Discussion	92

5.3.	Conclusions & Outlook.....	100
5.4.	Acknowledgements.....	101
5.5.	References and Notes.....	101
6.	Reducing the translocation speed of DNA in solid-state nanopores by photo-labile ruthenium complex decoration	103
6.1.	Introduction.....	104
6.2.	Results and Discussion	105
6.3.	Conclusions & Outlook.....	111
6.4.	Acknowledgements.....	111
6.5.	References and Notes.....	111
7.	[Ru(3)(biq)(STF-31)] ²⁺ : A lock-and-kill anticancer PACT agent	113
7.1.	Introduction.....	114
7.2.	Results and Discussion	116
7.3.	Conclusions & Outlook.....	122
7.4.	References and Notes.....	123
8.	Summary, Conclusions & Outlook	125
8.1	Summary.....	126
8.2	Conclusions and Outlook	133
	Appendix Chapter 2	137
	Appendix Chapter 3	153
	Appendix Chapter 4	165
	Appendix Chapter 5	185
	Appendix Chapter 6	191
	Appendix Chapter 7	195
	Samenvatting, conclusies en vooruitzichten	209
	List of publications.....	223
	Curriculum Vitae	225
	Acknowledgements	227

List of Abbreviations

(μ)RNA	(micro)-ribonucleic acid
(ADF)-STEM	(annular dark-field)- scanning transmission electron microscopy
(ATR)-IR	(attenuated total reflection) infrared spectroscopy
(ct)DNA	(calf thymus) deoxyribonucleic acid
(LC/HR)-MS	(liquid chromatography/high resolution) mass spectrometry
(r)GO	(reduced) graphene oxide
acac	acetylacetonate
AFM	atomic force microscopy
ANO-RCC	atomic natural orbitals (relativistic and (semi-)core correlation)
APS	ammonium persulfate
APTES	3-aminopropyltriethoxysilane
babppy	N,N'-di(pyrid-2-yl)-2,2'-bipyridine-6,6'-diamine
bbpya	N,N-bis(2-2'-bipyrid-6-yl)amine
biq	2,2'-biquinoline
bpy	2,2'-bipyridine
bpz	dihydrobis(pyrazolyl)borate
CAB	cellulose acetate butyrate
CAS(SCF)	complete active space (self-consistent field)
CEG	chemo-electric gating
CF	chemical fingerprint
CITS	current-imaging-tunneling spectroscopy
dAMP	2-deoxyadenosine monophosphate
dCMP	2-deoxycytidine monophosphate
dGMP	2-deoxyguanosine monophosphate
dTMP	2-deoxythymidine monophosphate
DCC	N,N'-dicyclohexylcarbodiimide
DCM	dichloromethane
DEME-TFSI	diethylmethyl(2-methoxyethyl)ammonium bis(trifluoromethylsulfonyl)imide
DMAP	4-dimethylaminopyridine
DMF	dimethylformamide
DMSO	dimethylsulfoxide
dppz	dipyrido[3,2-a:2',3'-c]phenazine
EDTA	ethylenediaminetetraacetic acid

EDX	energy-dispersive X-ray spectroscopy
Elem. Anal.	elemental analysis
EM	emission wavelength
Et ₂ O	diethyl ether
EX	excitation wavelength
GC	gas chromatography
GFET	graphene field effect transistor
GLUT1	glucose transporter, type 1
GS	ground state
HFIP	1,1,1,3,3,3-hexafluoro-2-propanol
HOPG	highly oriented pyrolytic graphite
HS	high spin
Htrz	1H-1,2,4-triazole
IC ₅₀	half maximal inhibitory concentration
ICYTES	3-isocyanatepropyltriethoxysilane
IL	ionic liquid
IP	intermediate phase
IPA	isopropyl alcohol
ITO	indium tin oxide
KNN	k-nearest neighbor
LDA	local density approximation
LED	light-emitting diode
LF	ligand field
LS	low spin
MC	metal center
MEAS	measurement (transistor name)
MeOH	methanol
MOF	metal organic framework
MLCT	Metal-to-ligand charge transfer
NAMPT	nicotinamide phosphoribosyltransferase
NB	Naive Bayesian
NH ₂ trz	4-amino-1,2,4-triazole
NMR	nuclear magnetic resonance
NP	nanoparticle
OTMS	octadecyltrimethoxysilane
PACT	photoactivated chemotherapy
PAH	polyaromatic hydrocarbon
PCA	principle component analysis
PDMS	polydimethylsiloxane

PDT	photodynamic therapy
phen	1,10-phenanthroline
pic	2-pyridine carboxylate
PMMA	poly(methyl methacrylate)
PTFE	polytetrafluoroethylene
QY	quantum yield
RBF	radial basis function
REF	reference (transistor name)
RF	Random Forest
ROS	reactive oxygen species
RPA	random phase approximation
RT	room temperature
sal	saliva
SCO	spin crossover
SERS	surface-enhanced Raman spectroscopy
SiN	silicon nitride
SMV	Support Vector Machines
SPPR	surface plasmon-polariton resonance
SPR	surface plasmon resonance
SQUID	superconducting quantum interference device
STF-31	4-((4-t-butyl)phenylsulfonamido)methyl)-N-(pyridin-3-yl)benzamide
STM	scanning tunneling microscopy
TCYTES	3-thiocyanatepropyltriethoxysilane
TEM	transmission electron microscopy
TLC	thin-layer chromatography
tpy	2,2':6',2''-terpyridine
UV-vis	ultraviolet-visible spectroscopy
XPS	X-ray photoelectron spectroscopy
XRD	X-ray diffraction

Chapter **1**

Introduction

Molecular and Nano-Engineering with Iron, Ruthenium
and Carbon: Hybrid structures for Sensing

1.1. Graphene and metal complexes: tools for engineers

Through careful monitoring of vital signs and biomarkers, healthcare has been able to skyrocket to the high level it is today. Personalized healthcare could alleviate drug side effects and strict conditions (*i.e.* long hospitalization, or heavy periodical treatments like dialysis) of a patient through an optimized treatment scheme. This requires highly sensitive and accurate sensors. In 2004, graphene has emerged, a single sheet of graphite with a honeycomb arrangement of sp^2 carbon atoms, which could very well be a key player in the development of next-generation sensors. Graphene, a semiconducting 2D material with properties that are very suitable for electrical engineering, for example for sensing technologies, has the potential to fulfill the demands of modern sensors for selectivity and sensitivity.

Yet, a single graphene sheet is in fact not very useful in electronic sensors. The sensitivity and selectivity of graphene-based sensors almost completely depends on what is present on this 2D sheet: the coating, or functionalization, of graphene should be chosen specifically to provide a graphene-based sensor with sensitivity and selectivity. This PhD thesis especially focuses on functionalizing graphene-based devices with metal complexes. The chemical versatility of metal complexes is wide, as for instance the nature of the metal, its oxidation state, and the ligands bound to it, altogether determine the properties of each metal complex. These metal complexes can be tuned by molecular design to get specific functions that are useful for the fabrication of selective devices. Among the many properties that have been ascribed to metal complexes, some are technologically more interesting, for example molecular switching of the spin of the complex, or photosubstitution of specific ligands. Both are examined in more detail throughout the chapters of this thesis, with a particular focus on using such properties for sensing with graphene-based devices.

1.2. Engineering with carbon – graphene based sensors

1.2.1. A brief introduction of graphene

Since its recognition, graphene has claimed its fair share of research interest. Graphene is a monolayer of sp^2 carbon atoms of infinite size. While graphite as a bulk material is an everyday commodity since ancient times, the extraction and characterization of a single crystalline honeycomb-structured carbon monolayer has only been achieved in 2004 by exfoliation of highly oriented pyrolytic graphite (HOPG). The first pieces of graphene were prepared by mechanical exfoliation and were micrometer-sized.^[1] Various synthetic methods for graphene have since then been developed, and sheets up to 30 inch wide have already been prepared.^[2] Its synthesis at such a large scale has opened new routes to use this 2D material in numerous macroscopic devices. Pristine graphene exhibits unique electronic properties, but in most graphene-based devices, graphene requires to be functionalized chemically or physically with molecules or (nano)particles to function.^[3] It should be noted here that, although pristine graphene is commonly pictured as a perfect honeycomb structure made of carbon atoms, usually defects in this lattice exist, *e.g.* grain boundaries (where two graphene crystals meet) and (pin)holes, which affect the electronic properties of graphene (see Figure 1.1).^[4]

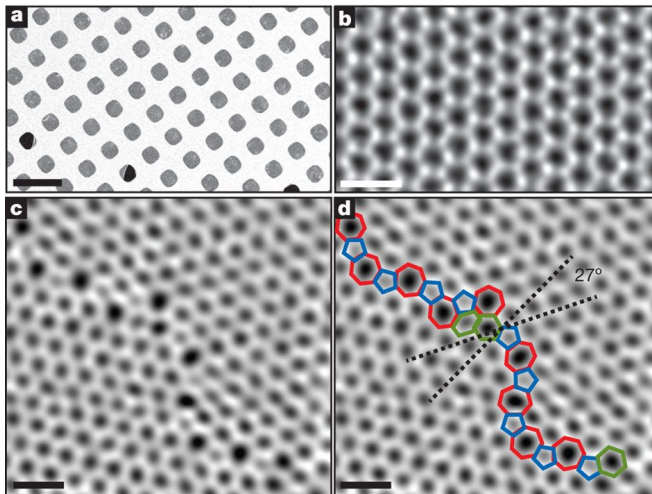


Figure 1.1: Annular dark-field scanning transmission electron microscopy (ADF-STEM) images of a monolayer graphene crystal. A) Graphene on a TEM grid, scale bar = 5 μm . B) The hexagonal structure of pristine graphene. C and D) Grain boundary in graphene, where the honeycomb structure is disrupted (coloured rings). B-D: scale bar = 5 \AA . Reprinted with permission from Huang et al., © Nature, 2011.^[4]

Graphene can be synthesized using various techniques, and the technique that is used will drastically influence the performance of the resulting graphene-based sensor. Synthetic approaches that yield pristine graphene are mechanical exfoliation^[1], chemical vapor deposition growth^[5] (CVD graphene) on a metal surface, and bottom-up synthesis^[6] from aromatic precursors. A common approach to produce graphene in bulk is the oxidation of graphite into graphene oxide (GO, an electrical insulator) using Hummer's method, an aggressive oxidation approach.^[7] The oxidized graphene flakes are then reduced chemically or thermally, yielding reduced graphene oxide (rGO). A clear distinction should always be made between pure graphene and rGO, as reduction of GO will never be complete; a certain amount of oxidation moieties will always remain at the surface and edges.^[8] rGO typically shows far lower conductivity than exfoliated or CVD-grown graphene and could thus be considered less suitable for use in electronic sensors than pristine graphene.^[9]

1.2.2. Electronic properties of pristine graphene

The properties of graphene originate mainly from the molecular arrangement of its sp^2 carbon atoms. The 2D honeycomb structure (which can be described as two overlapping triangular lattices with 2 atoms per unit cell; see Figure 1.2A) is hexagonal. The Brillouin zone of the graphene lattice is also hexagonal, however its corners \mathbf{K} and \mathbf{K}' are not equivalent. \mathbf{K} and \mathbf{K}' are called Dirac points; at these points the Dirac cones for electrons and electron holes contact each other (see Figure 1.2B).^[10] At the Dirac cones the valence and conducting electronic bands of graphene meet. Since these bands connect, but do not overlap, graphene is considered a zero-gap semiconductor.

In theory, 'perfect' graphene in an electrically and magnetically neutral environment does not exhibit electric conductivity at 0 K. At these conditions, the Fermi level lies exactly between the two electronic bands. Here the valence band is completely filled, while the conductance band is completely empty.^[10, 11] Without a partially filled electronic band there are no charge carriers, *i.e.* free electrons in the conductance band or electron holes in the valence band, and electrical resistance of the graphene sheet is maximal. The Dirac point is indeed represented by a resistance maximum in a resistivity (ρ) *vs.* gate voltage (V_g) plot (see Figure 1.2C).^[12] The gate voltage creates an electric field, to which the graphene sheet is sensitive, and as V_g moves away from the Dirac point, charge

carriers are created and graphene becomes conductive. Graphene therefore is a special kind of electrical material, showing both p- and n-type semiconductor character, depending on the sign and value of V_g .

The gate voltage dependence of the electric properties of graphene is exploited in graphene field-effect transistors (GFETs) produced from the single atom-thick carbon sheet. A typical GFET is shown schematically in Figure 1.2D. A graphene sheet is positioned on a silicon wafer of which the surface is a layer of the electrically insulating SiO_2 of ~ 300 nm thickness. The gate potential is applied to the silicon back side, creating an electric field through the SiO_2 layer. The graphene sheet is electrically connected through the source and drain electrodes, typically via nanometer-thick gold strips. The transistor is in ‘off’ mode at the Dirac point, where graphene is an insulator, and in ‘on’ mode when V_g is far away from the Dirac point and graphene is conductive.^[13]

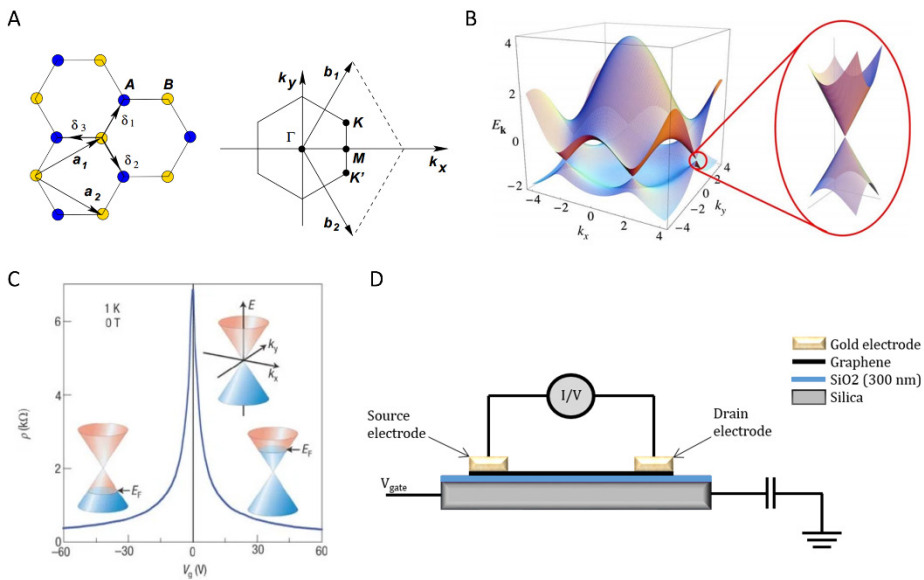


Figure 1.2: Electronic properties of graphene. A) Honeycomb lattice and Brillouin zone for graphene. B) Electronic dispersion in the Brillouin zone from pristine graphene. The conducting and the valence electronic bands meet at the Dirac point (zoom). Figure 1.2A and B reprinted with permission from Castro Neto et al., © American Physical Society, 2009.^[11] C) Resistivity (ρ) as a function of gate voltage (V_g) for pristine graphene at 1 K. Dirac cones are shown at a negative, positive and zero value of the applied gate voltage. Reprinted with permission from Geim et al., © Nature, 2007.^[12] D) Schematic view of a graphene field-effect transistor (GFET). A silicon wafer is used as the (back) gate in typical GFETs.

1.2.3. Sensitivity of graphene and sensor technology

Graphene-based devices are known to be sensitive to changes in the environment of the 2D carbon sheet, more specifically to dipole changes near the graphene surface.^[9] This opens a way for graphene devices to be used as sensors. For example, a GFET made of pristine graphene was able to detect the absorption of NO₂, even at the single molecule level. The sensitivity of this GFET sensor was attributed to the high surface-to-volume ratio, high conductivity, low defect concentration of the graphene 2D crystal, and the ability to do four-terminal sensing (using four electrodes instead of two for electrical measurements to eliminate contact resistance, which gives more precise measurements with it).^[14]

Being atomically thin, graphene and other 2D materials exhibit surface-to-volume ratios higher than any 3D material. In fact, the entire volume of the carbon material is exposed to an adsorbent to be detected, maximizing the sensing effect. Due to its high, metallic-like electrical conductivity (*i.e.* the Fermi level is in at least one energy band) and low noise levels (Johnson noise, *i.e.* electric noise generated by thermal agitation of the charge carriers, and 1/f noise, particularly for few-defect single crystals) graphene raised special interest for its implementation in sensing technologies.^[15] Low electric noise levels increase the signal-to-noise ratio, and thus increase the sensitivity of the sensing device.

In fact, the 2D nature of graphene can also be used for sensing. Nanopores in graphene membranes for example have been proposed for DNA sequencing by measuring the ionic current through the pore, *i.e.* the current generated by charged ions moving from the *cis* to the *trans* chamber of a flow cell driven by an electrostatic potential (see Figure 1.3A).^[16] When DNA is located in the nanopore, this ionic current is blocked, which can be observed as a current drop in the ionic current measurements. In theory each nucleotide blocks this current differently, and thus individual nucleotides may be identified. Currently, DNA sequencing is done in the clinics with biological nanopores (Oxford Minion) using this principle.^[17]

Solid-state nanopores, like graphene nanopores, have the advantage over biological pores (which are used in the Minion devices) that they can be precisely shaped and fabricated on a large scale and have a high chemical, thermal and mechanical stability.^[18] A rule of thumb for nanopore-based DNA sequencing dictates that the smaller the membrane, the higher the resolution of sensing is (as

the total current blockade originates from less nucleotides that are in the pore at the same time, see Figure 1.3B). Graphene-based nanopore devices, using an atomically thin membrane, can theoretically be used to obtain the highest possible base-calling accuracy (*i.e.* individual nucleobase readout) in DNA sequencing.^[16] The major drawback of solid-state nanopores is, however, the high speed of the DNA strand as it passes through the pore; current equipment for electrical measurements cannot measure within the time frame that is required to identify a single base passing through the pore.^[19] In Chapter 6, we describe how we aimed to use a ruthenium complex to control the speed of DNA through a nanopore using thermal binding of the ruthenium complex to DNA and its photoactivated release.

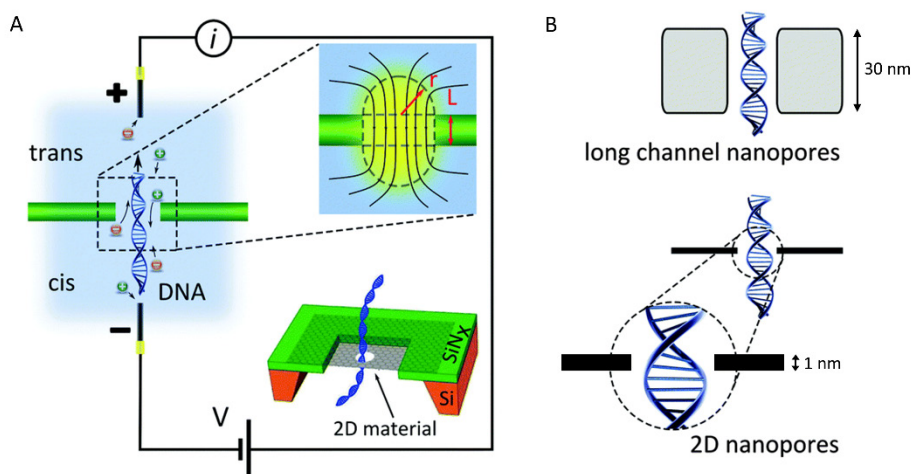


Figure 1.3: Nanopores for DNA sequencing. A) Operating principle of a nanopore device for DNA sequencing. As DNA travels through a nanopore, an ionic current from the *cis* to the *trans* chamber (or *trans* to *cis* for oppositely charged ions) of a flow cell is blocked, which is measured electrically. B) The thickness-resolution rule of thumb: the smaller the membrane with the pore, the less bases are measured at the same time: in thick pores (top, squares represent ~ 30 nm membrane), many DNA bases block the pore, while for thin membranes (bottom, lines represent ~ 1 nm membrane), only a small number of bases block the pore. Figure adapted from Arjmandi-Tash et al., © Royal Society of Chemistry, 2016.^[16]

1.2.4. Graphene functionalization

Graphene-based sensors usually function via the sensitivity of the graphene sheet to functional molecules or particles attached to or deposited on the surface of graphene.^[9] Placing a functional molecule on the surface of graphene is often referred to as graphene functionalization, and can be categorized into two main

classes, covalent and non-covalent functionalization (sometimes intercalation, which is also non-covalent, is mentioned as a third class), which refers to the binding interactions between the functionalizing molecules or nanoparticles and the graphene surface (see Figure 1.4). One of the consequences of covalent binding in particular, is that the the structure of the graphene lattice is permanently affected, hence its electrical properties. Non-covalent functionalization on the other hand changes the conductivity of graphene but does not change the lattice of graphene (as the conjugation of the 2D network of sp^2 carbon atoms remains intact).^[3]

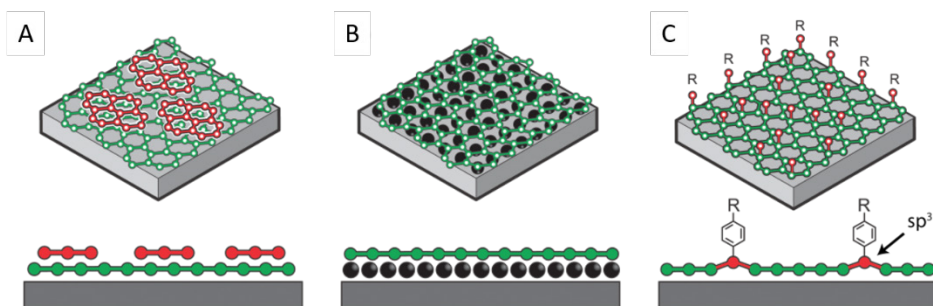


Figure 1.4: Graphene functionalization approaches, classified based on the mode of binding. A) Non-covalent functionalization. B) Intercalation. C) Covalent functionalization. Adapted from <http://surfchem.dk/research/projects/graphene-chemistry/>, accessed 17-03-2020.

The conjugated C-C double bonds of the graphene basal plane could be used for the covalent attachment of functional moieties through chemical reactions, for example through nucleophilic addition,^[20] 1,3-cycloaddition,^[21] and free radical reactions with diazonium salts.^[22] Another common strategy for covalent functionalization is to use plasma chemistry, for instance to use O_2 plasma to introduce oxygen containing groups, *i.e.* hydroxyl and epoxide moieties at the surface and carboxylic acid groups at the edges of the sheet.^[23, 24] Similarly, fluorine and nitrogen-containing groups were introduced on the surface of graphene by its treatment with their corresponding plasmas.^[24] In a different approach, hydrogenation of graphene was done electrochemically, effectively introducing sp^3 hybridized centers in the carbon plane.^[25] The graphene surface can also be electrochemically functionalized with aryl groups by applying a potential on graphene, used here as an electrode in an aqueous solution of an aryl iodonium or diazonium salt.^[26]

When the intrinsic semi-conductive properties of graphene should absolutely be maintained, while functionalization of its surface is desired, non-covalent functionalization is usually the preferred strategy. This type of surface modification does not induce chemical alteration of the 2D network of sp^2 carbon centers; instead, it exploits supramolecular interactions, *e.g.* van der Waals forces and π - π interactions, to attach functional moieties on the carbon surface. Typically, large aromatic anchors are used, like polyaromatic hydrocarbons (PAHs), to fix molecules to a graphene surface. A common PAH used in this approach is pyrene, which sticks to the graphene plane by π - π stacking. The binding energy of this interaction was calculated to be -1.09 eV (about one-third of the binding energy of the C-C bond in ethane, which is -3.91 eV^[27]), at a graphene-pyrene distance of 3.45 Å.^[28] Many studies have used the pyrene-based anchoring method to produce functional graphene devices; only a few of them will be mentioned here. For example, the surface of graphene could be functionalized with sensing molecules, for the sensing of *e.g.* glucose^[29] and μ RNA (see Figure 1.5).^[30]

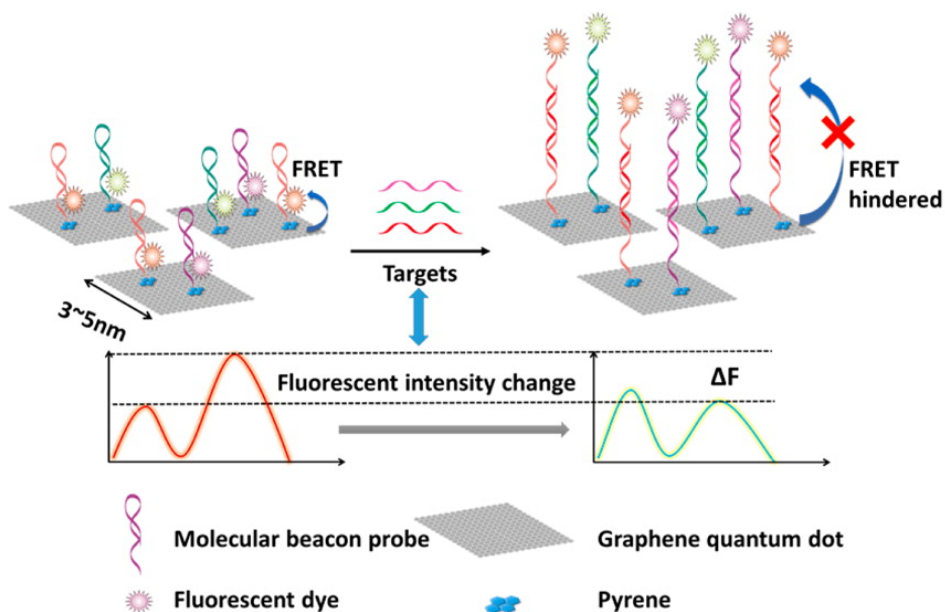


Figure 1.5: μ RNA sensing with a graphene device. Molecular probes, short RNA strands terminated with a fluorescent dye at one end and pyrene at the other end, are fixed to on graphene quantum dots. Introduction of target μ RNA activates the fluorescence of the dye. Reprinted with permission from Zhang et al., © American Chemical Society, 2015.^[30]

Introduction of light-sensitive complexes and particles with pyrene anchors gave rise to devices with widely varying functions. Photoswitching events were observed on graphene when it was functionalized with a zinc spirophan-pyrene complex,^[31] from which Zn^{2+} dissociated upon irradiation and coordinated in the dark, and with ruthenium bis(bipyridyl)-pyrene complexes, which induced a photocurrent across graphene when the device was irradiated with light.^[32] In others studies, the fluorescence of free silicon nanocrystals and PbS nanoparticles, both functionalized with pyrene moieties, was quenched when they were placed on graphene, effectively providing the carbon sheet with light-harvesting properties.^[33]

The examples mentioned here are the tip of the iceberg: functionalization of graphene plays a major role in the function of the device that is fabricated. There are many options to functionalize graphene and to design operational devices, some of which were exploited for the graphene-based sensors described in this thesis. In Chapter 2, in particular, it is described how graphene-based devices can react to molecular switches, even from a distance. We found that graphene field effect transistors reacted strongly to phase transitions in a crystal on which they were fabricated. This crystal was a single crystal of an iron compound that undergoes spin crossover.

1.3. Iron complexes as molecular switches: spin crossover

1.3.1. Magnetic switching in transition metals

In 1931, Cambi and Szegö were the first to write about dithiocarbamate iron(III) complexes showing anomalous magnetic properties.^[34] Later, the term ‘spin crossover’ (SCO for short) was coined for this magnetic switching behaviour, and reports on new SCO complexes based on *e.g.* Ni(II),^[35] Co(II),^[36] Fe(II),^[37] Fe(III),^[38] and Mn(II)^[39] appeared at a high pace.

A complex that exhibits SCO is able to drastically alter its magnetic, optical, dielectric and mechanical properties, without altering its chemical composition.^[40] SCO typically occurs upon external perturbation, *e.g.* a temperature change,^[41] irradiation with light,^[42] pressure variations,^[43] the application of a magnetic field,^[44] or an electrical potential.^[45, 46] The SCO phenomenon originates from the electronic sphere of a metal center, typically a first row transition metal center with $d^4 - d^7$ electronic configuration and octahedral coordination sphere. Such

metal centers have 5 d-orbitals, which are divided into two subgroups, the nonbonding t_{2g} orbitals (d_{xy} , d_{yz} and d_{xz}) and the antibonding e_g orbitals (d_{z^2} and $d_{x^2-y^2}$). Naturally, the non-bonding orbitals are lower in energy than the anti-bonding orbitals; hence an energy gap exists between the subgroups. The size of this energy gap, the ligand field splitting Δ , is determined by the ligand coordination sphere.^[47] To explain spin crossover, electron pairing should also be considered. The pairing of two electrons in a single molecular orbital requires that the spins of both electrons are opposite to each other, according to Pauli's principle. However, having two opposite spins brings an energetic cost; thus electrons tend to spread across degenerate orbitals (orbitals with the same energy) as much as possible to minimize spin pairing.^[48]

Distribution of the d-electrons over the t_{2g} and e_g orbitals is governed by minimizing the Gibbs free energy ΔG , which has an enthalpy (ΔH) and an entropy (ΔS) contribution, where $\Delta G = \Delta H - T\Delta S$ (see Figure 1.6). At a low temperature (T), the entropy contribution is low, since it is linearly correlated to the temperature, and the enthalpy is the dominating part of ΔG . The low spin (LS) state, *i.e.* 1A_1 for Fe^{II} , with six d electrons paired up in the t_{2g} orbitals, is favored under these conditions. This is the diamagnetic phase of Fe^{II} -based SCO material (total spin $S = 0$). The paramagnetic high spin (HS) state (5T_2 for Fe^{II} , with a total spin $S = 2$ and the electrons distributed in an unpaired fashion) on the other hand, is favored at high temperatures, as this state is more disordered than the low spin state (as metal to ligand bonds have lengthened). At the SCO transition temperature, the entropy contribution to ΔG equals the energy barrier from the LS to HS conversion (which originates mainly from the energy required to place the electrons in the higher e_g orbitals). When reaching this temperature in the heating mode, the sign of ΔG for this conversion changes from positive to negative, making the transition from LS to HS thermodynamically favoured, upon which the system switches to the high spin state.^[49, 50]

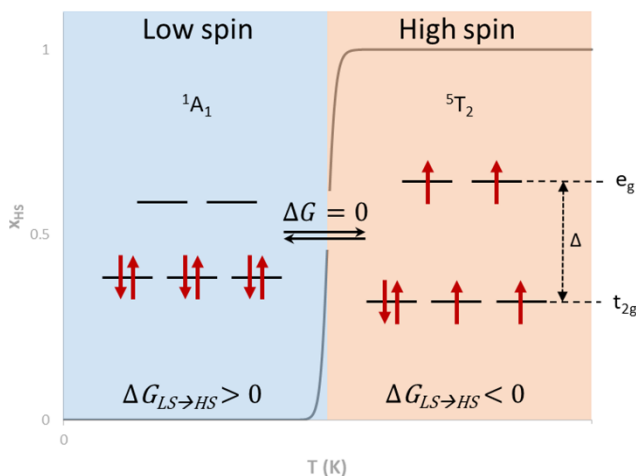


Figure 1.6: Schematic overview of spin crossover according to the ligand field theory. At low T , the low spin state 1A_1 is favored due to a large negative enthalpy ΔH contribution to ΔG . When T increases, the higher entropy of the high spin state 5T_2 brings ΔG to negative values and hence drives the spin state equilibrium towards the right.

1.3.2. Types of spin crossover behaviour and cooperativity

The spin crossover behaviour is not the same for each species that exhibits this phenomenon. The various behaviours of thermal SCO can be categorized into five classes, illustrated by the temperature evolution of the product of their molar magnetic susceptibility (χ_m) multiplied by the temperature (*i.e.* $\chi_m T$), or in a more simplified way, by the temperature evolution of the fraction of high spin molecules (γ_{HS}) in the sample (see Figure 1.7). We distinguish between gradual, abrupt, hysteretic, multi-step, and incomplete spin crossover. While during gradual spin crossover the phase transition occurs smoothly over a wide temperature range (>100 K), during abrupt transitions the transition is sharp and takes place over a short temperature range (<10 K).

Hysteresis is defined by cases where SCO occurs at a lower temperature when cooling the material than when heating the material. In such a case a hysteresis cycle opens over a temperature range that can span from a few degrees to 50 K or more. A hysteresis cycle is an indication of the existence of two metastable phases, one HS and one LS, which can co-exist at one given temperature. HS and LS complexes may also co-exist in a mixed intermediate spin phase, which appears for compounds showing multiple-step SCO. Finally, incomplete SCO are observed when the SCO compound does not reach full LS phase at low

temperatures, *i.e.* when γ_{HS} in the material never reaches 0 upon cooling.^[50] Combinations of the different SCO types described above can exist as well. For example, single crystals of $[\text{Fe}(\text{bapbpy})(\text{NCS})_2]$ (where bapbpy = N,N'-di(pyrid-2-yl)-2,2'-bipyridine-6,6'-diamine) display curious SCO behaviour. Single crystals of this complex exhibit SCO in a two-step-with-hysteresis fashion, with next to the HS and LS phase (phase I and III, respectively) an intermediate spin phase (phase II) where the ratio of molecules in the HS and LS state is 1:2. The transitions of the single crystal, phase I to II and phase II to III, are both abrupt and with hysteresis.^[51]

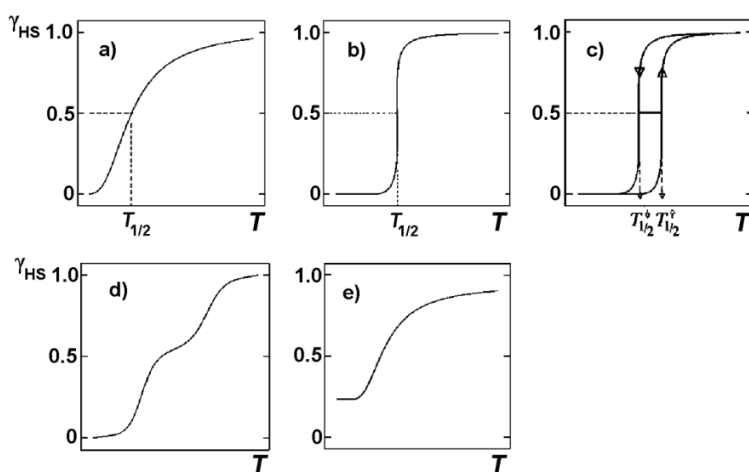


Figure 1.7: Different classes of spin crossover behaviour. Mole fraction γ_{HS} vs. T profiles of the different classes of spin crossover behaviour: gradual (a), abrupt (b), with hysteresis (c), multi-step (d) and incomplete (e). Reprinted with permission from Gütllich et al., © Beilstein-Institut, 2013.^[50]

The behaviour of SCO in a material is highly controlled by “cooperativity”. Cooperativity in this sense refers to the degree of interaction of an individual SCO molecule with its neighbors in the crystal lattice.^[52] In a crystal, a SCO phase transition, which is a 1st order transition, usually nucleates at an edge or a defect in the crystal, then grows through the crystal.^[53] Propagation of such a phase transition between two crystallographic phases (where the spin states of the molecules are not identical) defines a spin crossover front that can be seen as the transient region of the crystal where molecules go from one phase to the other. This front propagates in one or the other direction depending on temperature gradient in the sample for example, and propagation of the front is fast or slow depending on whether the interaction, or “communication”, between neighboring molecules, is strong or weak.^[54]

This cooperativity first of all can come from Van der Waals interactions; since the HS molecule is larger than the LS molecule, switching from LS to HS exerts a pressure on the neighboring molecules (as the HS molecule does not fit anymore in the LS crystal lattice), causing the neighboring molecules to switch as well, resulting in the propagation of the phase transformation through the crystal.^[54] Other forms of supramolecular interactions contributing to cooperativity can be hydrogen bonding and π - π stacking interactions. Such interactions were found to be responsible for the cooperativity in for example $[\text{Fe}(\text{bbpya})(\text{NCS})_2]$ (where bbpya = N,N-bis(2,2'-bipyrid-6-yl)amine), which shows an abrupt spin crossover with hysteresis (see Figure 1.8).^[55] Introducing a hydrogen bonding network, incorporation of π -stacking moieties and steric groups, and coordination of bridging ligands in the crystal lattice are common strategies to increase cooperativity in bulk materials.^[50, 54, 56] Controlling SCO behaviour in nanomaterials however, requires radically different approaches.

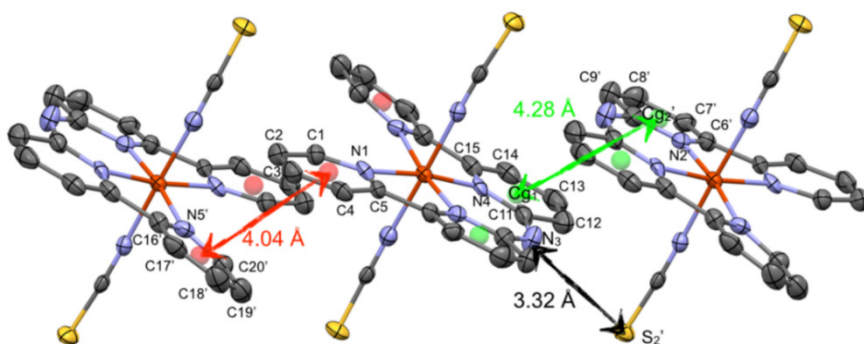


Figure 1.8: X-ray crystal structure of the SCO material $[\text{Fe}(\text{bbpya})(\text{NCS})_2]$. The interactions responsible for the cooperativity of this material are hydrogen bonding between H and S (black arrow) and π - π stacking (red and green arrows). Reprinted with permission from Zheng et al., © Wiley, 2015.^[57]

1.3.3. Small scale spin crossover: reduced size effect

For spin crossover materials to be used in nanotechnology, the size of the material should be reduced. However, scaling down to the nanometer scale can have a big impact on spin crossover properties. Common observations when scaling down SCO materials to the nanometer scale are hysteresis fading, decreasing spin transition temperatures, and complete transitions becoming incomplete.^[58] Theoretical models have been published that allow for explaining these observations.^[59] In a nutshell, spin crossover nanoparticles (SCO NPs) are typically a few nanometers in size, and their surface-to-volume ratio, which is

related to the fraction of molecules in the nanoparticle that “feel” the bulk environment, is limited.^[60] The SCO properties of the molecules that “feel” the modified surface environment, modify the SCO properties of the nanoparticles as a whole. The size of the nanoparticle has been appointed as critical for maintaining the bulk SCO behaviour in a nanoparticle of the same material, *e.g.* for the 3D metal organic framework [Fe(pyrazine)Pt(CN)₄] (see Figure 1.9)^[61] and the 1D chain coordination compound [Fe(NH₂trz)₃]Br₂·3H₂O (where NH₂trz = 4-amino-1,2,4-triazole).^[62] For the latter material critical nanoparticle sizes of about 45-50 nm^[63] and 30 nm^[64] have been reported. While the transition temperature did not change as the size decreased, the transition became less abrupt and the hysteresis loop became smaller when particles decreased in size, and even disappeared for particles of 30 nm.^[64] Interestingly, other triazole SCO complexes, *e.g.* [Fe(Htrz)₂(trz)](BF₄) (where Htrz = 1H-1,2,4-triazole) showed bulk SCO behaviour (with hysteresis) at much smaller sizes, with an average size of 11 and even 6 nm.^[65]

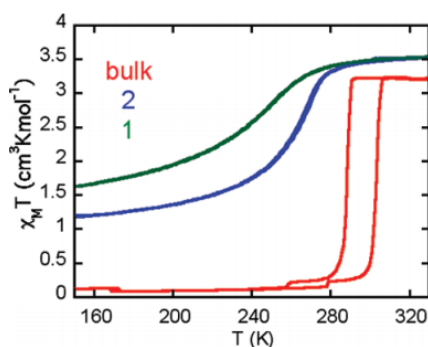


Figure 1.9: Reduced size effect of spin crossover. Magnetic susceptibility versus temperature plot showing the spin crossover behaviour of [Fe(pyrazine)Pt(CN)₄] bulk and nanoparticles (1: 7 nm; 2: 14 nm). Reprinted with permission from Volatron et al., © American Chemical Society, 2008.^[61]

Interestingly, coating NPs with an (inert) shell may help to retain the bulk SCO properties in the nanomaterial. This wrapping of a SCO NP can influence the SCO behaviour; this phenomenon is called the matrix effect.^[66] Strong variations in the spin transition characteristics of [Fe(pyrazine)Pt(CN)₄] NPs have been observed when they were coated with various shells. For example, a more elastic matrix leads to more gradual transitions, while a more rigid shell, like SiO₂, improved cooperativity and promoted abruptness of the transition and hysteresis.^[67] The matrix effect is a strong example of how the environment of an SCO NP can influence its cooperative behaviour.

Instead of nanoparticles, spin crossover compounds can also be grown into thin films with high control over film thickness, which is typically in the nanometer range. For example, a thin film of $[\text{Fe}(\text{pz})\text{Pt}(\text{CN})_4]$ with nanometer thickness was synthesized directly on a gold surface via layer-by-layer assembly, by sequential dipping of a pre-treated gold substrate into Fe^{2+} , $[\text{Pt}(\text{CN})_4]^{2-}$ and pyrazine solutions.^[68] Films could also be obtained, down to 7 nm, by evaporation under high vacuum, such as for the SCO complex $[\text{Fe}(\text{phen})_2(\text{NCS})_2]$ (where phen = 1,10-phenanthroline),^[69] which were still SCO-active. In the end, there is a range of techniques that can be used to produce thin films, *e.g.* spin coating, drop casting, layer-by-layer assembly, vacuum evaporation and Langmuir Blodgett.^[70] For thin films however, a similar limitation exists with regards to scaling down to the nano-level: the receiving surface plays a crucial role.

1.3.4. Spin crossover on surfaces

Similar to the matrix effect observed for SCO NPs, a surface in the near proximity of SCO thin layers can also influence the SCO behaviour of the layer. Interactions between the surface and nearby SCO molecules can interfere with or even inhibit spin crossover in these molecules. For example, a thin film of $[\text{Fe}(\text{bpz})_2(\text{phen})]$, (where bpz = dihydrobis(pyrazolyl)borate and phen = 1,10-phenanthroline) was produced on a gold surface. Spin crossover occurred in individual molecules of this compound, but once deposited on the gold surface the molecules closest to the surface were unable to flip their spin. In contrast, the 2nd row of molecules did switch their spins, as observed by a change in the dielectric constant associated with SCO. Moreover, they could even be actively switched by applying a potential pulse from the STM tip (see Figure 1.10).^[71]

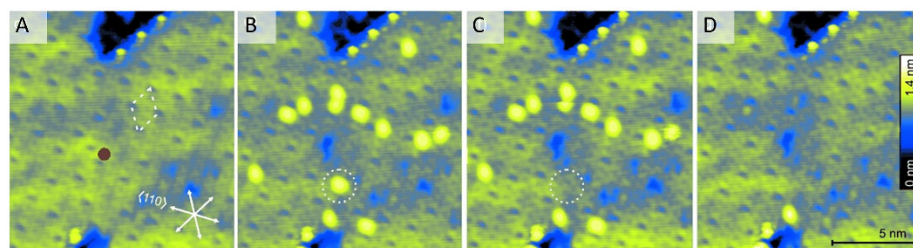


Figure 1.10: Spin switching in molecular thin films. STM image of a $[\text{Fe}(\text{bpz})_2(\text{phen})]$ thin film. The monolayer (faint yellow background) does not exhibit spin crossover. When a voltage pulse was applied at the red dot (A), several 2nd row molecules changed their dielectric state (bright yellow dots, B). The circled molecule was switched back to LS by applying a weaker pulse (C); other HS molecules could be returned to LS in the same way (D). Figure adapted from Gopakumar et al., © Wiley, 2011.^[71]

When spin crossover nanomaterials are to be implemented in electronic systems, patterning and organization of the particles at the nanoscale is of high importance. Currently, the industry standard for patterning is the lift-off process, which uses a sacrificial photoresist mask to expose the surface only where the mask was developed, *i.e.* by e-beam lithography.^[72] Patterning of $[\text{Fe}(\text{pyrazine})\text{Pt}(\text{CN})_4]$ particles was achieved with sub-10 nm precision using this technique.^[73] Micro-contact printing on the other hand uses a polymeric stamp to produce a pattern on a surface. In this way, a patterned monolayer of SCO NPs was deposited on nano-spaced gold electrodes, yielding devices that showed hysteresis near room temperature in I/V curves, corresponding to the SCO behaviour of the nanoparticles.^[46, 74] These are just two examples of a range of patterning techniques that can be applied to implement SCO nanomaterials in functional devices. In Chapter 3 of this thesis it is described how we used patterning for selective growth of thin films based on the SCO complex $[\text{Fe}(\text{bapbpy})(\text{NCS})_2]$.

1.3.5. The other challenge of SCO nanomaterials

Although producing thin films and nanomaterials with SCO properties and implementing them in electronic devices are challenges by themselves, analysis of spin crossover materials at the nanoscale can be equally a challenge and may require some unconventional techniques. Magnetic susceptibility measurements with a SQUID, typically used to analyze bulk SCO samples, is very challenging for thin films or for measuring the SCO of several NPs, as the amount of material is very small. To monitor SCO in thin films, surface analysis techniques may be more suitable, *i.e.* Surface Plasmon Polariton Resonance (SPPR),^[75] (Surface Enhanced) Raman Spectroscopy (SERS),^[68, 76, 77] and Surface Plasmon Resonance (SPR).^[76] Other techniques to observe SCO in nanoparticles (on surfaces) are Scanning Tunneling Microscopy (STM)^[71] and Current Imaging Tunneling Spectroscopy (CITS).^[78] Moreover, SCO could be observed through electrical measurements by connecting single particles^[46] and single molecules^[79] between nanometer-spaced electrodes; however this is technically difficult. These examples show that, although challenging, analysis of SCO nanomaterials can be done. In the end, integration of SCO (nano)materials in electronic devices remains challenging, and showing in a convincing way that the SCO of the materials in these devices is responsible for their electronic response, perhaps even more. Yet, the field continues to advance in connection with device engineering, highlighting the technological interest in spin crossover materials.^[80]

1.4. Ruthenium complexes – a matter of light and dark

1.4.1. Light-powered molecular switches

Going one step down from iron in the periodic table, is an element that also switches: ruthenium. Ruthenium polypyridyl complexes are known to react strongly to visible light by changing their chemical structure, while when irradiation is shut off, they may return to their dark state, thus realizing a light-responsive chemical equilibrium. Particularly representative examples of light-sensitive ruthenium complexes, that show some similarity to the switching behaviour of spin crossover complexes, are ruthenium(II) polypyridyl sulfoxide and sulfone complexes that may do phototriggered S \rightarrow O linkage isomerization, either in solution or within a crystal lattice.^[81] Spin crossover and linkage isomerization materials are indeed two well-studied examples of single-crystal-to-single-crystal transformations^[82] and were both used to fabricate mechanical actuators.^[83]

In phototriggered linkage isomerization, the coordination mode of for example a dimethylsulfoxide (DMSO) ligand to the ruthenium(II) center changes, upon visible light irradiation, from a sulfur-bound mode to an oxygen-bound mode (see Figure 1.11). While doing so, the bulk properties of a single crystal of this compound (its color, for example) change as a result of molecular changes within the crystal lattice.^[81] Complexes capable of linkage isomerization act as molecular switches, as do spin crossover complexes, and they may also be integrated as light-responsive switches in devices.

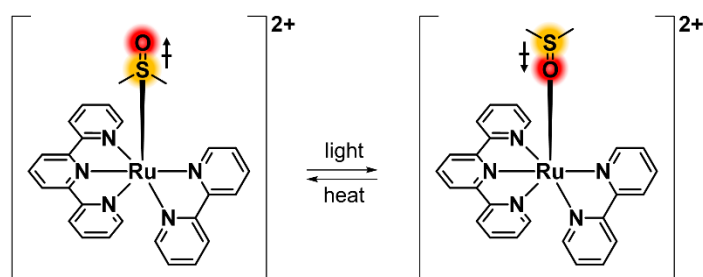


Figure 1.11: Phototriggered linkage isomerization. The DMSO ligand in $[\text{Ru}(\text{tpy})(\text{bpy})(\text{DMSO})]^{2+}$, where tpy = 2,2':6'2''-terpyridine and bpy = 2,2'-bipyridine, changes from S-bound to O-bound upon irradiation (S and O are indicated in yellow and red, respectively).^[81] The dipole moment of the DMSO ligand is indicated by the arrow.

1.4.2. Light-driven ligand exchange

Phototriggered linkage isomerization represents, however, only one of the multiple photochemical conversions that may occur when ruthenium polypyridyl complexes are irradiated with visible light. In particular, photosubstitutionally active ruthenium polypyridyl complexes exchange one (or more) ligand of their coordination sphere, by a solvent molecule, upon visible light irradiation.^[84] For example, irradiation of ruthenium polypyridyl complexes with monodentate thioether- or pyridine-based ligands leads to the dissociation of these monodentate ligands in solution, while in the dark the photodissociated ligand can coordinate back to the ruthenium center in a thermal substitution reaction.^[85] Like linkage isomerization, such systems can be described as a chemical equilibrium that is shifted by light irradiation. Figure 1.12 shows the Jablonski diagram for ruthenium polypyridyl complexes that are capable of photodissociating a ligand. Upon irradiation, the ground state 1GS is excited to a metal-to-ligand charge transfer excited state (1MLCT), followed by intersystem crossing to the corresponding triplet (3MLCT) state. From this state, one or several ligand-field (3LF) excited state can be reached thermally if the energy gap between the 3MLCT and 3LF states is sufficiently small; such internal conversion results in ligand dissociation.^[86]

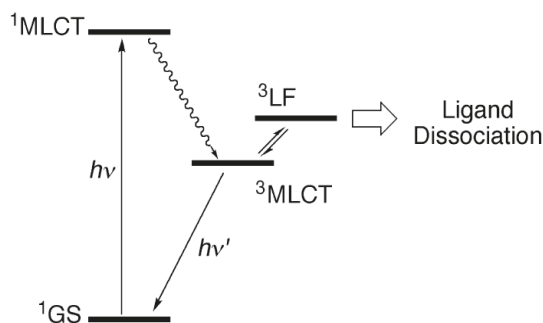


Figure 1.12: Typical Jablonski diagram for photosubstitutionally active ruthenium polypyridyl complexes. Reprinted with permission from Garner et al., © American Chemical Society, 2011.^[86]

1.4.3. Photosubstitution for therapy – ruthenium-based drugs

Photosubstitution processes raised attention in anti-cancer research, and led to prodrugs that can be switched on by *in situ* light irradiation at the tumor site. The switching of the biological activity of a ruthenium-photocaged drug is a treatment

modality often called “photo-activated chemotherapy” (PACT).^[87] In PACT, a cytotoxic compound is “caged” by carrier complex, for instance a photosubstitutionally active ruthenium complex. When this compound is caged, it is inactive and not toxic to cells. Through irradiation, the compound can be photosubstituted, which unlocks its ability to kill the cell.^[87] PACT provides hence irradiation-based selectivity of the drug towards (malignant) cells, as only irradiated cells are attacked by the activated compound, which leaves healthy, non-irradiated cells, intact.

However, a challenge in PACT is to determine where irradiation should occur, as most PACT compounds are not emissive. To solve this issue, a PACT compound was functionalized with a group that provides fluorescence only after drug cellular uptake, which can help to determine where irradiation should occur (see Chapter 7 of this thesis). In this work the ruthenium complex is a non-toxic “caging” group, and the photosubstituted ligand, a cytotoxic active pharmaceutical ingredient. One should realize though, that although a ruthenium “caging” complex may be relatively harmless as compared to the uncaged species, the complex may still interact with cellular components after it has photoreleased its cargo.

1.4.4. DNA binding of ruthenium: probes and sensors

After ligand photosubstitution, the vacant coordination site of a ruthenium complex “opens up” by weak coordination of a water ligand. The weakness of water coordination to ruthenium(II) also means that the ruthenium complex can be involved again in coordination reactions. In *vivo*, likely binding partners are biomolecules, like proteins, lipids, or DNA. More specifically, the interactions of ruthenium complexes with DNA have been studied extensively for their potential use in therapy and bio-imaging.^[88] Coordination reactions entail the direct binding of the metal center to nitrogen atoms of the DNA base pairs, which can be selective for certain nucleobases. For example, ruthenium(II) arene complexes were shown to bind specifically to the nucleobase guanine, through coordinating to the nitrogen N7 atom.^[89] Such ruthenium-purine bonds can in fact be light-sensitive as well, *i.e.* the Ru-N7 coordination bond can be broken upon irradiation with visible light.^[90] We re-evaluated this chemistry, and we found that the coordination of dGMP to $[\text{Ru}(\text{tpy})(\text{biq})(\text{OH}_2)]^{2+}$, where tpy = 2,2':6'2''-terpyridine, biq = 2,2'-biquinoline, is reversible with green light (see Chapter 6).

Next to direct coordination of nitrogen atoms from DNA to the metal center, ruthenium polypyridyl complexes can also bind to DNA via supramolecular interactions, which may involve either electrostatic interactions, hydrophobic interactions with the minor or major groove of the DNA strand, or intercalation of the ruthenium-coordinated aromatic ligands between the DNA base pairs.^[88] In some cases, the photophysical properties of ruthenium polypyridyl complexes were shown to change dramatically when they interacted with DNA. These complexes were therefore studied extensively as molecular probes for DNA sensing and nuclear imaging.

A famous example of imaging with a ruthenium DNA probe is based on the “light switch” effect, a massive increase of the phosphorescence of Ru^{II}(dppz)-based complexes (where dppz = dipyrido[3,2-a:2',3'-c]phenazine, see Figure 1.13A) upon intercalation of dppz into the DNA helix. As the dppz ligand inserts in the double strand, or even specifically in presence of DNA mismatches, the ruthenium complex becomes highly emissive, while in absence of DNA its emission is fully quenched.^[91] Through this emission switching, the complex ‘senses’ DNA, and this phenomenon has been used for example for DNA staining in cells for bio-imaging of the nucleus with confocal microscopy (Figure 1.13B).^[92] Similarly, ruthenium complexes could be used to obtain structural information by colorimetric methods. For example, specific groove binding in the minor groove of A/T-rich DNA strands changed the optical properties of ruthenium dimers in solution,^[93] while selective binding of the complex [Ru(bpy)₂(dmdppz-Br)]²⁺ (where dmdppz-Br = 11-Bromo-3,6-dimethyldipyrido[3,2-a :2',3'-c]phenazine) to G-quadruplex structures resulted in an increase of the emission of this complex.^[94]

These examples show that ruthenium complexes can bind to nucleotides and DNA regions selectively, and change their photophysical properties as their molecular environment changes. These properties makes ruthenium polypyridyl complexes especially interesting from a sensing point of view. Hence, we exploited these properties in this work to improve DNA sensing (Chapter 6) and to design a PACT drug that may show where it is located *in vivo*, prior to treatment with light (Chapter 7).

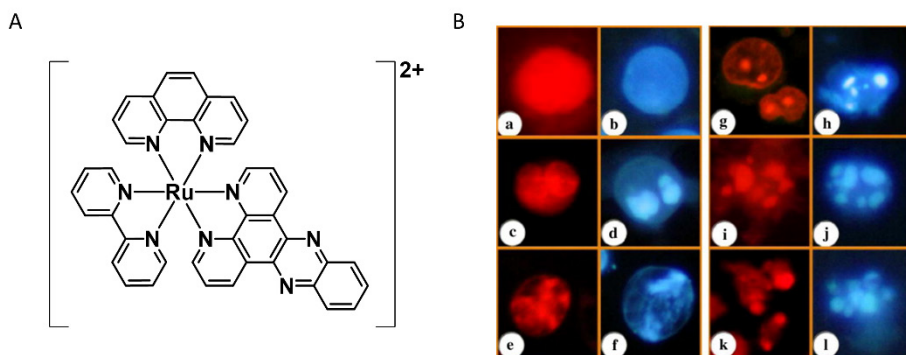


Figure 1.13: “Light switch” effect of DNA intercalation by a ruthenium complex. A) Molecular structure of $[\text{Ru}(\text{bpy})(\text{phen})(\text{dppz})]^{2+}$, where bpy = 2,2'-bipyridine, phen = 1,10-phenanthroline, and dppz = dipyrido[3,2-a:2',3'-c]phenazine. The dppz ligand intercalates in the DNA helix. B). Cell staining of NCI-H460 cancer cells with $[\text{Ru}(\text{bpy})(\text{phen})(\text{dppz})]^{2+}$ (red panels) and nuclear staining agent Hoechst (blue panels). The cells are going through multiple stages of cell death: healthy cells (a,b), nucleus splitting (c,d) collapsed nucleus (e,f), micronucleus formation (g,h), fragmented multinucleation (i,j) and late apoptotic (k,l). Figure B) reprinted with permission from Rajendiran et al., © Elsevier Inc, 2010.^[92]

1.5. Aim of this thesis

The work described in this thesis was aimed at finding out how GFET-based sensors and metal complexes can be used to produce devices for sensing, how metal complexes can improve sensing, and how metal complexes can be used as sensors themselves. First of all, in Chapter 2 we describe how single crystals of the SCO complex $[\text{Fe}(\text{bapbpy})(\text{NCS})_2]$ can be integrated in GFET devices that can detect spin switches in a contactless fashion. We found that a new mechanism of sensing, which we called chemo-electric gating, was largely responsible for the variation of the electronic properties of graphene when SCO occurred in the remote crystal. Building on this work, in chapter 3 it is discussed how to obtain nanometer-thick thin films based on the same spin crossover complex using a wet film-growing method.

In chapter 4, we removed the SCO material and discovered it was possible to build graphene sensors that were simply coated with a polymer. Depending on the nature of the polymer such sensors can detect vapours of small molecules by straightforward resistance measurements. Using an array of 3 sensors built with 3 different commercial polymer coatings we could detect and identify a large range of different chemical species.

In chapter 5, we reported GFET sensors that were fabricated on ordinary paper as a substrate. Paper is specifically interesting as a substrate, as its porosity is convenient for sensing in liquids, and it can be bent. We used these GFETs on paper to monitor the interaction between 2-deoxyguanosine monophosphate (dGMP) and a ruthenium complex: the formation of a Ru-N coordination bond in the dark and its cleavage via a photosubstitution reaction in aqueous solutions.

In the work described by the above-mentioned chapters, we used the semiconducting properties of graphene for sensing. In chapter 6, we explored the use of a ruthenium complex in nanopore sensing devices for DNA sequencing. The aim was to use the ruthenium complex to control the speed of DNA translocation through a nanopore using visible light. We envisioned that via thermal binding of a ruthenium complex to DNA in the dark, DNA can be slowed down by the additional friction of the complex. The complex can be released again under irradiation conditions which removes the friction, thus gaining control over the speed of the DNA strand by shining light.

Finally, in chapter 7 we move away from graphene-based sensing devices and into the field of photoswitchable anticancer drugs. A ruthenium complex used to photocage STF-31, a known cytotoxic inhibitor of the metabolic enzyme nicotinamide phosphoribosyltransferase (NAMPT), was equipped with an enzymatically cleavable sensor probe. The fluorescence of the probe is quenched as long as it remained in close proximity to ruthenium. However, ester cleavage by esterase enzymes released the probe from the ruthenium, unlocking its fluorescence. This design is a proof-of-concept for molecules aimed at showing a surgeon where to shine light during phototherapy. *In operando* fluorescence should show where the drug has been taken up by the cancer cells, which may be used to pinpoint where light irradiation should occur to release the cytotoxic drug STF-31, which in turn may cause cancer cell death and tumor regression.

1.6. References

- [1] K. S. Novoselov, A. K. Geim, S. V. Morozov, D. Jiang, Y. Zhang, S. V. Dubonos, I. V. Grigorieva, A. A. Firsov, *Science* **2004**, *306*, 666.
- [2] S. Bae, H. Kim, Y. Lee, X. Xu, J.-S. Park, Y. Zheng, J. Balakrishnan, T. Lei, H. R. Kim, Y. I. Song, Y.-J. Kim, K. S. Kim, B. Ozyilmaz, J.-H. Ahn, B. H. Hong, S. Iijima, *Nat. Nanotechnol.* **2010**, *5*, 574.
- [3] V. Georgakilas, M. Otyepka, A. B. Bourlinos, V. Chandra, N. Kim, K. C. Kemp, P. Hobza, R. Zboril, K. S. Kim, *Chem. Rev.* **2012**, *112*, 6156.

Chapter 1: Introduction

- [4] P. Y. Huang, C. S. Ruiz-Vargas, A. M. van der Zande, W. S. Whitney, M. P. Levendorf, J. W. Kevek, S. Garg, J. S. Alden, C. J. Hustedt, Y. Zhu, J. Park, P. L. McEuen, D. A. Muller, *Nature* **2011**, 469, 389.
- [5] Y. Zhang, L. Zhang, C. Zhou, *Acc. Chem. Res.* **2013**, 46, 2329.
- [6] J. Cai, P. Ruffieux, R. Jaafar, M. Bieri, T. Braun, S. Blankenburg, M. Muoth, A. P. Seitsonen, M. Saleh, X. Feng, K. Mullen, R. Fasel, *Nature* **2010**, 466, 470.
- [7] W. S. Hummers, R. E. Offeman, *J. Am. Chem. Soc.* **1958**, 80, 1339.
- [8] K. Erickson, R. Erni, Z. Lee, N. Alem, W. Gannett, A. Zettl, *Adv. Mater.* **2010**, 22, 4467.
- [9] W. Fu, L. Jiang, E. P. van Geest, L. M. C. Lima, G. F. Schneider, *Adv. Mater.* **2017**, 29, 1603610.
- [10] S. Das Sarma, S. Adam, E. H. Hwang, E. Rossi, *Reviews of Modern Physics* **2011**, 83, 407.
- [11] A. H. Castro Neto, F. Guinea, N. M. R. Peres, K. S. Novoselov, A. K. Geim, *Reviews of Modern Physics* **2009**, 81, 109.
- [12] A. K. Geim, K. S. Novoselov, *Nat. Mater.* **2007**, 6, 183.
- [13] F. Schwierz, *Nat Nano* **2010**, 5, 487.
- [14] F. Schedin, A. K. Geim, S. V. Morozov, E. W. Hill, P. Blake, M. I. Katsnelson, K. S. Novoselov, *Nat. Mater.* **2007**, 6, 652.
- [15] K. S. Novoselov, A. K. Geim, S. V. Morozov, D. Jiang, M. I. Katsnelson, I. V. Grigorieva, S. V. Dubonos, A. A. Firsov, *Nature* **2005**, 438, 197; A. A. Balandin, *Nat. Nanotechnol.* **2013**, 8, 549.
- [16] H. Arjmandi-Tash, L. A. Belyaeva, G. F. Schneider, *Chem. Soc. Rev.* **2016**, 45, 476.
- [17] M. Jain, H. E. Olsen, B. Paten, M. Akeson, *Genome Biol.* **2016**, 17, 239.
- [18] F. Haque, J. Li, H.-C. Wu, X.-J. Liang, P. Guo, *Nano Today* **2013**, 8, 56; Y. Goto, R. Akahori, I. Yanagi, K.-i. Takeda, *J. Hum. Genet.* **2020**, 65, 69.
- [19] B. Luan, G. Stolovitzky, G. Martyna, *Nanoscale* **2012**, 4, 1068.
- [20] S. P. Economopoulos, G. Rotas, Y. Miyata, H. Shinohara, N. Tagmatarchis, *ACS Nano* **2010**, 4, 7499.
- [21] M. Quintana, A. M. López, S. Rapino, F. M. Toma, M. Iurlo, M. Carraro, A. Sartorel, C. Maccato, X. Ke, C. Bittencourt, T. Da Ros, G. Van Tendeloo, M. Marcaccio, F. Paolucci, M. Prato, M. Bonchio, *ACS Nano* **2013**, 7, 811; X. Zhang, L. Hou, A. Cnossen, A. C. Coleman, O. Ivashenko, P. Rudolf, B. J. van Wees, W. R. Browne, B. L. Feringa, *Chem. Eur. J.* **2011**, 17, 8957; V. Georgakilas, A. B. Bourlinos, R. Zboril, T. A. Steriotis, P. Dallas, A. K. Stubos, C. Trapalis, *Chem. Commun.* **2010**, 46, 1766.
- [22] M. Grkovic, D. B. Stojanovic, A. Kojovic, S. Strnad, T. Kreze, R. Aleksic, P. S. Uskokovic, *RSC Adv.* **2015**, 5, 91280; R. N. Grass, W. J. Stark, M. Fedurco, A. Delfino, J. P. Meraldi, *WO2015193051A1*, **2015**; J. Hong, E. Bekyarova, P. Liang, W. A. de Heer, R. C. Haddon, S. Khizroev, *Sci. Rep.* **2012**, 2, 624; L. Ren, S. Huang, C. Zhang, R. Wang, W. W. Tjiu, T. Liu, *J. Nanopart. Res.* **2012**, 14, 1; M. Castelaín, G. Martínez, C. Marco, G. Ellis, H. J. Salavagione, *Macromolecules* **2013**, 46, 8980; M. B. Lerner, F. Matsunaga, G. H. Han, S. J. Hong, J. Xi, A. Crook, J. M. Perez-Aguilar, Y. W. Park, J. G. Saven, R. Liu, A. T. C. Johnson, *Nano Lett.* **2014**, 14, 2709.
- [23] X. Fang, J. Donahue, A. Shashurin, M. Keidar, *Graphene* **2015**, 4, 1; S. C. Hernández, V. D. Wheeler, M. S. Osofsky, G. G. Jernigan, V. K. Nagareddy, A. Nath, E. H. Lock, L. O. Nyakiti, R. L. Myers-Ward, K. Sridhara, A. B. Horsfall, C. R. Eddy Jr, D. K. Gaskill, S. G. Walton, *Surf. Coat. Technol.* **2014**, 241, 8.
- [24] B. M. Foley, S. C. Hernández, J. C. Duda, J. T. Robinson, S. G. Walton, P. E. Hopkins, *Nano Lett.* **2015**, 15, 4876; M. Baraket, S. G. Walton, E. H. Lock, J. T. Robinson, F. K. Perkins, *Appl. Phys. Lett.* **2010**, 96, 231501.
- [25] K. M. Daniels, B. K. Daas, N. Srivastava, C. Williams, R. M. Feenstra, T. S. Sudarshan, M. V. S. Chandrashekar, *J. Appl. Phys.* **2012**, 111, 114306.
- [26] C. K. Chan, T. E. Beechem, T. Ohta, M. T. Brumbach, D. R. Wheeler, K. J. Stevenson, *J. Phys. Chem. C* **2013**, 117, 12038; S. Eissa, C. Tlili, L. L'Hocine, M. Zourob, *Biosensors and Bioelectronics* **2012**, 38, 308.
- [27] S. J. Blanksby, G. B. Ellison, *Acc. Chem. Res.* **2003**, 36, 255.
- [28] S. Bailey, D. Visontai, C. J. Lambert, M. R. Bryce, H. Frampton, D. Chappell, *J. Chem. Phys.* **2014**, 140, 054708.

- [29] Y. Zhu, Y. Hao, E. A. Adogla, J. Yan, D. Li, K. Xu, Q. Wang, J. Hone, Q. Lin, *Nanoscale* **2016**, Ahead of Print; J. Wang, H. Zhu, Y. Xu, W. Yang, A. Liu, F. Shan, M. Cao, J. Liu, *Sens. Actuators, B* **2015**, *220*, 1186.
- [30] H. Zhang, Y. Wang, D. Zhao, D. Zeng, J. Xia, A. Aldalbahi, C. Wang, L. San, C. Fan, X. Zuo, X. Mi, *ACS Appl. Mater. Interfaces* **2015**, *7*, 16152.
- [31] A. Perry, S. J. Green, D. W. Horsell, S. M. Hornett, M. E. Wood, *Tetrahedron* **2015**, *71*, 6776.
- [32] S. Li, X. Zhong, H. Yang, Y. Hu, F. Zhang, Z. Niu, W. Hu, Z. Dong, J. Jin, R. Li, J. Ma, *Carbon* **2011**, *49*, 4239.
- [33] R. Mazzaro, M. Locritani, J. K. Molloy, M. Montalti, Y. Yu, B. A. Korgel, G. Bergamini, V. Morandi, P. Ceroni, *Chem. Mater.* **2015**, *27*, 4390; C. Ingrosso, G. V. Bianco, M. Corricelli, R. Comparelli, D. Altamura, A. Agostiano, M. Striccoli, M. Losurdo, M. L. Curri, G. Bruno, *ACS Appl. Mater. Interfaces* **2015**, *7*, 4151.
- [34] L. Cambi, L. Szegő, *Berichte der deutschen chemischen Gesellschaft (A and B Series)* **1931**, *64*, 2591.
- [35] G. A. Melson, D. H. Busch, *J. Am. Chem. Soc.* **1964**, *86*, 4830.
- [36] R. C. Stoufer, D. H. Busch, W. B. Hadley, *J. Am. Chem. Soc.* **1961**, *83*, 3732; J. S. Judge, W. A. Baker, Jr., *Inorg. Chim. Acta* **1967**, *1*, 68; M. Bacci, F. Mani, S. Midollini, *Gazz. Chim. Ital.* **1972**, *102*, 1019.
- [37] G. A. Renovitch, W. A. Baker, Jr., *J. Am. Chem. Soc.* **1967**, *89*, 6377; P. Spacu, M. Teodorescu, G. Filotti, P. Telnic, *Z. Anorg. Allg. Chem.* **1972**, *392*, 88; P. Spacu, M. Teodorescu, D. Ciomartan, *Monatsh. Chem.* **1972**, *103*, 1.
- [38] E. V. Dose, K. M. M. Murphy, L. J. Wilson, *Inorg. Chem.* **1976**, *15*, 2622; V. I. Shipilov, V. V. Zelentsov, A. V. Ablov, N. V. Gerbelev, C. V. Dyatlova, *Teor. Eksp. Khim.* **1975**, *11*, 781; M. F. Tweedle, L. J. Wilson, *J. Am. Chem. Soc.* **1976**, *98*, 4824.
- [39] J. H. Ammeter, R. Bucher, N. Oswald, *J. Am. Chem. Soc.* **1974**, *96*, 7833; J. H. Ammeter, N. Oswald, R. Bucher, D. Von Arx, *Chimia* **1975**, *29*, 525.
- [40] O. Kahn, C. J. Martinez, *Science* **1998**, *279*, 44.
- [41] M. A. Halcrow, *Chem. Lett.* **2014**, *43*, 1178.
- [42] S. Decurtins, P. Gütllich, C. P. Köhler, H. Spiering, A. Hauser, *Chem. Phys. Lett.* **1984**, *105*, 1; A. Hauser, *Chem. Phys. Lett.* **1986**, *124*, 543.
- [43] H. J. Shepherd, S. Bonnet, P. Guionneau, S. Bedoui, G. Garbarino, W. Nicolazzi, A. Bousseksou, G. Molnar, *Phys. Rev. B: Condens. Matter Mater. Phys.* **2011**, *84*, 144107/1.
- [44] A. Bousseksou, N. Negre, M. Goiran, L. Salmon, J.-P. Tuchagues, M.-L. Boillot, K. Boukheddaden, F. Varret, *The European Physical Journal B - Condensed Matter and Complex Systems* **2000**, *13*, 451.
- [45] C. Lefter, R. Tan, J. Dugay, S. Tricard, G. Molnár, L. Salmon, J. Carrey, W. Nicolazzi, A. Rotaru, A. Bousseksou, *Chem. Phys. Lett.* **2016**, *644*, 138.
- [46] F. Prins, M. Monrabal-Capilla, E. A. Osorio, E. Coronado, H. S. J. van der Zant, *Adv. Mater.* **2011**, *23*, 1545.
- [47] L. E. Orgel, *The Journal of Chemical Physics* **1955**, *23*, 1819.
- [48] L. G. Vanquickenborne, L. Haspeslagh, *Inorg. Chem.* **1982**, *21*, 2448.
- [49] O. Kahn, *VCH Publishers, Inc.(USA)*, 1993 **1993**, 393.
- [50] P. Gütllich, A. B. Gaspar, Y. Garcia, *Beilstein J. Org. Chem.* **2013**, *9*, 342.
- [51] S. Bonnet, M. A. Siegler, J. S. Costa, G. Molnar, A. Bousseksou, A. L. Spek, P. Gamez, J. Reedijk, *Chem. Commun. (Cambridge, U. K.)* **2008**, 5619.
- [52] H. Spiering, K. Boukheddaden, J. Linares, F. Varret, *Phys. Rev. B* **2004**, *70*, 184106.
- [53] K. Ridier, G. Molnár, L. Salmon, W. Nicolazzi, A. Bousseksou, *Solid State Sci.* **2017**, *74*, A1.
- [54] M. A. Halcrow, *Chem. Soc. Rev.* **2011**, *40*, 4119.
- [55] S. Zheng, N. R. M. Reintjens, M. A. Siegler, O. Roubeau, E. Bouwman, A. Rudavskyi, R. W. A. Havenith, S. Bonnet, *Chem. - Eur. J.* **2016**, *22*, 331.
- [56] Z. Arcis-Castillo, S. Zheng, M. A. Siegler, O. Roubeau, S. Bedoui, S. Bonnet, *Chem. Eur. J.* **2011**, *17*, 14826.

Chapter 1: Introduction

- [57] S. Zheng, N. R. M. Reintjens, M. A. Siegler, O. Roubeau, E. Bouwman, A. Rudavskiy, R. W. A. Havenith, S. Bonnet, *Chem. Eur. J.* **2016**, *22*, 331.
- [58] M. Mikolasek, G. Felix, W. Nicolazzi, G. Molnar, L. Salmon, A. Bousseksou, *New J. Chem.* **2014**, *38*, 1834.
- [59] A. Muraoka, J. Linares, K. Boukheddaden, "Monte Carlo simulation of the Ising-like model on size and surface effects in the spin crossover nanoparticles", 2010; A. Muraoka, K. Boukheddaden, *Mater. Sci. Forum* **2014**, *793*, 77; A. Atitoaie, R. Tanasa, C. Enachescu, *J. Magn. Magn. Mater.* **2012**, *324*, 1596.
- [60] G. Molnár, S. Rat, L. Salmon, W. Nicolazzi, A. Bousseksou, *Adv. Mater.* **2018**, *30*, 1703862.
- [61] F. Volatron, L. Catala, E. Rivière, A. Gloter, O. Stéphan, T. Mallah, *Inorg. Chem.* **2008**, *47*, 6584.
- [62] A. Grosjean, N. Daro, B. Kauffmann, A. Kaiba, J.-F. Letard, P. Guionneau, *Chem. Commun.* **2011**, *47*, 12382.
- [63] A. Rotaru, F. Varret, A. Gindulescu, J. Linares, A. Stancu, J. F. Létard, T. Forestier, C. Etrillard, *Eur. Phys. J. B* **2011**, *84*, 439.
- [64] T. Forestier, A. Kaiba, S. Pechev, D. Denux, P. Guionneau, C. Etrillard, N. Daro, E. Freysz, J.-F. Létard, *Chem. Eur. J.* **2009**, *15*, 6122.
- [65] J. R. Galan-Mascaros, E. Coronado, A. Forment-Aliaga, M. Monrabal-Capilla, E. Pinilla-Cienfuegos, M. Ceolin, *Inorg. Chem.* **2010**, *49*, 5706; E. Coronado, J. R. Galán-Mascarós, M. Monrabal-Capilla, J. García-Martínez, P. Pardo-Ibáñez, *Adv. Mater.* **2007**, *19*, 1359.
- [66] J. Linares, C.-M. Jureschi, A. Boulmaali, K. Boukheddaden, *Physica B Condens.* **2016**, *486*, 164.
- [67] Y. Raza, F. Volatron, S. Moldovan, O. Ersen, V. Huc, C. Martini, F. Brisset, A. Gloter, O. Stéphan, A. Bousseksou, L. Catala, T. Mallah, *Chem. Commun.* **2011**, *47*, 11501.
- [68] S. Cobo, G. Molnár, J. A. Real, A. Bousseksou, *Angew. Chem., Int. Ed.* **2006**, *45*, 5786.
- [69] S. Shi, G. Schmerber, J. Arabski, J. B. Beaufrand, D. J. Kim, S. Boukari, M. Bowen, N. T. Kemp, N. Viart, G. Rogez, E. Beaurepaire, H. Aubriet, J. Petersen, C. Becker, D. Ruch, *Appl. Phys. Lett.* **2009**, *95*, 043303.
- [70] M. Cavallini, *Phys. Chem. Chem. Phys.* **2012**, *14*, 11867.
- [71] T. G. Gopakumar, F. Matino, H. Naggert, A. Bannwarth, F. Tuczek, R. Berndt, *Angew. Chem., Int. Ed.* **2012**, *51*, 6262.
- [72] A. Bousseksou, G. Molnar, L. Salmon, W. Nicolazzi, *Chem. Soc. Rev.* **2011**, *40*, 3313; G. J. Dolan, *Appl. Phys. Lett.* **1977**, *31*, 337.
- [73] G. Molnár, S. Cobo, J. A. Real, F. Carcenac, E. Daran, C. Vieu, A. Bousseksou, *Adv. Mater.* **2007**, *19*, 2163.
- [74] J. Dugay, M. Giménez-Marqués, T. Kozlova, H. W. Zandbergen, E. Coronado, H. S. J. van der Zant, *Adv. Mater.* **2015**, *27*, 1288.
- [75] G. Felix, K. Abdul-Kader, T. Mahfoud, I. y. A. Gural'skiy, W. Nicolazzi, L. Salmon, G. Molnar, A. Bousseksou, *J. Am. Chem. Soc.* **2011**, *133*, 15342.
- [76] I. y. A. Gural'skiy, C. M. Quintero, K. Abdul-Kader, M. Lopes, C. Bartual-Murgui, L. Salmon, P. Zhao, G. Molnar, D. Astruc, A. Bousseksou, *J. Nanophotonics* **2012**, *6*, 063517.
- [77] C. Bartual-Murgui, A. Cerf, C. Thibault, C. Vieu, L. Salmon, G. Molnar, A. Bousseksou, *Microelectron. Eng.* **2013**, *111*, 365.
- [78] A. Grohmann, M. Haryono, K. Student, P. Mueller, M. Stocker, *Eur. J. Inorg. Chem.* **2013**, *2013*, 662.
- [79] A. C. Aragonés, D. Aravena, J. I. Cerda, Z. Acis-Castillo, H. Li, J. A. Real, F. Sanz, J. Hihath, E. Ruiz, I. Diez-Perez, *Nano Lett.* **2016**, *16*, 218; G. D. Harzmann, R. Frisenda, H. S. J. van der Zant, M. Mayor, *Angew. Chem., Int. Ed.* **2015**, *54*, 13425.
- [80] K. Senthil Kumar, M. Ruben, *Coord. Chem. Rev.* **2017**, *346*, 176.
- [81] J. J. Rack, J. R. Winkler, H. B. Gray, *J. Am. Chem. Soc.* **2001**, *123*, 2432; A. A. Rachford, J. L. Petersen, J. J. Rack, *Inorg. Chem.* **2005**, *44*, 8065; J. J. Rack, A. A. Rachford, A. M. Shelker, *Inorg. Chem.* **2003**, *42*, 7357.
- [82] A. Chaudhary, A. Mohammad, S. M. Mobin, *Cryst. Growth Des.* **2017**, *17*, 2893.

- [83] M. D. Manrique-Juárez, S. Rat, L. Salmon, G. Molnár, C. M. Quintero, L. Nicu, H. J. Shepherd, A. Bousseksou, *Coord. Chem. Rev.* **2016**, *308*, 395.
- [84] S. L. Hopkins, S. Bonnet, *Ligand Photosubstitution Reactions with Ruthenium Compounds*, in *Ruthenium Complexes*, Wiley-VCH Verlag GmbH & Co. KGaA, **2017**, 89; J. K. White, R. H. Schmehl, C. Turro, *Inorg. Chim. Acta* **2017**, *454*, 7; H. B. Ross, M. Boldaji, D. P. Rillema, C. B. Blanton, R. P. White, *Inorg. Chem.* **1989**, *28*, 1013.
- [85] R. E. Goldbach, I. Rodriguez-Garcia, J. H. van Lenthe, M. A. Sieglar, S. Bonnet, *Chem. Eur. J.* **2011**, *17*, 9924; D. V. Pinnick, B. Durham, *Inorg. Chem.* **1984**, *23*, 1440.
- [86] R. N. Garner, L. E. Joyce, C. Turro, *Inorg. Chem.* **2011**, *50*, 4384.
- [87] L. N. Lameijer, D. Ernst, S. L. Hopkins, M. S. Meijer, S. H. C. Askes, S. E. Le Dévédec, S. Bonnet, *Angew. Chem., Int. Ed.* **2017**, *56*, 11549; S. Bonnet, *Dalton Trans.* **2018**, *47*, 10330; B. S. Howerton, D. K. Heidary, E. C. Glazer, *J. Am. Chem. Soc.* **2012**, *134*, 8324; A. Li, C. Turro, J. J. Kodanko, *Acc. Chem. Res.* **2018**, *51*, 1415; A. Li, R. Yadav, J. K. White, M. K. Herroon, B. P. Callahan, I. Podgorski, C. Turro, E. E. Scott, J. J. Kodanko, *Chem. Commun.* **2017**, *53*, 3673; T. Respondek, R. N. Garner, M. K. Herroon, I. Podgorski, C. Turro, J. J. Kodanko, *J. Am. Chem. Soc.* **2011**, *133*, 17164; R. N. Garner, J. C. Gallucci, K. R. Dunbar, C. Turro, *Inorg. Chem.* **2011**, *50*, 9213; A. Li, C. Turro, J. J. Kodanko, *Chem. Commun.* **2018**, *54*, 1280.
- [88] M. R. Gill, J. A. Thomas, *Chem. Soc. Rev.* **2012**, *41*, 3179.
- [89] R. E. Morris, R. E. Aird, P. D. Murdoch, H. M. Chen, J. Cummings, N. D. Hughes, S. Parsons, A. Parkin, G. Boyd, D. I. Jodrell, P. J. Sadler, *J. Med. Chem.* **2001**, *44*, 3616; H.-K. Liu, S. J. Berners-Price, F. Wang, J. A. Parkinson, J. Xu, J. Bella, P. J. Sadler, *Angew. Chem., Int. Ed.* **2006**, *45*, 8153; Z. Adhireksan, G. E. Davey, P. Campomanes, M. Groessl, C. M. Clavel, H. Yu, A. A. Nazarov, C. H. F. Yeo, W. H. Ang, P. Dröge, U. Rothlisberger, P. J. Dyson, C. A. Davey, *Nat. Commun.* **2014**, *5*, 3462.
- [90] H. Chan, J. B. Ghayche, J. Wei, A. K. Renfrew, *Eur. J. Inorg. Chem.* **2017**, *2017*, 1679.
- [91] M. G. Walker, V. Ramu, A. J. H. M. Meijer, A. Das, J. A. Thomas, *Dalton Trans.* **2017**, *46*, 6079; A. E. Friedman, J. C. Chambron, J. P. Sauvage, N. J. Turro, J. K. Barton, *J. Am. Chem. Soc.* **1990**, *112*, 4960; C. Hiort, P. Lincoln, B. Norden, *J. Am. Chem. Soc.* **1993**, *115*, 3448; A. N. Boynton, L. Marcélis, J. K. Barton, *J. Am. Chem. Soc.* **2016**, *138*, 5020.
- [92] V. Rajendiran, M. Palaniandavar, V. S. Periasamy, M. A. Akbarsha, *J. Inorg. Biochem.* **2010**, *104*, 217.
- [93] V. Gonzalez, T. Wilson, I. Kurihara, A. Imai, J. A. Thomas, J. Otsuki, *Chem. Commun.* **2008**, 1868.
- [94] E. Wachter, D. Moyá, S. Parkin, E. C. Glazer, *Chem. Eur. J.* **2016**, *22*, 550.

Chapter 2

Contactless spin switch sensing by chemo-electric gating of graphene

Direct electrical probing of molecular materials is often impaired by their insulating nature. Here, graphene is interfaced with single crystals of a molecular spin crossover complex, [Fe(bapbpy)(NCS)₂], to electrically detect phase transitions in the molecular crystal through the variation of graphene resistance. Contactless sensing was achieved by separating the crystal from graphene with an insulating polymer spacer. Next to mechanical effects, which influence the conductivity of the graphene sheet but can be minimized by using a thicker spacer, a Dirac point shift in graphene was observed experimentally upon spin crossover. As confirmed by computational modeling, this Dirac point shift is due to the phase-dependent electrostatic potential generated inside the graphene sheet, by the crystal. This effect, named chemo-electric gating, suggests that molecular materials may serve as substrates for designing graphene-based electronic devices. Chemo-electric gating thus opens up new possibilities to electrically probe chemical and physical processes in molecular materials in a contactless fashion, from a large distance, which could enhance their use in technological applications, e.g. as sensors.

2.1. Introduction

Molecular materials, *i.e.* materials made of molecules, sometimes change their bulk properties as an effect of molecular transformations induced by external stimuli. Such materials have applications ranging from data storage, optoelectronics, photonics, nanotechnology, and quantum information processing.^[1] More specifically, transition metal complexes allow the design of a great diversity of molecular materials, particularly because the combination of metal ions and structurally diverse ligands creates a broad spectrum of chemical properties, *e.g.* phosphorescence or magnetism. Bulk transformations in molecular materials include single-crystal-to-single-crystal transformations,^[2] linkage isomerization^[3] and spin crossover for example.^[4] The sensitivity of these bulk transformations to the environment of the material makes them highly promising for sensing. However, a major drawback for the technological implementation of molecular materials for sensing is their insulating nature, which usually impairs their direct electrical readout by simple electrical measurements. Although conductive molecular materials do exist,^[5] most stimulus-responsive molecular materials, for instance iron(II) compounds with spin crossover (SCO) properties, have a negligible electrical conductivity.^[6]

Remarkably, the metal-based molecules in SCO materials have the unique ability to switch between different spin states under the influence of temperature variations, light or mechanical deformations.^[7] SCO materials have been proposed as active parts of memory devices and displays,^[8] mechanical actuators,^[9] and sensors for temperature, pressure^[10] or the presence of small molecules.^[11, 12] Integration of SCO materials into electronic devices sparked the design of SCO nanoparticles and SCO thin films, specifically for the development of sensing devices and actuators.^[13] Meanwhile, nanoparticles of SCO materials and single SCO molecules were also probed electrically by scanning tunneling microscopy^[14] or using molecular break junctions electrodes,^[15] which requires complex instrumental platforms that cannot be customized into simple electronic devices. Instead, hybrid SCO materials have been proposed in the form of adsorbed particles or molecules on graphene,^[16] where the conductivity of the graphene channel was related to spin switching events in the nanoparticles.^[17] However, the direct electrical readout of SCO phase changes in bulk SCO materials has been proven difficult due to their dielectric (insulating) nature.

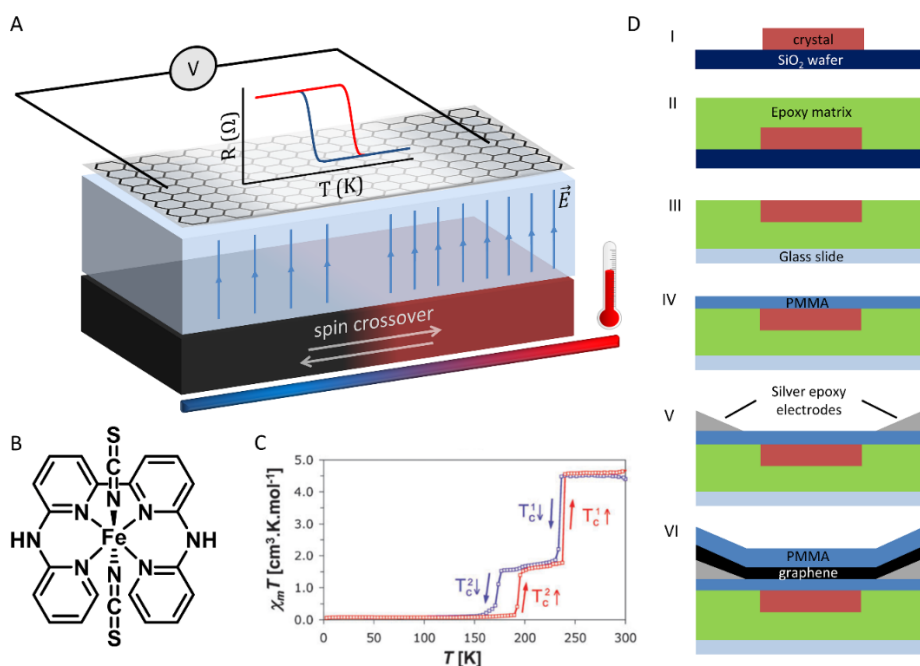


Figure 2.1: Device fabrication. A) Schematic representation of a graphene field effect transistor (GFET) constructed on a spin crossover (SCO) microcrystal, separated by a dielectric polymeric spacer (poly(methyl methacrylate), PMMA). Spin transitions are monitored remotely by changes in the electronic properties of graphene. B) Molecular structure of compound **1**, [Fe(bapbpy)(NCS)₂]. C) Magnetic susceptibility ($\chi_m T$) versus temperature for single crystals of compound **1**. Reproduced with permission.^[21] © 2008, The Royal Society of Chemistry. D) Side view step-by-step schematic representation of the fabrication of graphene transistors on SCO crystals. I: Single crystal of compound **1** grown on Si/SiO₂ wafer; II: crystal on wafer cast in epoxy resin; III: epoxy, holding crystal pulled from wafer and placed upside down on a microscope cover glass; IV: PMMA film transferred onto the epoxy and the crystal; V: solid silver epoxy electrodes placed close to crystal edges; VI: transfer of a PMMA-graphene film and removal of excess graphene to finish the device.

To address this challenge, we envisioned that graphene field effect transistors (GFETs), which are sensitive to electrostatic potential variations and have been widely used as sensing platforms,^[18, 19] can detect phase changes of switching molecular materials by using these materials as a substrate for the GFET (see Figure 2.1A). More specifically, single crystals of the coordination compound [Fe(bapbpy)(NCS)₂] (compound **1**, where bapbpy = N,N'-di(pyrid-2-yl)-2,2'-bipyridine-6,6'-diamine; see Figure 2.1B) were chosen to serve as a substrate for graphene. These crystals reversibly undergo abrupt, thermally induced SCO phase transitions (see Figure 2.1C) without suffering from mechanical damage,^[20, 21] in contrast to other SCO materials.^[22] Direct electrical probing of the molecular

state of the spin crossover crystals was achieved in GFETs fabricated over spin crossover crystals of **1** using a concept called 'chemo-electric gating' (CEG). CEG occurs through the generation of an electrostatic potential inside the graphene sheet, generated by the single crystal. Although mechanical stress induced by the SCO phenomenon also contributes to variations of the conductivity of the graphene sheet, separating the crystal and the graphene sheet by a thick (0.5 μm) polymer spacer minimized mechanical stress so that variations of the electric dipole fluctuation of each spin switching molecule inside the crystal leads to variations of the Dirac point of the graphene sheet, which is sensed through simple electrical readout. Importantly, CEG allows contactless sensing, as the SCO substrate and GFET are electrically and physically separated by a dielectric spacer that is only permeable to electrostatic effects induced by the SCO material. The polymer spacer appears hence as a critical component of such devices, as it separates graphene from the environment of the SCO material and protects it from the mechanical effects of SCO, without hampering the direct detection of the molecular transformations occurring within the SCO crystal.

2.1. Results and Discussion

2.1.1. Molecular materials as support for graphene devices

GFETs on spin crossover single crystals were fabricated from single crystals of compound **1**, typically few hundreds of micrometers in length and tens of micrometers in width, grown from a DMF/methanol solution directly on silicon wafers (Figure 2.1D, I).^[21] The crystals were cast in a flexible epoxy resin. The resin sheet embedding the crystals was removed from the wafer (II) and a slab with one single crystal only was cut from the resin sheet, and then placed on a thin glass slide with the crystal facing upwards (III). A poly(methyl methacrylate) (PMMA) spacer was then transferred on top of the crystal (IV). Source and drain electrodes were constructed close to the crystal using a silver-based epoxy and connected with copper wires (V). Last, a sheet of PMMA-graphene was transferred on top of the spacer – thus sandwiching graphene between the PMMA layers – and the excess of PMMA-graphene was removed mechanically to complete the device (VI, for a photo and top view schematic representation see Figure S2.1 and Figure S2.2). The deposition of a film-like material on the otherwise flat surface of the crystals was confirmed by AFM and Raman spectroscopy (see Figure S2.3).

Transistors typically had electrical resistance values up to 20 k Ω between the source and the drain electrodes of the device.

Next, GFETs on SCO crystals were subjected to iterative cooling-heating cycles to trigger the spin crossover events in the crystal. Notably, the spin crossover properties of the crystals used in this study appeared not to have been influenced by embedding them into the epoxy matrix; the transition temperatures and rates of the transitions were very similar to those of free crystals. Each spin crossover occurring between phase I, the phase observed at high temperature, where all molecules are high spin (HS), and phase II, the phase at intermediate temperatures where 2/3 of the molecules are low spin (LS) and 1/3 remains in the HS state,^[21] could be observed optically by a swift color change from red (phase I) to black.

2.1.2. Graphene responds to spin crossover events

Most importantly, each color change was accompanied by an abrupt change in the resistance R of graphene (see Figure 2.2A and B). Similarly, resistance variations were also observed for the transition between phase II to phase III, where all molecules in the crystal are LS; however this second transition was not studied extensively because of the difficulty to optically observe this second transition, together with the general technical difficulties of operating the SCO-graphene devices at very low temperatures (see Figure S2.4 and Figure S2.5). All results below are hence described for the high-temperature SCO only, *i.e.* the SCO between phase I and phase II.

For devices with the thickest spacer (0.5 μm), the direction of SCO was captured in the sign of dR/dt ; phase transitions gave peaks that are positive for phase I to II and negative for the reverse transition (see Figure 2.2C, black). As controls, graphene transistors were fabricated on an epoxy matrix without the presence of SCO crystals. The electrical resistance of these transistors did not show systematic abrupt variations and no distinct peaks were observed in dR/dt , even after four consecutive temperature sweep-cycles (Figure 2.2C, green). As shown in Figure 2.2A, R and the relative fraction of molecules in crystals of **1** that are the high spin state (x_{HS}), as measured by magnetic susceptibility measurements, were directly related during the temperature cycling: R and x_{HS} drastically varied at identical temperatures, *i.e.* the temperatures at which the phase transitions in fact occur. Thus, the graphene transistors successfully sensed the spin crossover events,

regardless of the thick PMMA layer (0.5 μm) separating the graphene sheet from the SCO single crystal.

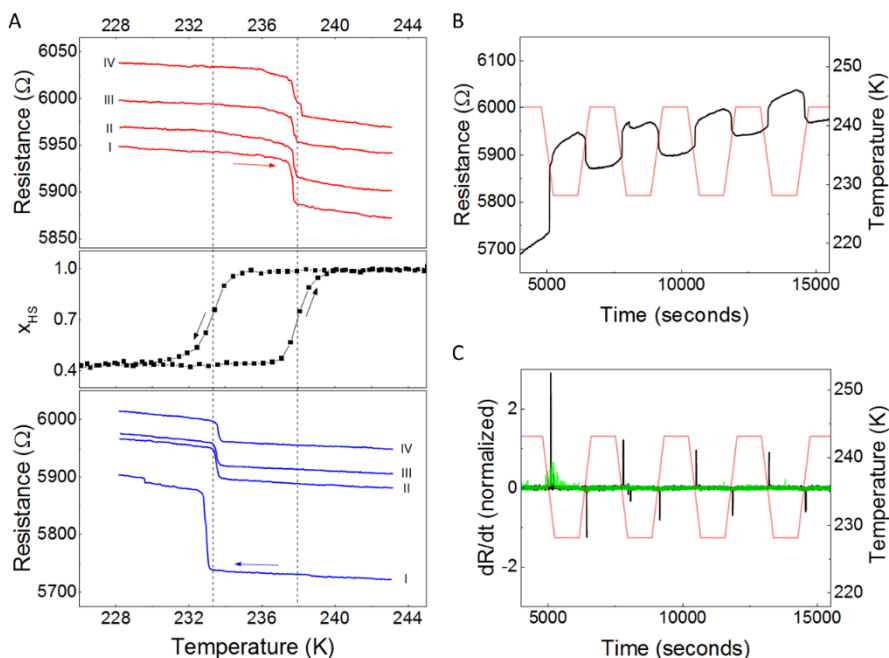


Figure 2.2: Electrical detection of spin phase transitions by chemo-electric gating. A) Electrical resistance (blue, red) and fraction x_{HS} of high spin molecules in the SCO material versus temperature (connected black squares) obtained from magnetic susceptibility measurements on SCO crystals grown on a silicon wafer; the electrical resistance during four heating/cooling cycles (indicated I to IV) in the SCO temperature region is indicated as red (heating at 2 K/min; top) and blue (cooling at 2 K/min; bottom), respectively. Dotted lines indicate phase transition temperatures from magnetic susceptibility measurements. B) Electrical resistance (black) and temperature (red) over time for a typical graphene transistor constructed on a single crystal of compound **1** (spacer thickness = 0.5 μm). C) dR/dt , normalized for R just before the first transition, and temperature versus time; graphene on a single crystal of **1** with a 0.5 μm spacer in black, reference graphene on epoxy without crystal in green.

During these experiments, the SCO properties of the crystal were retained as the device passed through several transition cycles. Notably, both transition temperatures, T_c^\uparrow and T_c^\downarrow , remained unaffected and the hysteresis loop continued to exist without significant variation of its width. The first transition usually occurred at a slightly lower temperature (see Figure 2.2A), which we interpret as a consequence of defect formation during the first SCO event. Cracks appearing in the crystal during the first transition may propagate during the following transitions (see Figure S2.6). Indeed, defects are known to serve as nucleation points for the phase transition in crystals of **1**;[23] an increase in defects could

therefore trigger the phase transition earlier (*i.e.* at slightly higher temperatures in the cooling mode) as more nucleation sites are available.

As such mechanical effects may have consequences on the integrity and conductivity of the graphene sheet lying on top of it, we studied the influence of the thickness of the polymeric PMMA spacer – *i.e.* the distance between the graphene sheet and the crystal – on $\Delta R/R_0$ upon series of spin crossover transitions. The thickness of the spacer was adjusted by using different spin coating rates (step IV in Figure 2.1D). The electrical resistance of the GFETs with the different spacers was monitored while the temperature was cycled from below and above the phase transition temperatures. Remarkably, regardless of the spacer thickness (0 μm = no spacer, 0.1 μm , 0.3 μm or 0.5 μm), the graphene devices responded to the spin crossover events. The electrical response to a spin crossover event, however, drastically decreased for increasing PMMA spacer thicknesses. As indicated above, with the thickest spacer (0.5 μm), the sign of the resistance variation $\Delta R/R_0$ – where ΔR is the resistance difference before and after the phase transition and R_0 the resistance right before the transition – was in agreement with the SCO direction (*i.e.* from phase I to phase II and vice versa): $\Delta R/R_0$ was positive when the crystal went from phase I to phase II and negative for reverse transitions. On the other hand, for devices with a spacer thickness of 0.1 μm or lower, the resistance always increased upon spin crossover, *i.e.* independently of the direction of the spin transition, while for a spacer of 0.3 μm , the sign of $\Delta R/R_0$ was always positive from phase I to II transitions but no clear trend was visible for the reverse II to I transitions (see Figure 2.3A and B; for resistance versus time and dR/dt versus time for devices with different spacers, see Figure 2.2B and C and Figure S2.7 to Figure S2.9). Moreover, for devices with a spacer of 0.3 μm or smaller, $\Delta R/R_0$ decreased with an increasing number of spin crossover cycles, while for devices with a spacer of 0.5 μm , $\Delta R/R_0$ did not vary strongly between up to four spin crossover cycles. Thus, a decrease in $\Delta R/R_0$ for the next phase transitions seemed to be mitigated by the overall increased distance between graphene and the SCO crystal, signifying a “buffering” effect imposed by the spacer. Clearly, the polymer spacer plays a critical role in the sensing mechanism, which may rely on a combination of mechanical and electrical effects (see section 2.1.5).

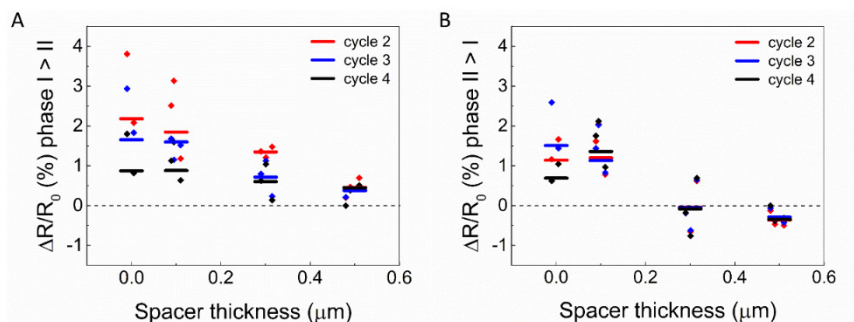


Figure 2.3: Remote detection of spin crossover with different spacer thicknesses. $\Delta R/R_0$ for devices with PMMA films of various thicknesses (0 μm , 0.1 μm , 0.3 μm and 0.5 μm). A) Device response to phase I to phase II transitions (cycle 2 to 4, resp. blue, red and green; horizontal bars represent average values of 3 devices, diamonds represent $\Delta R/R_0$ for individual devices). SCO cycle 1 is not regarded as $\Delta R/R_0$ was typically significantly higher than in following cycles, which we believe is due to initial defect formation during the first transition. B) Device response for phase II to I transitions, cycle 2 to 4 (color and symbol code the same as A). SCO cycle 1 is not regarded here as well.

Mechanical effects induced by a phase-transition in SCO materials are caused by the different volume of the coordination sphere of the metal complex in the HS and LS states, which is known to induce macroscale damages to SCO crystals.^[24] Although single crystals of compound **1** typically do not suffer appreciably from such mechanical damage as they undergo repeated SCO cycling (see Figure S2.6), the crystal lattice contracts (phase I to II) or expands (phase II to I) during spin crossover events,^[21] which could mechanically stress the graphene sheet. To study strain effects arising from the phase transitions and the ‘buffering’ effect of the spacer, the graphene sheet in electrode-free devices with different spacer thicknesses was inspected with Raman spectroscopy during multiple SCO cycles. Uniaxial strain is known to cause a red-shift of the 2D peak in the Raman spectrum of graphene.^[25] Indeed, a clear peak shift of the 2D peak occurred after the first transition, independent of the spacer thickness (phase I to II, see Figure 2.4A), while no significant shifts were observed during the following transitions (see Figure 2.4B). These results indicate that graphene was mechanically strained during the first phase transition. This effect appears to be a strong contributor to the exceptionally high resistance variation (in the positive direction) at the first transition. For the following transitions, any shifts in the 2D peak would be hidden by the large error bars, preventing any conclusion to be drawn about mechanical strain during these transitions; mechanical strain thus cannot be excluded from the sensing mechanism of the spin crossover events by such devices, but it was minimized by using thicker spacers. The standard deviation of

the 2D peak position increased most strongly in the absence of spacer, indicating a decreased homogeneity of the graphene, possibly due to mechanical damage. A 0.5 μm PMMA spacer appeared to optimally reduce the mechanical stress or damage to the graphene sheet during spin transitions; for the mechanistic studies described below we used devices with 0.5 μm spacer thickness.

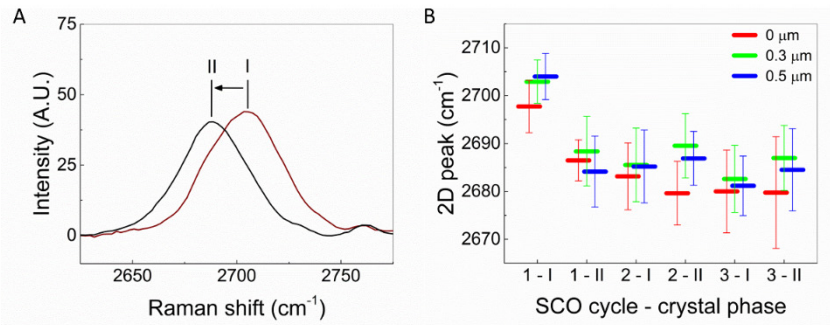


Figure 2.4: Raman spectroscopy study of electrode-free devices with different spacer thicknesses undergoing multiple spin crossover events. A) 2D peak for phase I at 243 K and phase II at 223 K in the first SCO cycle (resp. red and black, averages of 16 individual locations, 0.3 μm spacer). The spin transition caused the 2D peak of graphene to shift from 2704 cm^{-1} to 2689 cm^{-1} , an indication of mechanical strain applied to graphene. B) 2D peak after multiple transitions (spacer thickness: blue = 0 μm , red = 0.3 μm , green = 0.5 μm), each bar represents the average of 16 individual measurements at different locations on the coated crystal.

2.1.3. The Dirac peak shifts – an electrical effect

To further elucidate the spin crossover sensing mechanism of the devices, a gate electrode based on an ionic liquid (IL) was constructed on top of a graphene transistor for I/V characterization (see Figure 2.5A). To do so, the transistor was constructed with a PMMA-IL mixed film on graphene instead of pure PMMA, for gating purposes. The device was then exposed to oxygen plasma to completely remove the excess of graphene (Figure S2.2B, IV). Source and drain electrodes were protected with a dielectric epoxy resin (VII) and a droplet of the ionic liquid diethylmethyl(2-methoxyethyl)ammonium bis(trifluoromethylsulfonyl)imide (DEME-TFSI) was placed over the crystal, which was connected with a copper foil electrode to finalize the gate on top of the crystal (Figure S2.2B, VIII and Figure S2.1). When the gate voltage was swept between -1 V and $+1$ V, the ambipolar behavior of graphene was observed: the conductance of the graphene sheet ($1/R$), first decreased to reach a minimum (the Dirac point) and then immediately

increased again (see Figure 2.5B, for resistance versus gate potential see Figure S2.10).

This behavior arises from the zero-gap semiconducting nature of graphene, which has two distinct conductivity regimes. In the 'hole conductivity' regime the charge carriers are positively charged electron holes in the electron-deficient valence band, promoted by the negative electrostatic potential from the gate. In the 'electron conductivity' regime, on the other hand, the charge carriers are free electrons in the conduction band. At the Dirac point the valence band is full and the conduction band is empty, the carrier concentration and thus the conductance are minimal, *i.e.* the resistance is maximal.^[18, 26] In general, the filling of both bands is governed by the Fermi level, which can be altered by an electrostatic potential supplied by the gate electrode; hence the conductivity of the device responded to the changing gate voltage.

Interestingly, the ambipolar behavior was sensitive to spin phase transitions in the SCO crystal, which were thermally induced while performing the I/V characterization of the GFET. From 293 to 223 K, the ambipolar behavior was always characterized by a Dirac peak between 0.2 V and 0.4 V. Moreover, the Dirac point shifted over 0.1 V in the spin crossover temperature range both during the cooling and heating trajectory (see Figure 2.5C and Figure S2.11). This shift showed that the positive doping of the graphene sheet was higher at temperatures below the spin transition temperature, which indicates that phase II of the crystal induced an increased doping: the position of the Dirac peak and thus the doping level of the graphene sheet is dependent on the spin phase of the SCO crystal. Thus, the SCO crystal has a chemo-electric gating (CEG) effect on the graphene sheet. The changed doping resulted in a variation in resistance when the gate voltage was fixed (see Figure 2.5D); this is also what was observed for the devices operated without a gate electrode. Therefore, the variations in resistance in these devices arose from a Dirac point shift of the GFET, as graphene was doped differently by phase I or II of the CEG-substrate, suggesting that, next to mechanical interactions, electrostatic interactions were clearly involved in the sensing of the spin transitions by graphene.

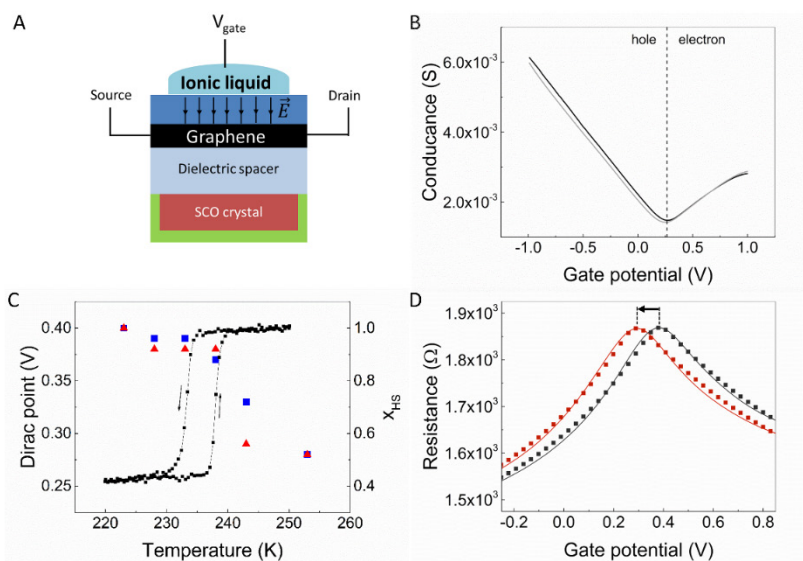


Figure 2.5: Dirac point shift induced by a spin phase transition in a top-gated GFET. A) Side-view schematic illustration of a top-gated GFET. The ionic liquid DEME-TFSI was used as it has a particularly low glass transition temperature (182 K), required for low-temperature gating.^[27] Liquid gating was performed through a mixed PMMA/DEME-TFSI (3:1) layer on graphene, with a droplet of the ionic liquid on top of this mixed layer for electrical contact. B) Conductance versus gate potential at 293 K before and after one temperature cycle (black and grey, respectively). To obtain the conductance of the graphene sheet, the contact resistance was subtracted by assuming linear conductance decrease away from the Dirac point in the hole regime, as the conductivity of graphene in pure hole or electron regions is known to be linearly proportional to the gate potential.^[18] C) Dirac point (left axis, blue squares and red triangles for the cooling and heating modes, respectively) and fraction x_{HS} of HS molecules in the SCO crystal (black squares, as determined by SQUID magnetic susceptibility measurements) *vs.* temperature. D) Resistance versus gate potential for high spin (phase I at 243 K, red line) and intermediate phase (phase II at 238 K, black line) from experimental work (lines, red and black for phase I and II, resp.) and fitting (squares, red and black for phase I and II, resp.) based on computational work. The arrow shows the direction of the Dirac point shift during a transition from phase II to phase I.

2.1.4. The electrostatic potential of the SCO crystal

At this point, we hypothesized that the Dirac point shift, and hence part of the resistivity variations of the GFET, were a consequence of long-distance chemo-electric gating of graphene by the crystal. Building on preceding electronic structure calculations,^[28] we indeed realized that the charge distribution of an individual molecule of **1** is subject to significant variations during a spin transition, which will affect the electrostatic potential created by the crystal inside the graphene sheet (see appendix Chapter 2). To support our hypothesis, we quantitatively examined the electrostatic potential induced by the spin crossover

crystal in graphene. For simplicity, we modeled the crystal surface by a set of parallel charged sheets stacked on top of each other. Each sheet consists of a 2D array of identical atoms whose charge density is distributed uniformly along the extension direction of the surface. As the charges borne notably by the Fe and N atoms of the complex (see Table S2.2) are different in the HS and LS states, not only the spacing between the charged sheets, but also the charge density borne by each sheet in phase I and II, are different; thus, the electrostatic potential induced in graphene by each sheet in either phase I or II, are different. For a thick crystalline slab of ≈ 21 to $129 \mu\text{m}$, the potential difference created in graphene between phase I and II was calculated to be ≈ 17 to 100 mV (see appendix Chapter 2), thus confirming theoretically the Dirac point shift observed experimentally when the crystal switched from one spin phase to the other (see Figure 2.5D). We note, however, that our model of stacked charged sheets offers a uniform electrostatic potential outside the crystal. Practically speaking, this approximation holds true as long as the length and width of the crystal surface are much larger than the distance between the graphene sheet and the crystal substrate, which was the case in our devices.

Based on this idea, our theoretical approach to model the resistivity ρ of graphene and fit experimental data accounts for the effect of electron-phonon coupling (ρ_{e-ph}),^[29] and of long-range scattering by the Coulomb potential of charged impurities (ρ_c),^[30-33] which according to Matthiessen's rule yields equation (1):

$$\rho = \rho_{e-ph} + \rho_c \quad (1)$$

Both ρ_{e-ph} and ρ_c were calculated as functions of the top-gate voltage V_g using the semiclassical Boltzmann transport theory,^[30] although the phonon-limited resistivity ρ_{e-ph} has been found to have only a minor contribution at the experimental temperatures $T = 238 \text{ K}$ and 243 K (ρ_{e-ph} is roughly two orders of magnitude smaller than ρ_c). In contrast, the inclusion of charge impurities is essential to reproduce the experimental results especially in view of the following two aspects: firstly, the measured charge conductivity (σ) varies approximately linearly at high carrier densities (n), which can be traced back to long-range electrostatic interactions with charged impurities;^[32, 33] secondly, the conductivity minimum near the neutrality point is indeed an indication of a residual carrier density n^* that can be induced by inhomogeneous potential fluctuations due to charged impurities^[32] Making use of a self-consistent theory as described by

Adam et al.,^[32] the experimental resistance was well reproduced for the values of $n^* = 7.2 \times 10^{11} \text{ cm}^{-2}$ and $n_i = 1.4 \times 10^{12} \text{ cm}^{-2}$, where n_i is the density of impurities (see Figure 2.5D and electronic supplementary information). On the basis of this theory and given the linearity of σ in n , the mobility of graphene was calculated to be $4.8 \times 10^2 \text{ cm}^2 \text{ V}^{-1} \text{ s}^{-1}$, using $\mu = \sigma / ne$.

Overall, the excellent fit between the experiment and theory observed in Figure 2.5D suggests that when the PMMA spacer is thick enough ($0.5 \text{ }\mu\text{m}$), chemo-electric gating is largely responsible for the contactless sensing of spin crossover by graphene field effect transistors. It should be noted that the different magnetic properties of **1** in the different spin states do not contribute here to the sensing mechanism. Whether diamagnetic or paramagnetic, the SCO crystal has no net magnetic moment in absence of an externally applied magnetic field. We can thus exclude that the changing magnetic susceptibility of the crystal upon spin crossover has any contribution to the resistance variations of the GFETs.

2.1.5. Chemo-electric gating: contactless sensing

In order to interpret how chemo-electric gating affects the transport properties of graphene simultaneously with spin switches in the crystal, one should solely consider the electrostatic effects occurring when the crystal undergoes spin crossover. As shown schematically in Figure 2.6, the electric dipole moment \vec{p} of each molecule of $[\text{Fe}(\text{bapbpy})(\text{NCS})_2]$ depends drastically on its spin state. Electronic structure calculations indicate that a spin switch shifts the molecular dipole moment by more than a factor three: in the HS state each molecule has a dipole moment of 1.1901 Debye, while in the LS state its dipole moment increases to 3.8958 Debye, giving a difference of 2.7057 Debye between the different states (see Table S2.2). Such a change is essentially the result of two electrons relocating from t_{2g} to e_g orbitals when the molecule goes from the LS to the HS state, and hence moving away from the metal towards the nitrogen ligands. Since the molecules are ordered in a single crystalline material, the dipole moments of individual molecules add up, which creates an electrostatic potential outside the crystal that interacts with the graphene sheet in a spin state-dependent manner. When a SCO event occurs and a large fraction of the molecules ($2/3$) switch their dipole moment from HS to LS at once, the electrostatic potential induced by the crystal changes in strength, and thereby modifies the Fermi level of graphene.

When the gate potential is fixed, such modifications of the Fermi level can induce large changes up to 73Ω in the resistance of graphene (see Figure 2.5D).

Usually, sensing SCO in (nano)materials relies on variations of magnetic moments,^[4] color variations,^[12] or differences in fluorescence quenching by the HS and LS molecules.^[34] In contrast, the mechanism described here relies on a combination of mechanical stress and of the electrostatic changes occurring in a SCO molecule undergoing a spin transition. This mechanism not only demonstrates that the electrostatic component of the SCO switch is strong enough to build sensors capable of detecting SCO; it also opens new routes for using combinations of graphene and molecular materials to build electronic devices capable of contactless sensing, *i.e.* sensing without the electronic part of the sensor having to be in direct contact with the sensed environment. Contactless sensing may also provide a protecting layer (the spacer in this case) preventing the electronic parts of the sensor to be in direct contact with the environment being sensed, which may lead to more stable devices.

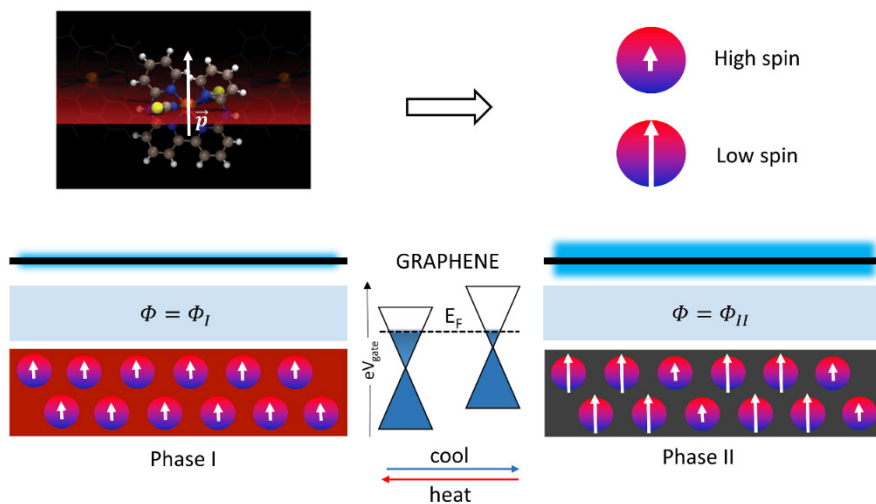


Figure 2.6: Schematic representation of chemo-electric gating of graphene. Due to changes in the electric dipole (\vec{p} , white arrows) of individual molecules in the SCO crystal, the electrostatic potential (Φ) between the SCO crystal and graphene changes, which affects the Fermi level and thus electrical properties of graphene.

2.2. Conclusions & Outlook

Based on experimental and computational investigations, we demonstrate here that phase transitions in single crystals of an electrically insulating SCO material can be probed electrically by a graphene transistor separated from the SCO crystal by a 0.5 μm -thick polymer spacer. Sensing is governed largely by chemo-electric gating, *i.e.* a variation of the Fermi level in graphene induced by the spin transition of a large number of SCO molecules, and partly by mechanical deformations of the graphene sheet (induced by cracks in the crystal undergoing SCO) which were minimized by the polymer spacer. Because the intrinsic doping of graphene by the electrostatic potential generated by the molecular changes when the phase of the crystal changes, the Dirac point and resistance of the graphene field effect transistor change as well. This resistance variation, which is a direct effect of the spin crossover event, can be easily measured by standard electronic equipment. We also discovered that the thickness of the polymer layer (at least three orders of magnitude thicker than graphene) between the crystal and graphene must be high enough to minimize mechanical effects and obtain robust and reproducible signals arising mostly from chemo-electric gating. Our design represents a new and versatile method to obtain electrical readout of spin crossover in large crystalline substrates, while the region where molecular switching occurs (the SCO crystal) and the detection circuit (the graphene sheet) are electrically separated. We believe the advantages of chemo-electric gating of graphene offers an additional design strategy towards graphene-based sensing technologies, as it allows for obtaining straightforward electrical readout of a remote change at the molecular level that impacts the dipole moment of the molecules in a material. Of course, we have focused here on thermally induced spin crossover, but we believe that this platform may be used also to fit a wide range of functional molecular materials where a change in the environment of the materials translates into a variation of the dipole moment of molecules.

2.3. References and Notes

- [1] D. W. Bruce, D. O'Hare, R. I. Walton, *Molecular Materials*, John Wiley & Sons, Ltd., **2011**.
- [2] A. Chaudhary, A. Mohammad, S. M. Mobin, *Cryst. Growth Des.* **2017**, *17*, 2893.
- [3] J. J. Rack, J. R. Winkler, H. B. Gray, *J. Am. Chem. Soc.* **2001**, *123*, 2432; M. R. Warren, S. K. Brayshaw, A. L. Johnson, S. Schiffers, P. R. Raithby, T. L. Easun, M. W. George, J. E. Warren, S. J. Teat, *Angew. Chem., Int. Ed.* **2009**, *48*, 5711.
- [4] P. Gütllich, A. B. Gaspar, Y. Garcia, *Beilstein J. Org. Chem.* **2013**, *9*, 342.
- [5] C. Faulmann, K. Jacob, S. Dorbes, S. Lampert, I. Malfant, M.-L. Doublet, L. Valade, J. A. Real, *Inorg. Chem.* **2007**, *46*, 8548; K. Takahashi, H.-B. Cui, Y. Okano, H. Kobayashi, Y. Einaga, O. Sato, *Inorg. Chem.* **2006**, *45*, 5739.
- [6] A. Rotaru, I. y. A. Gural'skiy, G. Molnár, L. Salmon, P. Demont, A. Bousseksou, *Chem. Commun.* **2012**, *48*, 4163.
- [7] J. A. Real, A. B. Gaspar, M. C. Munoz, *Dalton Trans.* **2005**, *0*, 2062.
- [8] O. Kahn, J. Kröber, C. Jay, *Adv. Mater.* **1992**, *4*, 718.
- [9] H. J. Shepherd, I. y. A. Gural'skiy, C. M. Quintero, S. Tricard, L. Salmon, G. Molnár, A. Bousseksou, *Nat. Commun.* **2013**, *4*, 2607.
- [10] C.-M. Jureschi, J. Linares, A. Boulmaali, R. P. Dahoo, A. Rotaru, Y. Garcia, *Sensors* **2016**, *16*, 187.
- [11] P. D. Southon, L. Liu, E. A. Fellows, D. J. Price, G. J. Halder, K. W. Chapman, B. Moubaraki, K. S. Murray, J.-F. Létard, C. J. Kepert, *J. Am. Chem. Soc.* **2009**, *131*, 10998; G. J. Halder, C. J. Kepert, B. Moubaraki, K. S. Murray, J. D. Cashion, *Science* **2002**, *298*, 1762; S. M. Neville, G. J. Halder, K. W. Chapman, M. B. Duriska, B. Moubaraki, K. S. Murray, C. J. Kepert, *J. Am. Chem. Soc.* **2009**, *131*, 12106; X. Bao, H. J. Shepherd, L. Salmon, G. Molnár, M.-L. Tong, A. Bousseksou, *Angew. Chem., Int. Ed.* **2013**, *52*, 1198.
- [12] M. Ohba, K. Yoneda, G. Agustí, M. C. Muñoz, A. B. Gaspar, J. A. Real, M. Yamasaki, H. Ando, Y. Nakao, S. Sakaki, S. Kitagawa, *Angew. Chem., Int. Ed.* **2009**, *48*, 4767.
- [13] K. Senthil Kumar, M. Ruben, *Coord. Chem. Rev.* **2017**, *346*, 176; G. Molnár, S. Rat, L. Salmon, W. Nicolazzi, A. Bousseksou, *Adv. Mater.* **2018**, *30*, 1703862; C. Lefter, V. Davesne, L. Salmon, G. Molnár, P. Demont, A. Rotaru, A. Bousseksou, *Magnetochemistry* **2016**, *2*, 18; G. Molnar, L. Salmon, W. Nicolazzi, F. Terki, A. Bousseksou, *J. Mater. Chem. C* **2014**, *2*, 1360; S. Suárez-García, N. N. Adarsh, G. Molnár, A. Bousseksou, Y. Garcia, M. M. Dírtu, J. Saiz-Poseu, R. Robles, P. Ordejón, D. Ruiz-Molina, *ACS Appl. Nano Mater.* **2018**, *1*, 2662.
- [14] T. Jasper-Toennies, M. Gruber, S. Karan, H. Jacob, F. Tuzcek, R. Berndt, *Nano Lett.* **2017**, *17*, 6613; T. G. Gopakumar, F. Matino, H. Naggert, A. Bannwarth, F. Tuzcek, R. Berndt, *Angew. Chem., Int. Ed.* **2012**, *51*, 6262; T. Miyamachi, M. Gruber, V. Davesne, M. Bowen, S. Boukari, L. Joly, F. Scheurer, G. Rogez, T. K. Yamada, P. Ohresser, E. Beaurepaire, W. Wulfhekel, *Nat. Commun.* **2012**, *3*, 938; A. C. Aragonès, D. Aravena, J. I. Cerdá, Z. Acís-Castillo, H. Li, J. A. Real, F. Sanz, J. Hihath, E. Ruiz, I. Díez-Pérez, *Nano Lett.* **2016**, *16*, 218.
- [15] G. D. Harzmann, R. Frisenda, H. S. J. van der Zant, M. Mayor, *Angew. Chem., Int. Ed.* **2015**, *54*, 13425; F. Prins, M. Monrabal-Capilla, E. A. Osorio, E. Coronado, H. S. J. van der Zant, *Adv. Mater.* **2011**, *23*, 1545.
- [16] M. Bernien, H. Naggert, L. M. Arruda, L. Kipgen, F. Nickel, J. Miguel, C. F. Hermanns, A. Krüger, D. Krüger, E. Schierle, E. Weschke, F. Tuzcek, W. Kuch, *ACS Nano* **2015**, *9*, 8960; D. Qiu, D.-H. Ren, L. Gu, X.-L. Sun, T.-T. Qu, Z.-G. Gu, Z. Li, *RSC Adv.* **2014**, *4*, 31323; K. Senthil Kumar, I. Šalitroš, Z. Boubegtiten-Fezoua, S. Moldovan, P. Hellwig, M. Ruben, *Dalton Trans.* **2018**, *47*, 35.
- [17] J. Dugay, M. Aarts, M. Giménez-Marqués, T. Kozlova, H. W. Zandbergen, E. Coronado, H. S. J. van der Zant, *Nano Lett.* **2017**, *17*, 186.
- [18] K. S. Novoselov, A. K. Geim, S. V. Morozov, D. Jiang, Y. Zhang, S. V. Dubonos, I. V. Grigorieva, A. A. Firsov, *Science* **2004**, *306*, 666.

- [19] D. Hernández-Sánchez, G. Villabona-Leal, I. Saucedo-Orozco, V. Bracamonte, E. Pérez, C. Bittencourt, M. Quintana, *Phys. Chem. Chem. Phys.* **2018**, *20*, 1685; W. Fu, L. Jiang, E. P. van Geest, L. M. C. Lima, G. F. Schneider, *Adv. Mater.* **2017**, *29*, 1603610.
- [20] S. Bonnet, G. Molnár, J. Sanchez Costa, M. A. Siegler, A. L. Spek, A. Bousseksou, W.-T. Fu, P. Gamez, J. Reedijk, *Chem. Mater.* **2009**, *21*, 1123.
- [21] S. Bonnet, M. A. Siegler, J. S. Costa, G. Molnar, A. Bousseksou, A. L. Spek, P. Gamez, J. Reedijk, *Chem. Commun.* **2008**, *0*, 5619.
- [22] Y. Miyazaki, T. Nakamoto, S. Ikeuchi, K. Saito, A. Inaba, M. Sorai, T. Tojo, T. Atake, G. S. Matouzenko, S. Zein, S. A. Borshch, *J. Phys. Chem. B* **2007**, *111*, 12508.
- [23] S. Bedoui, M. Lopes, S. Zheng, S. Bonnet, G. Molnár, A. Bousseksou, *Adv. Mater.* **2012**, *24*, 2475.
- [24] F. Varret, A. Slimani, K. Boukheddaden, C. Chong, H. Mishra, E. Collet, J. Haasnoot, S. Pillet, *New J. Chem.* **2011**, *35*, 2333.
- [25] T. M. G. Mohiuddin, A. Lombardo, R. R. Nair, A. Bonetti, G. Savini, R. Jalil, N. Bonini, D. M. Basko, C. Galiotis, N. Marzari, *Phys. Rev. B* **2009**, *79*, 205433; Z. H. Ni, T. Yu, Y. H. Lu, Y. Y. Wang, Y. P. Feng, Z. X. Shen, *ACS Nano* **2008**, *2*, 2301.
- [26] A. H. Castro Neto, F. Guinea, N. M. R. Peres, K. S. Novoselov, A. K. Geim, *Rev. Mod. Phys.* **2009**, *81*, 109.
- [27] T. Sato, G. Masuda, K. Takagi, *Electrochim. Acta* **2004**, *49*, 3603.
- [28] M. Kepenekian, J. S. Costa, B. Le Guennic, P. Maldivi, S. Bonnet, J. Reedijk, P. Gamez, V. Robert, *Inorg. Chem.* **2010**, *49*, 11057.
- [29] C.-H. Park, N. Bonini, T. Sohler, G. Samsonidze, B. Kozinsky, M. Calandra, F. Mauri, N. Marzari, *Nano Lett.* **2014**, *14*, 1113.
- [30] S. Das Sarma, S. Adam, E. H. Hwang, E. Rossi, *Rev. Mod. Phys.* **2011**, *83*, 407.
- [31] T. Stauber, N. M. R. Peres, F. Guinea, *Phys. Rev. B* **2007**, *76*, 205423.
- [32] S. Adam, E. H. Hwang, V. M. Galitski, S. Das Sarma, *Proc. Natl. Acad. Sci.* **2007**, *104*, 18392.
- [33] E. H. Hwang, S. Adam, S. D. Sarma, *Phys. Rev. Lett.* **2007**, *98*, 186806; T. Ando, *J. Phys. Soc. Jpn.* **2006**, *75*, 074716.
- [34] L. Salmon, G. Molnár, D. Zitouni, C. Quintero, C. Bergaud, J.-C. Micheau, A. Bousseksou, *J. Mater. Chem.* **2010**, *20*, 5499.

Chapter 3

Large-area thin films of the spin crossover complex $[\text{Fe}(\text{bapbpy})(\text{NCS})_2]$ grown selectively on graphene

Spin-crossover (SCO) nanomaterials have raised technological interest for e.g. sensors and data storage devices, yet they require a readout platform as these materials are typically electrically insulating. We have developed a method to chemically grow large-area thin films from a solution of the SCO complex $[\text{Fe}(\text{bapbpy})(\text{NCS})_2]$, with inherent selectivity for areas on silicon wafers that were coated with graphene. Extensive characterization of the films showed that the thin film material was chemically similar to single crystals of $[\text{Fe}(\text{bapbpy})(\text{NCS})_2]$, albeit the film was amorphous and the iron in the thin films was typically more oxidized than in the single crystal material. Moreover, magnetic measurements suggested that the films were SCO-active. The thin films were also grown on graphene field effect transistors (GFETs), but so far these GFETs could not detect SCO events through electronic readout. Thin films based on the SCO complex $[\text{Fe}(\text{bapbpy})(\text{NCS})_2]$ can thus be selectively grown from solution on graphene and GFETs, but whether spin switches can be electrically detected with these GFETs could not be demonstrated yet.

3.1. Introduction

Molecular materials, or switching materials, have been recognized for their great potential in technological applications like sensing and data storage.^[1] An important example is the class of spin crossover (SCO) materials, in which the switching of the spin state of individual molecules, triggered by external perturbations, results in the variations of for example the color and the magnetic susceptibility of the bulk material.^[2,3] However, a challenge in SCO research is to scale down the size of these materials, which is often required for their implementation in electronic devices.^[4] Although small-scale structures, such as nanoparticles or thin films, can be obtained using common nanotechnology techniques, SCO materials are notoriously sensitive to minute changes in their chemical composition, environment, and morphology,^[5] so that reducing the size of a 3D bulk material often comes with a trade-off; in the nanometer-size range, well-defined, complete spin crossover properties are often replaced for gradual and incomplete transitions, as was demonstrated with [Fe(pyrazine)]Pt(CN)₄ nanoparticles for example.^[6]

Here, we report the results of our investigation whether it is possible to scale down one of the dimensions of the 3D single crystal of [Fe(bapbpy)(NCS)₂] (where bapbpy = N,N'-di(pyrid-2-yl)-2,2'-bipyridine-6,6'-diamine) while keeping the bulk SCO properties intact, and if thin films of this compound could be used to build graphene-based electronic sensors as we did previously with a 3D crystal, described in Chapter 2.^[7] We used solution-based processes to grow the film, to not rely on technically complex methods like vacuum deposition.^[8] One of the challenges with such methods is to retain the spin crossover properties of the bulk material. The bulk SCO properties of [Fe(bapbpy)(NCS)₂] crystals for instance changed dramatically upon DMF inclusion in the crystal lattice as the crystallization protocol was changed.^[9] Wet thin film growth using DMF-containing solvent mixtures may hence produce thin films of different materials.

The nature of the surface on which the films grow is equally important. As has been demonstrated for example with calcite growth, surface modifications could alter the nucleation and crystal structure of materials grown on those surfaces, which could be used to tune the deposition process and properties of the deposited material.^[10] Here, graphene was used as a substrate for the thin films, as the electronic properties of graphene (high electron mobility, high surface to

volume ratio, and low noise) are very suitable for sensing: graphene is sensitive to changes in the dipole moment of nearby molecules.^[11] SCO molecules are known to undergo changes in their electric dipole when they switch their spin state from high spin to low spin;^[7, 12] interfacing a SCO thin film with graphene may thus be useful to obtain electronic readout of the spin state of the SCO film, and hence to obtain a graphene-based sensor that is sensitive to its environment. In this work, we studied the wet growth of molecular thin films of [Fe(bapbpy)(NCS)₂] on graphene-functionalized silicon wafers, and investigated GFET devices based on these films.

3.2. Results and Discussion

3.2.1. Chemical growth of thin films

Thin films were grown by vapor-liquid diffusion of methanol into a DMF solution of the [Fe(bapbpy)(NCS)₂] complex in presence of a bare or graphene-coated silicon wafer. This method differs from the classical method for growing 3D single crystals of [Fe(bapbpy)(NCS)₂], which consists of performing liquid-liquid diffusion of methanol in a DMF solution of the same complex in a plastic or glass tube.^[13] Here, vapor-liquid diffusion experiments were performed in a cuvette, sitting in a snap-cap sample vial, in which the silicon wafer was placed beforehand, positioned vertically with respect to the DMF-methanol interface (see Figure 3.1A; for a photograph, see Figure S3.1). Degassed methanol was placed outside the cuvette, into the sample vial; the methanol vapor slowly diffused into the DMF solution, which drove film growth. Depending on the surface functionalization of the wafer, the thin film started to grow on the wafers after one or several days, as confirmed visually by the light interference effect typical for thin films grown on silicon wafers. The color of thin layer materials on wafers was strongly dependent on the thickness of the film, which provided optical contrast when neighboring layers were different in thickness.

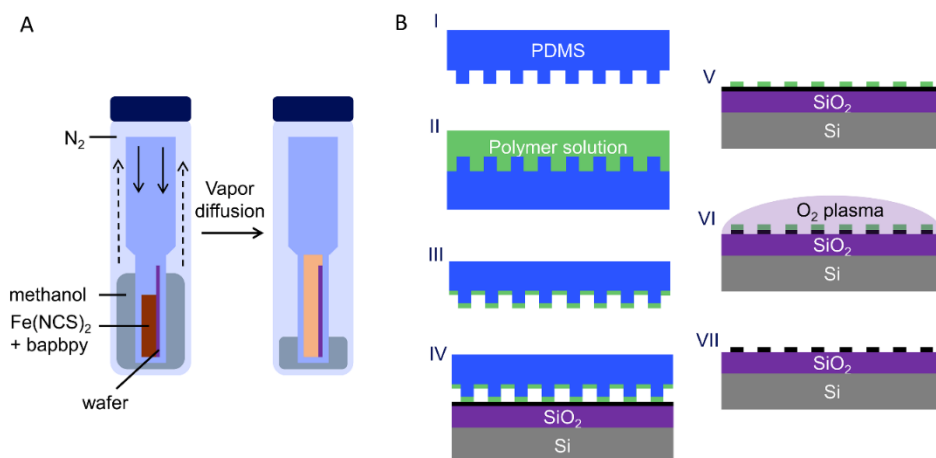


Figure 3.1: Thin film growth setup and graphene patterning. A) Schematic representation of the setup used for thin film growth via vapor diffusion of methanol. B) Schematic representation of μ -contact printing of polymer mask for graphene patterning. A stamp was created by PDMS casting on a patterned master (I), a droplet of polymer solution was placed on the stamp (II), and this solution was evenly distributed using spin coating (III). Next, the stamp was pressed on a silicon wafer, on which graphene (black line) was transferred before (IV), leaving the polymer at the surface where contact with the stamp was made (V). Oxygen plasma was used to remove unmasked graphene (VI) and the wafer was immersed in acetone to remove the mask and expose the patterned graphene (VII).

3.2.2. Thin films on graphene & patterned growth

To produce thin films of $[\text{Fe}(\text{bapbpy})(\text{NCS})_2]$ on graphene, silicon wafers were first coated with centimeter-sized monolayer graphene, grown in-house on copper using a hot-wall chemical vapor deposition (CVD) oven, and transferred onto the wafer using poly(methyl methacrylate) (PMMA) assisted transfer. The molecular films were then grown over one to ten days as described above, which afforded centimeter-sized films with relatively uniform thicknesses, as observed qualitatively by their color (see Figure S3.2 for a film grown over five days). While methanol vapor diffusion yielded thin films, direct layering of liquid methanol on top of the complex solution on the other hand typically gave single crystals of the compound very quickly, already within one hour. Simply slowing down diffusion of methanol into the DMF solution of the complex thus had a large effect on the morphology of the material that was being deposited.

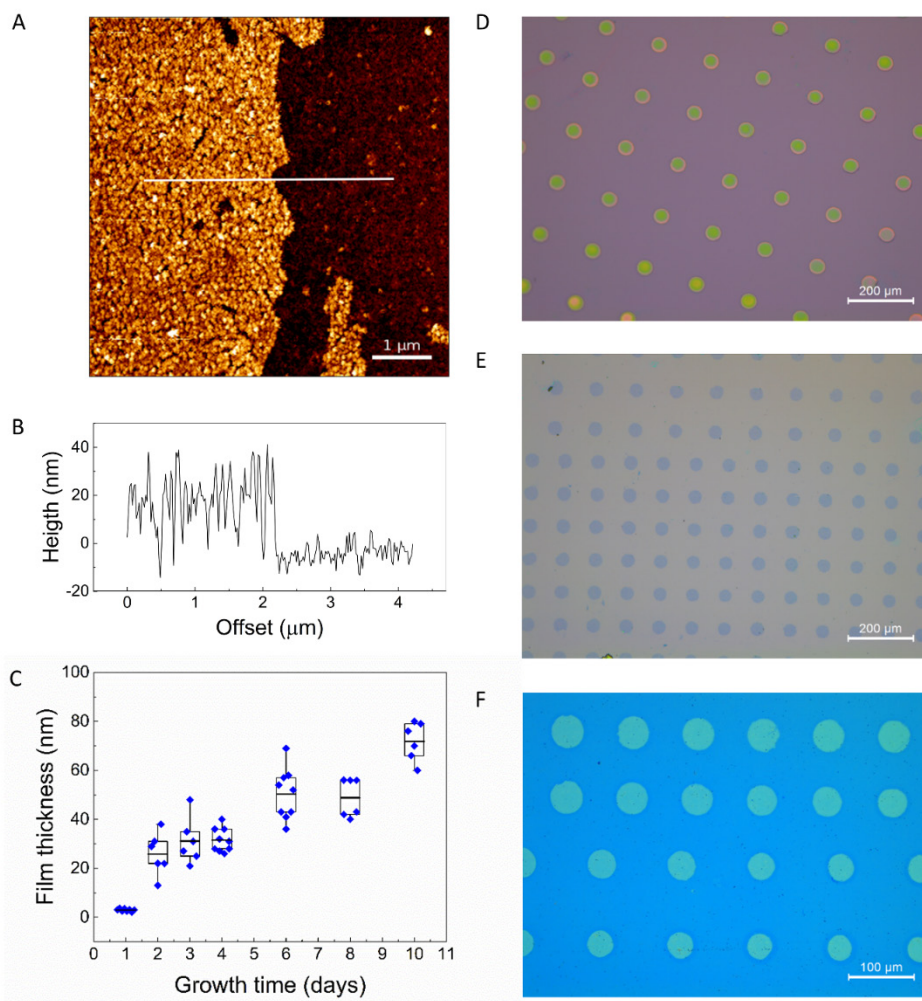


Figure 3.2: Physical characterization of thin films obtained by vapor diffusion, directly grown on graphene. A) AFM image of the thin film on large area graphene, growth time for the film was three days. The edge of the film was produced by making a scratch using a razor blade. B) Height profile of a cross section of the thin film shown in A. White line indicates the position of the cross section. C) Box plot of film thickness on large-area graphene as measured by AFM *vs.* growth time. The box represents 25-75% probability, the average is indicated by the horizontal line in the box, and whiskers represent 1- 99% probability. Blue squares are individual measurements. D) Optical image of a PMMA mask printed on graphene on silicon wafer with μ -contact printing. E) Patterned graphene on a silicon wafer, obtained by plasma etching of excess graphene and removing of the polymer mask. F) Thin films grown by vapor diffusion of methanol into a DMF solution of $[\text{Fe}(\text{bapbpy})(\text{NCS})_2]$ (15 mM) on patterned graphene after 6 days. Color contrast between graphene coated and non-coated wafer indicates the film grew faster on graphene coated areas, *i.e.* the film grows selectively on graphene.

A quantitative study of the thickness and topology of the films using atomic force microscopy (AFM) showed that already after one day of immersion, the thickness of the hybrid film was ~4 nm, as compared to ~2 nm for a bare graphene sheet, indicating that deposition already started after one day in solution. The thickness of these films was uniform at the micrometer scale (see Figure 3.2A and B). For graphene-coated wafers immersed in the solution of the complex for a longer time (up to ten days), the thickness of the film measured by AFM increased linearly with the growth time (see Figure 3.2C).

When films were grown on wafers that were partially coated with graphene (half of their surface), the thin films had a preference for growing on the graphene-coated area, as compared to the bare wafer surface (SiO₂). In other words, the thickness of the films was typically higher on graphene-coated areas of the wafer. With limited growth time (one to two days immersion in solution), the film in fact grew exclusively on graphene-coated areas, while with increased growth time, the films started to settle on the bare wafer surface as well (see Figure S3.3A-C). The preference of the film to grow on graphene was confirmed by growing films on micro-sized graphene patterns, *i.e.* graphene circles with a few tens of micrometers in diameter. To obtain micro-sized graphene patterns, a polymer solution (PMMA, 6wt% in anisole) was μ -contact printed on a graphene-coated wafer (see Figure 3.1B: I to V and Figure 3.2D). The patterned polymer layer was used as a mask for a subsequent oxygen plasma cleaning step, during which all unmasked graphene was removed. After dissolving the PMMA mask in acetone, the patterned graphene on the wafer surface was exposed to the thin film growth solution (see Figure 3.1B: VI & VII and Figure 3.2E). Thin films formed mainly on the graphene discs, similar to large-area graphene. The film thickness on each disc, but also from disc to disc, was uniform, as seen optically by the light interference effect obtained in presence of the silicon wafer background (see Figure 3.2F, and Figure S3.3D-F for large area images).

3.2.3. Chemical and morphological characterization of the film

The chemical identity of thin films grown by methanol vapor diffusion into a DMF solution of [Fe(bapbpy)(NSC)₂] (grown over multiple days) on graphene was studied using Raman spectroscopy, X-ray diffraction (XRD), energy-dispersive X-ray spectroscopy (EDX), and X-ray photoelectron spectroscopy (XPS). For thicker films, *i.e.* films with a thickness of a few tens of nanometers obtained with film growth times of >5 days, the identity of the film could

unambiguously be assigned to $[\text{Fe}(\text{bapbpy})(\text{NCS})_2]$, as the Raman peak pattern and relative intensities of the film fitted well with that of the bulk (see Figure 3.3A, for a zoom see Figure S3.4). The Raman signature of thinner films (< 20 nm) also seemed to match in wavenumber with the spectrum of the bulk material, but two major differences were observed. First, the peaks of the thinner films were much broader and hence less resolved than the Raman peaks from thicker films or from the bulk material. Second, the thiocyanate stretching mode at 2100 cm^{-1} in the bulk spectrum was absent. To explain these differences, several control experiments were done.

First, the broadening of the Raman peaks for thinner films of $[\text{Fe}(\text{bapbpy})(\text{NCS})_2]$ was studied by growing well-identified 3D single crystals of $[\text{Fe}(\text{bapbpy})(\text{NCS})_2]$ on a wafer, and then intentionally damaging them by sonicating the wafer (immersed in water) for 10 seconds, leaving a thin residue that originated from the crystal on the wafer, the chemical nature of which was hence known. The height of this thin residue was measured with AFM while Raman spectra were recorded at the same location (see Figure S3.5). With decreasing thicknesses of the crystal residue, the Raman peaks in the range of 1100 to 1600 cm^{-1} indeed broadened, starting from the well-resolved spectrum of the bulk material when the film thickness was 20 nanometer or higher, to end up with three broad peaks at 1334 , 1429 , and 1579 cm^{-1} when the thickness was less than 15 nm. Thin materials of $[\text{Fe}(\text{bapbpy})(\text{NCS})_2]$ thus show broad peaks in Raman spectroscopy.

Second, Raman spectra of 3D single crystals of $[\text{Fe}(\text{bapbpy})(\text{NCS})_2]$ grown on wafer were recorded at different orientations with respect to the Raman laser incidence. The relative intensities of several bapbpy-based Raman modes and the stretching mode of thiocyanate were found to vary with the sample rotation angle. The thiocyanate stretching mode even completely disappeared at certain angles (Figure S3.6). This effect, typical for crystalline materials, originates from the relation between the local crystallographic orientation and the polarization of the Raman laser,^[14, 15] and was used before to study the local crystallographic orientation in for example silicon crystals and thin films^[14, 16], and graphene.^[17] For thin films of $[\text{Fe}(\text{bapbpy})(\text{NCS})_2]$, rotating the wafer did not change the Raman peak intensities, indicating that the thin films were not crystalline, *i.e.* amorphous, which was confirmed by performing X-ray-diffraction (XRD) analysis of thin films of various thickness (see Figure S3.7). Overall, Raman and XRD analysis

strongly suggested that the thin films were composed of $[\text{Fe}(\text{bapbpy})(\text{NCS})_2]$ molecules arranged in an amorphous film.

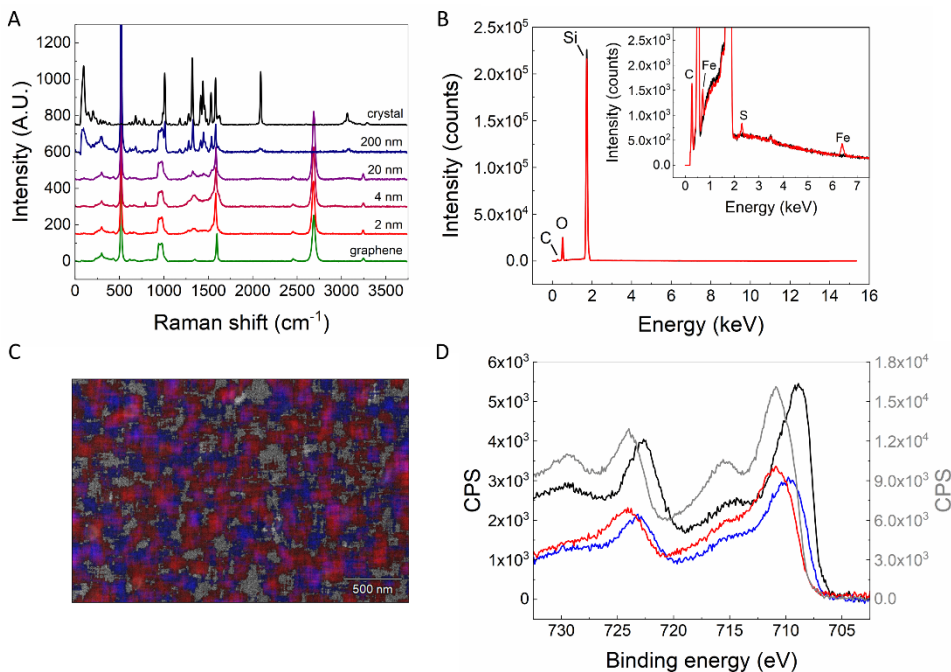


Figure 3.3: Chemical characterization of thin films obtained by vapor diffusion grown on graphene.

A) Raman spectrum of bare graphene on silicon wafer (green), graphene coated with thin films of $[\text{Fe}(\text{bapbpy})(\text{NCS})_2]$ with different thicknesses (red to blue), and single crystals of the HS phase of $[\text{Fe}(\text{bapbpy})(\text{NCS})_2]$ (black) at room temperature. B) EDX analysis of 20 nm thin film (red) and graphene (black) on silicon wafer. Inset: zoom showing iron and sulfur peaks in the thin film. C) EDX elemental mapping (atomic%) of a 20 nm thin film, overlay of iron (red) and sulfur (blue). D) XPS analysis in Fe 2p peak range of thin films grown under oxygenic conditions (red) and under nitrogen (blue) and of ground $[\text{Fe}(\text{bapbpy})(\text{NCS})_2]$ crystals (black), all on the left y-axis, and FeCl_3 (grey) on the right y-axis. Counts per second (CPS) was set to 0 at 700 eV for all spectra for clarity.

To study the elemental composition of the thin films on graphene we used energy-dispersive X-ray spectroscopy (EDX), which can be used as a qualitative method for element detection in surfaces. The EDX spectra showed small peaks at 0.28, 2.31 and 6.40 keV, characteristic for respectively carbon (C), sulfur (S) and iron (Fe), next to the intense peaks at 0.53 and 1.74 keV for oxygen and silicon from the silicon oxide wafer (see Figure 3.3B). The C, S and Fe peaks were especially more intense for thicker films. The presence of nitrogen (N) in the film could not be confirmed with EDX, as the nitrogen peak at 0.39 keV overlapped with the intense

oxygen peak. The sulfur could hypothetically originate from the etching process of copper with ammonium persulfate, however S (or Fe) was not found in the EDX spectra of control samples made of bare graphene on silicon wafer. Elemental EDX maps showed an even distribution of carbon, iron and sulfur over micrometer-sized areas (see Figure 3.3C and Figure S3.8). Overall, elemental analysis of these thin films by EDX showed that both iron and sulfur originating from the $[\text{Fe}(\text{bapbpy})(\text{NCS})_2]$ complex were present.

To further assess the chemical composition of the films and notably on the oxidation state of iron (II *vs.* III), we turned to X-ray photoelectron spectroscopy (XPS). XPS is a more powerful analysis technique than EDX, as it not only gives qualitative information about the presence of certain elements, but also has a higher sensitivity, and can provide information about the oxidation state of these elements. First of all, the full XPS spectra of the thin films (20 nm, growth time = 3 days) showed good overlap with the spectrum of the bulk $[\text{Fe}(\text{bapbpy})(\text{NCS})_2]$ crystals (see Figure S3.9). The Fe 2p peak at 709.8 eV for samples grown under nitrogen atmosphere showed a mixed iron(II)-iron(III) character. While the peak for bulk $[\text{Fe}(\text{bapbpy})(\text{NCS})_2]$, which is a pure iron(II) species, appeared at 708.9 eV (Figure 3.3D), films that were grown under atmospheric oxygen and hence contained mainly oxidized iron(III) species were characterized by an iron peak at 710.9 eV that was essentially the same as that of FeCl_3 , which was used as a reference for Fe(III). The shift to higher binding energies of the Fe 2p peak for thin films grown under nitrogen, but not in a glove box, demonstrated that these films were only partially protected from oxygen. Overall, the films grown by methanol vapor diffusion into DMF solution of the complex were amorphous films that were composed by a mixture of $[\text{Fe}^{\text{II}}(\text{bapbpy})(\text{NCS})_2]$ molecules that may show spin-crossover properties, but also of $[\text{Fe}^{\text{III}}(\text{bapbpy})(\text{NCS})_2]^+$ molecules, for which SCO has never been observed.

3.2.4. Switching behavior of the thin films

Considering that the films were (at least partially) composed of paramagnetic $[\text{Fe}^{\text{II}}(\text{bapbpy})(\text{NCS})_2]$ molecules, we examined the magnetic properties of the thin films, not grown on graphene, but grown on bare silicon wafer (20 nm) to eliminate any additional magnetic contributions due to graphene transfer. The $\chi \cdot T$ product, where χ is the magnetic susceptibility and T the temperature (as the mass of the material was unknown, we could not obtain the molar magnetic susceptibility, $\chi_m \cdot T$) was dominated by the strongly diamagnetic silicon wafer,

which gave a negative constant contribution χ_{dia} to $\chi \cdot T$. Yet after subtracting χ_{dia} , we found that variations in $\chi \cdot T$ occurred in 1 of the 4 measured samples, in both the cooling and heating mode at $T_{1/2} = 122$ K, with equal absolute magnitude Δ (see Figure 3.4). These variations resembled a semi-gradual spin transition without hysteresis, which is significantly different from the SCO behavior of 3D crystals of $[\text{Fe}(\text{bapbpy})(\text{NCS})_2]$. This difference can be attributed to the amorphous nature of the film, which would lower the cooperativity of spin crossover. The differences between the four samples were likely due to ageing of the films before measurement, during which partial aerial oxidation of the thin films could take place. Thus, these results points towards thin films that would be able to perform SCO. Yet, partial oxidation and inconsistencies in the SCO behavior of different thin film samples suggest that film should be grown in an oxygen-free environment and the thin films should be protected from O_2 .

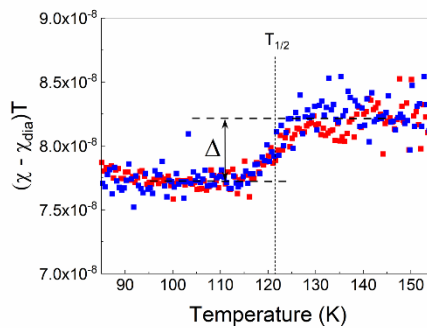


Figure 3.4: SCO behavior of an $[\text{Fe}(\text{bapbpy})(\text{NCS})_2]$ -based thin film grown on silicon wafer. Magnetic susceptibility times temperature $\chi \cdot T$ (diamagnetic contribution subtracted) *vs.* temperature of a thin film on silicon wafer (20 nm), measured by SQUID magnetometry, during cooling (blue) and heating (red) mode. The temperature was cycled between 300 and 4 K, at 2 Kmin^{-1} .

3.2.5. Thin film coated device fabrication

We used the preferred growth of films of $[\text{Fe}(\text{bapbpy})(\text{NCS})_2]$ on graphene-covered areas of the wafer to produce graphene-based GFET devices, to see whether SCO could be electrically sensed by graphene. GFETs were fabricated by transferring graphene over gold electrodes that were deposited on a silicon wafer using gold sputtering (75 nm Au @ 5 nm Cr, Figure 3.5A). We used a 6 parallel electrode configuration: the outside electrodes A & F were used to drive a current through the graphene sheet (to eliminate contact resistance) and the potential was read between the inner electrodes B & C, and D & E, referred to as MEAS(urement) and REF(erence) (Figure 3.5B). The GFETs were coated with the

thin film by using them as the substrate in thin film growing experiments. Again, the film formed preferentially on graphene-coated areas, as observed with the naked eye and with AFM. Importantly, for the GFETs it was essential to limit the film growth time, as the DMF/MeOH solutions that were used to produce the molecular thin film visibly etched the gold electrodes. Yet, when the growth time was <48 h, the electrodes could still be electrically connected with copper wire to produce intact GFETs (for a photograph of a GFET, see Figure S3.10).

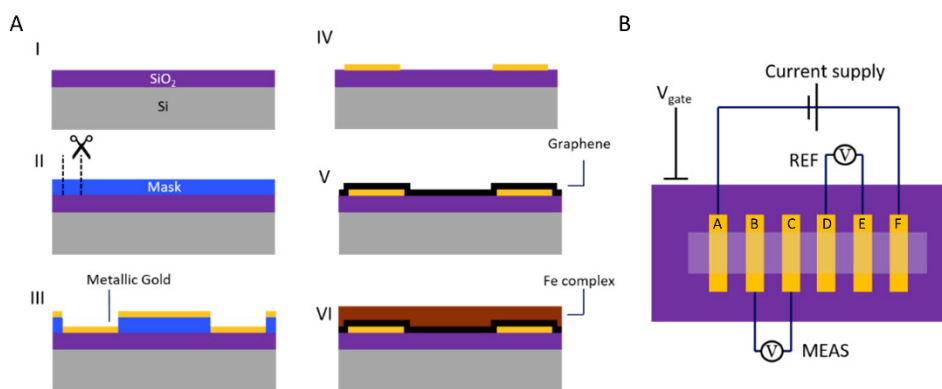


Figure 3.5: GFETs coated with a thin film. A) Schematic representation of fabrication of graphene-PMMA sensors, step by step. A silicon wafer was cleaned (I), coated with a mask with the electrodes cut out (II). A layer of chromium (5 nm), then gold (75 nm) was deposited on the masked wafer (III) and the mask was removed (IV). Next, graphene was transferred over the electrodes (V). Lastly, a thin film of the $[\text{Fe}(\text{bapbpy})(\text{NCS})_2]$ was grown on the device by methanol vapor diffusion into a DMF solution of the complex (15 mM) over one or two days (VI). B) Schematic top view of typical devices with reference (REF) and measurement (MEAS) transistors. A gate voltage was applied on the back side of the silicon wafer to apply an electric field to the GFET through the SiO₂ layer.

The thin-film coated GFETs were subjected to cooling and heating over a wide temperature range (293 to 138 K). While going through the temperature cycle, the resistance of the graphene sheets coated with the thin film was measured continuously. While SCO was recorded as a resistance variation when 3D single crystals of $[\text{Fe}(\text{bapbpy})(\text{NCS})_2]$ were interfaced with graphene (see Chapter 2),¹⁷¹ no resistance variations could be observed upon temperature cycling for the thin film-coated GFETs (see Figure S3.11). In other words, either the thin film had no SCO properties, or they occurred at temperatures outside the tested temperature range, as suggested by the magnetic susceptibility measurements (see Figure 3.4). On the other hand, the effects of such SCO properties on graphene resistance could be too minute to be observed via resistance measurements in this experimental configuration.

For now, it is difficult to distinguish between these three different interpretations. Although the physical-chemical analyses of the films strongly suggests that the thin films were composed of the same molecules as the bulk single crystals of $[\text{Fe}(\text{bapbpy})(\text{NCS})_2]$, it is not certain how much the presence of oxidized iron(III) centers disturbs the SCO properties of nearby iron(II) molecules. Also, due to technical limitations of our setup, temperatures lower than 138 K could not be reached in the graphene resistance measurements, while according to magnetometry the amorphous thin film seemed to undergo SCO at lower temperatures. Clearly, either iron(III) impurities or amorphousness^[2] prevents the film from showing the highly cooperative SCO observed in 3D crystal. Lacking abrupt transitions complicates the detection of SCO by graphene resistance measurements, as the SCO-induced changes in resistance are spread out over a large temperature range, thus leading to small signal-to-noise ratios. This effect is expected to be especially challenging considering the smaller magnitude expected for GFET functionalized with thin films, compared to GFET functionalized with thick bulk single crystals. Overall, the amorphousness of the thin films, and the resulting poor cooperativity of their SCO, appear as major challenges for the detection of SCO via resistance measurements in thin-film functionalized GFET.

3.3. Conclusions & Outlook

Thin films of the complex $[\text{Fe}(\text{bapbpy})(\text{NCS})_2]$ were produced on graphene-coated silicon wafers on a centimeter scale through a methanol vapor diffusion method. Formation of the thin film was found to be selective for graphene-coated areas of the wafer, as compared to clean silicon wafer, both for large graphene areas and for patterned, micrometer-sized patches of graphene. The thin films on graphene were tunable in thickness ranging from few nanometers to hundreds of nanometers by simply increasing the growth time. A combination of physical and chemical techniques showed that the films have the same molecules, but different morphology and crystal structure as the bulk 3D $[\text{Fe}(\text{bapbpy})(\text{NCS})_2]$ crystals, and that the iron complex in the film was partly oxidized. Magnetic susceptibility experiments hinted on the existence of spin crossover in the thin films, albeit at lower temperatures and with less cooperativity than in the bulk. Reproduction will be required to confirm this, if possible with the samples strictly protected from molecular oxygen. When these thin films were grown on graphene field effect transistors, their SCO behavior could not be detected by electrical resistance measurements, as has been reported in Chapter 2 for bulk single crystals of

[Fe(bapbpy)(NCS)₂]. We believe that, to allow detection, the cooperativity and oxidation state of the bulk material should be retained in the films. Finally, this work contributes to the field by presenting a method to produce large-area molecular thin films that form with a high preference onto graphene.

3.4. Acknowledgements

We kindly acknowledge Dr. W. Noorduin for supplying μ -contact printing stamps and for scientific discussions. Ted de Haas and Reinout Ubbink are thanked for experimental contributions and scientific discussion.

3.5. References and Notes

- [1] D. W. Bruce, D. O'Hare, R. I. Walton, *Molecular Materials*, John Wiley & Sons, Ltd., **2011**; O. Kahn, C. J. Martinez, *Science* **1998**, 279, 44.
- [2] P. Gütllich, A. B. Gaspar, Y. Garcia, *Beilstein J. Org. Chem.* **2013**, 9, 342.
- [3] J. A. Real, A. B. Gaspar, M. C. Munoz, *Dalton Trans.* **2005**, 0, 2062.
- [4] G. Molnár, S. Rat, L. Salmon, W. Nicolazzi, A. Bousseksou, *Adv. Mater.* **2018**, 30, 1703862; C. Lefter, V. Davesne, L. Salmon, G. Molnár, P. Demont, A. Rotaru, A. Bousseksou, *Magnetochemistry* **2016**, 2, 18.
- [5] K. Senthil Kumar, M. Ruben, *Coord. Chem. Rev.* **2017**, 346, 176; M. A. Halcrow, *Chem. Lett.* **2014**, 43, 1178; O. Roubeau, *Chem. Eur. J.* **2012**, 18, 15230; A. Bousseksou, G. Molnar, L. Salmon, W. Nicolazzi, *Chem. Soc. Rev.* **2011**, 40, 3313.
- [6] Y. Raza, F. Volatron, S. Moldovan, O. Ersen, V. Huc, C. Martini, F. Brisset, A. Gloter, O. Stéphan, A. Bousseksou, L. Catala, T. Mallah, *Chem. Commun.* **2011**, 47, 11501.
- [7] E. P. van Geest, K. Shakouri, W. Fu, V. Robert, V. Tudor, S. Bonnet, G. F. Schneider, *Adv. Mater.* **2020**, 32, 1903575.
- [8] T. G. Gopakumar, F. Matino, H. Naggert, A. Bannwarth, F. Tuczek, R. Berndt, *Angew. Chem., Int. Ed.* **2012**, 51, 6262.
- [9] S. Bonnet, G. Molnár, J. Sanchez Costa, M. A. Siegler, A. L. Spek, A. Bousseksou, W.-T. Fu, P. Gamez, J. Reedijk, *Chem. Mater.* **2009**, 21, 1123.
- [10] C. N. Kaplan, W. L. Noorduin, L. Li, R. Sadza, L. Folkertsma, J. Aizenberg, L. Mahadevan, *Science* **2017**, 355, 1395; J. Aizenberg, D. A. Muller, J. L. Grazul, D. R. Hamann, *Science* **2003**, 299, 1205.
- [11] W. Fu, L. Jiang, E. P. van Geest, L. M. C. Lima, G. F. Schneider, *Adv. Mater.* **2017**, 29, 1603610.
- [12] M. Kepenekian, J. S. Costa, B. Le Guennic, P. Maldivi, S. Bonnet, J. Reedijk, P. Gamez, V. Robert, *Inorg. Chem.* **2010**, 49, 11057.
- [13] S. Bonnet, M. A. Siegler, J. S. Costa, G. Molnar, A. Bousseksou, A. L. Spek, P. Gamez, J. Reedijk, *Chem. Commun.* **2008**, 0, 5619.
- [14] J. B. Hopkins, L. A. Farrow, *J. Appl. Phys.* **1986**, 59, 1103.
- [15] Q. Song, X. Pan, H. Wang, K. Zhang, Q. Tan, P. Li, Y. Wan, Y. Wang, X. Xu, M. Lin, X. Wan, F. Song, L. Dai, *Sci. Rep.* **2016**, 6, 29254.
- [16] K. Mizoguchi, S. i. Nakashima, *J. Appl. Phys.* **1989**, 65, 2583; Z. Q. Lu, T. Quinn, H. S. Reehal, *J. Appl. Phys.* **2005**, 97, 033512.
- [17] M. Huang, H. Yan, C. Chen, D. Song, T. F. Heinz, J. Hone, *Proc. Natl. Acad. Sci.* **2009**, 106, 7304.

Chapter 4

Polymer-coated graphene-based gas sensors: chemical fingerprinting by simultaneous sensing

Graphene is very suitable for building electronic sensors, for example to detect biomarkers, yet it is challenging to obtain clean, polymer-free graphene, as often polymer residues remain on the graphene sheet after polymer-assisted transfer and polymer removal. Here we show that graphene-based transistors can keep the intact transfer polymer layer, to yield sensitive sensors for the detection of various chemicals in the gas phase. In such sensors, the polymer layer functions as the sensitizing material, and it protects the graphene sheet, which reduces the noise of the device significantly. Using such systems, chemical vapors were electrically sensed down to the ppm level, and components of mixtures (methanol/ethanol and ethanol/water) could be quantified with these sensors. Yet, single polymer-coated sensors were not selective. Combining three sensors with three different polymer coatings yielded chemical fingerprint (CF) arrays with which the chemical fingerprint of 42 different chemical vapors were obtained, based on the combined response of the three individual sensors. Such “chemical fingerprinting” could be used for identification of chemical vapors: the CF array data could indeed be used to feed supervised machine learning algorithms for compound classification and identification with high accuracy. Polymer-coated graphene sensors can thus sense and identify chemical vapors at low concentrations through common electrical readout.

4.1. Introduction

In medical clinics, detection of biomarkers plays an important role as a guide for early and reliable diagnoses.^[1] The importance of biomarkers is in the deviations of their natural levels, an indication that the human body might be suffering from an illness; biomarker detection is in fact mentioned for the diagnosis of various diseases, and molecular changes in biomarkers and their relationship to illnesses have been widely researched.^[2] Breath analysis has been mentioned as a screening method to track lung cancer, for instance.^[3] Common methods to analyze a patient's breath range from small and low-cost sensors, *i.e.* solid-state (metal oxide) gas sensors that are useful for continuous measuring of known compounds, to advanced techniques based on optical spectroscopy, (high resolution) mass spectroscopy and gas chromatography for example, which have the advantage that they can be used to identify unknown compounds for untargeted breath analysis.^[4, 5] An important disadvantage of these advanced techniques is that they often require expensive equipment and trained personnel, which is too expensive if the analysis is to be performed on a large group of subjects with screening and risk assessment in mind. On the other hand, solid-state sensors typically suffer from poor selectivity, which is sometimes resolved by using sensor arrays in e-noses for combinational selectivity through pattern recognition.^[5] Ideally, devices for biosensing should detect biomarkers preferably without any pretreatment of the breath sample, meaning they need to measure in the low ppm to ppt range (the concentration range of common biomarkers in breath^[6]), should be chemically selective, and should be cheap and easy to use.

Graphene has been mentioned as a good candidate to be used in sensing devices that can fulfil these requirements.^[7, 8] Yet, to unlock its sensing potential, graphene needs to be functionalized: a molecule or (nano)particle has to be introduced on its surface, which provides graphene-based sensors with sensitivity and selectivity.^[9] To be functionalized, graphene is commonly transferred to a substrate by the aid of a transfer polymer.^[10] This polymer usually has to be removed after transfer, typically by dissolving it with acetone, to expose the graphene surface for further functionalization. However, solubilizing the polymer is not a clean procedure; often residues from the transfer polymer remain.^[11] These residues can strongly influence the electrical and thermal properties of graphene, as well as the performance of graphene-based sensors.^[12]

^{13]} On the other hand, the transfer polymer itself and the residues can also act as the functionalization itself. Indeed, sensors with poly(methyl methacrylate) (PMMA) residues on the graphene sheet have been reported to respond to a variety of chemical species (for example water, nonanal, and octanoic acid vapors), while cleaned devices did not respond to these vapors. Atomic force microscopy showed that these residues were randomly distributed on the graphene sheet.^[13] In principle the random, uncontrolled deposition of polymer residues on graphene complicate reproducibility of graphene-based sensing devices, as the amount and chemical nature of the residues can vary strongly between sensors.

In this work, the transfer polymer was left intact on the graphene sensor to circumvent this reproducibility issue, and to obtain a homogenous functional layer which is the sensitizing component of the graphene sensor. An additional advantage of leaving the transfer polymer intact is that it physically protects the graphene sheet, thereby reducing electronic noise. Polymer-coated sensors were hence made that respond reliably to a wide range of vapors, as the polymer has limited molecular-based selectivity (as opposed to streptavidin-based biotin and aptamer sensors for example, which are selective to single targets, their biological binding partner^[8]). However, different transfer polymers do give rise to different responses; by making arrays of three sensors with different transfer polymers, it was possible to generate array sensors that showed excellent chemical selectivity. The combined information of the multiple sensors creates a unique profile of sensing responses, in other words a chemical fingerprint for each chemical species. The presence of a certain chemical species in an unknown sample could then be deduced using this fingerprint, *i.e.* through algorithmic deconvolution of the signal and machine learning to obtain qualitative (the chemical identities) and quantitative information about the chemical species that was sensed (see Figure 4.1).

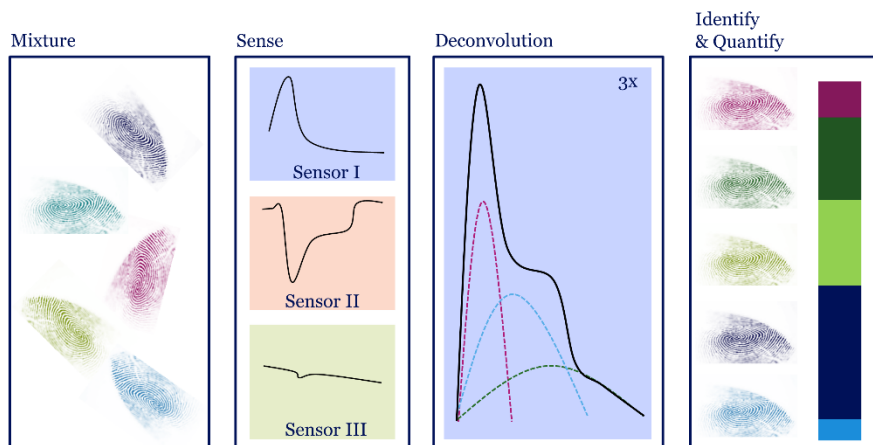


Figure 4.1: Schematic workflow of identification of chemical vapors with polymer-coated graphene-based sensors using the chemical fingerprint of the vapors. When a mixture of unknown composition is sensed by an array of sensors, the responses of these sensors could be used for the deconvolution of the sensing response by using the chemical fingerprints, *i.e.* the response of chemical vapors to the same sensors, to identify and quantify the individual components of the mixture.

4.2. Results and Discussion

4.2.1. Fabrication of polymer-coated sensors

A cleaned silicon wafer of 10 × 20 mm (see Figure 4.2A, I) was exposed to oxygen plasma and coated with masking tape that had cutouts for the electrodes of the sensor (II). Electrodes were produced using Tollens' reagent yielding a layer of metallic silver (III). After 15 minutes at room temperature, the silvering solution was removed and the wafer was rinsed with water (IV). Next, the mask was removed and the wafer was sonicated for 5 minutes in acetone and rinsed with acetone, ultrapure water, and 2-propanol to remove any remaining silver particles (V). Graphene was then transferred using polymer-assisted transfer (VI). This transfer polymer was not removed after graphene transfer. Finally, copper wires were connected to the silver electrodes and to the silicon back side of the wafer, to finish the device (for a photograph of a finished device, see Figure S4.1). Importantly, the devices had six electrodes A to F, to eliminate contact resistance by applying the current I_{AF} on the outer electrodes, while measuring the potential between the inner electrodes B & C and D & E. By installing four inner electrodes (instead of two, which is conventional in 4-terminal sensing), two transistors could be measured simultaneously, denoted MEAS(urement) (V_{BC}) and REF(erence) (V_{DE}), to make sure a sensing response is a true signal and not an

artefact in the measurement (see Figure 4.2B). Notably, for devices with polymer-coated graphene, the resistivity values of MEAS and REF were often very similar (in the range of hundreds of ohms). In contrast, for devices where graphene was exposed by removing the transfer polymer resistivity values were typically higher (kilo-ohms) and differed more strongly between MEAS and REF as compared to the polymer-coated devices, indicating that the exposed graphene devices were more defected; furthermore, their electrical noise was significantly higher.

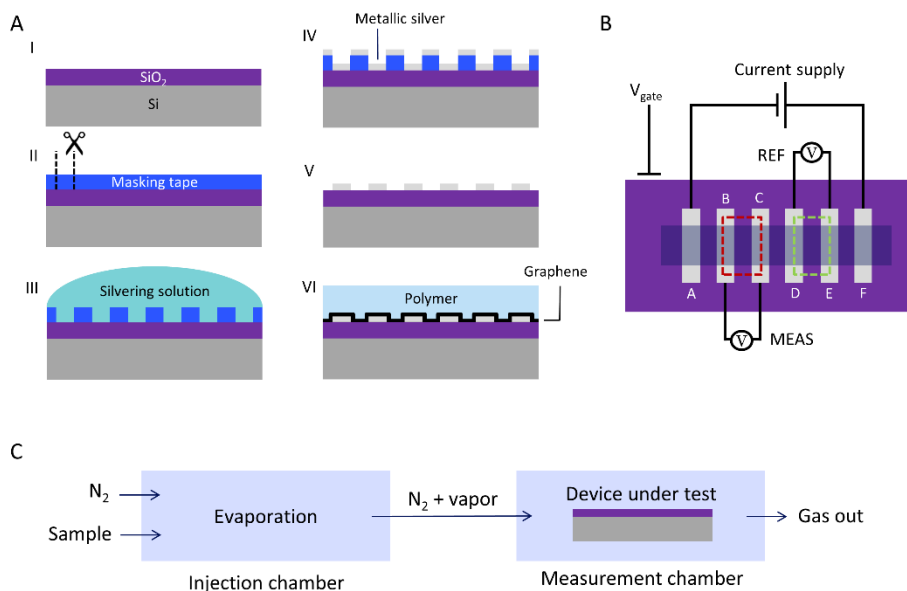


Figure 4.2: Polymer-coated sensors. A) Schematic representation (side view) of the fabrication process for a polymer-coated graphene-based sensor, step by step. A silicon wafer was cleaned and treated with O₂ plasma (I) and coated with pre-shaped masking tape (II). Next, a silvering solution, *i.e.* Tollen's reagent, was placed on the masked wafer (III) to deposit a layer of metallic silver (IV). Then, the masking tape was removed and the wafer was sonicated (V), after which polymer coated-graphene was transferred without removing the polymer (VI), and finally the electrodes A to F were connected to finish the device. B) Schematic top view of a typical device with the reference and measurement transistors (MEAS and REF, red and green rectangle, respectively). The gate voltage was set to 0 V for all devices. C) Gas measurement setup (side view), consisting of an injection chamber where volatile samples were injected with a syringe and evaporated; the vapor was then carried by a nitrogen flow to the measurement chamber containing the sensor.

4.2.2. A polymer layer for protection and reproducibility

To study in the first place if the polymer-coated sensors could give reproducible responses to chemical vapors, initially a PMMA coating was used for vapor detection experiments. For some sensors, PMMA was dissolved with acetone to

check the influence of the polymer on sensing. Devices with or without PMMA were placed in the measurement chamber that was connected to a separate injection chamber. Volatile samples were injected manually in the injection chamber (typically 10 μl per injection), and the vapors were carried to the measurement chamber by a nitrogen flow (see Figure 4.2C, for a photograph, see Figure S4.2). In a first stage, 15 volatile compounds were tested to make sure the injected volume evaporated and passed the measurement chamber within a period of 500 s, which was used as the time between two consecutive injections. The resistance R of MEAS and REF graphene sheets were measured continuously.

The transfer polymer PMMA had a large impact on the behavior of the sensors. In the plot of resistivity *vs.* time of the PMMA-coated device, the response peaks that appeared, for example when 4 injections of acetone were introduced in the injection chamber, were very similar in shape and intensity. On the other hand, when the PMMA layer was absent, no response to acetone could be observed at all (see Figure 4.3A). The large difference between PMMA-coated devices and PMMA-free devices highlighted the protective role of the polymer for the graphene sensors, and its critical role for gas sensing. In fact, PMMA-coated graphene sensors responded to a large number of the compounds that were injected (see Table S4.1). However, the time responses of the resistance to the various compounds injected were often different (see Figure S4.3). To compare vapor responses, the sheet resistivity ρ ($\rho = R \times w / l$, where w and l are the width and the length of the sheet) was normalized with respect to the resistivity value at the start of the measurement ($\rho_{t=0}$) to obtain ρ_{norm} (where $\rho_{norm} = \rho / \rho_{t=0} \times 100$). The curve ρ_{norm} *vs.* time was integrated over a range of 500 s with a linear baseline correction, starting from the moment of injection, to obtain the peak area A_{norm} (see Figure 4.3B). Most of the times, the ρ *vs.* time curves obtained for a series of multiple injections of the same compound were reproducible (water was an exception here, as discussed in section 4.2.3). The peak areas A_{norm} were reproducible as well for all compounds except water, as indicated by the small error bars on the average peak area (see Figure 4.3C and Table S4.1), which is required to identify the chemical vapors through analyzing the sensor response.

In fact, some compounds could already be identified by the value of the peak area for PMMA-coated devices. Acetonitrile, for example, was the only compound of this set that gave a negative peak area. Interestingly, the peak areas for the alcohol series (methanol, ethanol, 1-propanol, and 2-propanol) which are chemically very

similar, strongly differed, showing that these devices can reliably differentiate between chemically similar compounds. Similarly, different aromatic species showed distinct responses: pyridine for example gave a strong response, while toluene, anisole and benzonitrile gave low responses. On the other hand, some compounds could not be detected as no peak in R vs. time appeared. This is the case for diethyl ether and pentane for example. We believe that these differences in response of the vapors are due to the different interactions of the sensed molecules with the PMMA layer as the vapor is absorbed by the layer, leading to specific conformational changes in the PMMA layer. Graphene is sensitive to such changes, and hence the electronic properties of graphene change, giving a sensing response. Over time, the nitrogen flow desorbs the molecule, and the resistivity returns to the baseline.

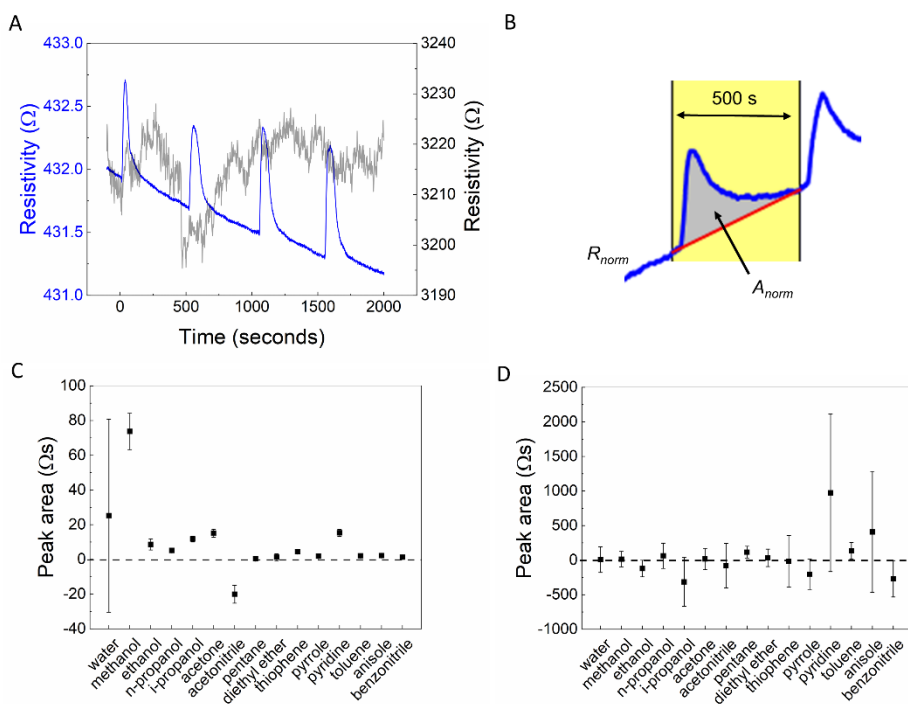


Figure 4.3: PMMA-graphene based devices responded to manually injected chemical vapors. A) Resistivity ρ vs. time for a typical PMMA-coated (blue) and PMMA-free (grey) graphene device. Acetone was injected 4 times, 10 μ l per injection, with the first injection at $t = 0$ s, then at intervals of 500 s. B) Integration of the peak area from the normalized resistivity ρ_{norm} over 500 s, yielded the peak area, A_{norm} . C-D) Peak area (A_{norm}), averaged for each compound, for a PMMA coated device (C) and PMMA-free graphene device (D). Each data point represents 4 sequential injections of 10 μ l of the same compound with 500 s between each injection, except acetone, which was injected 6 times. The data that was used to construct C and D is shown in Table S4.1.

Notably, the response reproducibility that was obtained with PMMA-coated graphene devices was not achieved with exposed graphene devices, as the error bars in the peak intensities for the different compounds for these devices were much larger than the errors for PMMA-coated devices (see Figure 4.3D and Table S4.1). Thus, the reproducibility of the responses to a large set of compounds was strongly enhanced by the presence of the PMMA coating, and the sensor could differentiate between various compounds, even if they are chemically similar.

4.2.3. Water saturation, and how to overcome saturation

The response of PMMA-coated devices appeared to be not reproducible for water. When water was injected, the device with PMMA coating quickly saturated with water, as shown by a large decrease of $\Delta\rho$ for the 2nd, 3rd and 4th injection as compared to the 1st injection, see Figure 4.4A. The saturation and long recovery time for water (>500 s) was problematic for these sensors, yet could be overcome by subsequent injections of acetonitrile. After saturation of a sensor by injecting water ($4 \times 10 \mu\text{l}$), the resistivity of the sensor could be decreased by injecting acetonitrile ($4 \times 10 \mu\text{l}$), back to values that were even below the initial value (*i.e.* before the first water injection, see Figure 4.4A). Alternating injections of water and acetonitrile showed that the sensitivity of the sensor to water was restored every time after an acetonitrile injection, as indicated by the positive peak area for water after an injection of acetonitrile, in contrast to the negative peak areas for sequential injections of water (see Figure 4.4B and C). Importantly, the error bars on the average peak area for water were severely reduced by following each water injection with an acetonitrile injection instead of another water injection (see Figure 4.4D), showing that saturation of the sensor with water could be cleared by flushing the sensor with acetonitrile. Acetonitrile thus functioned as a “reset button” for PMMA-coated sensors after saturation with water.

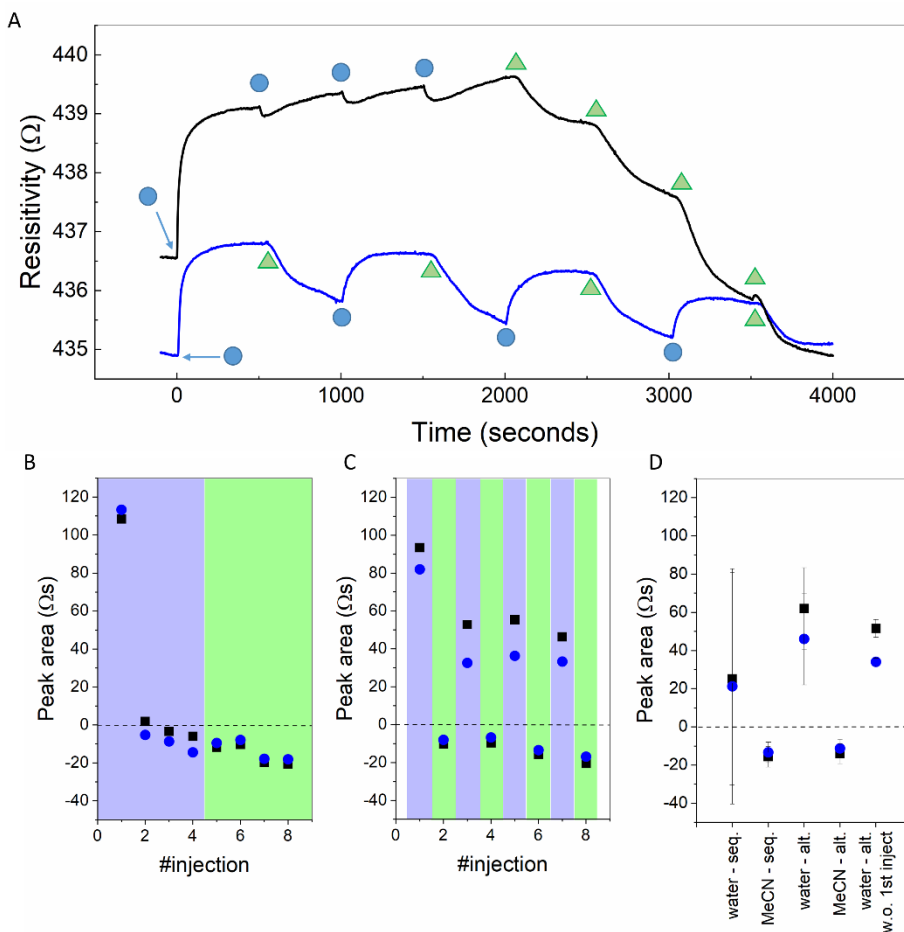


Figure 4.4: Acetonitrile as a “reset button” for PMMA-coated sensor saturation by water. A) Resistivity ρ vs. time for sequential and alternating injections (black and blue line, respectively) of water and acetonitrile (blue circles and green triangles, respectively), 10 μl per injection. B-C) Peak area for sequential (B) and alternating (C) injection of water and acetonitrile for MEAS (V_{BC} , blue) and REF (V_{DE} , black), light blue box = water, light green box = acetonitrile, 10 μl per injection. D) Averages of the peak area for water and acetonitrile when injected sequentially or alternating (for the last input, the data from the first water injection was during alternated injection was excluded).

4.2.4. Detection limit & component quantification in mixtures

To evaluate the sensing performance and limitations of the PMMA-coated devices, methanol was used either pure or in mixtures, in particular because the sensor gave strong responses on exposure to methanol. First, we studied how the sensor responded to lower amounts of methanol by lowering the injected volume. Methanol could be detected with injected volumes in the range of 5 to 0.1 μl (see

Figure 4.5A). Moreover, the peak area of the response decreased as the amount of methanol was lowered, which followed a linear trend (Figure 4.5B). The peak area was thus directly related to the amount of the sample that was injected, which is useful for compound quantification with PMMA-coated graphene sensors.

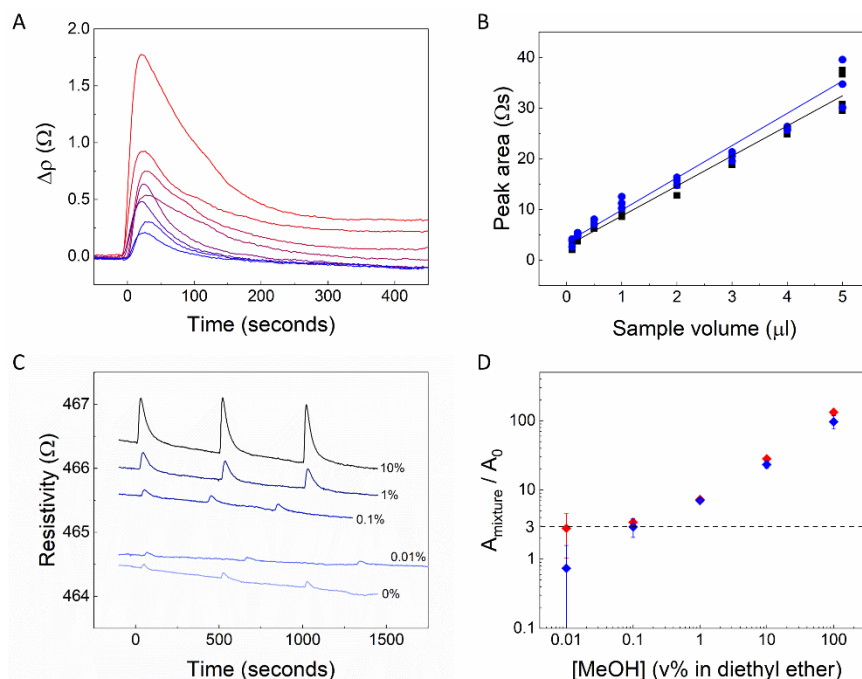


Figure 4.5: Detection limit for methanol and component quantification in mixtures for PMMA-coated devices. A) Resistivity change $\Delta\rho$ of a PMMA-coated graphene sensor (MEAS, V_{BC}) upon injection of decreasing amounts of pure methanol (from red to blue: 5, 4, 3, 2, 1, 0.5, 0.2, and 0.1 μl). B) Peak area A_{norm} from normalized resistivity vs. volume of methanol injection, MEAS (blue, $R^2 = 0.9814$) and REF (V_{DE} , black, $R^2 = 0.971$). C) Resistivity (MEAS) upon multiple injections (10 μl per injection) of methanol/ether mixtures, the percentage indicates the volumetric concentration of methanol. D) Peak area A_{norm} of a methanol/ether mixture relative to the peak area for pure ether, $A_{mixture}/A_0$, vs. v% methanol in diethyl ether for MEAS (blue) and REF (red). When $A_{mixture}/A_0 > 3$, (indicated by the dashed line), methanol is considered as “detected”.

To find the detection limit of these sensors for methanol, solutions of methanol in diethyl ether (0, 0.01, 0.1, 1, 10 and 100v% methanol) were injected, using diethyl ether as an “inert” carrier solvent here, as ether gave only a very small response on the sensor (see Figure 4.5C and Figure S4.4). Quantification of the amount of methanol (by peak area) in ether was done using a sensing threshold of $A_{mixture}/A_0 \geq 3$, where $A_{mixture}$ is the peak area of methanol solution in diethyl ether and A_0 is the peak area of pure diethyl ether. The factor 3 was chosen, as

signal to noise usually has to be higher than 3 to claim the detection of a species. The background peak from diethyl ether, here functioning as a carrier solvent, was considered as the noise in this experiment. The signal will not be affected significantly with decreasing amount of diethyl ether in the mixture, so we can assume this contribution as continuous throughout the experiment. Using these criteria, methanol presence in the solutions could be detected down to 0.1v% methanol in 10 μl injections (see Figure 4.5D), which corresponds to 0.01 μl of methanol. With the system volume estimated to be 0.5 l, the detection limit of methanol for these sensors was estimated to be 6 ppm. The responses from PMMA-coated graphene devices can thus be used to determine the composition of methanol/ether mixtures and to find the detection limit of the sensor.

To further analyze the sensor response to mixtures of chemicals, we investigated first mixtures of ethanol and methanol, then mixtures of water and ethanol. A series of different concentrations of methanol in ethanol (0 to 100v%, injections of 1 μl , see Figure 4.6A) showed a strong linear relationship between the peak area of the normalized resistivity *vs.* methanol content (Figure 4.6B). Due to the specific response of the PMMA sensors with water, quantification of the ethanol content in water was not determined by considering the peak area of the resistivity traces (Figure 4.6C), but by analyzing the full-width-half-maximum (FWHM) of the resistivity trace (after linear baseline subtraction). We found a linear relationship between the FWHM, an indication of the tail of the peak, and concentration of water in ethanol (Figure 4.6D): the shorter the tail of the peak indicated by a low FWHM value, the higher the ethanol content, likely because ethanol was easier to be removed from the sensor than water. This linear relationship may be used to determine the ethanol content in water. The PMMA coated sensor can thus be used for quantification of the composition of (binary) mixtures of chemically similar compounds.

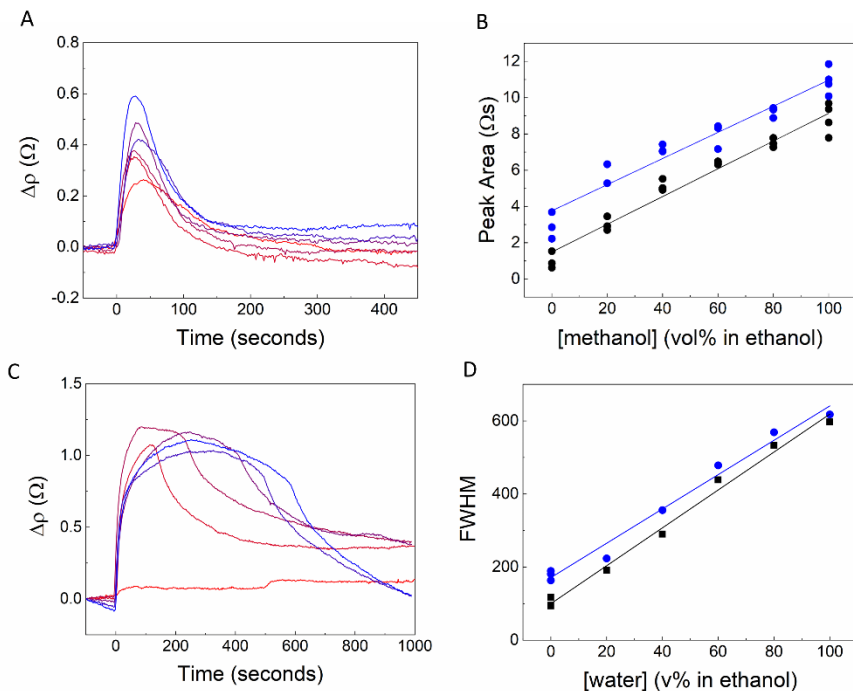


Figure 4.6: Component determination of mixtures with PMMA-coated graphene devices. A) Resistivity change $\Delta\rho$ upon injection of solutions of methanol in ethanol (from red to blue: 0, 20, 40, 60, 80, and 100% methanol, injections of 1 μl , MEAS, V_{BC}). B) Peak area A_{norm} vs. v% methanol in an ethanol solution showed a linear relationship, MEAS (blue, $R^2 = 0.9206$) and REF (V_{DE} , black, $R^2 = 0.9602$). C) Resistivity change $\Delta\rho$ upon injection of solutions of water in ethanol (from red to blue: 0, 20, 40, 60, 80, and 100v% water in ethanol, injections of 1 μl , MEAS). NB: 0% water was injected twice, at 0 s and 500 s. D) Full-width half maximum of the peaks (after linear baseline correction, interval between injections = 1000 s) in normalized resistivity vs. v% water. A clear linear relationship was observed for MEAS (blue, $R^2 = 0.9918$) and REF (black, $R^2 = 0.9838$).

Yet, to identify unknown compounds, and more importantly mixtures of unknown compounds, the chemical selectivity of PMMA-coated sensor was too low. To tackle this problem, we investigated other polymer coatings, as we realized that by producing an array of sensors with different polymer coatings, we may reconstruct chemical selectivity in sensing by analyzing the “fingerprint” response of an array of sensors.

4.3. Chemical fingerprint (CF) vapor sensors

4.3.1. A sensor array with different polymer coatings

To study whether the chemical composition of the polymer influences the sensing response of the graphene sensor to different chemicals, two additional polymer

coatings were used to build the graphene sensors, *i.e.* Nafion® 117 and cellulose acetate butyrate (CAB), to create identical sensors but with coatings that are chemically different in nature. Then, three graphene sensors with the three different polymer coatings were placed in an sensor array, in a single chamber, so the resistance of the three sensors could be monitored simultaneously while they were exposed to the same chemical vapors. We hypothesized that each sensor in the array will give a poorly specific, but different response to vapors compared to the two other sensors as their coatings are chemically different, and that the combination of these different responses may be used to construct a “chemical fingerprint” of the vapor that was in the sensor space, to afford high chemical specificity.

Sensor arrays built for this purpose, denoted below as “chemical fingerprint (CF) arrays”, were made using the same techniques as those described for the PMMA-coated sensors above (see section 4.2.1). First, a mother chip was produced, *i.e.* a silicon wafer (1 × 4 cm) with two silver electrodes stretching over the length of the wafer, bridged by a sheet of graphene coated with PMMA, Nafion® 117 or CAB (which were used as the transfer polymer). Next, daughter chips were created by cutting the mother wafer perpendicular to the two electrodes (see Figure 4.7A, Figure S4.5 and supplementary text). Wiring the daughter chips yielded single CF sensors (Figure S4.6) to be implemented in the CF array. The resulting CF sensors were small in width (2 to 3 mm) to ensure that they fitted in a sample chamber that was sufficiently small to avoid vapor dilution. Gas-tight sensor caps were fabricated that fitted on a cut gas chromatography (GC) column (Figure S4.7). Finally, three CF sensors (one of each of the PMMA, Nafion® 117, and CAB coated sensors), were placed in a single CF array tube, which was capped and sealed (Figure S4.8) to finish the CF array (see Figure 4.7B). For a photograph of a finished CF array, see Figure S4.9.

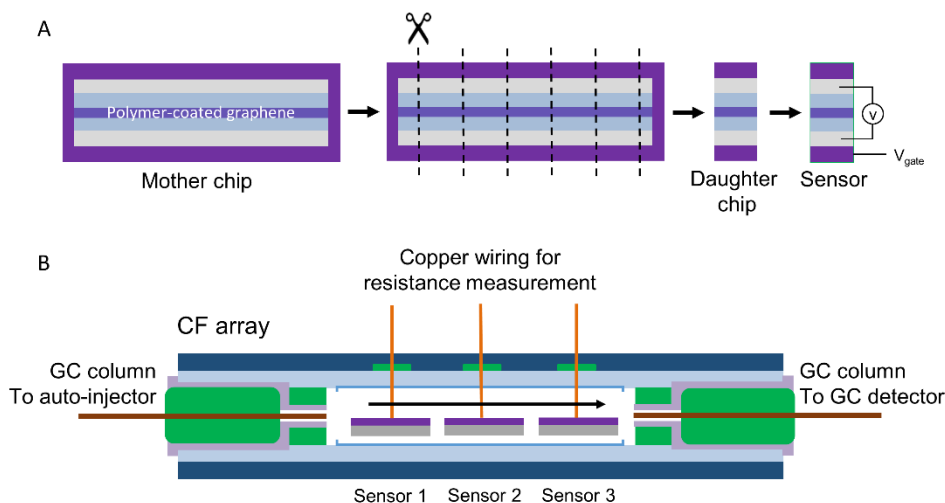


Figure 4.7: Chemical fingerprint array. A) Fabrication, in short, of a CF sensor. A mother chip with two electrodes stretching over the whole length of the surface, bridged by a polymer-coated graphene sheet, was cut to produce identical daughter chips, which were wired to create fabricate individual CF sensors with similar response. B) Schematic representation of a chemical fingerprint (CF) array, built with three CF sensors, each of which is coated with a different polymer on graphene. The three sensors were assembled in a gas-tight, multi-walled sensor tube that was connected to a GC column for automated chemical vapor injection. Arrow indicates flow direction.

4.3.2. Continuous CF array measurement with auto-injection

In order to enable automated, continuous measurements in presence of many different chemicals, CF arrays were connected inside the oven of a GC system. The GC allowed to control the temperature of the sensors (typically set to 30 °C), ensured a steady gas flow of the carrier gas (helium), and most importantly, allowed the use of the auto-sampler connected to the GC. The advantage of the auto-sampler was that all compounds were injected multiple times in the same manner, bypassing human errors, for example variations in volume and temperature of the injected species. The CF array was attached to the column of the GC (that was cut ~30 cm away from the auto-injection port of the GC) by inserting the cut ends of the column in the caps of the CF array (see Figure S4.10). This connection was gas-tight, as the hole in the caps through which the column ends were inserted were smaller in diameter than the column itself, and the cap material was elastic, which sealed the connection between the cap and the column. The sample injector was set to 300 °C to ensure complete evaporation of the injected species. Samples were injected multiple times in volumes of 1 μl at a split ratio of 1:40, meaning only 1/40th of the 1 μl sample was introduced on the

GC column and thus reached the sensor; the remainder was discarded by the GC apparatus. CF arrays were thus operated under standard GC conditions.

4.3.3. Establishing the fingerprints for 42 different chemical vapors

The resistance of the sensors in a CF array was monitored continuously over several days, while the GC auto-injector introduced the samples automatically and repeatedly with a time interval of 830 s between two consecutive injections. In total, 42 different compounds (see Table S4.2) were introduced 4 times each to the CF array, to build a database of chemical fingerprints of these compounds obtained from the CF array sensors, and study the reproducibility of the signal. The obtained resistance R vs. time traces were different for the three individual sensors in each array coated with the three different polymers. For 38 of the 42 compounds, a significant peak was found in at least one of the sensors; only pentane, cyclopentane, 1-pentene and 1-chlorohexane did not show response on any of the sensors of the CF array (see Figure S4.11). Notably, CAB-coated sensors showed a higher signal-to-noise ratio and shorter recovery time than PMMA- or Nafion® 117-coated sensors, for reasons that are not obvious to us.

To investigate if the position of the compounds in the series of injections introduced in the array sensors influenced the response of the sensor to these compounds, the measurement with the same compound database was repeated on the same CF array, while the injection sequence was randomized. The response of the CF sensors appeared the same to all compounds, regardless of the injection sequence. The order of introducing compounds to the sensor thus seemed to have no effect on the response of the CF array (see Figure S4.12).

The two essential characteristics of the chemical fingerprint of each injected compound were the shapes of the curves of the R_{norm} vs. time traces for all three polymers, where $R_{norm} = R / R_{t=0} \times 100\%$, as well as the 3 integrated areas A_{norm} under these curves, as explained above for PMMA (see Figure 4.8 and Figure S4.13). Importantly, the error bars were small for the average value of A_{norm} for each compound on each type of polymer coating, indicating the responses of sensors to the compounds were reliable (see Table S4.3). This was true unless saturation occurred, similar to the saturation of PMMA-coated devices by water as described in section 4.2.3, which was the case for pyrrolidine and piperidine for example. Moreover, the peak area values that were obtained from three differently coated graphene sensors for a typical compound was not the same for the different

sensors, showing that the response behavior is determined by the polymer coating type, and adding sensors with a different polymer coating to the array provides additional data for a chemical fingerprint. Importantly, the peak area values that were obtained also differed between different compounds that were introduced. The CF array was thus able to discriminate between the different injected compounds, which is required for the precise identification of the chemical vapor flowing above the CF array sensor.

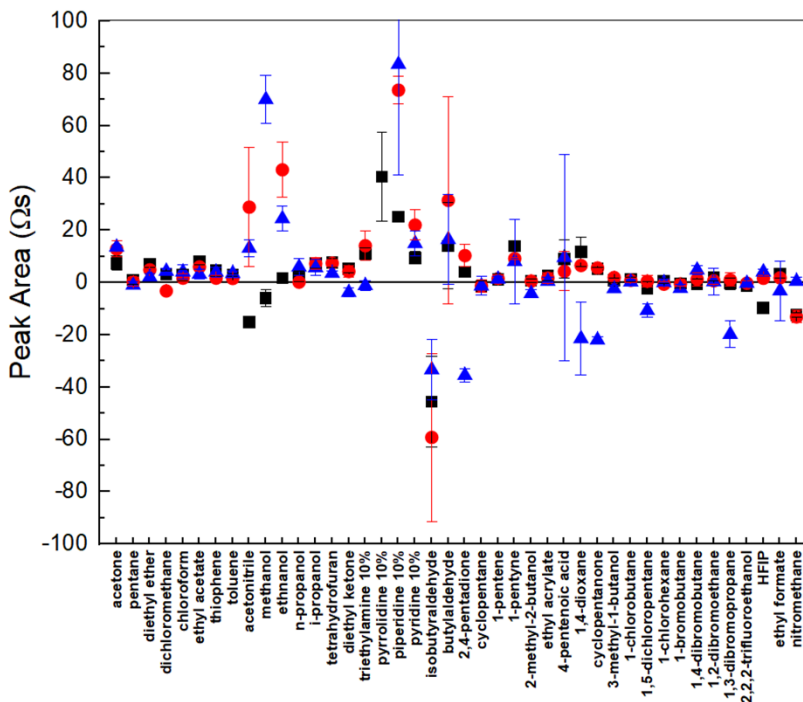


Figure 4.8: Chemical fingerprint of a series of 42 different chemicals, based on the average peak area, A_{norm} , obtained from normalized resistivity data ($R/R_0 \times 100$) on CF array 1, containing three graphene sensors coated with PMMA, Nafion® 117, or CAB (black squares, red circles and blue triangles, respectively). The peak areas shown are averages obtained for 4 individual injections (1 μ l, split ratio = 1:40) for each species, except for acetone, which is an average of 6 injections. HFIP = 1,1,1,3,3,3-hexafluoro-2-propanol. Notably, the peak areas from certain compounds were out of range for the scale of this graph. The full graph and data that was used to construct the graph are shown in the supplementary information (Figure S4.13 and Table S4.3).

From the obtained data with one CF array, some chemicals could be already identified by a simple look at the raw data. For example, nitromethane could be recognized from the strong response on all three CF sensors and typical profile on the PMMA sensor (first a sharp decrease, followed by a bell-shaped peak, see

Figure S4.14), as well as 1,1,1,3,3,3-hexafluoro-2-propanol (HFIP), which could be recognized by the strong response and typical profile on the three sensors (for example, on the PMMA and Nafion® 117 coated sensors, HFIP showed first an increase, then shortly a slow decrease, then a sharp drop after 50 – 100 seconds, see Figure S4.15). Visual inspection of the raw data can thus already be used to identify some of the chemical species, showing that the CF arrays can be more useful for compound identification than a single graphene sensor with a single polymer coating. Yet, we hypothesized supervised learning could be a far more powerful tool for compound identification from the CF array datasets than the naked eye.

4.3.4. Machine learning for compound identification

The CF array data of 34 out of 42 compounds were found suitable for analysis by supervised machine learning using the criterion that a compound must give a response to all three sensors in the array (see Table S4.3). In total, we tested three different batches of data (run I, II and III), in which there were four samples for each compound. Batch I and III were merged and used as the training set, while batch II was used as an independent test set. After removing the noise and blank samples, there were 238 and 110 samples in the training and test set, respectively. For each sample, 10 features were extracted from sensor data as is illustrated in Figure 4.9A, including maximum and minimum values of resistance R_1 and R_2 , the time points of the maximum and minimum of resistance t_2 and t_4 , the largest and smallest slope S_1 and S_2 , the time points of largest and smallest slope t_1 and t_4 , and the area of response process A_1 and area of recovery process A_2 .

Subsequently, supervised machine learning models were constructed for multi-label classification, which take these 10 features as the input and categories of molecules as output, respectively. Four algorithms were benchmarked for model construction: Random Forest (RF),^[14] K-Nearest Neighbours (KNN),^[15] Naïve Bayesian (NB),^[16] and Support Vector Machines (SVM).^[17] The RF, KNN, NB and SMV models were implemented through Scikit-Learn. In RF, the number of trees was set as 1000 and split criterion was “gini”. In KNN, the number of neighbours was set as 3. In SVM, a radial basis function (RBF) kernel was used and the parameter space of C (the cost of misclassification parameter) and γ (the free parameter of the RBF kernel) were set as $[2^{-5}, 2^{15}]$ and $[2^{-15}, 2^5]$, respectively.

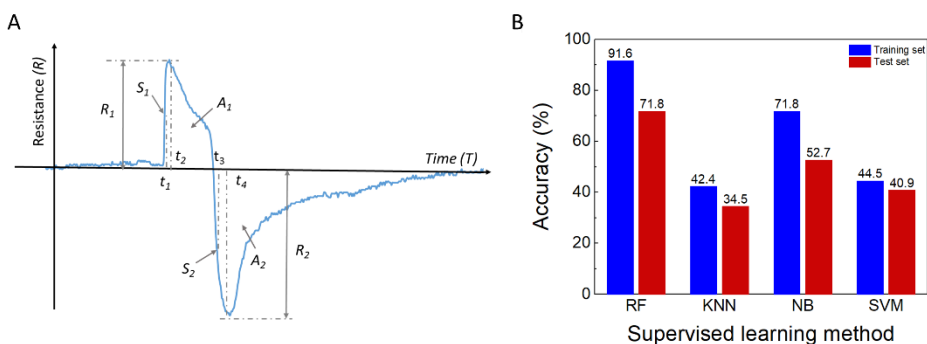


Figure 4.9: Data analysis by supervised learning. A) Features were extracted from the CF array data of one sample, including maximum of resistance (R_1), the largest slope (S_1), the time point of largest slope (t_1), the time point of maximum of resistance (t_1), the area of response process (A_1), minimum of resistance (R_2), the smallest slope (S_2), the time point of smallest slope (t_4), the time point of minimum of resistance (t_4) and the area of recovery process (A_2). B) Performance comparison between different supervised learning methods on both training set with cross validation and test set with independent test, respectively.

A principal component analysis (PCA)^[18] was employed on the feature data, shown as 3D plot in Figure S4.16, and we found that almost all of the samples from the same compound were located closely. However, the compounds could not be clustered into distinct groups. Moreover, the PCA could not reflect an apparent relationship between the patterns of sensor data and properties of these molecules. The classification models, on the other hand, could accurately assign compound labels to the samples of our dataset (see Figure 4.9B). We found that among the different algorithms, the RF algorithm achieved the highest accuracy for compound classification on both the cross validation (training) and the independent (test) set, with accuracies of 91.6 and 71.8%, respectively. Using the RF algorithm, we could thus use the CF array data to classify and identify the different compounds that were introduced to the array with high accuracy.

We should emphasize here that this method does not require the development of radically different sensors, nor do they require complex, molecularly specific functional molecules or nanoparticles on the graphene sheet. The range of polymers which can be applied in such devices is enormous, making these sensors potentially cheap (polymers do not have to be designed specifically) and easy to fabricate. Here CF arrays made of 3 different sensors with 3 different polymers have been realized, but it is easy to imagine CF sensors with 4, 5, or 6 different polymers, which increases the chemical selectivity with each additional polymer.

4.4. Conclusions & Outlook

Our findings showed that leaving the transfer polymer layer on graphene in a graphene-based sensor unlocks their sensing capacity. PMMA-coated sensors responded to a wide range of chemical vapors, and the sensor response to these vapors varies with the chemical nature of the vapors. Devices coated with a polymer layer showed much higher signal-to-noise ratios than bare graphene ones, which we interpret as a protective function of the polymer layer. The PMMA-coated sensors reached the low ppm range for specific species, *i.e.* 6 ppm for methanol, while other compounds, like diethyl ether or pentane, could not be detected due to low response of the PMMA sensors. We demonstrated herein that such compounds can be used as inert carrier solvents for measuring low concentration of compounds that give a high response, such as methanol or water, respectively. Moreover, PMMA sensors also had the ability to distinguish between highly similar molecular compounds in mixtures, *i.e.* methanol and ethanol, or ethanol and water. Albeit these sensors saturated quickly in presence of water, acetonitrile was able to resolve this issue by quickly lowering the resistivity of the sensor after water saturation, thereby restoring the sensitivity of the sensor.

Although a single sensor with a single PMMA coating sensed different chemicals with some chemical selectivity, the selectivity was limited. To overcome this problem, we constructed chemical fingerprint arrays, which had three graphene sensors with three different polymer coatings that sensed the same chemical vapors by three simultaneous resistance measurements. These CF arrays were integrated in an auto-injection system, which allowed to measure the response of all three graphene sensors to 42 different chemical vapors: 38 of them triggered a response to at least one of the three sensors in the array. Through combining the information of the three sensors, the “chemical fingerprint” of each chemical vapor could be constructed, for the direct identification of the vapors. Using supervised machine learning techniques with the CF array data as input, compounds could indeed be classified and identified with high accuracy. Thus, with the CF array much higher selectivity was obtained than with single sensors. Moreover, the data from the CF array could be used to achieve excellent chemical recognition especially using machine learning, which paves the way to unlock the full potential of this CF array sensing technology.

4.5. References and Notes

- [1] R. Mayeux, *NeuroRX* **2004**, *1*, 182.
- [2] S. G. Coca, R. Yalavarthy, J. Concato, C. R. Parikh, *Kidney Int.* **2008**, *73*, 1008; B. Olsson, R. Lautner, U. Andreasson, A. Öhrfelt, E. Portelius, M. Bjerke, M. Hölltä, C. Rosén, C. Olsson, G. Strobel, E. Wu, K. Dakin, M. Petzold, K. Blennow, H. Zetterberg, *Lancet Neurol.* **2016**, *15*, 673; W. Whiteley, M.-C. Tseng, P. Sandercock, *Stroke* **2008**, *39*, 2902; N. L. Henry, D. F. Hayes, *Mol. Oncol.* **2012**, *6*, 140; R. Khoury, E. Ghossub, *BIONPS* **2019**, *1*, 100005.
- [3] R. Capuano, M. Santonico, G. Pennazza, S. Ghezzi, E. Martinelli, C. Roscioni, G. Lucantoni, G. Galluccio, R. Paolesse, C. Di Natale, A. D'Amico, *Sci. Rep.* **2015**, *5*, 16491; R. Enoch Amor, M. K. Nakhleh, O. Barash, H. Haick, *Eur. Respir. Rev.* **2019**, *28*, 190002.
- [4] T. Bruderer, T. Gaisl, M. T. Gaugg, N. Nowak, B. Streckenbach, S. Müller, A. Moeller, M. Kohler, R. Zenobi, *Chem. Rev.* **2019**, *119*, 10803; O. Lawal, W. M. Ahmed, T. M. E. Nijssen, R. Goodacre, S. J. Fowler, *Metabolomics* **2017**, *13*, 110; K. H. Kim, S. A. Jahan, E. Kabir, *TrAC - Trend. Anal. Chem.* **2012**, *33*, 1; S. Scarlata, G. Pennazza, M. Santonico, C. Pedone, R. Antonelli Incalzi, *Expert Rev. Mol. Diagn.* **2015**, *15*, 933.
- [5] C. Di Natale, R. Paolesse, E. Martinelli, R. Capuano, *Anal. Chim. Acta* **2014**, *824*, 1.
- [6] M. Righettoni, A. Amann, S. E. Pratsinis, *Mater. Today* **2015**, *18*, 163.
- [7] A. Nag, A. Mitra, S. C. Mukhopadhyay, *Sens. Actuator A Phys.* **2018**, *270*, 177; H. Huang, S. Su, N. Wu, H. Wan, S. Wan, H. Bi, L. Sun, *Front. Chem.* **2019**, *7*.
- [8] W. Fu, L. Jiang, E. P. van Geest, L. M. C. Lima, G. F. Schneider, *Adv. Mater.* **2017**, *29*, 1603610.
- [9] V. Georgakilas, M. Otyepka, A. B. Bourlinos, V. Chandra, N. Kim, K. C. Kemp, P. Hobza, R. Zboril, K. S. Kim, *Chem. Rev.* **2012**, *112*, 6156.
- [10] J. Kang, D. Shin, S. Bae, B. H. Hong, *Nanoscale* **2012**, *4*, 5527; X. Li, Y. Zhu, W. Cai, M. Borysiak, B. Han, D. Chen, R. D. Piner, L. Colombo, R. S. Ruoff, *Nano Lett.* **2009**, *9*, 4359.
- [11] M. Chen, R. C. Haddon, R. Yan, E. Bekyarova, *Materials Horizons* **2017**, *4*, 1054; T. Hallam, N. C. Berner, C. Yim, G. S. Duesberg, *Adv. Mater. Interfaces* **2014**, *1*, 1400115; Y. Chen, X.-L. Gong, J.-G. Gai, *Adv. Sci.* **2016**, *3*, 1500343.
- [12] M. Ishigami, J. H. Chen, W. G. Cullen, M. S. Fuhrer, E. D. Williams, *Nano Lett.* **2007**, *7*, 1643; J. W. Suk, W. H. Lee, J. Lee, H. Chou, R. D. Piner, Y. Hao, D. Akinwande, R. S. Ruoff, *Nano Lett.* **2013**, *13*, 1462; A. Pirkle, J. Chan, A. Venugopal, D. Hinojos, C. W. Magnuson, S. McDonnell, L. Colombo, E. M. Vogel, R. S. Ruoff, R. M. Wallace, *Appl. Phys. Lett.* **2011**, *99*, 122108; J. H. Choi, J. Lee, M. Byeon, T. E. Hong, H. Park, C. Y. Lee, *ACS Appl. Nano Mater.* **2020**, *3*, 2257.
- [13] Y. Dan, Y. Lu, N. J. Kybert, Z. Luo, A. T. C. Johnson, *Nano Lett.* **2009**, *9*, 1472.
- [14] L. Breiman, *Mach. Learn.* **2001**, *45*, 5.
- [15] N. S. Altman, *Am. Stat.* **1992**, *46*, 175.
- [16] P. Domingos, M. Pazzani, *Mach. Learn.* **1997**, *29*, 103.
- [17] C. Cortes, V. Vapnik, *Mach. Learn.* **1995**, *20*, 273.
- [18] S. Wold, K. Esbensen, P. Geladi, *Chemom. Intell. Lab. Syst.* **1987**, *2*, 37.

Chapter 5

Monitoring a ruthenium-based photoreaction with graphene on paper

Paper-based graphene devices are appealing sensors, as the porosity of cellulose paper brings analytes in solutions close to the graphene-paper interface. We fabricated graphene field effect transistors (GFETs) on paper to sense the chemical reactions between the metal complex $[\text{Ru}(\text{tpy})(\text{biq})(\text{OH}_2)]^{2+}$, obtained from hydrolysis of $[\text{Ru}(\text{tpy})(\text{biq})(\text{Cl})]\text{Cl}$, and the ligand 2-deoxyguanosine monophosphate (dGMP): in the dark, dGMP binds to ruthenium giving $[\text{Ru}(\text{tpy})(\text{biq})(\text{dGMP})]^{2+}$, while it releases upon visible light irradiation. After the devices were soaked with aqueous solutions of either $[\text{Ru}(\text{tpy})(\text{biq})\text{Cl}]\text{Cl}$, the complex $[\text{Ru}(\text{bpy})_3]\text{Cl}_2$ (which does not exchange ligands upon light irradiation), or KNO_3 , they showed a strong light response: the resistance abruptly varied when the irradiation was switched on and off. When the gate potential was varied, we could observe the Dirac peak in the plots of R vs. V_{gate} , which did not shift as we switched the lamp on and off. Yet, a plot of the leak current vs. V_{gate} did show peaks indicative of electrochemistry taking place. Finally, phototriggered release of dGMP from $[\text{Ru}(\text{tpy})(\text{biq})(\text{dGMP})]^{2+}$ appeared to cause a negative shift in the Dirac point, yet we could not definitively conclude that this shift is due solely to the photochemical conversion, as multiple electrochemical processes seem to contribute to the light response of the GFET. With this work, we demonstrated the power of paper in graphene devices, thus adding new concepts to the field of flexible electronics and graphene-based sensing.

5.1. Introduction

Electronic devices are typically constructed on silicon wafer chips, the current industry standard.^[1] Yet, these chips are brittle, as are some electronic components like the commonly used electrode indium tin oxide (ITO) for example, and both components cannot be bent or stretched.^[2] For the development of flexible electronics, for instance flexible sensors, solar panels, LEDs and transistors that can for example be worn on the body, such brittle components have to be replaced.^[3] ‘Ordinary’ paper (cellulose paper) was proposed as a good candidate to replace brittle silicon wafer substrates, because next to its abundance and flexibility, paper is a porous material, which allows solutions to be transferred inside the material through capillary forces.^[4] Moreover, fluidic systems for aqueous solutions can be designed in paper substrates by simply infusing parts of the paper with a hydrophobic material, for instance wax or a photoresist, to create a (micro)fluidic system in the paper itself, which is useful for sensing technologies that probe liquid samples (*e.g.* blood or urine).^[5]

Next to paper, the 2D semiconductor graphene (mono- and few layer) is an interesting candidate to be used in flexible electronics as it has shown great resilience to mechanical deformations.^[6] The electronic properties of graphene are in fact very suitable for sensing.^[7] For example, graphene-on-paper-based NO₂ sensors were developed, which could detect NO₂ up to 300 ppt.^[8] Notably, paper-supported graphene (as large sheets or flakes) were used for example in supercapacitors, water purification devices, biomimetic devices, sensors, and energy devices.^[9] These examples show the technological versatility of paper as a support for graphene, graphene oxide and reduced graphene oxide.

We wondered if we could use the sensing abilities of graphene on paper for electrical monitoring of a chemical reaction. We chose to study a photochemical reaction, using aqueous solutions of [Ru(tpy)(biq)Cl]Cl (**[1]Cl**, where tpy = 2,2';6',2''-terpyridine and biq = 2,2'-biquinoline), which is converted into [Ru(tpy)(biq)(dGMP)]²⁺ (**[2]²⁺**) when a dGMP ligand (2-deoxyguanosine monophosphate) coordinates in the dark to [Ru(tpy)(biq)(OH₂)]²⁺ (**[3]²⁺**). Complex **[3]²⁺** was obtained from **[1]Cl** by hydrolysis when this complex is dissolved in chloride-free aqueous solutions.^[10] Ruthenium-purine bonds, like the Ru-dGMP bond, can be photo-labile;^[11] indeed, the equilibrium between **[2]²⁺** and **[3]²⁺** is sensitive to light (as described in Chapter 6). Upon visible light irradiation of

complex $[2]^{2+}$, the ruthenium-dGMP coordination bond is broken and dGMP is released to afford $[3]^{2+}$ (see Figure 5.1A). These reactions may occur in the paper substrate, if the paper is soaked with the ruthenium-containing solution. We switched the light on and off while monitoring the resistance of the graphene sheet on top of the soaked paper (see Figure 5.1B). The aim was to study if the electrical resistance of graphene would vary upon phototriggered release of dGMP from $[2]^{2+}$, as this photoreaction is expected to change the dipole moments of the reagents in solution, while graphene is sensitive to dipole changes at its surface.^[7] As such, graphene on paper may be used as a sensing platform for chemical reactions in solution (see Figure 5.1B).

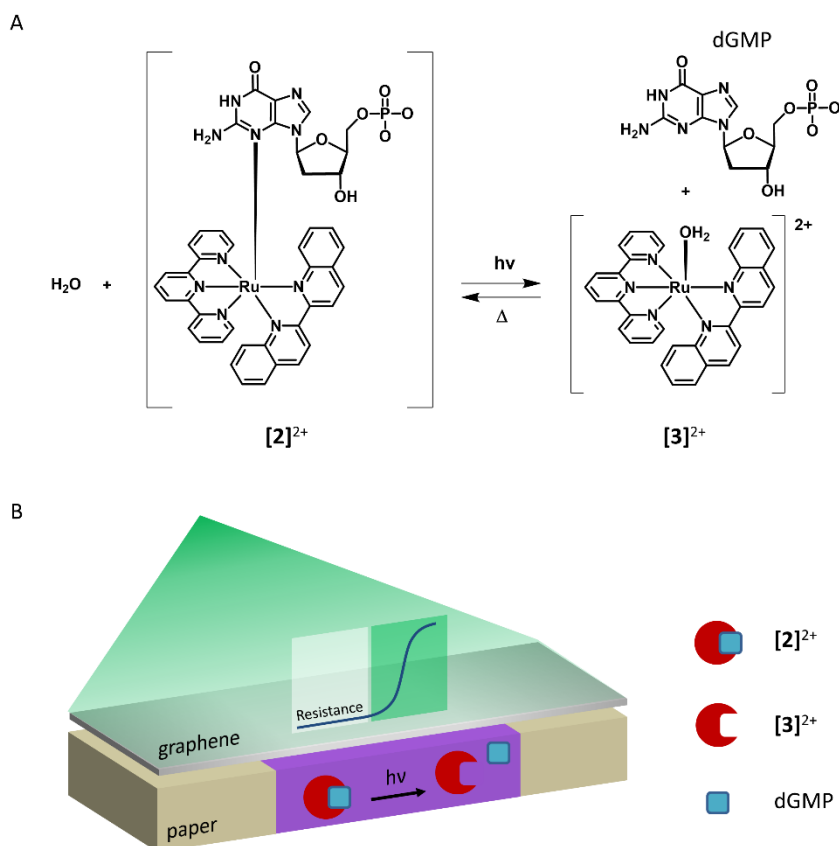


Figure 5.1: Monitoring a photochemical conversion with a GFET on paper. A) Equilibrium reaction of $[\text{Ru}(\text{tpy})(\text{biq})(\text{dGMP})]^{2+}$: complex $[2]^{2+}$ is stable in the dark, while green light irradiation breaks the coordination bond between Ru and dGMP, yielding free dGMP and $[\text{Ru}(\text{tpy})(\text{biq})(\text{OH}_2)]^{2+}$, complex $[3]^{2+}$. B) Schematic representation of a graphene field effect transistor on paper for monitoring the light-sensitive equilibrium reaction between complex $[2]^{2+}$ in the dark and complex $[3]^{2+}$ + free dGMP upon green light irradiation.

5.2. Results and Discussion

5.2.1. Device fabrication

Graphene field-effect transistors (GFETs) on standard printing paper (Xerox, 80 g/m², A4) were fabricated in a step-by-step fashion (see Figure 5.2). First, the paper was cut to size (2 x 3 cm, I). Then, the paper was immersed in a cellulose acetate butyrate (CAB) solution from two opposite sides to make these areas hydrophobic, leaving an untreated, hydrophilic channel in the center (II). After fixing the paper to a glass slide used as a support, the electrodes *A*, *B*, *C* and *D* were fabricated using a silver-based conductive epoxy directly on the CAB-coated areas (III). We used a four-terminal configuration for these devices: the outer electrodes *A* and *D* were used for current supply, and the inner electrodes *B* and *C* for measuring the electrical potential. Next, a sheet of PMMA-coated graphene was transferred over the electrodes (IV) and a strip of copper foil, electrically connected with a copper wire, was inserted underneath the untreated channel (V). This copper foil functioned as a gate electrode for gating experiments. The epoxy electrodes were connected to copper wires as well to finish the device (VI). For a photograph of a finished device, see Figure S5.1. Typically, the electrical resistance between electrodes *B* and *C* bordering the channel was in the range of 1-10 k Ω . A reservoir was placed in contact with the top of the paper device to ensure constant wetting of the hydrophilic channel during measurements (VII). This reservoir could be filled with a solution of interest, which soaked the untreated channel in the paper with this solution.

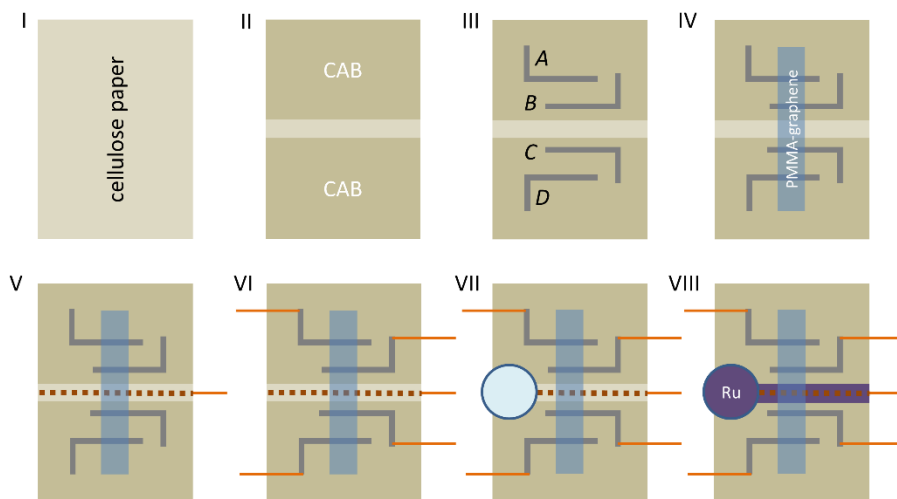


Figure 5.2: Schematic representation of the fabrication process for graphene field effect transistors on paper. First, the paper was cut to size (I), then soaked with a CAB solution, leaving a hydrophilic channel (II). Electrodes *A*, *B*, *C*, and *D* were fabricated (III), and PMMA-coated graphene was transferred on top (IV). A copper foil back gate was installed (V), and the electrodes were connected with Cu wires (VI). Finally, a reservoir was placed (VI) for wetting of the devices with the solution of interest (VIII).

5.2.2. Resistance responses to light

Finished devices were electrically connected in a closed steel box setup to shield them from electrical interference and ambient light (see Figure S5.1). On the lid of the box, a green-light LED (530 nm, $P = 8.15$ mW) was installed to irradiate the devices with green light, which fits with the absorption maximum of $[3]^{2+}$ ($\lambda_{\max} = 550$ nm).^[10] The devices were characterized using resistance (R) measurements *vs.* time ($V_{AD} = 250$ mV, see Figure 5.3A). Devices were first wetted with solutions of $[1]Cl$ which hydrolyses into $[3]^{2+}$ (1 mM), $[Ru(bpy)_3]Cl_2$ ($[4]Cl_2$, where bpy = 2,2'-dipyridine, 1 mM), or KNO_3 (1 mM). We used $[4]Cl_2$ as it is a known photocatalyst which can efficiently transfer an electron to an electron acceptor upon visible light irradiation ($\lambda_{\max} = 452$ nm),^[12] for instance to perform water oxidation^[13] or hydrogen evolution,^[14] but which cannot do photosubstitution at room temperature (Figure 5.3B). After stabilization of the soaked device in the dark for 1000 seconds, the green light intensity on the device was varied between 0 and 8.15 mW, by switching on and off the LED every 500 seconds.

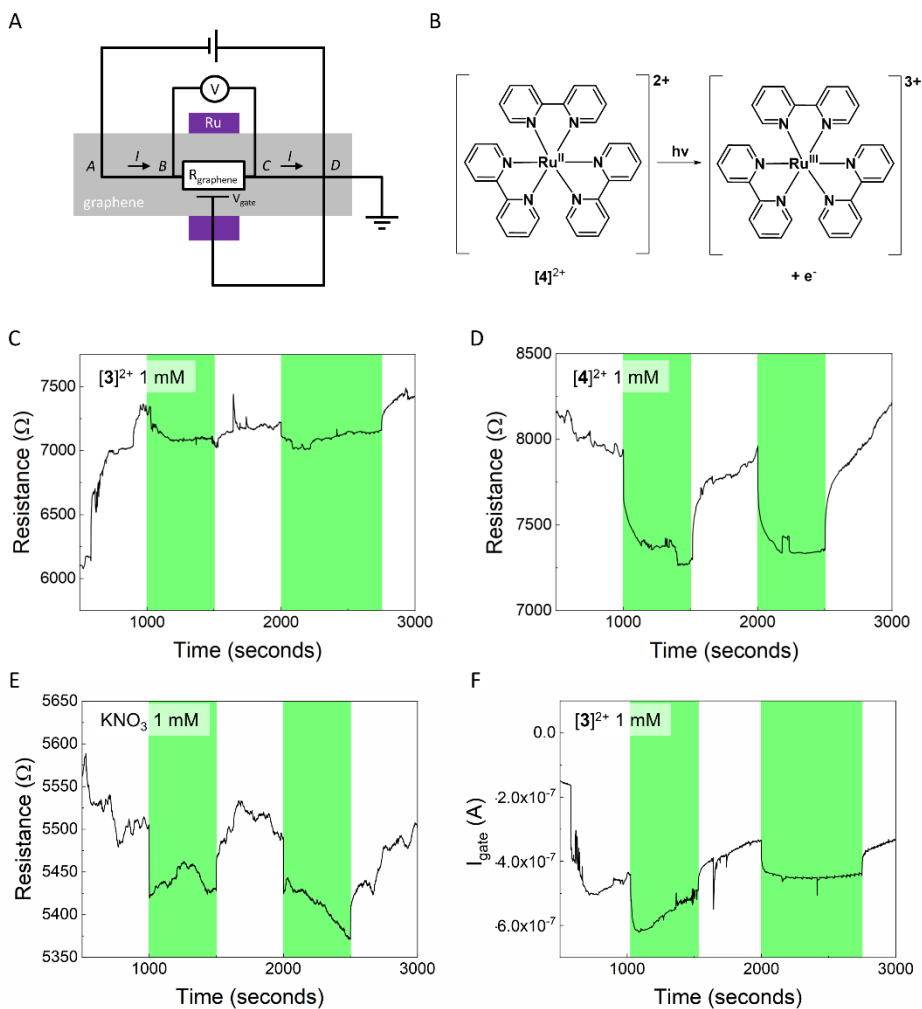


Figure 5.3: Electrical characterization of GFETs on paper: resistance over time. A) Electrical scheme for the four-terminal resistance measurements of graphene on paper devices. Resistance (R) was measured between electrodes B and C , while a potential was applied on A and D , $V_{AD} = 250$ mV, $V_{gate} = 0$ V. B) Reaction scheme for the photo-oxidation of $[4]^{2+}$, the electron can be transferred to an electron acceptor. C) R vs. time in dark (white regions) and light-irradiated conditions (green regions) for a GFET on paper, soaked with a solution of $[3]^{2+}$ (1 mM) in water. D) R vs. time in dark (white regions) and light-irradiated conditions (green regions) for a GFET on paper, soaked with a solution of $[4]^{2+}$ (1 mM) in water. E) R vs. time in dark (white regions) and light-irradiated conditions (green regions) for a GFET on paper, soaked with a solution of KNO_3 (1 mM) in water. F) I_{gate} vs. time for the same GFET as in C. Green boxes indicate when devices were irradiated with green light (530 nm, $P = 8.15$ mW).

Interestingly, independently from the chemical nature of the additive in the soaking solution, the GFETs on paper showed the same response to green light irradiation (Figure 5.3C-E): when the irradiation was turned on, R between

electrodes *B* and *C* suddenly dropped, while when light was turned off, the resistance abruptly increased. *R vs.* time was in fact quite unstable, yet the current from the gate electrode to the graphene sheet I_{gate} , or leak current, was more stable than *R vs.* time and also dropped abruptly when the device was irradiated and increased abruptly when light was turned off (Figure 5.3F for [3]²⁺ and Figure S5.2 for [4]²⁺ and KNO₃). However, the behavior of I_{gate} *vs.* time was also independent from the chemical composition of the solution. The presence of the complex [3]²⁺ in the device wetting solutions was thus not directly responsible for the resistance or leak current variations of the devices to green light, and further study was required to examine the role of ruthenium in the solutions.

5.2.3. Electrical gating of Ru-soaked devices

To further investigate the effect of green light irradiation on GFETs on paper, in presence of [3]²⁺, [4]²⁺ or KNO₃, gating experiments were performed to electrically characterize the graphene sheet of the devices. Gating cycles were performed in the dark (state I), during irradiation with green light (state II) and again in the dark (state III). In each state, the gate voltage (V_{gate}) was cycled 5 times between 0 and 1.5 V, while prior to state I, 10 cycles were performed for stabilization. We observed the ambipolar behavior of graphene^[15] in *R vs.* V_{gate} in all states (dark-light-dark) for GFETs soaked with either of the solutions containing [3]²⁺, [4]²⁺ or KNO₃ (all 1 mM): the Dirac point of graphene (a maximum in *R vs.* V_{gate}) was located at $V_{gate} = 0.8$ V for these devices when sweeping backward (1.5 to 0 V, see Figure 5.4A, C and E). Notably, in forward sweeps *R vs.* V_{gate} typically was less constant, *i.e.* the differences between separate gating cycles were larger than in the backward sweeps (see Figure S5.3). While for [3]²⁺ the difference between forward and backward sweeps was not very large (Figure S5.3A and B), we found that for [4]²⁺ R_{max} in the forward sweep was always much higher (up to 130 k Ω) than during the backward sweep ($R_{max} \leq 28$ k Ω , Figure S5.3C and D), which was also the case for KNO₃ (Figure S5.3E and F, $R_{max} \leq 70$ k Ω and 40 k Ω for the forward and backward sweeps, respectively). In fact, for [4]²⁺ we found that R_{max} varied between sweeps, most strongly in the forward sweeps, but also in the backward sweeps. We believe the large differences in R_{max} between the forward and backward sweeps were due to electrochemical processes occurring during the forward sweep, in the same V_{gate} range (0.5 - 1.0 V) as the Dirac point was located, indicated by the peaks in I_{gate} *vs.* V_{gate} at $V_{gate} = 0.7$ V during the forward sweeps (see Figure 5.4B, D and F), possibly from an oxidation reaction.

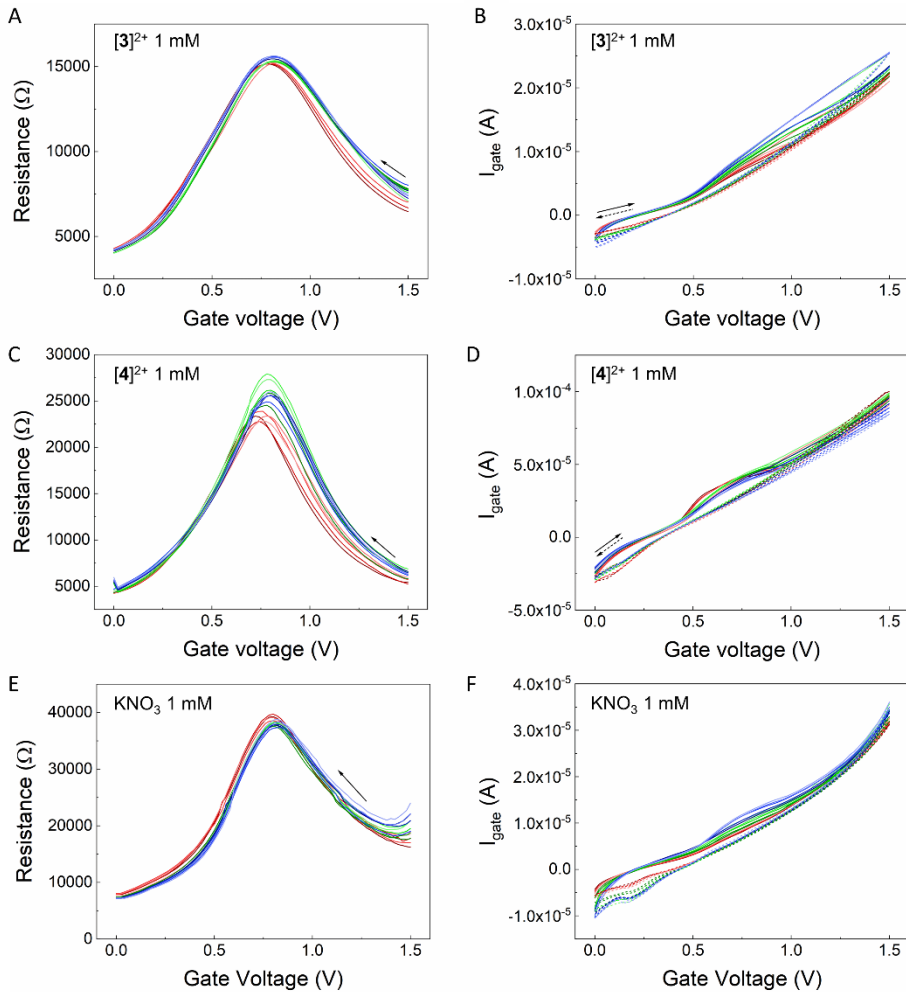


Figure 5.4: Electrical characterization of GFETs on paper: gate sweeping. Resistance R and leak current I_{gate} vs. V_{gate} for devices wetted with [1]Cl, hydrolyzed into [3]²⁺ (1mM, A-B), [4]²⁺ (1 mM, C-D), or KNO₃ only (1 M, E-F). A, C and E show the backward sweeps of R vs. V_{gate} , while B, D, F, show I_{gate} vs. V_{gate} . Starting in the dark (state I, red lines), a typical device was irradiated with green light (state II, green lines), then put back to dark conditions (state III, blue lines). After 10 dark stabilization cycles, 5 V_{gate} cycles were recorded for each state between 0 and 1.5 V which are shown as their corresponding dark to light colors (dark to light red for state I, etc.), solid/dashed line indicates forward/backward sweep, varied at 0.02 V s⁻¹. R was measured between electrodes B and C , while a potential was applied on A and D , $V_{AD} = 250$ mV. Devices were irradiated with green light (530 nm, $P = 8.15$ mW).

In the backward sweep, we could not observe peaks in the leak current in the V_{gate} range of the Dirac point (1.0 – 0.5 V), albeit a reduction peak appeared at 0.2 V for [4]²⁺ and KNO₃, and we think that electrochemical processes did not influence the R vs. V_{gate} profiles. Therefore, we mainly considered the backward sweeps for

comparison between devices, which did not show notable changes in the Dirac point for devices soaked with solutions of $[3]^{2+}$, $[4]^{2+}$ or KNO_3 (Figure 5.4A, C and E). The Dirac point of the graphene sheet in GFETs on paper soaked with these solutions did thus not change as a result of irradiation, but R_{max} could change, possibly due to electrochemical processes.

5.2.4. Monitoring a photoreaction with graphene on paper

After the electronic characterization of the GFETs on paper, we wanted to investigate if we could use these GFETs to monitor the coordination reaction of dGMP to $[3]^{2+}$, forming $[2]^{2+}$ in the dark, as well as the reverse photosubstitution reaction upon irradiation. Devices that were soaked with a solution of $[3]^{2+}$ and dGMP that was kept in the dark overnight prior to use to allow the formation of $[2]^{2+}$, were irradiated with green light (530 nm, $P = 8.15$ mW, irradiation periods of 500 s) to trigger the release of dGMP from complex $[2]^{2+}$ while the resistance of the graphene sheet was monitored over time. We assumed that the opacity of the paper would not be problematic for the photoreaction as the graphene sheet only feels the molecules that react close to the graphene-paper interface, where the light is most intense (as graphene and PMMA are transparent, the light will travel unhindered until it reaches the graphene-paper interface, see Figure 5.5A). Here, R vs. time and I_{gate} vs. time both responded to irradiation with an abrupt decrease and increase when irradiation was turned on and off, respectively (Figure 5.5B and Figure S5.2D), similar to devices that were wetted with either $[3]^{2+}$, $[4]^{2+}$, or KNO_3 (all 1 mM). Thus, when we consider R and I_{gate} vs. time, we cannot convincingly monitor the conversion of $[2]^{2+}$ to $[3]^{2+}$ and dGMP under irradiation, or vice versa (in the dark).

We turned again to the gating experiments to further study the light effect on GFETs wetted with $[3]^{2+}$ and dGMP (both 1 mM). Interestingly, in the backward sweeps R vs. V_{gate} did not remain constant but showed a Dirac peak shift to less positive values upon irradiation (Figure 5.5C), unlike what we observed for GFETs on paper wetted with $[3]^{2+}$, $[4]^{2+}$, or KNO_3 (all 1 mM). This peak shift appeared to be reversible; in the dark after irradiation (state III), the Dirac peak shifted to more positive values again. In the backward sweep, we only observed a peak in I_{gate} vs. V_{gate} at 0.2 V, far away from the Dirac point in the backward sweep (Figure 5.5D), so electrochemistry did not seem to affect the R vs. V_{gate} plots during the backward sweep. In the forward sweeps, we found in fact two peaks in I_{gate} vs.

V_{gate} at 0.6 and 1.3 V, indicative of two different electrochemical reactions taking place, possibly because two ruthenium species were present in solution, *i.e.* $[2]^{2+}$ and $[3]^{2+}$. Moreover, R_{max} increased in the forwards sweep as more gate cycles were performed (Figure S5.4A and B), similar to what we observed for $[4]^{2+}$ and KNO_3 , possibly due to similar electrical processes. Overall, the negative Dirac point shift in the backward sweeps of GFETs wetted with $[3]^{2+}$ and dGMP could be the result of the light-driven dissociation of dGMP from $[2]^{2+}$ taking place, but it is hard to conclude, as the Dirac peak shift is rather small, and other electrochemical processes appear to be involved as well.

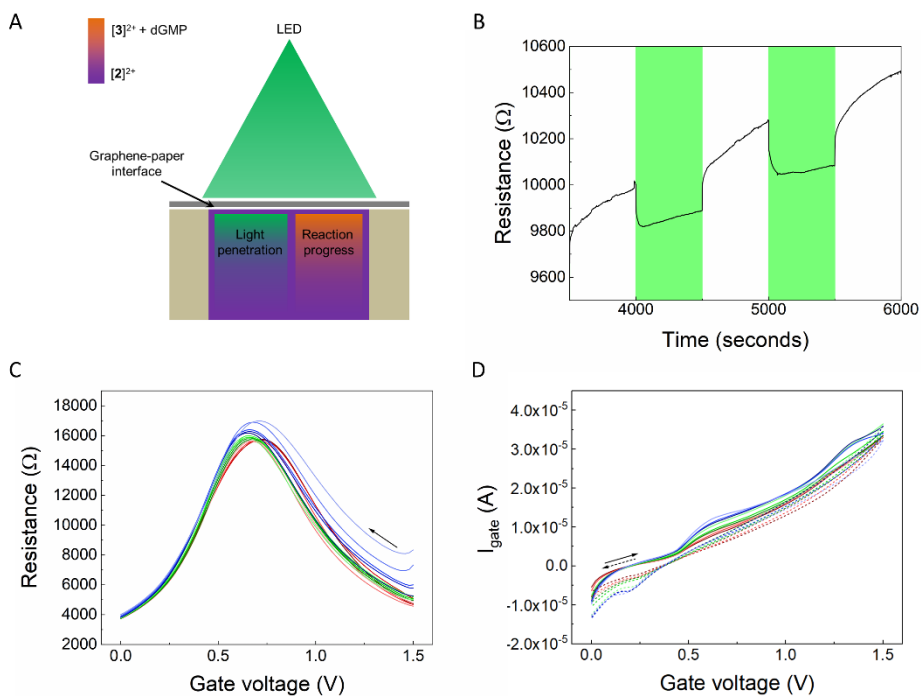


Figure 5.5: Light response of a GFET device wetted with a solution of $[3]^{2+}$ (1mM) + dGMP (1 mM).

A) Schematic of green light penetration and reaction progress at the graphene-paper interface. The PMMA layer on top of graphene is not shown here, as it is fully transparent and does not interfere with irradiation. B) R vs. time in dark (white regions) and light-irradiated conditions (green regions) for a GFET on paper, soaked with a solution of $[3]^{2+}$ (1 mM) + dGMP (1 mM) in water. Green boxes indicate when the device was irradiated with green light (530 nm, $P = 8.15$ mW). C, D) R vs. V_{gate} and I_{gate} vs. V_{gate} for devices wetted with $[3]^{2+}$ (1mM) + dGMP (1 mM) in water. C shows the backward sweep of R vs. V_{gate} , while D shows I_{gate} vs. V_{gate} . Starting in the dark (state I, red), a typical device was irradiated with green light (state II, green line), back to dark (state III, blue line). After 10 dark stabilization cycles, 5 V_{gate} cycles were recorded for each state between 0 and 1.5 V which are shown as their corresponding dark to light colors (dark to light red for state I, etc.), solid/dashed line indicates forward/backward sweep, varied at 0.02 Vs^{-1} . R was measured between electrodes B and C, while a potential was applied on A and D, $V_{AD} = 250$ mV.

5.2.5. Photochemistry versus electrochemistry

The electrical behavior of all soaked devices, both in presence and absence of ruthenium complexes, strongly suggested that electrochemical processes occurred near or at the graphene sheet in all cases, possibly modifying the sheet itself. As the modifications in R vs. V_{gate} appear to be reversible, the graphene sheet itself seems not to be permanently modified by these processes.^[16] We likely observed oxidation (in the forward sweep) and reduction (in the backward sweep) of the ruthenium complexes $[2]^{2+}$, $[3]^{2+}$ and $[4]^{2+}$, as suggested by the peaks in I_{gate} vs. V_{gate} . For $[3]^{2+}$, I_{leak} vs. V_{gate} suggests the complex is being oxidized and reduced again during the gate sweeps. Yet, R vs. V_{gate} appears not to be affected by these processes, as the forward and backward sweep overlapped perfectly and R vs. V_{gate} did not change over the course of the gating experiment. Therefore, we think that graphene is not actively reacting with complex $[3]^{2+}$. In the case of $[4]^{2+}$, oxidation from $[Ru^{II}(bpy)_3]^{2+}$ to $[Ru^{III}(bpy)_3]^{3+}$ may lead to an electron transfer process (see Figure 5.3B), with graphene acting as the electron acceptor, similar to an immobilized Ru complex on graphene.^[17] The electron transfer may be why we see the large increase of R_{max} in the forward sweep, when the oxidation occurs; as $[4]^{2+}$ is oxidized, the current in the graphene sheet is increased, indicated by a peak in the gate current. This gate current appears to play an important role in the high values of R_{max} : due to this second current adding to the circuit, the measurement is likely affected and the measured R values are higher than the actual graphene resistance: the higher the gate current, the higher the resistance (as the residual measurement current in the circuit is lower). For KNO_3 , reactions with the copper gate electrode may be involved, as after the gating experiments, occasionally depositions of solid copper appeared to be present on the graphene sheet (see Figure S5.5), which points to the reduction of Cu^{2+} to Cu^0 at the graphene sheet; these Cu^{2+} ions must have been produced by oxidation of the gate copper electrode. Moreover, in R vs. V_{gate} we observed an increase in R_{max} in the forwards sweep, which can also be attributed to the oxidation of Cu^0 to Cu^{2+} , with an increase of the gate current in the forward sweep, causing R to be overstated.

It should be noted that the existence of the gate current was present in all devices, and possibly overstated the resistance values in all devices. The Dirac point position was not significantly affected by the leak current though, and can still be used for analysis of the gating experiments.

For the GFETs wetted with $[3]^{2+}$ + dGMP, it is hard to say what exactly is going on, as multiple processes are occurring at the same time. While multiple species exist in solution, including $[2]^{2+}$, $[3]^{2+}$ and dGMP, the ratio between these species is also expected to vary as a result of light irradiation. We saw that the intensity of the peaks in the leak current (Figure 5.5D) indeed varies during the experiment: for example, the peak at 0.2 V in the backward sweep seemed to be higher during and after irradiation than before irradiation. At the same time, we observed a negative Dirac peak shift, which points to the photochemical conversion taking place, which is being sensed by graphene. At this point, due to the complexity of the results, we cannot exclude either the photochemical reaction or the electrochemical processes from the possible reasons of the Dirac point shift we observed.

5.3. Conclusions & Outlook

Graphene field effect transistors were fabricated on paper, which were found to be green-light responsive when they were soaked with solutions of $[3]^{2+}$, $[4]^{2+}$, KNO_3 , or $[3]^{2+}$ + dGMP. When the resistance of the devices was monitored as a function of time, in all cases sharp decreases in R occurred when irradiation was started, while R increased abruptly again when the light was turned off. When the resistance was monitored while at the same time the potential of the gate electrode V_{gate} was varied, we could observe the typical Dirac peak in the R vs. V_{gate} profile independent of the solution the GFET on paper was wetted with. As we applied multiple gate potential cycles, switching from dark, to light and back to dark, we found that the Dirac point in the R vs. V_{gate} did not change in the backward sweep (1.5 – 0 V) for devices that were wetted with solutions of $[3]^{2+}$, $[4]^{2+}$ or KNO_3 . In the forwards sweep, R_{max} increased for $[4]^{2+}$ and KNO_3 , which is likely due to an overstatement of the measured R due to an increased gate current by electrochemical processes. Consistent for all devices, the leak current I_{gate} showed reduction and oxidation peaks, which seemed to indicate that the graphene sheet was involved in electrochemical processes, *i.e.* reduction and oxidation of the ruthenium complexes for $[3]^{2+}$ and $[4]^{2+}$ and of copper originating from the gate electrode for KNO_3 . Finally, devices that were wetted with a photoreactive solution containing $[3]^{2+}$ and the dGMP ligand showed a Dirac point shift to less positive values, possibly due to the photochemical conversion taking place. Yet, due to multiple electrochemical processes of this multi-species solution as indicated by multiple peaks in I_{gate} vs. V_{gate} , we could not definitively conclude

that these resistance variations were caused by the photoreaction occurring near the graphene sheet, or due to the electrochemical processes in which the graphene sheet itself may be involved as well. We believe that these paper-based devices show the power of paper for electronic gating and sensing, and that these concepts advance the field of graphene sensors and flexible electronics.

5.4. Acknowledgements

The ruthenium complex [Ru(tpy)(biq)(Cl)](Cl) was kindly provided by Dr. Lucien Lameijer. Jonathan de Ruyter, Daan van den Bos and Camille Blet are thanked for their experimental contributions and scientific discussions. Prof. Dr. Jan van Ruitenbeek is thanked for scientific discussions.

5.5. References and Notes

- [1] D. Neumaier, S. Pindl, M. C. Lemme, *Nat. Mater.* **2019**, *18*, 525.
- [2] D. R. Cairns, R. P. Witte, D. K. Sparacin, S. M. Sachsman, D. C. Paine, G. P. Crawford, R. R. Newton, *Appl. Phys. Lett.* **2000**, *76*, 1425.
- [3] T.-H. Han, H. Kim, S.-J. Kwon, T.-W. Lee, *Mater. Sci. Eng. R Rep* **2017**, *118*, 1.
- [4] M. Sher, R. Zhuang, U. Demirci, W. Asghar, *Expert Rev. Mol. Diagn.* **2017**, *17*, 351.
- [5] C. Renault, J. Koehne, A. J. Ricco, R. M. Crooks, *Langmuir* **2014**, *30*, 7030; E. Carrilho, A. W. Martinez, G. M. Whitesides, *Anal. Chem.* **2009**, *81*, 7091; A. W. Martinez, S. T. Phillips, B. J. Wiley, M. Gupta, G. M. Whitesides, *Lab Chip* **2008**, *8*, 2146.
- [6] E. Han, J. Yu, E. Annevelink, J. Son, D. A. Kang, K. Watanabe, T. Taniguchi, E. Ertekin, P. Y. Huang, A. M. van der Zande, *Nat. Mater.* **2020**, *19*, 305; C. Lee, X. Wei, J. W. Kysar, J. Hone, *Science* **2008**, *321*, 385.
- [7] W. Fu, L. Jiang, E. P. van Geest, L. M. C. Lima, G. F. Schneider, *Adv. Mater.* **2017**, *29*, 1603610.
- [8] G. Yang, C. Lee, J. Kim, F. Ren, S. J. Pearton, *Phys. Chem. Chem. Phys.* **2013**, *15*, 1798; S. Kumar, S. Kaushik, R. Pratap, S. Raghavan, *ACS Appl. Mater. Interfaces* **2015**, *7*, 2189.
- [9] M. Zhang, C. Hou, A. Halder, H. Wang, Q. Chi, *Mater. Chem. Front.* **2017**, *1*, 37; Z. Weng, Y. Su, D.-W. Wang, F. Li, J. Du, H.-M. Cheng, *Adv. Energy Mater.* **2011**, *1*, 917.
- [10] A. Bahreman, B. Limburg, M. A. Siegler, E. Bouwman, S. Bonnet, *Inorg. Chem.* **2013**, *52*, 9456.
- [11] H. Chan, J. B. Ghayche, J. Wei, A. K. Renfrew, *Eur. J. Inorg. Chem.* **2017**, *2017*, 1679.
- [12] K. Kalyanasundaram, *Coord. Chem. Rev.* **1982**, *46*, 159.
- [13] B. Limburg, E. Bouwman, S. Bonnet, *ACS Catal.* **2016**, *6*, 5273.
- [14] K. Kalyanasundaram, J. Kiwi, M. Grätzel, *Helv. Chim. Acta* **1978**, *61*, 2720; M. Kirch, J.-M. Lehn, J.-P. Sauvage, *Helv. Chim. Acta* **1979**, *62*, 1345.
- [15] K. S. Novoselov, A. K. Geim, S. V. Morozov, D. Jiang, Y. Zhang, S. V. Dubonos, I. V. Grigorieva, A. A. Firsov, *Science* **2004**, *306*, 666.
- [16] V. Georgakilas, M. Otyepka, A. B. Bourlinos, V. Chandra, N. Kim, K. C. Kemp, P. Hobza, R. Zboril, K. S. Kim, *Chem. Rev.* **2012**, *112*, 6156.
- [17] X. Liu, E. K. Lee, J. H. Oh, *Small* **2014**, *10*, 3700.

Chapter 6

Reducing the translocation speed of DNA in solid-state nanopores by photolabile ruthenium complex decoration

Nanopores in thin membranes are useful for detecting single DNA molecules. So far, the major drawback of solid-state nanopores is that the translocation speed of DNA is too high to sequence the DNA strand. We decorated DNA with ruthenium complexes that stay bound in the dark but are released upon visible light irradiation. As demonstrated with single nucleotides, the ruthenium complex $[\text{Ru}(\text{tpy})(\text{biq})(\text{OH}_2)]^{2+}$, obtained by the hydrolysis of $[\text{Ru}(\text{tpy})(\text{biq})\text{Cl}]\text{Cl}$, coordinates specifically to guanosine nucleotides in the dark, and the formed complex releases the nucleotide upon green light irradiation. When Ru-functionalized DNA translocated through a nanopore in silicon nitride, the translocation speed of this decorated strand was not significantly changed compared to non-functionalized DNA, but the ionic current blockade was higher. Our results showed that the ruthenium complexes co-translocated with DNA, which led to stronger DNA detection signals. We envision that if the ruthenium complex would be fixed to the surface of the pore-containing membrane, the photolabile binding of DNA to the metal may be used to control the translocation speed of DNA using light.

6.1. Introduction

In 2015 a major breakthrough in DNA sequencing was made when Oxford Nanopore Technologies introduced MiniON, the first commercially available DNA-sequencing device.^[1] The MiniON, which uses biological nanopores (membrane proteins embedded in lipid membranes) for DNA sequencing, demonstrated that nanopores can be used as sequencing devices for human genome sequencing.^[2] Next to biological nanopores, solid-state nanopores are an appealing alternative for DNA sequencing devices as they can be precisely shaped and fabricated on a large scale, have high mechanical robustness, and good chemical and thermal resilience.^[3]

In spite of its potential, DNA sequencing in solid-state nanopores has not been accomplished so far. A major challenge for solid-state nanopore sequencing is to reduce the velocity at which each DNA translocates through the pore. For double-stranded DNA, a translocation speed of ~ 30 bases/ μs was measured, meaning a single base resides in the pore for only 20 nanoseconds, a time too short for precise identification of each base pair.^[4] The translocation speed could already be lowered by one order of magnitude through tuning the viscosity of the solutions, which increases friction.^[5] Yet, also in this case DNA could still move at relatively high speed through the pore, thus preventing precise DNA sequencing using this type of devices.

Herein, we propose an alternative method to slow down the translocation of DNA as it passes through a solid-state nanopore. Ruthenium complexes are known to be able to bind to DNA via the formation of coordination bonds.^[6, 7] Importantly, the ruthenium-purine coordination bond can be photolabile if the right ruthenium polypyridyl complex is chosen,^[8] so that the coordination equilibrium between DNA and ruthenium in the dark may thus be shifted by irradiation with visible light. We hypothesized that when the DNA is decorated with the bulky ruthenium complexes, the translocation speed of the strand would decrease as the complexes may provide additional friction in the nanopore. As the number of complexes that are attached to the DNA strand can be varied by simply varying the light intensity, simultaneously the friction of the DNA strand and thus the translocation speed can be controlled with light (see Figure 6.1).

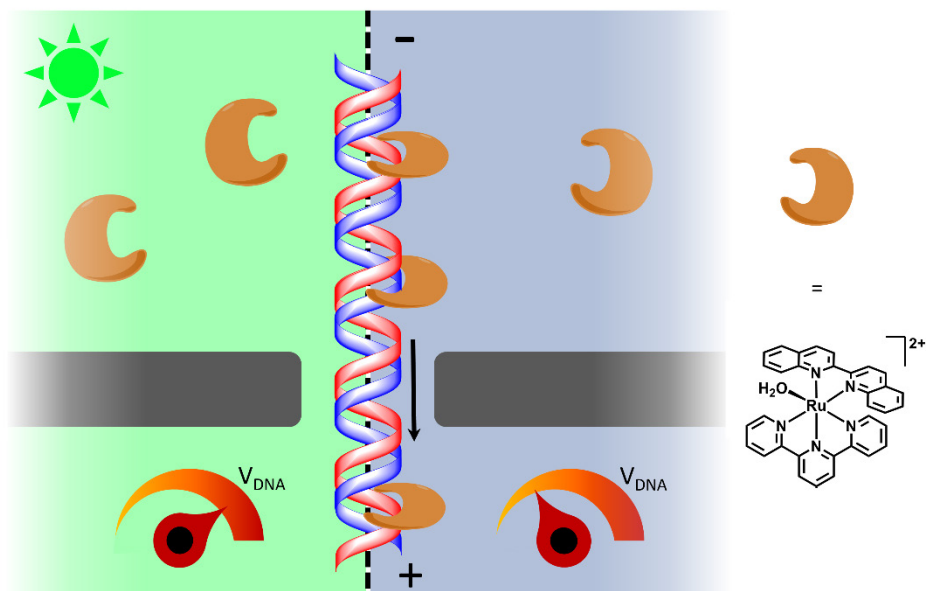
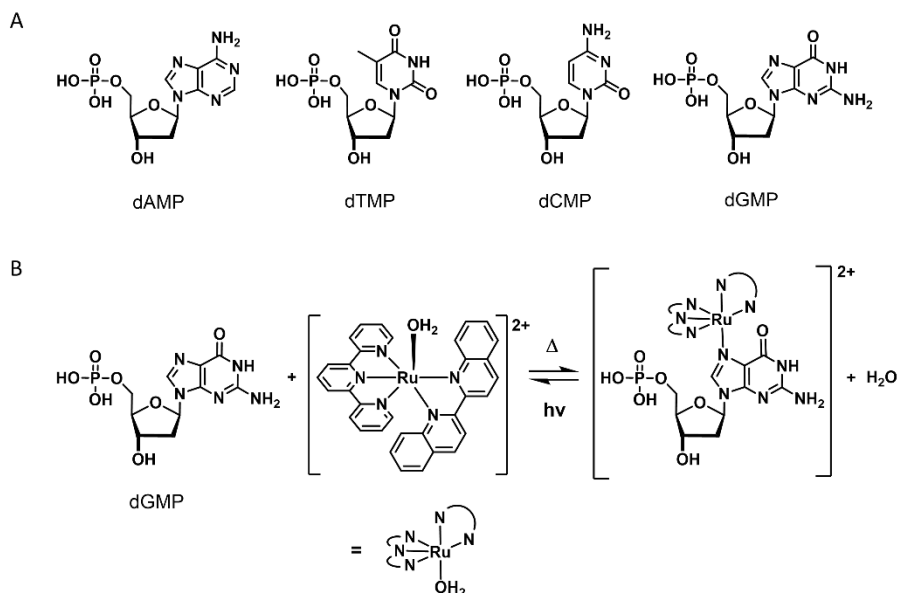


Figure 6.1: Ruthenium-decorated DNA in a nanopore device. A nanopore separates two chambers of the flow cell filled with electrolyte. When a potential is applied over the membrane, DNA translocates through the nanopore. The anchored ruthenium complex coordinates to DNA in the dark (right, grey) and slows down the translocation speed of the DNA strand, while the ruthenium complexes can be removed from the DNA again through visible light irradiation (green, left).

6.2. Results and Discussion

6.2.1. Light-sensitive ruthenium-nucleotide interactions

The ruthenium complex $[\text{Ru}(\text{tpy})(\text{biq})\text{Cl}]\text{Cl}$ (**[1]Cl**), where tpy = 2,2':6'2''-terpyridine and biq = 2,2'-biquinoline, was synthesized using reported methods,^[9] and the interactions of this complex with the four nucleotides (see Scheme 6.1A), *i.e.* 2-deoxyadenosine monophosphate (dAMP), 2-deoxythymidine monophosphate (dTMP), 2-deoxycytidine monophosphate (dCMP) and 2-deoxyguanosine monophosphate (dGMP), and with DNA were studied with UV-vis spectroscopy to investigate the interaction of the ruthenium complex with DNA. When complex **[1]Cl** is dissolved in demineralized water, the coordinated Cl ligand dissociates, yielding the aqua complex $[\text{Ru}(\text{tpy})(\text{biq})(\text{OH}_2)]^{2+}$ (**[2]²⁺**),^[10] which can engage with different coordination reactions, for example with nucleotides (see Scheme 6.1B).



Scheme 6.1: Reaction of complex $[2]^{2+}$ with nucleotides. A) Structure of the four model DNA nucleotides used in this work. B) Interconversion between the aqua complex $[2]^{2+}$ and its dGMP analogue $[3]^{2+}$. This equilibrium is shifted towards the formation of $[3]^{2+}$ in the dark, but towards the formation of $[2]^{2+}$ under visible light irradiation.

Mass spectroscopy showed that the reaction of dGMP with $[2]^{2+}$ results in the formation of $[Ru(tpy)(biq)(dGMP)]^{2+}$ ($[3]^{2+}$) by the appearance of a peak at $m/z = 937.0$, *i.e.* $[3 - H]^+$. The coordination of dGMP could simply be reversed by irradiation of the reaction mixture with visible light (530 nm): the peak at $m/z = 937.0$ was no longer present after irradiation. UV-vis spectroscopy showed a shift from 546 to 549 nm of the metal-to-ligand charge transfer (MLCT) band from the ruthenium complex and a clear isosbestic point at 540 nm, indicating a direct conversion of the dGMP species $[3]^{2+}$ to the aqua complex $[2]^{2+}$ (see Figure 6.2A and Figure S6.1). Furthermore, UV-vis showed that this reaction is selective for dGMP; compound $[2]^{2+}$ does not react with the other nucleotides dAMP, dTMP and dCMP in the same conditions, which is in agreement with the selectivity for dGMP reported for a similar ruthenium complex, $[Ru(tpy)(bpy)Cl]PF_6$ ($bpy = 2,2'$ -bipyridine).^[11]

When complex $[2]^{2+}$ was mixed with calf thymus DNA (ctDNA) in water, the coordination of double-stranded DNA to the ruthenium center was again observed with UV-vis spectroscopy, as well as the photodriven release of DNA. This behavior was similar to the (photo)reactivity of $[2]^{2+}$ in presence of dGMP

(see Figure 6.2B). The nucleotides in a DNA strand can thus still interact with the ruthenium complex. As the coordination reaction of $[2]^{2+}$ with nucleotides was selective for dGMP, we assume that in ctDNA the guanine nucleobases selectively coordinate to the ruthenium complex, likely through binding of the N7 position, which is typically the preferred binding site for ruthenium complexes.^[7, 12] Importantly, the binding is reversed by light irradiation, giving control over the loading of the DNA fragment with ruthenium complexes.

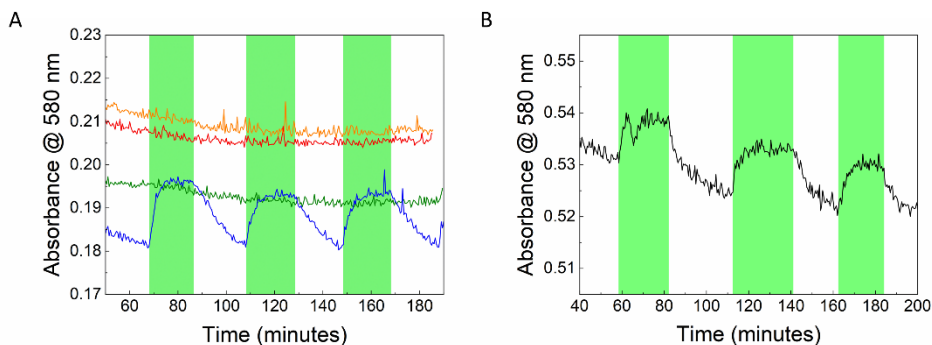


Figure 6.2: UV-vis study of the interactions between $[2]^{2+}$ and nucleotides or DNA. A) Evolution of the absorbance of solutions of $[2]^{2+}$ + dAMP, dTMP, dCMP or dGMP (red, orange, green and blue, respectively, $[Ru] = 50 \mu M$, $[nucleotide] = 250 \mu M$) in water, either in the dark or upon irradiation with light (530 nm, $P = 5.64$ mW). Temperature: 37 °C. Irradiation periods are indicated by green regions. B) Evolution of the absorbance of a solution of $[2]^{2+}$ + calf thymus DNA (black, $[Ru] = 50 \mu M$, $[ctDNA] = 100 \mu M$) in water, either in the dark or upon irradiation with light (530 nm, $P = 5.64$ mW). Temperature: 37 °C. Irradiation periods are indicated by the green regions.

6.2.2. Ruthenium-decorated DNA in nanopore devices

After we confirmed that $[2]^{2+}$ is able to bind to DNA and release again upon irradiation, we used the ruthenium complex for nanopore translocation measurements. First, nanopores had to be fabricated; solid-state nanopores in silicon nitride chips (SiN, membrane thickness = 30 nm) were fabricated in situ. The nanopore setup, in which the chip was mounted, consisted of a *cis* and *trans* chamber both filled with an ionic solution (KCl), and separated by the SiN membrane of the chip (see Chapter 1, Figure 1.3). A hole in the membrane was produced by dielectric breakdown, which by applying a large potential over the membrane creates a pore at the weakest point in the thin silicon nitride membrane through electrical etching, ultimately connecting the two chambers.^[13] Once the electrical etching was complete, as seen from a strong drop of the electrical resistance R between the *cis* and *trans* chamber, the current was cut to prevent

further etching. The approximate diameter of the pore could be determined by measuring R between the *cis* and *trans* chamber after the pore was created (larger pores give smaller values for R),^[14] and was typically in the order of tens of nanometer.

DNA detection measurements were done using the nanopore setup with ruthenium-decorated DNA. To ensure coordination of ruthenium, λ -DNA (linear, 48502 base pairs, from *E. coli* bacteriophage λ ; 10 ng/ μ L) was first incubated with $[2]^{2+}$ in the dark to allow the ruthenium to bind to the DNA strand. As a reference, λ -DNA (10 ng/ μ L) was used that was not incubated with the metal complex. The DNA solutions were injected in the *cis* chamber, where the strands with their negative phosphate backbones were driven through the pore by applying a positive potential from the *trans* chamber. While DNA translocated, the ionic current over the SiN membrane was measured, which was then correlated to the pore diameter; smaller pores gave lower ionic currents. Translocation of individual molecules in the pore, in this case DNA (either with or without ruthenium), causes a narrowing of the pore that leads to a current blockade (see Figure 6.3A), and represents so-called translocation events.^[15]

Typically, ionic current data were acquired for several minutes in order to detect several hundreds of events (bare λ -DNA: 295 events; Ru-incubated λ -DNA: 321 events). For each event the magnitude of the current blockade and the duration of translocation, also called “dwell time”, was recorded. Interestingly, the histogram of event frequency *vs.* current blockade showed that the binding of the ruthenium complex to DNA had a strong effect on the translocation events. Although the dwell time statistical distribution was identical in presence and in absence of the ruthenium complex, always in the range of a few milliseconds (1.29 +/- 0.67 and 1.48 +/- 0.81 milliseconds, respectively, see Figure 6.3B), current blockades were typically higher when the ruthenium complex was coordinated to the DNA strands (see Figure 6.3C). While bare λ -DNA led to a statistical distribution of current blockade characterized by a single maximum at 256 ± 46 pA, Ru-incubated λ -DNA, on the other hand, led to a distribution with not one but two maxima at higher current blockades (320 ± 38 pA and 573 ± 83 pA, see Figure 6.3D). Thus, the presence of the ruthenium complex did not significantly affect the dwell time, however it did increase the magnitude of the ionic current blockade.

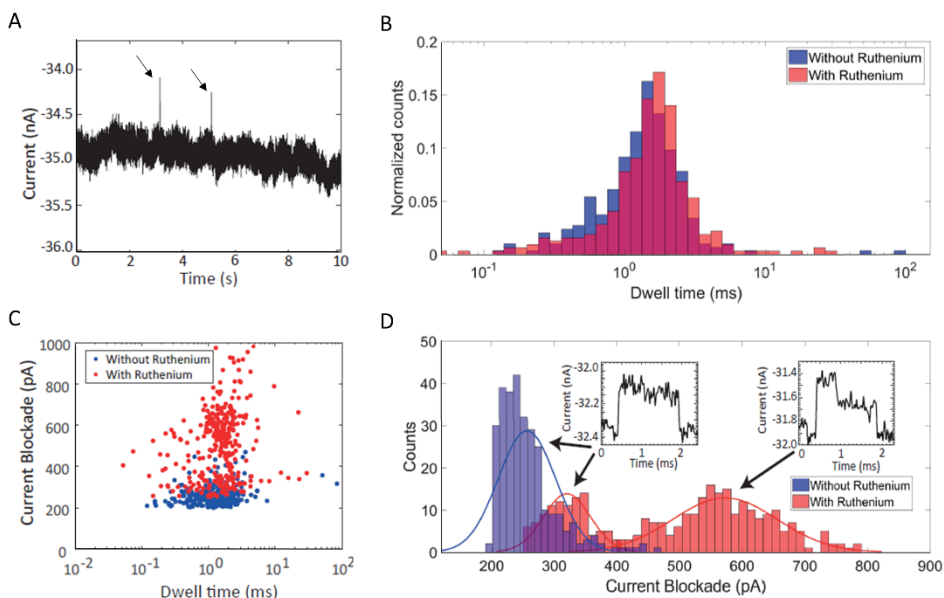


Figure 6.3: Event detection with a 40 nm nanopore in silicon nitride. A) Typical ionic current trace measured with a ± 40 nm sized nanopore after addition of DNA. Two translocation events are visible as upward peaks (indicated by arrows). Applied voltage: -100 mV, pH = 8. All experiments were done in 1 M KCl buffered with 10 mM Tris and 1 mM EDTA. B) Dwell time histogram of the translocation events for bare DNA (blue) and DNA incubated with $[2]^{2+}$ (red). C) Scatterplot of all detected events of bare λ -DNA ($N = 295$, blue) and λ -DNA incubated with complex $[2]^{2+}$ ($N = 321$, red). D) Current blockade histogram of the events with corresponding normal distribution fits for bare DNA (blue) and DNA incubated with $[2]^{2+}$ (red). The insets show two types of translocation events. The arrows show in which part of the current blockade distribution these event types were found.

The existence of the two peaks in the current blockade histogram (Figure 6.3D) obtained in presence of $[2]^{2+}$ indicates that there were two types of DNA molecules that passed through the nanopores. One interpretation is that the DNA did not maintain a single average shape in the presence of complex $[2]^{2+}$, but that there were two conformations that gave rise to two different ion current profiles upon translocation; indeed, ruthenium complexes are known to be able to induce conformational changes in DNA.^[16] More information about the possible different conformations of DNA in presence of complex $[2]^{2+}$ could be obtained from the detailed ion current *vs.* time profile of each translocation event. For λ -DNA without $[2]^{2+}$ and for the low-current blockade events (between 250 and 400 pA) obtained with Ru-incubated λ -DNA, a continuous current plateau was observed until the strand had travelled through the pore, while for high-current blockade events obtained with Ru-incubated λ -DNA (between 400 and 800 pA), an increase to a first plateau was accompanied by a drop to a second plateau in the ion

current, before the strand left the pore and the current dropped back to the baseline (see Figure 6.3D, insets). This current drop could be due to folding of the DNA strand; a folded strand would provide a larger blockade of the pore and thus a higher ion current blockade (see Figure 6.4A); complex $[2]^{2+}$ appears to promote folding of the DNA strand. Why this folding occurs only in presence of $[2]^{2+}$ and only for the larger current blockades is not obvious. The folding could be due to electrostatic interactions of Ru^{2+} with the negatively charged phosphate backbone of DNA. Bridging of Ru between DNA by coordination only is very unlikely, as only one site is available for the coordination of a DNA base pair to the complex. Possibly, the coordinated ruthenium gives the DNA strand a positive charge, to which the negative backbone of the same strand binds by electrostatic forces (Figure 6.4B).

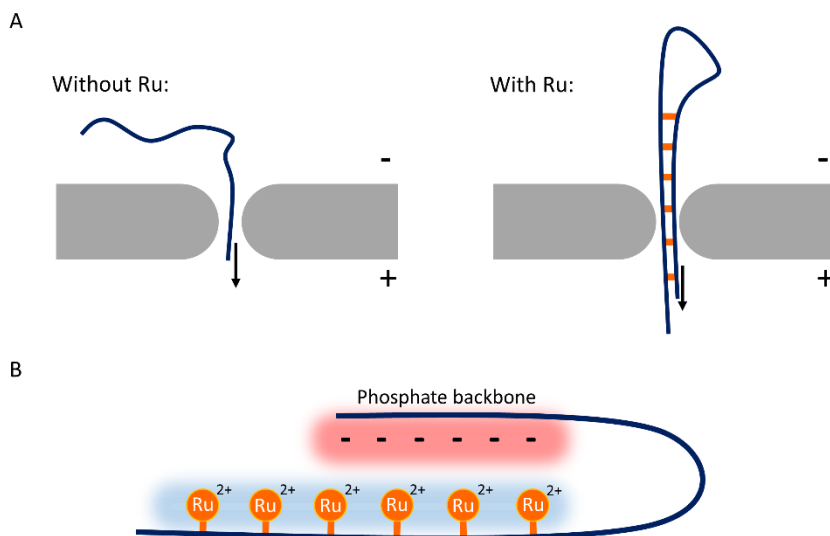


Figure 6.4: Schematic representation of folded DNA in a nanopore. A) While the undecorated DNA strand appears to be linear when it translocates through the pore (left), the larger ionic current for ruthenium-decorated DNA indicated that DNA could be folded (right). B) When a DNA strand is decorated with ruthenium complexes, the positive charges of the complexes could be involved in electrostatic interaction with the phosphate backbone, causing the DNA to fold.

Overall, the presence of the ruthenium complex $[2]^{2+}$ did not affect the dwell time of translocation events, but increased the current blockade in DNA detection experiments, likely because the conformation of the DNA changed, possibly by folding. Based on these experiments and the UV-vis results, we believe that the ruthenium complex co-translocated with the DNA through the nanopore.

6.3. Conclusions & Outlook

Ruthenium complex $[2]^{2+}$, which is obtained by hydrolysis of $[1]Cl$ in aqueous solutions, binds to DNA specifically on the dGMP nucleotides according to UV-vis spectroscopy. This coordination interaction was found to be an equilibrium, which upon green light irradiation (530 nm) can be shifted towards the aqua complex $[2]^{2+}$. Thermal binding and photodriven dissociation of dGMP or guanine nucleobases in DNA could be cycled several times with limited decomposition. During translocation of λ -DNA through a nanopore in a silicon nitride membrane (30 nm thickness), the current blockade with a DNA strand pre-incubated with $[2]^{2+}$ was higher than with bare λ -DNA, while the dwell time remained unaffected. We hypothesized that ruthenium co-translocated with the DNA strand, making the DNA more bulky, which increased the current blockade as a larger portion of the pore was blocked by the DNA strands. However, the time spent in the pore by each translocating DNA fragment did not change upon ruthenium binding. These results present a first step towards nanopores that are covalently functionalized with ruthenium complexes like $[2]^{2+}$ that are able to bind to DNA in the dark and slow down translocation, and unbind upon visible light irradiation. Ultimately, shining visible light onto such systems may be used to control the translocation speed of DNA by shifting the binding equilibrium of $[2]^{2+}$ to the DNA fragment.

6.4. Acknowledgements

Roderick Versloot and Sorraya Popal are thanked for their experimental contributions and scientific discussions as part of Team Slow-Motion (Topsector research in chemistry competition 2017). Pauline van Deursen and Dr. Lucien Lameijer are thanked for scientific discussions and their supervisory role for Team Slow-Motion. NWO is acknowledged for funding via Topsector research in chemistry competition 2017.

6.5. References and Notes

- [1] M. Jain, H. E. Olsen, B. Paten, M. Akeson, *Genome Biol.* **2016**, *17*, 239.
- [2] R. Bowden, R. W. Davies, A. Heger, A. T. Pagnamenta, M. de Cesare, L. E. Oikkonen, D. Parkes, C. Freeman, F. Dhalla, S. Y. Patel, N. Popitsch, C. L. C. Ip, H. E. Roberts, S. Salatino, H. Lockstone, G. Lunter, J. C. Taylor, D. Buck, M. A. Simpson, P. Donnelly, *Nat. Commun.* **2019**, *10*, 1869; M. Jain, S. Koren, K. H. Miga, J. Quick, A. C. Rand, T. A. Sasani, J. R. Tyson, A. D. Beggs, A. T. Dilthey,

Chapter 6: Slow-motion DNA in nanopores

- I. T. Fiddes, S. Malla, H. Marriott, T. Nieto, J. O'Grady, H. E. Olsen, B. S. Pedersen, A. Rhie, H. Richardson, A. R. Quinlan, T. P. Snutch, L. Tee, B. Paten, A. M. Phillippy, J. T. Simpson, N. J. Loman, M. Loose, *Nat. Biotechnol.* **2018**, *36*, 338.
- [3] F. Haque, J. Li, H.-C. Wu, X.-J. Liang, P. Guo, *Nano Today* **2013**, *8*, 56; Y. Goto, R. Akahori, I. Yanagi, K.-i. Takeda, *J. Hum. Genet.* **2020**, *65*, 69; M. Wanunu, *Phys. Life Rev.* **2012**, *9*, 125.
- [4] B. Luan, G. Stolovitzky, G. Martyna, *Nanoscale* **2012**, *4*, 1068.
- [5] D. Fologea, J. Uplinger, B. Thomas, D. S. McNabb, J. Li, *Nano Lett.* **2005**, *5*, 1734.
- [6] H.-K. Liu, S. J. Berners-Price, F. Wang, J. A. Parkinson, J. Xu, J. Bella, P. J. Sadler, *Angew. Chem., Int. Ed.* **2006**, *45*, 8153; P. M. van Vliet, S. M. Toekimin, J. G. Haasnoot, J. Reedijk, O. Nováková, O. Vrána, V. Brabec, *Inorg. Chim. Acta* **1995**, *231*, 57; N. Grover, T. W. Welch, T. A. Fairley, M. Cory, H. H. Thorp, *Inorg. Chem.* **1994**, *33*, 3544; O. Novakova, H. Chen, O. Vrana, A. Rodger, P. J. Sadler, V. Brabec, *Biochemistry* **2003**, *42*, 11544.
- [7] S. Liu, A. Liang, K. Wu, W. Zeng, Q. Luo, F. Wang, *Int. J. Mol. Sci.* **2018**, *19*.
- [8] H. Chan, J. B. Ghayche, J. Wei, A. K. Renfrew, *Eur. J. Inorg. Chem.* **2017**, *2017*, 1679.
- [9] L. N. Lameijer, D. Ernst, S. L. Hopkins, M. S. Meijer, S. H. C. Askes, S. E. Le Dévédec, S. Bonnet, *Angew. Chem., Int. Ed.* **2017**, *56*, 11549.
- [10] A. Bahreman, B. Limburg, M. A. Siegler, E. Bouwman, S. Bonnet, *Inorg. Chem.* **2013**, *52*, 9456.
- [11] J. Rodríguez, J. Mosquera, J. R. Couceiro, M. E. Vázquez, J. L. Mascareñas, *Angew. Chem., Int. Ed.* **2016**, *55*, 15615.
- [12] Z. Adhireksan, G. E. Davey, P. Campomanes, M. Groessl, C. M. Clavel, H. Yu, A. A. Nazarov, C. H. F. Yeo, W. H. Ang, P. Dröge, U. Rothlisberger, P. J. Dyson, C. A. Davey, *Nat. Commun.* **2014**, *5*, 3462; R. E. Morris, R. E. Aird, P. D. Murdoch, H. M. Chen, J. Cummings, N. D. Hughes, S. Parsons, A. Parkin, G. Boyd, D. I. Jodrell, P. J. Sadler, *J. Med. Chem.* **2001**, *44*, 3616; H. Chen, J. A. Parkinson, R. E. Morris, P. J. Sadler, *J. Am. Chem. Soc.* **2003**, *125*, 173.
- [13] H. Kwok, K. Briggs, V. Tabard-Cossa, *PLOS ONE* **2014**, *9*, e92880; K. Briggs, M. Charron, H. Kwok, T. Le, S. Chahal, J. Bustamante, M. Waugh, V. Tabard-Cossa, *Nanotechnology* **2015**, *26*, 084004.
- [14] A. Fragasso, S. Pud, C. Dekker, *Nanotechnology* **2019**, *30*, 395202; S. W. Kowalczyk, A. Y. Grosberg, Y. Rabin, C. Dekker, *Nanotechnology* **2011**, *22*, 315101.
- [15] C. Plesa, C. Dekker, *Nanotechnology* **2015**, *26*, 084003.
- [16] O. Novakova, J. Kasparkova, V. Bursova, C. Hofr, M. Vojtiskova, H. Chen, P. J. Sadler, V. Brabec, *Chem. Biol.* **2005**, *12*, 121.

Chapter 7

[Ru(**3**)(biq)(STF-31)]²⁺: A lock-and-kill anticancer PACT agent

*Ruthenium complexes have gained attention by the anticancer research community as potential prodrugs for photo-activated chemotherapy (PACT), but their fate in the cell is hard to trace because they are usually not emissive. We have developed a ruthenium prodrug that releases a fluorescent label, pyrene, when an ester linker installed between the ruthenium complex and the fluorophore is degraded by intracellular proteases. Upon hydrolysis of the ester linkage, the fluorescence of pyrene is no longer quenched by the complex, which allows for seeing the location of the prodrug and hence where irradiation with visible light should be realized. The complex, [Ru(**3**)(biq)(STF-31)](PF₆)₂, (where **3** = 3-([2,2':6',2''-terpyridin]-4'-yloxy)propyl-4-(pyren-1-yl)butanoate)) released the STF-31 ligand, a known cytotoxic nicotinamide phosphoribosyltransferase (NAMPT) inhibitor, upon light irradiation. The ester linker was found to be labile both under enzymatic and acidic conditions, which may allow for visualizing cancer cells specifically due to their higher drug metabolism and acidity. Confocal imaging and cell cytotoxicity should show if cells indeed become fluorescent upon treatment with the compound, and if the compound is more toxic after light irradiation. This new lock-and-kill principle could help to identify the malignant cells and hence know where to shine light for activating the compound, which will contribute to the development of photoactivated chemotherapy.*

7.1. Introduction

Nowadays, a wide range of transition metals are considered for medicinal application against cancer, including platinum, palladium, copper, and ruthenium.^[1] Many ruthenium drugs and prodrugs have been prepared, some of which have reached clinical trial.^[2] In photodynamic therapy (PDT) and photoactivated chemotherapy (PACT), a ruthenium prodrug is activated upon visible light irradiation of the tumor, to induce cell death only at that place, while the complex when left in the dark is non-toxic, or much less toxic.^[3] While PDT typically relies on the production of reactive oxygen species by energy or electron transfer to O₂ by the excited state of the ruthenium complex, in PACT the excited state releases a cytotoxic compound via a photosubstitution reaction independent of the presence of O₂. This specific mode of activation of PACT is relevant for oncology, as many tumors are hypoxic in their core, which makes them more difficult to treat.^[4]

The cytotoxic species in PACT may be the ruthenium polypyridyl complex itself, but the complex may also be used as a photocage, to bind a toxic species which when bound is inactive, but can be activated by removing the ruthenium photocage.^[5] A recent example from our group is the photoactivatable ruthenium complex [Ru(tpy)(biq)(STF-31)](PF₆)₂, where tpy = 2,2':6'2''-terpyridine, biq = 2,2'-biquinoline and STF-31 = 4-((4-*t*-butyl)phenylsulfonamido)methyl)-N-(pyridin-3-yl)benzamide.^[6] This complex bears the biologically active STF-31 moiety, which is a known nicotinamide phosphoribosyltransferase (NAMPT) inhibitor.^[7] When bound to the ruthenium metal center, STF-31 is 20 times less active than the free inhibitor. When the STF-31 molecule is released from the metal complex, it recovers its ability to inhibit NAMPT, which causes the cell to die.

Importantly, for efficient phototherapy in a patient, a surgeon needs to know where irradiation should be realized. PDT compounds (*i.e.*, protoporphyrin IX) are often luminescent, which is typically used to monitor the uptake of the PDT agent or to diagnose, using a strategy called photodynamic diagnosis (PDD),^[8] but also to pinpoint where to shine light *in vivo*.^[9] On the other hand, PACT compounds are generally not emissive.^[10] Localizing where a PACT compound has been taken up is thus inherently difficult, which could potentially complicate the treatment of a cancer patient with PACT. To address this issue, we functionalized the [Ru(tpy)(biq)(STF-31)](PF₆)₂ PACT complex with a fluorescent

tag by the attachment of a pyrene fluorophore to the tpy ligand *via* an intracellularly degradable ester linker. The complex $[\text{Ru}(\mathbf{3})(\text{biq})(\text{STF-31})](\text{PF}_6)_2$ ($[\mathbf{1}](\text{PF}_6)_2$, where $\mathbf{3} = 3-([2,2':6',2'']\text{-terpyridin-}4'\text{-yloxy})\text{propyl-}4\text{-(pyren-1-yl)butanoate}$, is shown in Figure 7.1A. In this work, we present the synthesis and photochemical properties of $[\mathbf{1}](\text{PF}_6)_2$, and provide proof-of-concept that pyrene-based fluorescence can indeed be recovered through ester cleavage by esterases and under acidic conditions, thereby showing where the PACT complex should be irradiated. Ester cleavage in a living cell has been shown to occur quickly, which has been applied for prodrug activation, bio-imaging and uptake visualization,^[11] and generally is faster in cancerous cells due to esterase overexpression.^[12] Cancerous tissues are thus likely to light up more strongly than healthy tissue, giving an optical contrast which reveals the location of a tumor and shows where the irradiation should be done to kill the tumor through photo-activated release of STF-31 (Figure 7.1B-D).

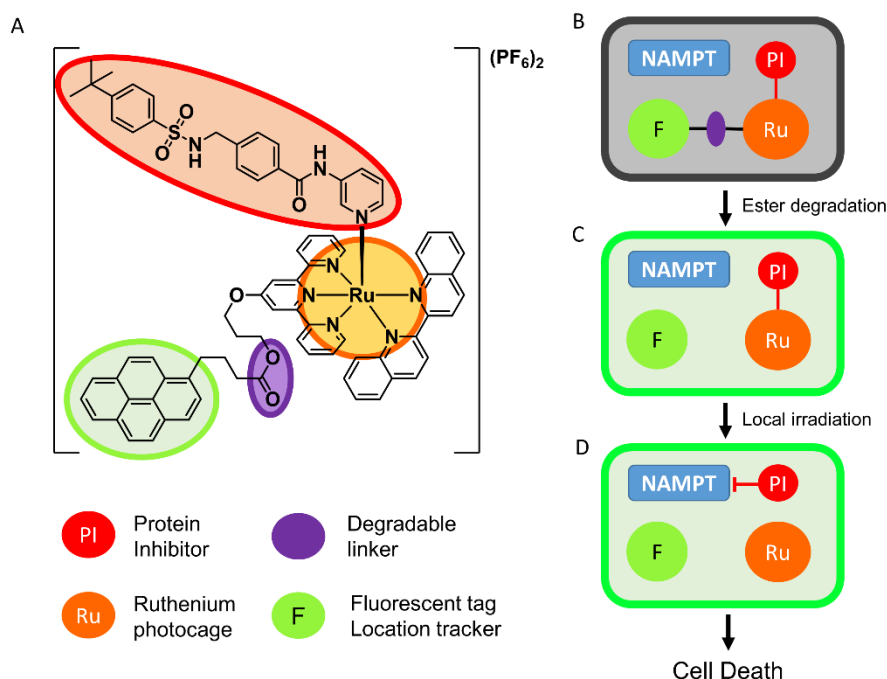
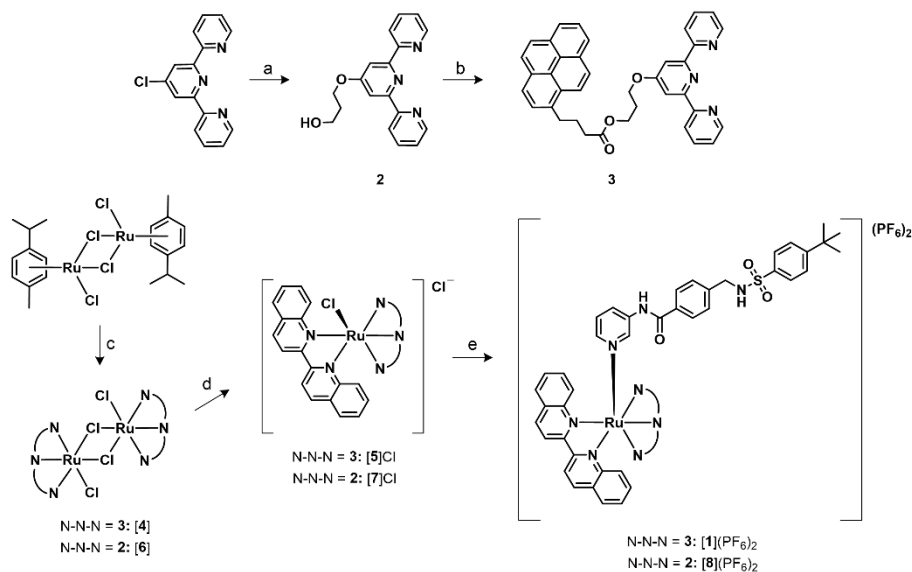


Figure 7.1: A lock-and-kill PACT agent. A) Molecular structure of $[\text{Ru}(\mathbf{3})(\text{biq})(\text{STF-31})](\text{PF}_6)_2$ ($[\mathbf{1}](\text{PF}_6)_2$). The moieties with specific functionalities are highlighted in different colors. B-D) When the prodrug is internalized in a cell (B), the ester connection (violet) is cleaved by intracellular enzyme activity, which makes the fluorescence of the pyrene tag (green) no longer quenched by the ruthenium complex, hence lighting up the cell (C). The luminescent cells can then be treated by light irradiation, to release the STF-31 cytotoxic inhibitor (red) from the photocage (orange) and induce cell death (D).

7.2. Results and Discussion

7.2.1. Synthesis

[1](PF₆)₂ was synthesized using a modified protocol for making the fluorophore-free complex.^[6] In short, 1,3-propanediol was reacted with 4'-chloro-2,2':6',2''-terpyridine to obtain compound **2** (see Scheme 7.1), to which pyrene was attached by esterification with 1-pyrenebutyric acid, to afford compound **3**. [(Ru(*p*-cymene)Cl₂)₂] was then reacted with ligand **3** to obtain [(Ru(**3**)Cl₂)₂] (compound [4]), which was converted into [Ru(**3**)(biq)Cl]Cl (compound [5]Cl) by coordination of 2,2'-biquinoline (biq). [5]Cl was then converted into [1](PF₆)₂ via substitution of the chlorido ligand for STF-31. As a reference, the same complex deprived of the pyrene moiety, [8](PF₆)₂, was prepared via the same route, but starting from ligand **2** instead of pyrene-functionalized ligand **3**. The reference complex [Ru(tpy)(biq)(STF-31)](PF₆)₂ ([9](PF₆)₂) was provided by R. Vadde.



Scheme 7.1: Synthesis route towards [1](PF₆)₂ and [8](PF₆)₂. a) 1,3-propanediol, KOH, DMSO, 60 °C. b) 1-pyrenebutyric acid, DMAP, DCC, DCM, rt. c) compound **3** or **2**, DCM, rt. d) 2,2'-biquinoline, ethylene glycol, 180 °C. e) SFT-31, AgPF₆, acetone/water 1:1, 50 °C.

7.2.2. Photodriven release of STF-31

UV-vis spectroscopy was used to determine the photochemical properties of $[1](PF_6)_2$. Although $[1]^{2+}$ is dicationic, the strongly hydrophobic ligands and PF_6 counter ions prevent complex $[1](PF_6)_2$ from being soluble in water, so we used a methanol solution instead ($[Ru] = 25 \mu M$) to study photosubstitution of the STF-31 ligand by methanol upon irradiation. At first, the solution was kept in the dark while the absorbance was monitored over time; the absorbance profile did not change over 1 hour, showing the complex is stable in such conditions. After 1 hour, the solution was irradiated with green light (530 nm), upon which the absorbance spectra changed rapidly; within minutes λ_{max} shifted from 540 nm (pink solution) to 554 nm (purple solution) with a clear isosbestic point at 556 nm (see Figure S7.2A). Mass spectroscopy after irradiation confirmed that the starting complex was no longer present and the complex had been converted to the Ru-MeOH analogue ($m/z = 483.6$ and 966.4 for $[1 - STF-31 + MeOH]^{2+}$ and $[1 - STF-31 + MeO]^+$).

For complex $[8](PF_6)_2$ we found very similar behavior to green light irradiation as observed for the pyrene-labelled compound $[1](PF_6)_2$, as well as for the unmodified compound $[9](PF_6)_2$ (Figure S7.1). The photosubstitution of STF-31 was rapid in all cases, as complete conversion was reached within 15 minutes of irradiation, *i.e.* the UV-vis spectra showed no change over time after 15 minutes (see Figure S7.2B) and MS showed that no starting material or only trace amounts remained after irradiation. The quantum yield (QY, the slope of the amount of the ruthenium STF-31 complex in solution n Ru-STF in mol over $Q(t)$, the total amount of photons absorbed over time) for STF-31 photoexpulsion differs between the three complexes, however (see Figure S7.2C). For both ether-functionalized complexes $[1](PF_6)_2$ and $[8](PF_6)_2$ the quantum yield is very similar (QY = 0.0052 and 0.0058, respectively), while on the other hand, the unmodified complex $[9](PF_6)_2$ has a higher quantum yield (QY = 0.012), similar to the value reported in water using red light (QY = 0.013).^[6] On the one hand, the photosubstitution quantum yield is significantly influenced by ether functionalization of the tpy ligand. We think this effect is due to the electron-donating effect of the ether substituent on the terpyridine ligand, which likely increases the ligand field splitting energy, and hence the energy between the 3MLCT and 3MC state, thereby making ligand photosubstitution less likely to occur. On the other hand, however, the presence of the pyrene moiety on the

ether-modified tpy ligand of $[1](PF_6)_2$ has only little influence on the photoreactivity of the ruthenium complex.

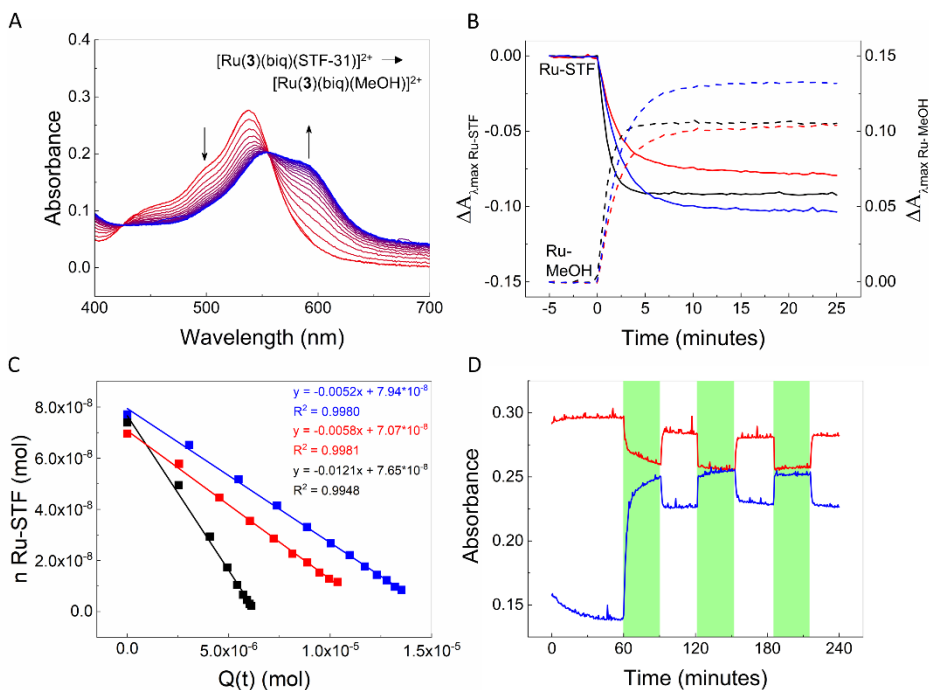


Figure 7.2: Photosubstitution of SFT-31. A) Evolution of absorbance of a solution of $[1](PF_6)_2$ in pure methanol (25 μ M), upon irradiation with 530 nm light (photon flux = 1.36×10^{-7} mol \cdot s $^{-1}$) after 1 h equilibration in the dark. Spectra show the absorbance at the start of irradiation (red) to 10 minutes after irradiation started (blue), recorded every 30 seconds. B) Absorbance change ΔA over time at λ_{max} for $[1](PF_6)_2$, $[8](PF_6)_2$, and $[9](PF_6)_2$ in the dark (denominated Ru-STF: blue, red and black solid line, resp. 540, 538 and 531 nm), and for their corresponding photoproducts (denominated Ru-MeOH: blue, red and black dashed line, resp. 554, 552 and 580 nm). C) Evolution of the amount of Ru-STF complexes in solution, n Ru-STF in mol, vs. the total amount of photons absorbed by the Ru-STF complexes since $t = 0$, $Q(t)$ in mol, for $[1](PF_6)_2$, $[8](PF_6)_2$, and $[9](PF_6)_2$ (blue, red and black); the slope of these plots are the quantum yields of the photosubstitution in pure methanol. D) Absorbance vs. time at absorption maximum λ_{max} for $[1](PF_6)_2$ and the photoproduct (red and blue, $\lambda_{max} = 540$ and 587 nm, respectively) in a 95:5 methanol/water mixture. Irradiation started at $t = 60$ min and was switched off and on (green bars) repeatedly, every 30 min. Spectra were recorded every 30 seconds.

For all three complexes, STF-31 photosubstitution in methanol is an irreversible process, *i.e.* when light was switched off, no back-coordination of STF-31 to the ruthenium methanol complex was observed. However, when the same experiment was carried out in presence of 5% water (MeOH/H₂O 95:5), the photoreaction became reversible, as demonstrated by UV-vis spectroscopy upon alternatively switching on and off a source of light and monitoring the spectrum

of the solution (see Figure S7.2D and Figure S7.2). The obtained reversibility by adding water could be due to solvation effects: in pure methanol, the liberated STF-31 and the ruthenium photoproduct are very soluble and can thus diffuse away from each other, which inhibits them from reacting again to form $[1]^{2+}$. However with water present the reaction products, which are sparsely soluble in water, diffuse less than in methanol, as they are kept close to each other in a solvent 'cage' by the water molecules, and the back-reaction is thus more likely to occur.^[13] Such reversibility, though interesting, is probably not a problem in a biological setting: cells are full of hydrophobic regions (proteins, membranes, DNA, etc.), which would be capable of solvating the photoproducts of photosubstitution in $[1]^{2+}$. Overall, all three complexes release the STF-31 ligand upon green light irradiation, and adding the pyrene group did not prevent this photosubstitution to occur.

7.2.3. Unlocking fluorescence by releasing pyrene

As pyrene and the ruthenium complex can be studied independently by shining UV or visible light, respectively, it was also possible to study the effect of the ruthenium complex on pyrene emission. Initially, we hypothesized that the presence of the ester linker would be detrimental for the emission properties of the pyrene group, and that such quenching by the ruthenium complex would be relieved when the ester linker is cleaved (see Figure 7.3A). In order to test this hypothesis, we first studied the luminescence properties of the intact complex $[1](PF_6)_2$ and $[5]Cl$ (the complexes with and without STF-31), and that of the ester degradation products $[7]Cl$ and 1-pyrenebutyric acid in methanol. $[1](PF_6)_2$ was found to be not fluorescent, while complex $[5]Cl$ showed weak emission at 395 nm and 375 nm upon excitation at 354 nm. On the other hand, upon mixing 1-pyrenebutyric acid and $[7]Cl$ at the same concentration (50 μM), strong emission was observed at 395 and 375 nm, showing that pyrene quenching by an unbound ruthenium complex is not very strong (see Figure 7.3B and Figure S7.3). It did occur to some extent though, as 1-pyrenebutyric acid alone showed stronger fluorescence at 375 to 400 nm in absence of any ruthenium complex. As the ruthenium complex absorbs in the region where free pyrene emits (see Figure 7.3C), and fluorescence quenching was much stronger when pyrene is covalently attached to the complex, quenching likely occurs *via* Förster resonance energy transfer (FRET), similar to the quenching mechanism for a similar pyrene-labeled ruthenium(II) trisbipyridine complex.^[14] We calculated the Förster distance R_0 (see

appendix Chapter 7), at which quenching of the fluorescence by FRET is 50%, for the donor/acceptor pair 1-pyrenebutyric acid/[8](PF₆)₂ in methanol, and found $R_0 = 24.4 \text{ \AA}$, while in a model of [1]²⁺ (simulated with Yasara, see Figure S7.4) we found the Ru-pyrene distance to be 20 \AA , which confirms that pyrene is quenched by FRET in our system. Moreover, we calculated the FRET efficiency ϕ_{FRET} for 1-pyrenebutyric acid/[8](PF₆)₂ and found that $\phi_{\text{FRET}} = 0.77$, hence FRET quenching is efficient. Overall, in methanol the fluorescence of pyrene is indeed quenched by its ruthenium neighbor when pyrene is covalently attached to the ruthenium complex, and quenching occurs through the FRET mechanism.

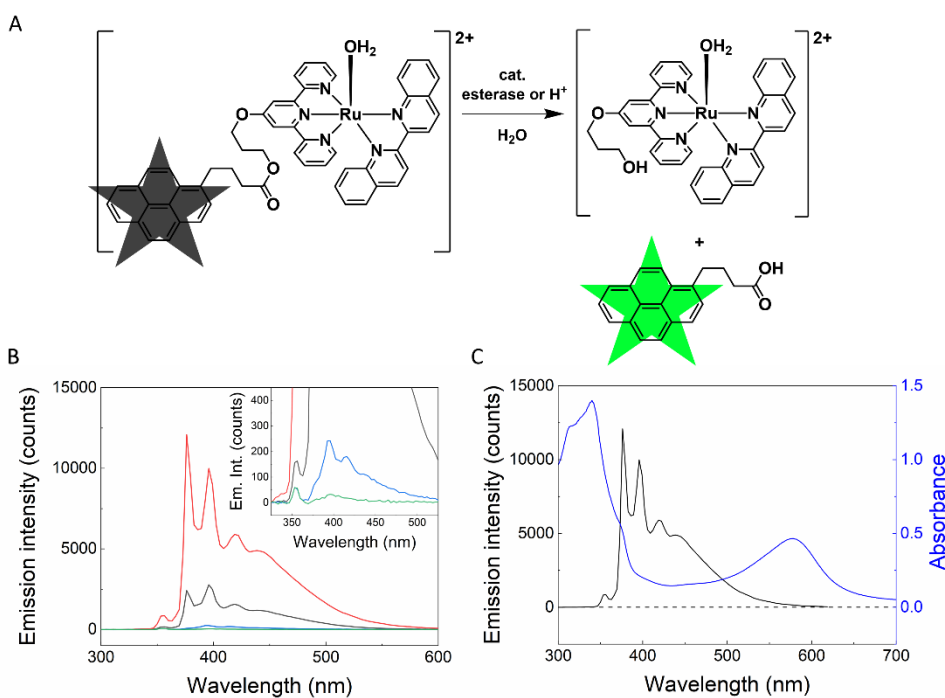


Figure 7.3: Quenching of pyrene emission by ruthenium. A) Upon cleavage of the ester bond, the initially quenched pyrene (black star) is liberated as free 1-pyrenebutyric acid, which is no longer quenched by the ruthenium complex and shows strong fluorescence (green star). B) Emission intensity of a methanol solution of [1](PF₆)₂ (green), of [5]Cl (blue), of a 1:1 mixture of [7]Cl and 1-pyrenebutyric acid (black), and of 1-pyrenebutyric acid alone (red), all excited at 354 nm. Concentration of all species was 50 μM . Inset: zoom of emission intensity (Em. Int.). C) Spectral overlap between the emission of 1-pyrenebutyric acid (black, left axis, excited at 354 nm) and absorbance of [7]Cl (blue, right axis), both 50 μM in methanol. Dashed line is the baseline.

7.2.4. Ester degradation

To study if the ester connection between the ruthenium complex and pyrene can indeed be degraded in aqueous solutions by esterase activity to release free pyrene and obtain fluorescence, we carried out a relatively simple experiment with [5]Cl, as [1](PF₆)₂ is insoluble in water: to a solution of [5]Cl (1 mM in water) fresh, filtered human saliva was added, which is known to have esterase activity, among other enzyme activities.^[15] The solution was stirred at 37 °C and the luminescence was measured at different time points (3, 24, 48, 72, 120 and 168 hours, final [Ru] = 50 μM; Ru/saliva solution volume ratio = 1:19). As a purple precipitation occurred, the sample was centrifuged at 4000 rpm for 10 minutes and the luminescence of the supernatant was measured. An increase of emission in the emission range of 375–450 nm, resembling the emission of pyrene (excited at 354 nm) within 24 hours indicated that the ester connection was hydrolysed and pyrene was liberated (see Figure 7.4A and Figure S7.5), unlike a solution [5]Cl without the enzymes or the solution of saliva alone itself. Thus, the ester bond of [5]Cl is indeed degraded by enzyme activity, which recovers the emission properties of the liberated pyrene moiety.

The acid sensitivity of the ester linker in [5]Cl was also demonstrated in a separate crystallization experiment. When a solution of [5]Cl in methanol was acidified with triflic acid, single crystals were obtained that were suitable for X-ray structure determination. The obtained crystal structure showed the formed crystals to be of the complex [Ru(2)(biq)(OH₂)](OTf)₂ (see Figure 7.4B). The large torsion angle over N3-Ru1-N1-C1 (107.1°) shows that the biq ligand is tilted with respect to ligand 2, likely due to steric effects,^[16] as the Ru1-N1 bond (2.102 Å) from biq is relatively long compared to the Ru1-N4 (1.990 Å) bond (see Table 7.1). Most importantly, the crystal structure revealed that the ester bond between pyrene and ruthenium in [5]Cl is also cleaved in acidic conditions. Overall, [1](PF₆)₂ can hence release two fragments: a NAMPT inhibitor, when the complex is irradiated with visible light; and a pyrene group, when the ester bond in the complex is cleaved either by esterases or acid, upon which the pyrene group becomes fluorescent as it is no longer quenched by the covalently attached ruthenium complex.

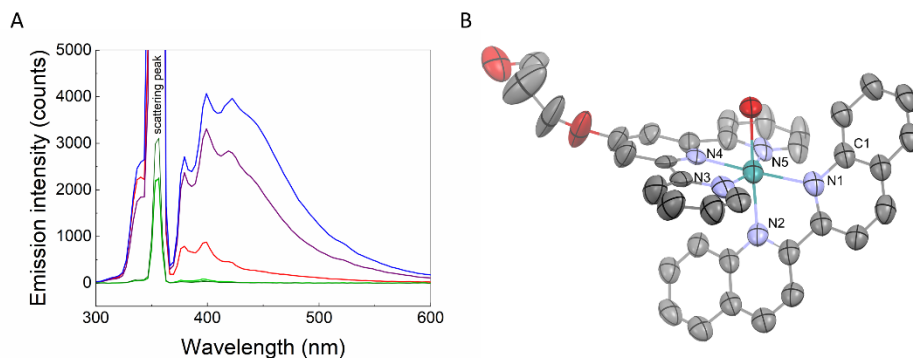


Figure 7.4: Fluorescence activation. A) Luminescence intensity *vs.* emission wavelength, excited at 354 nm, for a mixture of [5]Cl (50 μ M) and saliva at 3 h, 24 h and 48 h (red to blue) and the same complex in water at the same concentration and time points (dark to light green). The peak at 354 nm is due to light scattering. B) Displacement ellipsoid plot (50% probability) of the structure of [Ru(2)(biq)(OH₂)](OTf)₂, obtained from a solution of [5]Cl in a methanol that was acidified with triflic acid. Hydrogen atoms and the triflate counter ions have been omitted for clarity.

Table 7.1: Selected bond lengths (\AA) and torsion angle ($^\circ$) for [Ru(2)(biq)(OH₂)](OTf)₂.

[Ru(2)(biq)(OH ₂)](OTf) ₂			
Ru1-N1	2.102(6)	Ru1-N4	1.990(8)
Ru1-N2	2.073(5)	Ru1-N5	2.087(8)
Ru1-N3	2.080(2)	N3-Ru1-N1-C1	107.1(6)

7.3. Conclusions & Outlook

Ruthenium complex [1](PF₆)₂ was synthesized, bearing a hydrolysable pyrene fluorophore and a light-cleavable STF-31 ligand. Upon green light irradiation in methanol, STF-31 is photosubstituted by a solvent molecule. The presence of the pyrene group does not affect the kinetics of this photoreaction, but the presence of the ruthenium complex strongly quenches the fluorescence of the pyrene moiety. When the ester linker between the ruthenium complex and the pyrene moiety is cleaved, catalyzed either by esterases or acid, the fluorescence of the pyrene tag is “unlocked”. We envision that this principle could be used for visualizing prodrug uptake in cancer cells, which are more acidic and contain highly active esterases. Light activation of the PACT prodrug should be realized by specifically aiming the laser at fluorescent cells, which, if this concept can be translated *in vivo*, may allow for having a highly selective anticancer action.

To further demonstrate that this principle will work in a biological context, confocal studies should be first done *in vitro* to see if cells indeed light up after drug uptake, while confocal microscopy with full living organisms, *i.e.* zebrafish embryo or mice, may show whether the cancer tissues light up more strongly due to prodrug uptake, compared to non-cancerous tissues. Finally, cytotoxicity studies should be done with [1](PF₆)₂, possibly in a liposomal formulation to increase the water solubility of the complex and ease administration, to assess the difference in anticancer efficacy of the drug between dark and light irradiation conditions.

7.4. References and Notes

- [1] K. D. Mjos, C. Orvig, *Chem. Rev.* **2014**, *114*, 4540.
- [2] M. J. Clarke, *Coord. Chem. Rev.* **2002**, *232*, 69; R. E. Morris, R. E. Aird, P. D. Murdoch, H. M. Chen, J. Cummings, N. D. Hughes, S. Parsons, A. Parkin, G. Boyd, D. I. Jodrell, P. J. Sadler, *J. Med. Chem.* **2001**, *44*, 3616; G. Sava, S. Zorzet, C. Turrin, F. Vita, M. Soranzo, G. Zabucchi, M. Cocchietto, A. Bergamo, S. DiGiovine, G. Pezzoni, L. Sartor, S. Garbisa, *Clin. Cancer Res.* **2003**, *9*, 1898; S. Monro, K. L. Colón, H. Yin, J. Roque, P. Konda, S. Gujar, R. P. Thummel, L. Lilge, C. G. Cameron, S. A. McFarland, *Chem. Rev.* **2019**, *119*, 797.
- [3] C. Mari, V. Pierroz, S. Ferrari, G. Gasser, *Chem. Sci.* **2015**, *6*, 2660; R. Friederike, S. Wiktor, *Curr. Med. Chem.* **2017**, *24*, 4905; C. Mari, V. Pierroz, R. Rubbiani, M. Patra, J. Hess, B. Spingler, L. Oehninger, J. Schur, I. Ott, L. Salassa, S. Ferrari, G. Gasser, *Chem. Eur. J.* **2014**, *20*, 14421.
- [4] S. Bonnet, *Dalton Trans.* **2018**, *47*, 10330; P. Vaupel, A. Mayer, *Cancer Metastasis Rev.* **2007**, *26*, 225.
- [5] J.-A. Cuello-Garibo, M. S. Meijer, S. Bonnet, *Chem. Commun.* **2017**, *53*, 6768; A. Li, R. Yadav, J. K. White, M. K. Herroon, B. P. Callahan, I. Podgorski, C. Turro, E. E. Scott, J. J. Kodanko, *Chem. Commun.* **2017**, *53*, 3673; B. A. Albani, B. Peña, N. A. Leed, N. A. B. G. de Paula, C. Pavani, M. S. Baptista, K. R. Dunbar, C. Turro, *J. Am. Chem. Soc.* **2014**, *136*, 17095; R. N. Garner, J. C. Gallucci, K. R. Dunbar, C. Turro, *Inorg. Chem.* **2011**, *50*, 9213.
- [6] L. N. Lameijer, D. Ernst, S. L. Hopkins, M. S. Meijer, S. H. C. Askes, S. E. Le Dévédec, S. Bonnet, *Angew. Chem., Int. Ed.* **2017**, *56*, 11549.
- [7] D. Kraus, J. Reckenbeil, N. Veit, S. Kuerpig, M. Meisenheimer, I. Beier, H. Stark, J. Winter, R. Probstmeier, *Cell. Oncol.* **2018**, *41*, 485.
- [8] I. Kausch, M. Sommerauer, F. Montorsi, A. Stenzl, D. Jacqmin, P. Jichlinski, D. Jocham, A. Ziegler, R. Vonthein, *Eur. Urol.* **2010**, *57*, 595; Y. Matoba, K. Banno, I. Kisu, D. Aoki, *Photodiagn. Photodyn. Ther.* **2018**, *24*, 52; H. Fukuhara, S. Yamamoto, T. Karashima, K. Inoue, *Int. J. Clin. Oncol.* **2020**; Z. Malik, *Transl. Biophotonics* **2020**, *2*, e201900022; H. Kostron, *Photodynamic Diagnosis and Therapy for Brain Malignancies from the Bench to Clinical Application*, in *Photodynamic Therapy: From Theory to Application*, Springer Berlin Heidelberg, **2014**, 165.
- [9] S. Mallidi, B. Q. Spring, S. Chang, B. Vakoc, T. Hasan, *Cancer J.* **2015**, *21*, 194.
- [10] B. Siewert, M. Langerman, Y. Hontani, J. T. M. Kennis, V. H. S. van Rixel, B. Limburg, M. A. Siegler, V. Talens Saez, R. E. Kieltyka, S. Bonnet, *Chem. Commun.* **2017**, *53*, 11126.
- [11] B. Rotman, B. W. Papermaster, *Proc. Natl. Acad. Sci. U. S. A.* **1966**, *55*, 134; L. D. Lavis, T.-Y. Chao, R. T. Raines, *ACS Chem. Biol.* **2006**, *1*, 252; C. Molenaar, J.-M. Teuben, R. J. Heetebrij, H. J. Tanke, J. Reedijk, *J. Biol. Inorg. Chem.* **2000**, *5*, 655; B. M. Liederer, R. T. Borchardt, *J. Pharm. Sci.* **2006**, *95*, 1177.

Chapter 7: A lock-and-kill PACT agent

- [12] H. Dong, L. Pang, H. Cong, Y. Shen, B. Yu, *Drug Delivery* **2019**, *26*, 416; E. Afrimzon, A. Deutsch, Y. Shafran, N. Zurgil, J. Sandbank, I. Pappo, M. Deutsch, *Clin. Exp. Metastasis*. **2008**, *25*, 213.
- [13] R. Breslow, *Acc. Chem. Res.* **1991**, *24*, 159.
- [14] M. Vonlanthen, A. Cevallos-Vallejo, E. Aguilar-Ortíz, A. Ruiu, P. Porcu, E. Rivera, *Polymer* **2016**, *99*, 13.
- [15] H. Yamahara, V. H. L. Lee, *Adv. Drug Delivery Rev.* **1993**, *12*, 25.
- [16] D. M. Klassen, *Inorg. Chem.* **1976**, *15*, 3166.

8

Summary, Conclusions & Outlook

Molecular and Nano-Engineering with Iron, Ruthenium
and Carbon: Hybrid structures for Sensing

8.1 Summary

8.1.1 General Introduction (CH 1)

Monitoring and measuring is at the basis of modern healthcare, and sensitive and selective sensors are in high demand. Graphene is an all-carbon 2D semiconductor material that is very suitable for such sensing technologies due to its electronic properties. Yet for graphene-based sensors, the graphene sheet has to be functionalized with molecules that probe the environment. These functional molecules undergo changes when they react with a binding partner, and these changes can be detected by graphene, as graphene is sensitive to molecular changes near its surface. As a result of these changes, the electronic properties of the graphene sheet are altered, which can be read out electronically through standard electronic measurement equipment.

Metal complexes can fulfill the role of functional molecule on a sensor. Due to the nearly unlimited tunability of metal complexes through changing the ligand environment surrounding a metal center and the accessibility of multiple charged states of the metal center itself, metal complexes can show a wide range of chemical behaviors that can be useful for sensing technologies. For example, iron(II)-based complexes can do spin crossover (SCO), which is a rearrangement of electrons in the d^6 configuration from a high spin state to a low spin state and vice versa, changing the chemical and physical properties of the molecule and the bulk material. This molecular switching effect is technologically interesting, but technological implementation of these typically dielectric materials is difficult. Through nanotechnology and device engineering approaches, ways have been found to read-out the switching behavior in the nanoscale. Yet, scaling down SCO materials strongly influences the switching properties.

Triggered by light, ruthenium polypyridyl complexes can switch properties as well, for example by photodriven linkage isomerization or ligand exchange. Moreover, these complexes can interact with biomolecules like DNA. These interactions can be used for bio-imaging and sensing, as the complexes change their photophysical properties upon binding; they can for example become light-emissive upon binding. Furthermore, binding of ruthenium complexes to nucleotides can be used to improve sensing, for instance by labeling specific nucleotides. Ruthenium complexes are thus appealing as molecular probes and labels for sensing.

8.1.2 Contactless spin switch sensing by chemo-electric gating of graphene (CH 2)

In chapter 2, it is described how graphene senses spin switches in a dielectric molecular material that has spin crossover (SCO) behavior. Graphene field effect transistors were fabricated over single crystals of the SCO complex $[\text{Fe}(\text{bapbpy})(\text{NCS})_2]$. The graphene sheet and the SCO crystal were separated by a polymer spacer, so that they were electrically disconnected. Abrupt resistance variations occurred as the devices were cooled down or heated up to trigger the phase transitions, accompanied by a strong color change of the SCO crystal. The phase transitions in the SCO crystal could thus be sensed electrically by the graphene transistor.

We found that the thickness of the polymer spacer played a crucial role in the sensing mechanism for these devices, and that the mechanism of sensing involved two effects. First, mechanical effects of the phase transition (expansion and contraction of the SCO crystal) contributed to a minor amount of the resistance variations upon spin crossover. The mechanical effects, studied by a careful analysis of the 2D peak of graphene in Raman spectroscopy, were especially strong in the very first phase transition in spin phase cycling experiments. This was in agreement with the much stronger resistance variation at the first phase transition than for following phase transitions. Importantly, with the thickest spacer (0.5 μm) these mechanical effects were largely buffered by the polymer spacer.

Second, the resistance variations were mainly due to changes in the electrostatic potential of the spin crossover crystal. As the molecules in the crystal lattice of the single crystal are highly ordered, the dipoles of all the molecules in the bulk crystal are directed similarly, giving the crystal an electrostatic potential. Upon SCO, the dipole of the molecules in the single crystals changes all at once, as the phase transition of the crystal occurs within seconds, and thus the electrostatic potential changes as well. In effect, the graphene that is nearby the crystal is feeling that the potential changed; the doping of the graphene sheet changes. This is a new mechanism of sensing with graphene, we called chemo-electric gating, which opens opportunities for the integration of molecular materials in electronic devices.

8.1.3 Large-area thin films of the spin crossover complex [Fe(bapbpy)(NCS)₂] grown selectively on graphene (CH 3)

Continuing on chapter 2, in chapter 3 it is described how the spin-crossover material based on [Fe(bapbpy)(NCS)₂] can be scaled down to thin films. We found that a film based on this complex deposited over time when methanol was evaporated slowly into a solution of the metal complex. Interestingly, the films were found to be growing with a strong preference on graphene-coated areas over clean SiO₂ silicon wafer surfaces, on the centimeter scale as well as on micrometer-sized disks of graphene on SiO₂ surfaces. A study of the film with AFM revealed that the film grew homogeneously, and the thickness increased slowly in the range of nanometers per day. Raman spectroscopy showed particularly convincingly for thicker films (>20 nm) good similarity between the spectra for the films as compared to the bulk materials. Additionally, Raman and XRD showed that the film was amorphous. Lastly, XPS showed that the iron centers in the films were at least partially oxidized to Fe(III); the level of oxidation of iron depended on the means of oxygen protection during film growth.

Measuring the spin crossover properties of these films was challenging. Samples were analyzed by SQUID magnetometry; the low amount of material in the film and strong diamagnetic background signal of the wafer itself made interpretation of the SQUID results difficult. For only one out of four samples, a reversible transition was found, which could mean that this film was spin crossover active; however, no hard conclusions can be drawn from the SQUID analysis. Whether oxidation of the films (during growth and/or storage) played a role remains to be an important research question.

The films could be grown on graphene field effect transistors, with a preference again for growing on the graphene sheet. Only very thin films could be obtained however, as the electrodes of the devices were etched in the thin film solution and devices could thus be immersed for a limited time only. Functional devices were produced, yet no sign of spin crossover could be found though examining the resistance variations of the devices upon cooling and heating from room temperature down to 150 K to induce spin crossover. Altogether, no strong evidence was found that the films were spin-crossover active.

8.1.4 Polymer coated graphene-based gas sensors: chemical fingerprinting by simultaneous sensing (CH 4)

In chapter 4, a graphene-based sensor is described that is not functionalized with a metal complex or material that has a specific interaction for a binding partner. Instead, the sensors described here were functionalized with the transfer polymer layer. Graphene-based sensors (fabricated on standard silicon wafers) that were coated with a 300 nm-thick layer of the transfer polymer poly (methyl methacrylate) (PMMA) were subjected to chemical vapors of 15 compounds (single injections were carried by a nitrogen flow to the measurement chamber). Resistance variations, or responses, were observed for most compounds, and were highly reproducible. The peak intensity was different for different species, showing the sensors to discriminate between compounds.

We used this discrimination between compounds in our advantage to evaluate the response to mixtures of compounds. By lowering the concentration of methanol in diethyl ether (methanol gave strong responses, while diethyl ether gave hardly any response), we estimated that the lower detection limit of the PMMA-coated sensors for methanol was 6 ppm. Moreover, we could also use the PMMA-coated sensor for quantification of complex binary mixtures; good linear relations were found between peak intensity and the percentage of methanol in ethanol, and between the full-width half maximum of the response and the percentage of water in ethanol.

These results showed the potential of the PMMA-coated sensor, but the sensors were poorly selective and could thus not be used for compound identification. To use polymer coated sensors for identification, we produced arrays of graphene sensors, each with a different transfer polymer coating (PMMA, Nafion® 117, and cellulose acetate butyrate (CAB)). The sensors were packed in a small tube configuration that could be integrated in a gas chromatography (GC) setup, enabling auto-injection for continuous sampling to produce chemical fingerprints of the vapors: the combined information of the responses of the sensors in the array, which all responded simultaneously to the vapor in the chamber. The chemical fingerprinting (CF) array data could be used for classification and identification by supervised machine learning, reaching an accuracy of 92%. Using these chemical fingerprints, the selectivity was thus strongly increased so that the acquired data could be used for accurate compound identification.

8.1.5 Monitoring a ruthenium-based photoreaction with graphene on paper (CH 5)

In chapter 5, we introduced a new substrate for graphene sensors: ordinary paper. Using paper as a substrate has the advantage that solutions of interest can be soaked in the paper, and analytes can easily reach the graphene-paper interface, where sensing happens. We soaked these devices with solutions containing either the photosubstitutionally active ruthenium complex $[\text{Ru}(\text{tpy})(\text{biq})(\text{OH}_2)]^{2+}$, the ruthenium complex $[\text{Ru}(\text{bpy})_3]\text{Cl}_2$ which is a good electron transfer agent but cannot do photosubstitution, or with KNO_3 . Remarkably, when we monitored the resistance of the graphene sheet, all devices responded to light, independent of the chemical nature of the solution.

When we electrically gated these devices by varying the potential underneath the graphene sheet between 0 and 1.5 V, we could see the typical Dirac peak for all devices, showing that these devices are very suitable for such gating experiments. The Dirac peak did not move for the devices wetted with the previously mentioned solutions. To initiate a chemical reaction in solution, we added a ligand, 2-deoxyguanone monophosphate (dGMP) to allow for a coordination reaction between the ligand and $[\text{Ru}(\text{tpy})(\text{biq})(\text{OH}_2)]^{2+}$ in the dark and the phototriggered release of the ligand with visible light. When we irradiated devices with this solution, we could observe a small peak shift, which seemed to indicate that the graphene sheet indeed senses the chemical reaction taking place.

At the same time however, we noticed that a current was flowing from the gate electrode to the graphene sheet as we varied the gate potential. Peaks appeared in the plots of this current versus the gate potential, which indicated electrochemistry was taking place. The exact nature of the electrochemical reaction, possibly the oxidation and reduction of the ruthenium complexes, could not be determined, however. The question whether the graphene sheet has sensed the (photo)chemical conversions in the paper substrate is thus not definitively answered, as we could not exclude these electrochemical processes from a possible sensing mechanism. Further research is required to fully understand the processes taking place in the graphene on paper devices, and to develop graphene on paper as a sensing platform.

8.1.6 Reducing the translocation speed of DNA in solid-state nanopores by photo-labile ruthenium complex decoration (CH 6)

Chapter 6 takes us to a different kind of sensing with nanodevices. In a nanopore device, an ionic current flows between two chambers, separated by a membrane with a single pore. If DNA is located in one of the chambers, it is driven by an electrostatic potential to the other chamber. While the DNA strand travels through the pore, the ionic current is blocked, as the bulky DNA effectively narrows the pore. Careful analysis of the ionic current behavior in theory could be used to tell which bases are located in the pore. For solid-state nanopores, the challenge lies in slowing down the translocation of DNA through the pore, as the DNA travels too fast to determine its sequence.

To slow down DNA translocation, we proposed to attach ruthenium complexes to the DNA strand, which can be released again with visible light. When the ruthenium complex is attached, the DNA experiences more friction by the added bulk, which should decrease its motion. Upon irradiation, the DNA is released and is free to travel. In this way, the motion of DNA in a nanopore can be controlled with light irradiation.

With UV-vis, we found that the ruthenium complex $[\text{Ru}(\text{tpy})(\text{biq})(\text{Cl})]\text{Cl}$, hydrolysed to $[\text{Ru}(\text{tpy})(\text{biq})(\text{OH}_2)]^{2+}$ in aqueous solutions, coordinated to ctDNA and specifically to the nucleotide dGMP. No binding was found with dAMP, dTMP, and dCMP. DNA was incubated with the ruthenium complex and translocated through a nanopore in a silicon nitride membrane of 30 nm thickness. The translocation speed of DNA was not lowered, but the ionic current drop was significantly larger with the complexes attached. This indicated that the ruthenium complex co-translocated with the DNA strand: with the ruthenium complexes attached, the DNA was more bulky, resulting in the larger current drop, but its speed was not decreased as the ruthenium complexes could not provide sufficient drag.

Further research should be done to see if the ruthenium complexes can be attached to the surface of the membrane and inhibit DNA movement, and what will be the effect of visible light irradiation on the DNA translocation speed through a nanopore in a ruthenium-modified membrane.

8.1.7 [Ru(3)(biq)(STF-31)]²⁺: A lock-and-kill anticancer PACT agent (CH 7)

Moving away from sensing using electronic devices, in the final experimental chapter we describe how molecules themselves can be used for sensing. A ruthenium complex was designed and synthesized that is thought to play a dual role in anticancer therapy with light, known as photoactivated chemotherapy (PACT). We hypothesized that the complex [Ru(3)(biq)(STF-31)](PF₆)₂ (**3** = 3-([2,2':6',2''-terpyridin]-4'-yloxy)propyl-4-(pyren-1-yl)butanoate), biq = 2,2'-biquinoline and STF-31 = 4-((4-*t*-butyl)phenylsulfonamido)methyl)-N-(pyridin-3-yl)benzamide) can show that it was taken up by a cell through a fluorescence signal. This information could be very helpful for a surgeon to pinpoint where the prodrug is located in the body and thus to know where irradiation needs to be done; upon irradiation with visible light the complex releases an inhibitor for the NAMPT protein that is vital to cell survival, which eventually kills the irradiated cells.

First of all, the ruthenium ion – the photocage – was photoreactive and expelled the STF-31 ligand – the inhibitor – upon irradiation with green light. Kinetic studies showed that the pyrene group attached to the tridentate ligand did not affect the quantum yield of photoexpulsion, but that the quantum yield was lower because of the ether connection to the tpy ligand. The pyrene moiety did thus not affect the photochemistry of the ruthenium complex. Second, ligand **3** attaches the pyrene group – the fluorescent tag – to the ruthenium complex via an ester bond. Fluorescence studies showed that when pyrene was attached to the ruthenium complex its fluorescence was quenched. When the ester bond, which connected the ruthenium complex and the pyrene group, was broken by esterase activity the liberation of the pyrene group unlocked its fluorescence. This ester bond is expected to be cleaved quickly after entering the cell by esterase activity, yet will remain intact in the blood stream, where no esterases are present. Ester bond cleavage leads to fluorescence, and cells which have taken up the complex are thus expected to light up over cells that did not internalize the prodrug.

In the near future, confocal microscopy should point out whether cells that have taken up the ruthenium complex indeed become fluorescent. Furthermore, the potential of these complexes to kill malignant cells should be studied through in vitro tests and the effect of irradiation on cell death after treatment should be evaluated to see if the complex is indeed more toxic upon irradiation.

8.2 Conclusions and Outlook

8.2.1 General conclusions

Graphene and metal complexes have shown to be valuable tools in the design of sensing devices and molecular sensors. The various properties of these materials could be exploited in a number of sensing platforms. The options to design these platforms are numerous. We constructed graphene devices on common substrates, *i.e.* silicon wafers, but also on extraordinary substrates, including micrometer-sized single crystals grown from an iron complex with spin crossover properties, and ordinary paper. We could fabricate devices that exploited the properties of these substrates: phase transitions in the spin crossover crystal could be detected due to the electrostatic potential of this crystal, which changes as spin crossover occurred. Also, using paper as a substrate for graphene sensors allowed us to bring analytes in aqueous ionic solutions close to the graphene surface where they could be sensed, while at the same time we could efficiently gate these devices to carefully inspect the electronic properties of graphene. Thus, the ability of graphene to be transferred to various substrates by the aid of a polymer makes this material suitable for construction of graphene devices on functional substrates.

Moreover, we found that coating the surface of the graphene sheet was a fruitful approach to fabricate devices. Thin films of the spin crossover iron complex were found to grow specifically on graphene, even in a field effect transistor configuration; however we could not yet detect phase transitions in the thin films with these devices. The transfer polymer, on the other hand, turned out to be an ideal component for the sensors, crucially providing protection to the graphene sheet when it was placed on the single crystal and on paper, thus safeguarding the integrity of the devices. The transfer polymer could even be the sensitizing component of graphene-based vapor sensors: by using an array of multiple sensors with different polymer coatings, high selectivity could be obtained for a wide range of compounds. In fact, leaving the transfer polymer on graphene intact was perhaps the design principle that was the most beneficial for the devices reported in this thesis.

We also explored the possibility of using metal complexes, and in particular ruthenium complexes that are light-active, to enhance sensing and as molecular sensors. Ruthenium polypyridyl complexes which bound to DNA were found to

improve DNA detection, by increasing the signal strength when a DNA passed through a nanopore by making the DNA strand more bulky, and thus better observable. Moreover, a ruthenium complex was found to be suitable to quench a fluorescent tag, pyrene, when this tag was covalently attached to the complex via an enzymatically degradable linker. Degradation of this linker unlocked the fluorescence of this tag: hence this complex, a light-activatable anticancer prodrug, may help to show where the compound is taken up as the linker is degraded and cells become fluorescent, which can help to pinpoint where irradiation should occur *in vivo*. These cases showed that the photophysical properties of ruthenium are very helpful to improve sensing techniques and to design molecular sensors.

In the end, the strategy of using metal complexes with graphene devices turned out to be an efficient one. Yet, we only explored the use of a very limited number of metal complexes, with functions that were focused on sensing. The versatility of metal complexes and the flexibility in graphene-based device architectures means that we have only revealed the tip of the iceberg. It is our belief that, through molecular and nano-engineering with graphene and metal complexes, hybrid structures can be designed, not only for sensing devices, but for virtually any type of device.

8.2.2 Outlook

Of course, the principles that are described in this work are not final. The lines that we have presented could be continued in various directions, and thereby offer a plethora of possible roadmaps for further research.

Using switchable substrates like the spin crossover single crystals for graphene field effect transistors could go two ways. First of all, other types of crystals may be used instead of the spin crossover crystal. For example, crystals of ruthenium DMSO complexes could be used that can undergo linkage isomerization,^[1] so switching can be achieved specifically with light instead of with temperature. Moreover, single crystals of gas-sensitive metal-organic frameworks (MOFs) could be used as well, to provide devices that detect a gas by responding to the phase transitions in the MOF crystal that are triggered by the gas.^[2] Second, heading towards device engineering, one could think of constructing nano-sized devices on the single crystals, using for example (e-beam) lithographic methods.^[3] The crystals are micrometers in size, giving enough space to design complex

architectures for nanodevices. By intentionally damaging the crystal with laser ablation,^[4] (nano)sized domains may be produced in the SCO crystal itself as well, creating SCO domains that can be switched independently. These small domains, together with scaled-down GFETs, could possibly leads to a large array of switching devices produced on one crystal. This could be useful for data storage.

In fact, further study of the thin films based on the [Fe(bapbpy)(NCS)₂] may go into the same direction. Because the films grow selectively on graphene, 'traditional' techniques may be used to design complex architectures for graphene-based electronic devices, which may then be coated with the thin film grown selectively on the graphene areas. Possible applications of devices that are coated with spin crossover active thin films would be again data storage, but other types of thin films are envisioned for sensing, as the molecules of the thin film are expected to be sensitive to their environment.^[5]

In line with this sensing application, of course, are the chemical fingerprint arrays. The CF arrays presented in this work were 1st generation prototypes; further research should be focused on producing high-quality data that can be used to reliably detect and identify chemical species using machine learning techniques.^[6] The results we found for the 1st generation were encouraging; yet, a challenge is to overcome device-to-device variations. Producing devices that always respond in the same way gives the advantage of using a machine-generated learning model from one CF array onto the data produced by other CF arrays. In that way, one optimized algorithm can be used for all CF arrays, thus maximizing the reliability of the CF array. Eventually, CF arrays may be used as a breath analysis device for patient screening and diagnosis in the clinics.

Similarly, graphene on paper has been explored as a sensing platform. Seemingly due to interference by electrochemical processes, the platform has not reached its full potential in our opinion. Studying these electrochemical processes should help understand which processes occur during the GFET measurements; a deeper understanding of these processes could help to further develop the GFETs on paper. On the other hand, efforts to sense a reaction involving strictly non-redox active species (within the gate potential range, *i.e.* 0 – 1.5 V) could be very successful, and may provide a simplified and more conclusive view on the sensing capabilities of the GFETs on paper.

We have shown that ruthenium complexes can be useful to improve DNA detection using solid-state nanopores, but we have yet only made a start to show how useful they can be. To continue on this line, crucially, the effect of light on ruthenium-decorated DNA translocation should be examined. The photoreactivity of ruthenium may be exploited to control the binding and unbinding of the complex to DNA: using an anchored complex, *i.e.* a complex that is fixed to the surface of the nanopore, the complex may provide the friction that is required to slow down DNA when it is bound. Irradiation may break the Ru-DNA bond, thus releasing the DNA and allowing the DNA to travel. With light, control can be gained over the translocation speed of DNA in this way. A complex that can do this is presented in fact in chapter 7; the pyrene group on this complex can be used as an anchor on graphene-based nanopore devices.

The complex described in chapter 7 may of course also be studied further as a PACT agent and uptake indicator at the same time. We could see the fluorescence of the pyrene tag upon degradation of the ester connection, but not yet *in vitro*, which is required to see if indeed cells light up when they internalize the complex. Moreover, the cytotoxicity in the dark and under irradiation should be evaluated. To circumvent the poor solubility of the complex, liposomes may be used as a drug carrier, as the complex is amphiphilic and should easily be incorporated in a lipid membrane.^[7] Eventually this complex may be an effective PACT agent while showing where irradiation should take place to kill malicious tissue.

8.2.3 References and notes

- [1] J. J. Rack, J. R. Winkler, H. B. Gray, *J. Am. Chem. Soc.* **2001**, *123*, 2432; J. J. Rack, A. A. Rachford, A. M. Shelker, *Inorg. Chem.* **2003**, *42*, 7357.
- [2] D. E. Jaramillo, D. A. Reed, H. Z. H. Jiang, J. Oktawiec, M. W. Mara, A. C. Forse, D. J. Lussier, R. A. Murphy, M. Cunningham, V. Colombo, D. K. Shuh, J. A. Reimer, J. R. Long, *Nat. Mater.* **2020**, *19*, 517; D. A. Reed, B. K. Keitz, J. Oktawiec, J. A. Mason, T. Runčevski, D. J. Xiao, L. E. Darago, V. Crocellà, S. Bordiga, J. R. Long, *Nature* **2017**, *550*, 96.
- [3] G. J. Dolan, *Appl. Phys. Lett.* **1977**, *31*, 337.
- [4] S. Bedoui, M. Lopes, S. Zheng, S. Bonnet, G. Molnár, A. Bousseksou, *Adv. Mater.* **2012**, *24*, 2475.
- [5] K. Senthil Kumar, M. Ruben, *Coord. Chem. Rev.* **2017**, *346*, 176.
- [6] T. Hayasaka, A. Lin, V. C. Copa, L. P. Lopez, R. A. Loberternos, L. I. M. Ballesteros, Y. Kubota, Y. Liu, A. A. Salvador, L. Lin, *Microsyst. Nanoeng.* **2020**, *6*, 50.
- [7] J. Shen, H.-C. Kim, J. Wolfram, C. Mu, W. Zhang, H. Liu, Y. Xie, J. Mai, H. Zhang, Z. Li, M. Guevara, Z.-W. Mao, H. Shen, *Nano Lett.* **2017**, *17*, 2913.

Appendix

Chapter 2

Materials and methods for device fabrication

Bapbpy was synthesized using a previously reported protocol.^[1] Single crystals of Fe(bapbpy)(NCS)₂ were prepared using a liquid-liquid diffusion method developed in our group.^[2] Shortly, a solution of Fe(SCN)₂ in degassed methanol (0.1 M, 0.17 ml) was carefully layered on top of a solution of bapbpy in DMF (1.5 mM, 1.0 ml, filtrated before use) in a 15 ml corning tube containing two vertically positioned silica wafers (Prime grade, 285 nm SiO₂ on 0.5 mm Si, single side polished; approx. 8x8 mm in size; functionalized with trimethoxyoctadecyl silane (OTMS). Silanization was done on cleaned wafers (sonication in acetone, MilliQ and isopropanol, then O₂ plasma: 0.30 mbar, 100 W, 2 minutes) by immersing them in a 1% OTMS solution in hexane, overnight at room temperature, then rinsing them with hexane, toluene, ethanol and MilliQ. The wafers were positioned at the DMF-methanol interface in the crystallization tube for crystal growth on the polished silicon oxide surface. On top of the Fe(SCN)₂ layer, an excess of methanol (7 ml, degassed by nitrogen bubbling) was carefully layered to not disturb the DMF-methanol interface. After 3 days, methanol was diffused into the DMF layer and single crystals had grown on the silica wafers and the tube walls. The crystallization liquid was removed and wafers were rinsed thoroughly with methanol thrice, then left to dry on air.

Graphene transistors on SCO single crystals were fabricated on single crystals that were grown on the wafers. Full wafers were cast in a flexible epoxy film (Reprorubber Thin Pour, film thickness 0.15 ± 0.02 mm) which was extracted from the wafer carefully, to avoid damaging the crystals. Wafers were functionalized with OTMS beforehand to decrease the affinity of the epoxy film for the wafer surface. From the epoxy sheet, turned upside down with crystals facing upwards, individual crystals (with parallelogram-shaped surface) were selected and transferred together with their epoxy matrix by mechanical cutting, the epoxy film with one crystal was placed on a thin glass slide (0.15 ± 0.02 mm) with the crystal facing up, and fixed to the slide using little of the flexible epoxy resin. Once cured, excess resin was removed (as close as possible to the acute corners of the crystal, at an 90° angle with the long sides of the crystal surface), leaving the crystal on a strip of epoxy resin.

For devices with a spacer, a poly(methyl methacrylate) (PMMA) film was spin-coated on copper foil; spacer thickness varied with rotation speed (6000 rpm = 0.1 μm, 4000 rpm = 0.3 μm, 1000 rpm = 0.5 μm). Copper was then etched with an ammonium persulfate solution (0.2 M in MilliQ), the film was rinsed by transferring the sheet in three MilliQ baths consecutively, then transferred on the crystal by fishing the floating film from below. The unfinished device was then heated at 120°C for 1 hour. Next, electrically conductive silver epoxy (Gentec, EPOTEK EJ2189-LV) was manually placed next to the long edges of the crystal surface, as close as possible to the crystal, without touching (the electrodes did not physically touch the substrate crystal to prevent mechanical effects of the electrodes during cooling or heating). Copper wires were attached to the silver epoxy electrodes and the epoxy was allowed to cure overnight at room temperature.

A piece of PMMA-coated graphene (grown by chemical vapor deposition (CVD), monolayer on copper foil; purchased from Graphenea or grown in-house in a CVD tube oven), spin-coated with PMMA (6% in anisole, Allresist GmbH., AR-P 662.06; 4000 rpm for 60 s, heated at 85°C for 10 minutes, then back-etched in oxygen plasma (0.30 mbar, 100 W, 2 minutes) was transferred using the same method as the PMMA spacer (see above). The sheet was transferred to the crystal and silver epoxy electrodes by fishing from below with the unfinished device. Excess water was removed with soft tissue and the device was heated at 120°C for at least 1 hour. Excess graphene was removed

mechanically using a razor blade, leaving the graphene on and between the silver epoxy electrodes intact, to finish the device (see Figure S2.1).

For devices with a gate electrode, the same procedure was followed, however the graphene transferring polymer was slightly different; instead of spin-coating the PMMA solution as received, 2wt% of the ionic liquid DEME-TFSI, where DEME-TFSI = N,N-diethyl-N-methyl-N-(2-methoxyethyl)ammonium bis(trifluoromethanesulfonyl)imide, was premixed with the PMMA solution to form a PMMA/DEME-TFSI hybrid film on top of graphene. The introduction of DEME-TFSI did not influence the graphene etching and transfer step or any of the following fabrication steps. After the graphene transfer, devices were treated with O₂ plasma (0.30 mbar, 100 W, 1 minute), then the source and drain electrodes were protected with Reprorubber epoxy resin (see Figure S2.2B). Next, a piece of copper foil was cut into a sharp tip with a large base for electrical connection of the gate electrode. The far end of the tip was placed above the crystal, then the copper foil electrode was locked in place with Reprorubber epoxy and a droplet of ionic liquid was carefully placed between the protected electrodes and on top of the crystal (the size of the droplet was as such that the full area was covered without overflowing) to complete the gated graphene field effect transistor (see Figure S2.1).

Oxygen plasma was generated using a capacitively coupled plasma system with radio-frequency of 40 kHz and 200 W power from Diener electronic (Femto), employed at room temperature. Spin coating was done with a POLOS SPIN150i tabletop spin coater. Optical images were obtained using a Leica DM2700 M Brightfield microscope fitted with Leica MC120 HD camera. AFM images were recorded on a JPK Nanowizard Ultra. Magnetic measurements were performed using a Quantum Design MPMS XL SQUID Magnetometer. Raman spectra were recorded on a Witec Alpha500 R Raman spectrometer using a 532 nm laser at low power (0.23 mW). Electrical characterization of devices was performed using a Keithley Sourcemeeter model 2450 and 2400 in combination with Kickstart measuring software. Gate voltage (for top-gated devices) was supplied using a Keithley Sourcemeeter (model 2400) while measuring resistance with a separate Keithley Sourcemeeter (model 2450), both earthed on the same point. Optical footage of the device inside the chamber was recorded using the optical camera equipped to the Raman microscope setup. Temperature cycling experiments were performed using a Linkam THMS600E microscope heating/cooling stage equipped on the Raman spectrometer in combination with LINK temperature control software. During temperature cycle experiments, the devices were electrically connected inside the heating/cooling stage. To prevent condensation, the chamber was purged with N₂ (N3.0 or higher) at the start each experiment, according to the manufacturer's protocol.

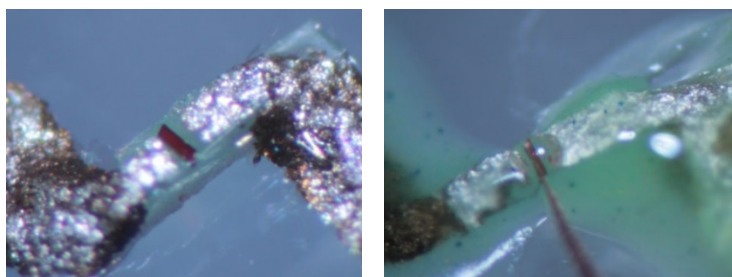


Figure S2.1: Finished graphene transistor constructed on spin crossover crystal without gate electrode (left) and with gate electrode (right).

Schematic representation of fabrication step-by-step

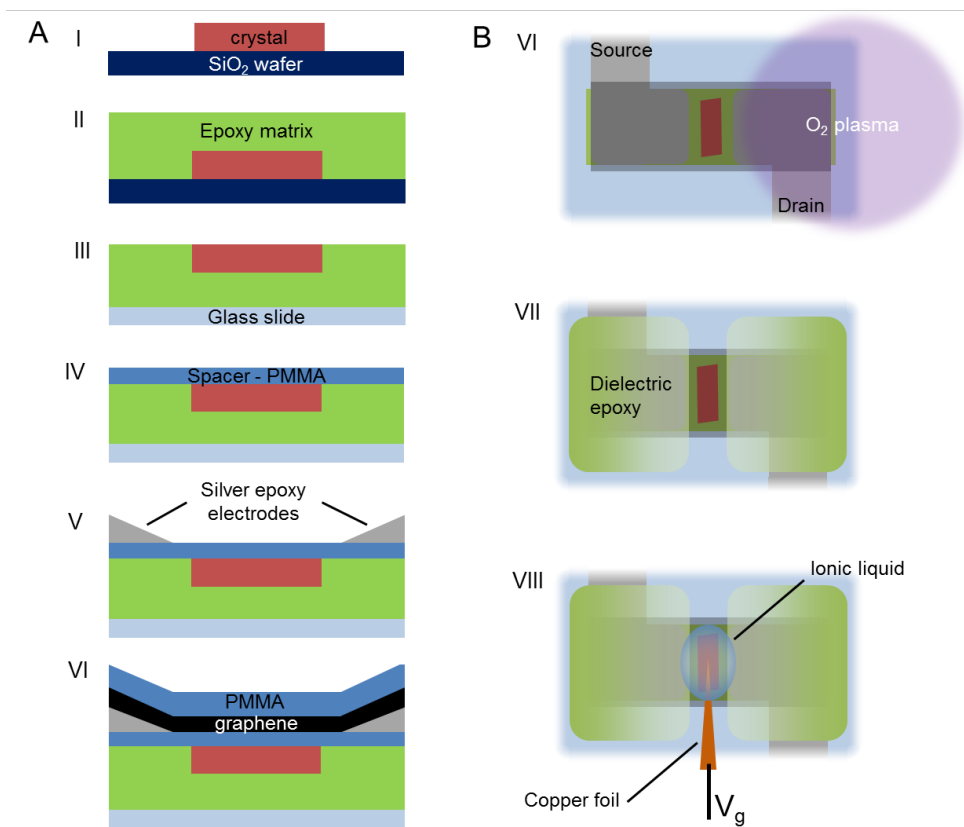


Figure S2.2: A) Side view step-by-step schematic representation of the production process of graphene transistors on SCO crystals. I: Single crystal of **1** grown on Si/SiO₂ wafer; II: crystal on wafer cast in epoxy resin; III: epoxy, holding crystal pulled from wafer and placed upside down on a microscope cover glass; IV: PMMA film transferred onto the epoxy and the crystal; V: solid silver epoxy electrodes placed close to crystal edges; VI: transfer of a PMMA-graphene film (graphene below; for gated devices a premixed PMMA/DEME-TFSI film was used for graphene transfer) and mechanical removal of excess graphene to finish the device. B) VI: Top-side view of finished device – for gating, the devices were subjected to oxygen plasma; VII: protection of source and drain electrodes with dielectric epoxy resin; VIII: construction of gate electrode from copper foil and placement of ionic liquid DEME-TFSI on the crystal area for gating experiments.

Graphene characterization by AFM and Raman spectroscopy

AFM images of the surface of a typical crystal on a wafer showed a particularly smooth and clean surface of a bare crystal (see Figure S2.3A). Notably, micrometer-sized terraces and trenches were identified with step sizes of about 1 nm, *i.e.* single molecule thickness. After transferring graphene and removing the carrier polymer, the surface topology was wave-like, indicative of an intact, slightly

wrinkled graphene sheet on top of the crystal (see Figure S2.3B). The deposits on the surface were likely remains of PMMA after the transfer. Raman spectra of coated crystals showed the 2D peak at 2705 cm^{-1} typical for graphene, while it was not present for uncoated crystals (see Figure S2.3C). A line scan showed that the presence of graphene is continuous (see Figure S2.3C, inset). Moreover, a peak indicative of structural defects in graphene, typically observed near 1350 cm^{-1} , was not observed. Thus, graphene was successfully transferred on the single crystal of **1** and was of high quality.

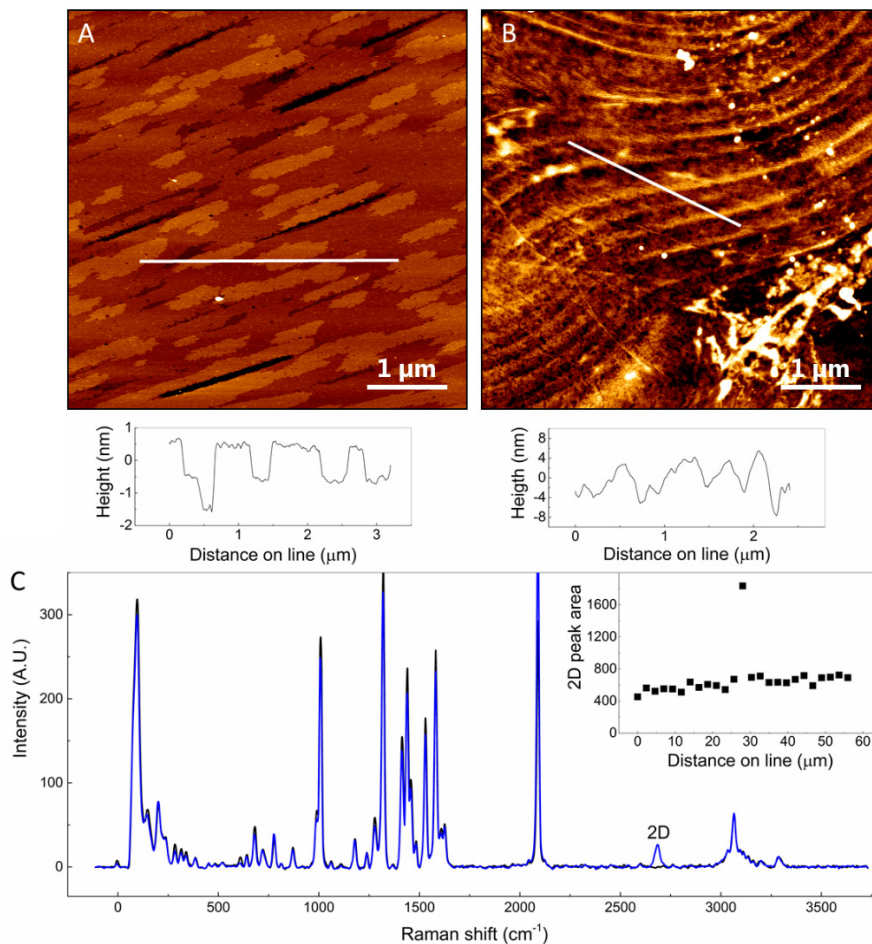


Figure S2.3: AFM images of an uncoated (A) and graphene-coated (B) single crystal of compound **1** (PMMA removed after graphene transfer) and corresponding height profiles. C) Raman spectrum of the uncoated (black) and coated (blue) single crystal of **1**, showing the 2D peak typical for graphene at 2700 cm^{-1} for the coated crystal. Inset: a line scan across the coated crystal shows continuous presence of graphene, *i.e.* the 2D peak, at the crystal surface. NB: the elevated point is considered an artefact (*i.e.* a wrinkle in graphene).

Resistance measurements for low-temperature phase II to phase III transitions

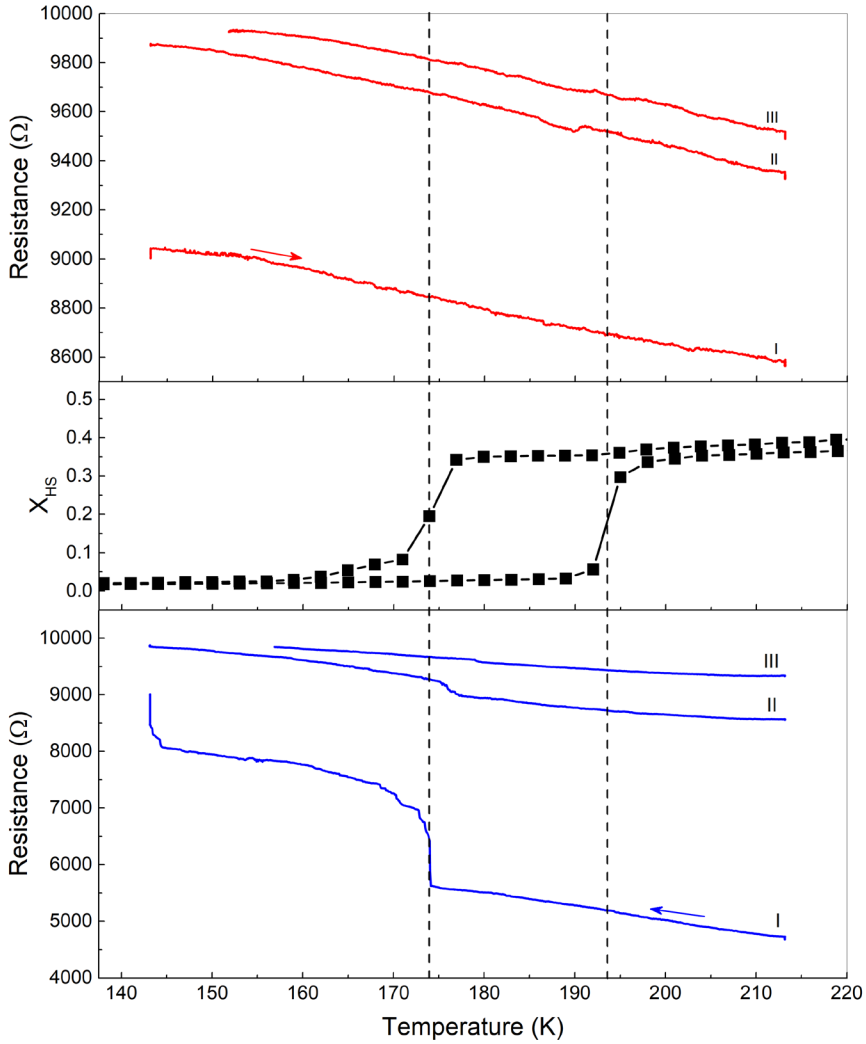


Figure S2.4: Resistance (red = heating mode, blue = cooling mode) and single crystal high-spin fraction x_{HS} (connected black squares) vs. temperature for a device with 0.5 μm spacer. Dashed lines indicate transition temperatures. The number of the cooling-heating cycle is denoted with I, II and III.

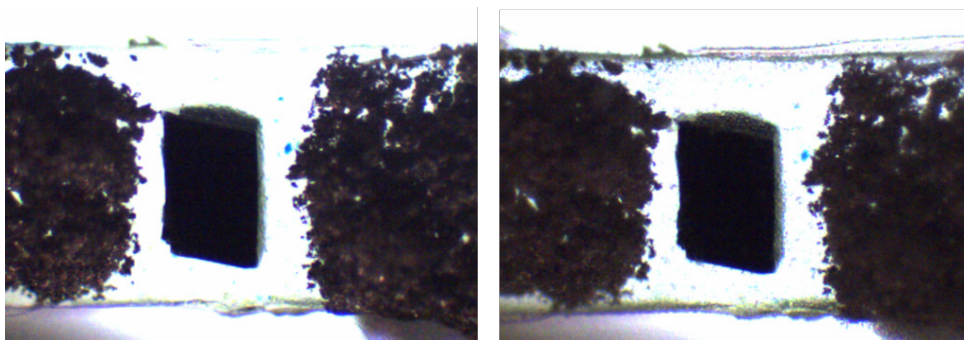


Figure S2.5: Optical image of a spin crossover crystal (in a device) in phase II (left) and in phase III (right). Crystal length and width are 225 μm and 160 μm .

Mechanical resilience to multiple temperature-induced spin crossover cycles

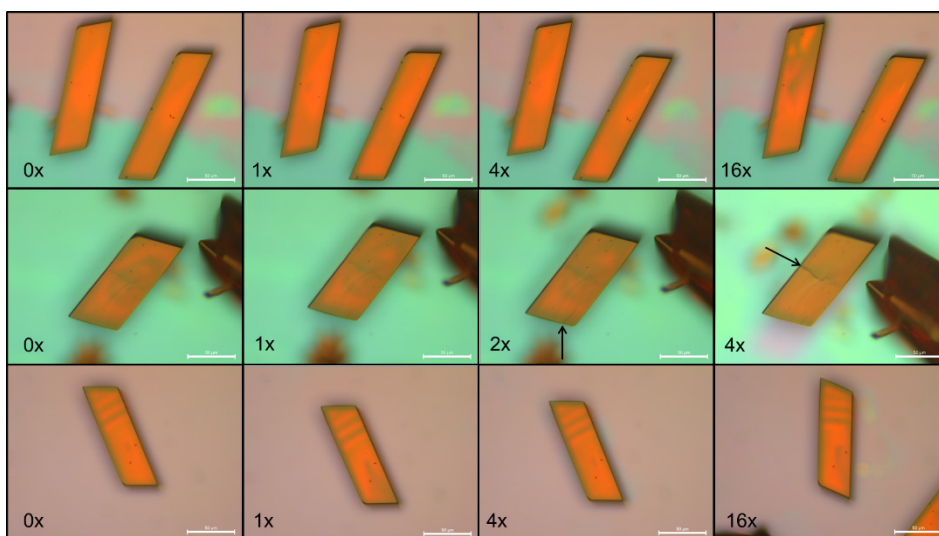


Figure S2.6: SCO events (phase I to phase III) were induced in crystals of compound 1 on silicon wafer by repeatedly cooling to 77 K by immersing them in liquid nitrogen, then heating back to 293 K. Crystals had good resistance against defect formation during multiple spin crossover cycles (top, bottom), but formation of defects could trigger crack formation in the crystal, indicated by the arrows (middle). Scale bar = 50 μm .

Resistance measurements with varying spacer thickness

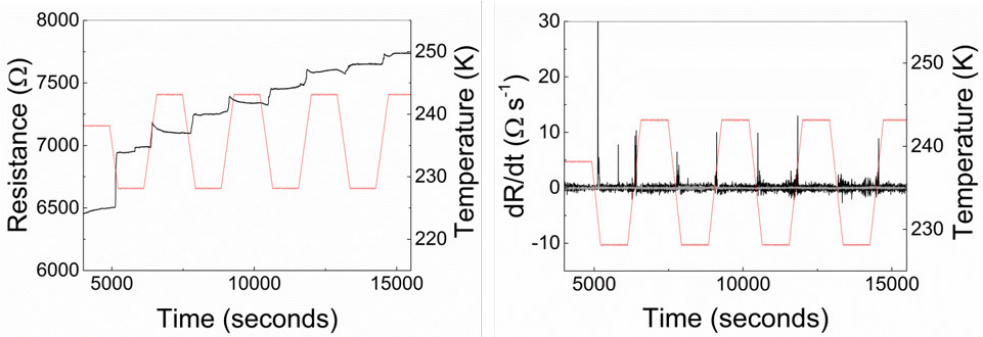


Figure S2.7: R and T vs. time and dR/dt and T vs. time for a device with 0 μm spacer.

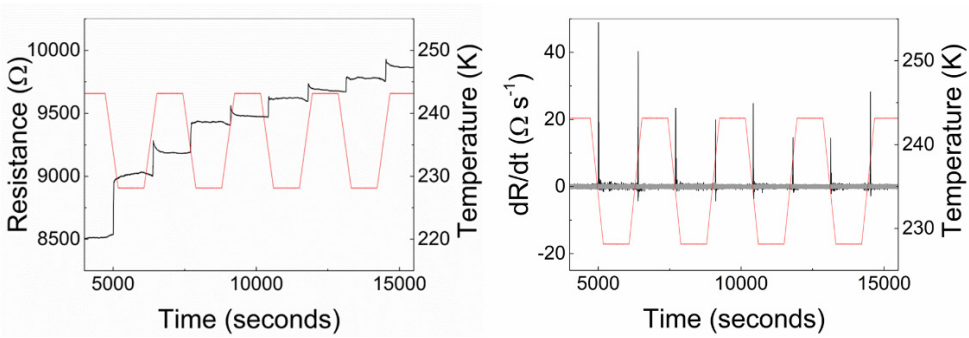


Figure S2.8: R and T vs. time and dR/dt and T vs. time for a device with 0.1 μm spacer.

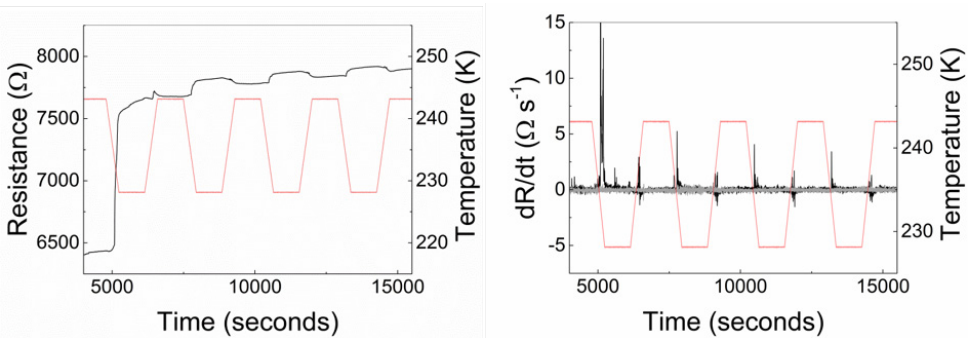


Figure S2.9: R and T vs. time and dR/dt and T vs. time for a device with 0.3 μm spacer.

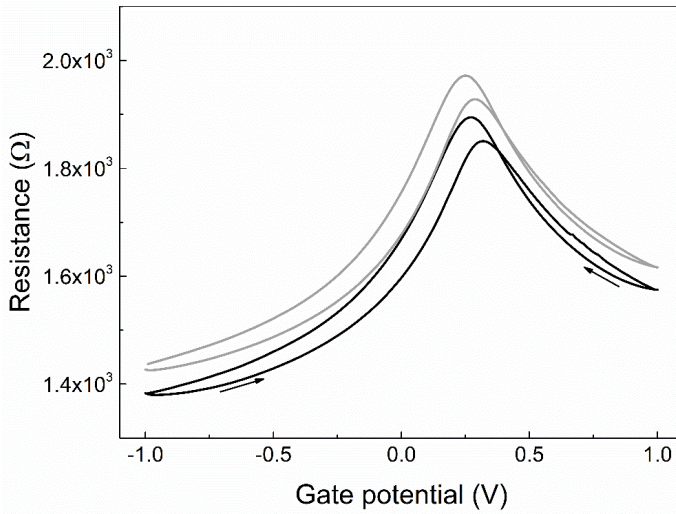
***I/V* characterization of GFET before and after temperature cycling**

Figure S2.10: Resistance *vs.* gate potential for a device with a 0.5 μm spacer, at 293 K, before (black) and after (grey) a temperature cycle; from 293 to 213 K and back, steps of 10 K outside SCO region and 5 K in SCO region, where the SCO region is from 243 to 223 K. Gate potential was varied at 0.01 Vs^{-1} .

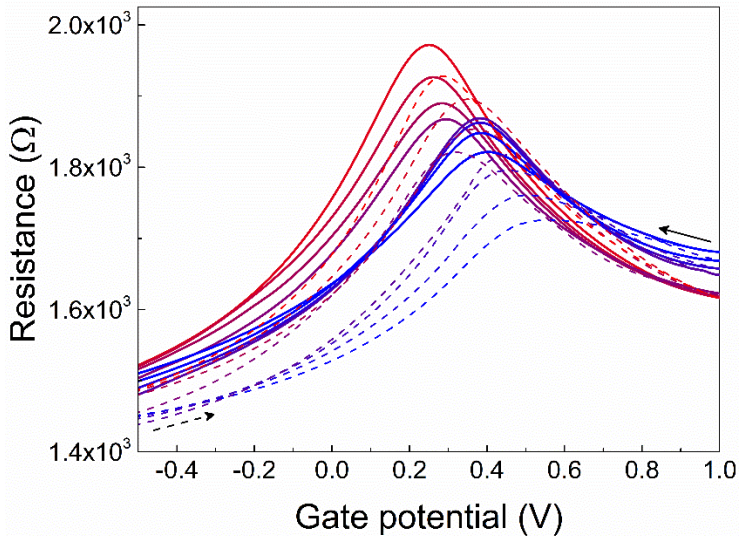


Figure S2.11: Resistance *vs.* gate potential for forward and backward sweeps at different temperatures (recorded during heating mode, from 223 K to 293 K, indicated by blue and red, respectively). Solid lines represent gate sweeps from +1.0 V to -1.0 V, dashed lines represent the opposite direction, -1.0 V to +1.0 V.

Supplementary Text

Phase-dependent electrostatic potential of Fe(bapbpy)(NCS)₂

The long-range electrostatic potential induced by the SCO crystal has been computed from the data presented in Table S2.2. Given the micrometer-scale dimensions of the grown crystal consisting of roughly 10^{15} - 10^{17} atoms, a direct numerical approach to the induced potential comes with high computational costs. To avoid this computational bottleneck, the crystal has been modeled according to Figure S2.12 by a set of parallel charged sheets stacked on top of one another, each of which yields an electric potential of

$$\phi_i(y) = -\frac{\sigma_i}{2\epsilon_r\epsilon_0}y + \phi_0, \quad (S1)$$

at the normal distance $y \gg \max(a_x, c_z)$, where a_x and c_z are the in-plane lattice constants. In equation (S1), $\sigma_i = c_i/(a_x c_z)$ is the charge density per unit area which depends on the net atomic charge c_i (see Table S2.2), ϵ_r is the relative permittivity of the surrounding substance, and ϕ_0 is the constant reference potential. The overall potential ϕ at the place of graphene is thus given by superimposing partial contributions from all charged planes as

$$\phi = -\sum_i \left[\frac{\sigma_i}{2\epsilon_0} \left(\frac{h}{\epsilon_r^{PMMA}} + \frac{\delta_i}{\epsilon_r^{SCO}} \right) + \phi_0 \right]. \quad (S2)$$

Here, h is the thickness of the PMMA spacer and $h + \delta_i$ specifies the distance between the i th charged plane and the graphene sheet. In view of the fact that the SCO complex is electronically neutral ($\sum_i \sigma_i = 0$), the first contribution in equation (S2) vanishes. Therefore, the potential shift arising from a phase transition, for instance IP \rightarrow HS (phase II to phase I), can be calculated from

$$\phi^{HS} - \phi^{IP} = -\frac{1}{2\epsilon_r^{SCO}\epsilon_0} \sum_i (\sigma_i^{HS} \delta_i^{HS} - \sigma_i^{IP} \delta_i^{IP}). \quad (S3)$$

For simplicity, in deriving equation (S3), we have omitted the dependence of the dielectric parameter ϵ_r^{SCO} on variations of the electronic state during IP \rightleftharpoons HS transitions. We note, however, that the hysteretic deviations of ϵ_r^{SCO} , which have been observed experimentally for similar SCO compounds,^[3] are sufficiently superficial to have no severe consequences for the induced potential drop.

To further lift the computational burden, the sum over i in equation (S3) can be split according to the periodicity of the crystal along the stacking direction y . Assuming that the crystal surface resembles an array of N iterative slabs whose thickness is Nb_y , where b_y is the lattice constant along the stacking direction, the first sum in equation (S3) yields

$$\sum_i \sigma_i^{HS} \delta_i^{HS} = \sum_{n=0}^{N-1} \sum_{j=1}^M \sigma_j^{HS} (\delta_j^{HS} + nb_y) = N \sum_{j=1}^M \sigma_j^{HS} \delta_j^{HS} + \sum_{n=0}^{N-1} nb_y \sum_{j=1}^M \sigma_j^{HS}, \quad (S4)$$

where j enumerates the charged sheets per slab. Given the charge neutrality of each slab, *i.e.*, $\sum_{j=1}^M \sigma_j^{HS} = 0$, we directly obtain from equations (3) and (4) that

$$\phi^{HS} - \phi^{IP} = -\frac{N}{2\epsilon_r^{CO}\epsilon_0} \sum_{j=1}^M (\sigma_j^{HS} \delta_j^{HS} - \sigma_j^{IP} \delta_j^{IP}). \quad (S5)$$

The potential shift $\Delta\phi = |\phi^{HS} - \phi^{IP}|$ is presented in Table S2.1 for different thicknesses Nb_y of the SCO crystal. It is worth mentioning that the theoretical model above holds true as long as the thickness h of the PMMA spacer is small compared to the length and width of the crystal surface. In this case, h has no influence on the remote detection of SCO events in the crystal, which is fully consistent with our experimental observations.

Table S2.1: Potential shift $\Delta\phi = |\phi^{HS} - \phi^{IP}|$, in volts, for different thicknesses of the SCO crystal. The dielectric constant $\epsilon_r^{CO} \approx 4$. The normal lattice constant at IP and HS phases is $b_y = 10.72$ and 10.97 \AA , respectively.

$N (\times 10^4)$	Thickness at IP phase [μm]	$\Delta\phi$ [V]
2	21.4	0.017
4	42.9	0.033
6	64.3	0.050
8	85.8	0.067
10	107.2	0.083

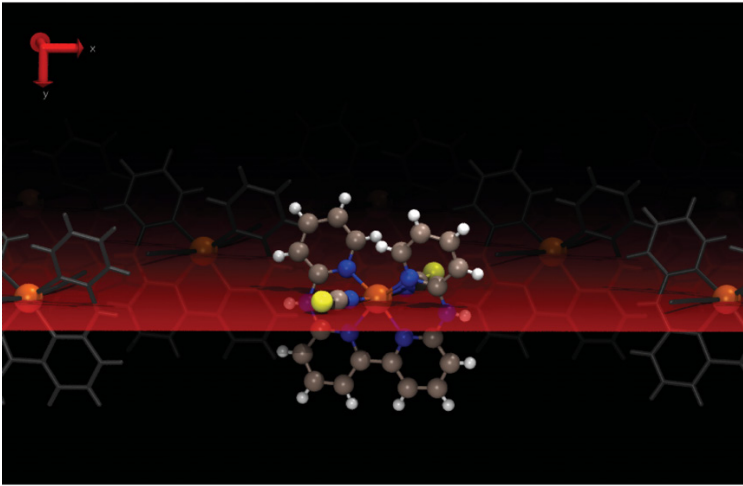


Figure S2.12: Side view of the uppermost surface layer of crystalline $[\text{Fe}(\text{bapbpy})(\text{NCS})_2]$ which is extended parallel to the (x,z) plane. The flat plane shown in red contains Fe atoms which, in micrometer scale, make an extended charged sheet with a uniform charge density. Considering a similar scenario for other atoms, the SCO crystal can be modeled by a set of charged sheets stacked parallel to one another. The charge density of each sheet is proportional to the net charge allocated to its individual atoms.

Appendix – Chapter 2

Charge transport in graphene

It has previously been demonstrated by comparing between theory and experiment that the scattering of graphene's mobile carriers by long-range interactions with charged impurities yields a linear conductivity at high carrier densities.^[4, 5] Charged impurities, on the other hand, create inhomogeneous potential fluctuations and charge puddles,^[6] giving rise to a residual carrier density n^* independent of the applied gate voltage. The presence of n^* in our experiments has been witnessed by a nonzero conductivity measured at the Dirac point, which is much larger than if the conductivity was created by temperature. To address the problem of electronic transport under the influence of charged impurities we employ the semiclassical Boltzmann transport theory,^[5-9] according to which the electrical conductivity is given by^[8]

$$\sigma = \frac{e^2}{2} \int v_k^2 D(E) \tau(E) \left(-\frac{\partial f}{\partial E} \right) dE. \quad (S6)$$

In equation (S6), $\vec{v}_k = \left(\frac{1}{\hbar}\right) \vec{\nabla}_k E$ corresponds to the group velocity of electrons, $D(E)$ is the density of states per unit area, f the Fermi function, and τ denotes the relaxation time. Assuming that the process of scattering is predominantly elastic, the value of τ for a linear energy dispersion relation $E = \pm \hbar v_F |\mathbf{k}|$ (v_F is the Fermi velocity) can be obtained from^[9]

$$\frac{1}{\tau(E)} = \frac{n_i}{8\hbar} D(E) \int |V_q|^2 (1 - \cos^2 \theta) d\theta. \quad (S7)$$

Here, n_i is the impurity concentration, V_q is the electrostatic potential created by charged impurities in Fourier space, and $q = 2E \sin(\theta/2) / (\hbar v_F)$ and θ specify the scattering wave vector $q e^{i\theta}$ in polar coordinates. Owing to the fact that V_q is screened by graphene's two-dimensional electron system, we obtain^[5, 6]

$$V_q = \frac{e^2}{2\kappa \epsilon_0 \epsilon(q, T)} e^{-qd}, \quad (S8)$$

where $\kappa \approx 3.8$ is the background dielectric constant, d corresponds to the normal distance of graphene from charged impurities, and ϵ is the static dielectric function. The procedure of calculating $\epsilon(q, T)$, within the random phase approximation (RPA), has been detailed in Ref. [10]. Nevertheless, for temperatures much less than the Fermi temperature, *i.e.*, $T \ll T_F$, it is possible to describe ϵ using the following analytical expression^[10]

$$\epsilon(q, T \ll T_F) \approx \frac{\tilde{\kappa}}{k} + \frac{g_{sv} r_s k_F}{q} \begin{cases} 1 - \frac{\pi q}{8k_F} & q \leq 2k_F, \\ 1 - \frac{1}{2} \sqrt{1 - \left(\frac{2k_F}{q}\right)^2} - \frac{q}{4k_F} \sin^{-1} \frac{2k_F}{q} & q > 2k_F, \end{cases} \quad (S9)$$

where $g_{sv} = 4$ accounts for the spin and valley degrees of freedom of electrons in graphene, and $\tilde{\kappa} = \kappa \left(1 + \frac{g_{sv}\pi r_s}{8}\right)$ is the effective dielectric constant with $r_s = e^2/(4\pi\epsilon_0\kappa\hbar v_F)$ being the fine structure.

In order to compare the measured transport components with theory, the conductivity σ (equation S6) has to be computed as a function of the top gate voltage V_g . To do so, it is first necessary to obtain the V_g -induced doping concentration (n_g) according to^[11]

$$V_g = \frac{\hbar v_F \sqrt{\pi n_g}}{e} + \frac{e n_g}{C_g}, \quad (\text{S10})$$

where C_g is the geometric capacitance due to formation of a nanometer-thick Debye layer at graphene/PMMA-ionic liquid interface. Subsequently, the effective carrier density characterizing the electrical conductivity is given, as an approximation, by $n = |n_g| + |n^*|$.^[12] As the last step, we must evaluate the residual carrier density n^* . For doing this, we employed a self-consistent theory,^[6] according to which n^* is explicitly a function of the impurity density n_i , *i.e.*,

$$n^* = 2 r_s n_i C_0^{RPA}(r_s, 4d\sqrt{\pi n^*}), \quad (\text{S11})$$

where C_0^{RPA} is the correlation function obtained from the random phase approximation.

Phonon-limited resistivity

Although the dominant contribution to the resistivity of our graphene sample originates from the electrostatic scattering by charged impurities, the effect of electron-phonon interaction has also been incorporated into our transport calculations as a minor correction. To this end, we have used the Boltzmann transport equation. By simplifying this equation using variational methods, the phonon-limited resistivity is given by^[13]

$$\rho_{e-ph} = \frac{3\sqrt{3}\pi a^2}{e^2 n_\uparrow v^2} \int_0^\infty \frac{\frac{\hbar\omega}{2k_B T}}{\sinh^2\left(\frac{\hbar\omega}{2k_B T}\right)} \alpha_{tr}^2 F(\omega) d\omega, \quad (\text{S12})$$

where $a \approx 1.4076 \text{ \AA}$ is the C-C bond length, v the velocity averaged over the Fermi surface, and n_\uparrow is the density of states per unit cell per spin at E_F . In equation (S12), the transport Eliashberg function $\alpha_{tr}^2 F(\omega)$ is determined by the electron-phonon coupling as follows

$$\begin{aligned} \alpha_{tr}^2 F(\omega) &= \frac{1}{n_\uparrow A_{bz}^2} \sum_{m'mv} \iint d\mathbf{p} d\mathbf{q} |g_{m',m}^v(\mathbf{p}, \mathbf{q})|^2 \times \left(1 - \frac{\mathbf{v}_{\mathbf{p}+\mathbf{q},m'} \cdot \mathbf{v}_{\mathbf{p},m}}{|\mathbf{v}_{\mathbf{p},m}|^2}\right) \\ &\times \delta(\epsilon_{\mathbf{p}+\mathbf{q},m'} - E_F) \delta(\epsilon_{\mathbf{p},m} - E_F) \delta(\hbar\omega_q^v - \hbar\omega). \end{aligned} \quad (\text{S13})$$

Here, $A_{bz} = 8\sqrt{3}\pi^2/9a^2$ is the area of the first Brillouin zone of graphene, $|\mathbf{p} + \mathbf{q}, m'\rangle$ and $|\mathbf{p}, m\rangle$ correspond to the final and initial scattering states, respectively, and ω_q^v denotes the angular frequency of the v -th phonon mode for wave vector \mathbf{q} . The elements of the electron-phonon interaction matrix, *i.e.*, $g_{m',m}^v(\mathbf{p}, \mathbf{q})$, have already been modeled by Park *et al.*^[13] using the local density approximation (LDA) method (see Table 1 in Ref. 13).

Appendix – Chapter 2

By evaluating equation (S12) for the experimental temperatures $T = 238$ and 243 K we concluded that the contribution of ρ_{e-ph} to the overall resistivity is roughly two orders of magnitude less than that of charged impurities.

Charge distribution in the HS and LS molecules

Complete active space self-consistent field (CASSCF) calculations were performed upon the isolated basic units of the $[\text{Fe}(\text{bapbpy})(\text{NCS})_2]$ complex. This methodology, working with the exact Hamiltonian, is known to provide satisfactory descriptions of electronic structures, which is a major concern in our approach. A limited number of electrons distributed over a set of valence molecular orbitals defined the complete active space (CAS). As reported in literature,^[14] the standard CAS consists of the 3d orbitals with mainly Fe character, extended with a set of virtual orbitals of the same symmetry (so-called 3d' orbitals), and two occupied "e_g-like" symmetry orbitals with mainly ligand character. Thus, a CAS[10,12] including ten electrons in twelve active orbitals was used in the calculations. This extended active space accounts for the important charge fluctuations accompanying the $S=0 \rightarrow S=2$ spin change. Net charges were estimated from the LoProp tool, based on the one-electron density. The values we used were slightly different from the ones given in a previous inspection,^[15] since charges were then condensed onto the iron and the surrounding nitrogen atoms.

All our calculations were performed with the Molcas8.0 program,^[16] including atomic natural orbitals (ANO-RCC) as basis sets.^[17] As stated previously,^[14] finely balanced basis sets are necessary to properly describe the energetics of SCO phenomenon. Thus, a [7s6p5d3f2g1h] contraction was used for Fe, whereas the contractions [3s2p1d], [4s3p1d], [4s3p1d], [3s3p1d], and [1s] were used for C, N, O, S, and H, respectively.

Table S2.2: Calculated geometry and total charge for individual atoms and the dipole moment for the complete molecule in the HS and LS state. NB: the origin of the operator for the dipole moments is the Fe atom.

Atom	High spin				Low spin			
	x	y	z	Net Charge [Debye]	x	y	z	Net Charge [Debye]
Fe1	0.0000	0.0000	0.0000	1.3900	0.0000	0.0000	0.0000	1.0685
S2	-2.9643	0.5322	-3.8675	-0.4259	-2.8011	-0.2033	-3.8093	-0.4450
S3	2.9643	0.5322	3.8675	-0.4259	2.8671	0.5129	3.7471	-0.4450
N4	-1.2900	1.1720	1.2514	-0.3750	-1.2456	1.1420	1.0319	-0.3234
N5	-3.0302	-0.4078	1.3663	-0.3029	-2.9267	-0.5039	1.1464	-0.2975
N6	-1.1862	-1.6668	0.6103	-0.3886	-0.9265	-1.6088	0.5700	-0.3138
N7	-1.4500	0.2307	-1.5680	-0.5773	-1.1918	-0.0882	-1.5191	-0.4911
N8	1.2900	1.1720	-1.2514	-0.3788	1.3103	-1.2826	-0.6445	-0.3139
N9	3.0302	-0.4078	-1.3663	-0.3096	2.9075	0.3363	-1.2633	-0.2961
N10	1.1862	-1.6668	-0.6103	-0.3301	0.8705	1.4962	-0.9758	-0.3226
N11	1.4500	0.2307	1.5680	-0.5779	1.2006	0.1779	1.5154	-0.4965
C12	-0.8731	2.4176	1.5353	0.0772	-0.8267	2.3646	1.4608	0.0765
C13	-1.6629	3.3813	2.0803	-0.1829	-1.6213	3.2563	2.1113	-0.1781
C14	-2.9704	3.0556	2.3778	-0.0201	-2.9429	2.9096	2.3725	-0.0212
C15	-3.4080	1.7920	2.1427	-0.2064	-3.3708	1.6544	2.0339	-0.2003
C16	-2.5423	0.8598	1.5790	0.3091	-2.4789	0.7743	1.3969	0.3027
C17	-2.4447	-1.6085	1.0545	0.3214	-2.2169	-1.6616	0.9368	0.3071
C18	-3.2346	-2.7522	1.2028	-0.2006	-2.8898	-2.8838	1.0804	-0.1892
C19	-2.7140	-3.9532	0.8726	-0.0192	-2.2245	-4.0506	0.8255	-0.0257
C20	-1.4223	-4.0290	0.3942	-0.1906	-0.9065	-4.0085	0.3956	-0.1705
C21	-0.6898	-2.8772	0.2695	0.1760	-0.3012	-2.7726	0.2512	0.1672
C22	-2.0953	0.3704	-2.5032	0.1281	-1.8753	-0.1297	-2.4467	0.1104
C23	0.6898	-2.8772	-0.2695	0.1443	1.0302	-2.5797	-0.3321	0.1670
C24	1.4223	-4.0290	-0.3942	-0.1499	1.9402	-3.5970	-0.5389	-0.1694
C25	2.7140	-3.9532	-0.8726	-0.0462	3.1869	-3.2810	-1.0626	-0.0263
C26	3.2346	-2.7522	-1.2028	-0.1762	3.4997	-1.9709	-1.3264	-0.1883
C27	2.4447	-1.6085	-1.0545	0.2885	2.5384	-0.9779	-1.0793	0.3067
C28	2.5423	0.8598	-1.5790	0.3110	2.1425	1.4721	-1.3974	0.3046
C29	3.4080	1.7920	-2.1427	-0.2079	2.7562	2.5772	-2.0048	-0.2023
C30	2.9704	3.0556	-2.3778	-0.0199	2.0049	3.6879	-2.2736	-0.0213
C31	1.6629	3.3813	-2.0803	-0.1851	0.6538	3.6804	-1.9578	-0.1810
C32	0.8731	2.4176	-1.5353	0.0772	0.1432	2.5797	-1.3264	0.0788
C33	2.0953	0.3704	2.5032	0.1289	1.9060	0.3323	2.4207	0.1102
H34	0.0117	2.6344	1.3475	0.1388	0.0766	2.6095	1.2947	0.1429
H35	-1.3321	4.2336	2.2480	0.1301	-1.2804	4.1004	2.3826	0.1277
H36	-3.5444	3.6928	2.7356	0.1335	-3.5372	3.5314	2.7782	0.1302
H37	-4.2809	1.5518	2.3569	0.1245	-4.2602	1.3809	2.2267	0.1227
H38	-4.1043	-2.6875	1.5235	0.1274	-3.7991	-2.9005	1.3530	0.1246
H39	-3.2246	-4.7254	0.9676	0.1354	-2.6638	-4.8855	0.9396	0.1324
H40	-1.0528	-4.8504	0.1596	0.1263	-0.4313	-4.8095	0.2067	0.1263
H41	1.0528	-4.8504	-0.1596	0.1276	1.7180	-4.4958	-0.3284	0.1261
H42	3.2246	-4.7254	-0.9676	0.1342	3.8187	-3.9679	-1.2376	0.1326
H43	4.1043	-2.6875	-1.5236	0.1288	4.3536	-1.7402	-1.6700	0.1247
H44	4.2809	1.5518	-2.3569	0.1242	3.6799	2.5559	-2.2254	0.1224
H45	3.5444	3.6928	-2.7356	0.1333	2.4013	4.4537	-2.6705	0.1299
H46	1.3321	4.2336	-2.2480	0.1298	0.0974	4.4199	-2.1734	0.1275
H47	-0.0117	2.6344	-1.3475	0.1384	-0.7839	2.5759	-1.1222	0.1410
H48	-3.8284	-0.4938	1.6147	0.2571	-3.7546	-0.6650	1.3352	0.2548
H49	3.8284	-0.4938	-1.6147	0.2559	3.7296	0.4022	-1.5432	0.2530
Dipole moment				<u>Total (Debye)</u>				<u>Total (Debye)</u>
	-0.2011	-1.1705	-0.0759	1.1901	-0.0126	-3.8956	0.0342	3.8958

References

- [1] S. Bonnet, M. A. Siegler, J. S. Costa, G. Molnar, A. Bousseksou, A. L. Spek, P. Gamez, J. Reedijk, *Chem. Commun.* **2008**, 0, 5619.
- [2] S. Zheng, M. A. Siegler, O. Roubeau, S. Bonnet, *Inorg. Chem.* **2014**, 53, 13162.
- [3] T. Guillon, S. Bonhommeau, J. S. Costa, A. Zwick, J.-F. Létard, P. Demont, G. Molnár, A. Bousseksou, *Phys. Status Solidi A* **2006**, 203, 2974; A. Bousseksou, G. Molnár, P. Demont, J. Menegotto, *J. Mater. Chem.* **2003**, 13, 2069.
- [4] J. H. Chen, C. Jang, S. Adam, M. S. Fuhrer, E. D. Williams, M. Ishigami, *Nat. Phys.* **2008**, 4, 377.
- [5] E. H. Hwang, S. Adam, S. D. Sarma, *Phys. Rev. Lett.* **2007**, 98, 186806.
- [6] S. Adam, E. H. Hwang, V. M. Galitski, S. Das Sarma, *Proc. Natl. Acad. Sci.* **2007**, 104, 18392.
- [7] T. Ando, *J. Phys. Soc. Jpn.* **2006**, 75, 074716.
- [8] S. Das Sarma, S. Adam, E. H. Hwang, E. Rossi, *Rev. Mod. Phys.* **2011**, 83, 407.
- [9] T. Stauber, N. M. R. Peres, F. Guinea, *Phys. Rev. B* **2007**, 76, 205423.
- [10] E. H. Hwang, S. Das Sarma, *Phys. Rev. B* **2007**, 75, 205418.
- [11] A. Das, S. Pisana, B. Chakraborty, S. Piscanec, S. K. Saha, U. V. Waghmare, K. S. Novoselov, H. R. Krishnamurthy, A. K. Geim, A. C. Ferrari, A. K. Sood, *Nat. Nanotechnol.* **2008**, 3, 210.
- [12] J. Xia, F. Chen, J. Li, N. Tao, *Nat. Nanotechnol.* **2009**, 4, 505; S. Samaddar, I. Yudhistira, S. Adam, H. Courtois, C. B. Winkelmann, *Phys. Rev. Lett.* **2016**, 116, 126804.
- [13] C.-H. Park, N. Bonini, T. Sohier, G. Samsonidze, B. Kozinsky, M. Calandra, F. Mauri, N. Marzari, *Nano Lett.* **2014**, 14, 1113.
- [14] M. Kepenekian, V. Robert, B. Le Guennic, C. De Graaf, *J. Comput. Chem.* **2009**, 30, 2327.
- [15] M. Kepenekian, J. S. Costa, B. Le Guennic, P. Maldivi, S. Bonnet, J. Reedijk, P. Gamez, V. Robert, *Inorg. Chem.* **2010**, 49, 11057.
- [16] F. Aquilante, J. Autschbach, R. K. Carlson, L. F. Chibotaru, M. G. Delcey, L. De Vico, I. Fdez. Galván, N. Ferré, L. M. Frutos, L. Gagliardi, M. Garavelli, A. Giussani, C. E. Hoyer, G. Li Manni, H. Lischka, D. Ma, P. Å. Malmqvist, T. Müller, A. Nenov, M. Olivucci, T. B. Pedersen, D. Peng, F. Plasser, B. Pritchard, M. Reiher, I. Rivalta, I. Schapiro, J. Segarra-Martí, M. Stenrup, D. G. Truhlar, L. Ungur, A. Valentini, S. Vancocillie, V. Veryazov, V. P. Vysotskiy, O. Weingart, F. Zapata, R. Lindh, *J. Comput. Chem.* **2015**, 37, 506.
- [17] B. O. Roos, R. Lindh, P.-Å. Malmqvist, V. Veryazov, P.-O. Widmark, *J. Phys. Chem. A* **2004**, 108, 2851.

Appendix
Chapter 3

Materials and Methods

Bapbpy was synthesized using a previously reported protocol.^[1] Single crystals of $[\text{Fe}(\text{bapbpy})(\text{NCS})_2]$ were prepared using an adapted liquid-liquid diffusion method developed in our group.^[2] Shortly, a DMF-resistant single-use cuvette (BRAND® UV microcuvette) was placed in a glass snap-cap vial (VWR, 10 ml, 22x50 mm). A wafer (typically 15x8 mm Prime grade, 285 nm SiO_2 , single-side polished, Siegert Wafer GmbH) was placed vertically in the cuvette. The cuvette was put under N_2 and closed with the snap-cap, and a solution of $[\text{Fe}(\text{SCN})_2]$ in methanol (0.1 M, 0.035 ml) was added with a solution of bapbpy in DMF (15 mM, 0.22 ml, filtrated before use). Both solutions were degassed by the freeze-pump-thaw method beforehand; solutions were added with a needle-fitted gas-tight syringe through the snap-cap to disturb the N_2 atmosphere as little as possible. The solutions were mixed by shaking. Next, 2.0 ml of methanol (degassed by N_2 bubbling, with ~5 mg ascorbic acid) was added in the snap-cap vial for vapor diffusion into the solution in the cuvette. After addition of all solutions, the punctured caps were replaced with intact ones carefully, to not disturb the atmosphere in the vial. For thin film formation, the wafer was left one or multiple days in solution before extracting, rinsing with methanol and blow-drying the wafer.

Monolayer graphene was home-grown on Cu foil (Alfa Aesar, 0.025 mm, Puratronic®, 99.999% metals basis) using a hot-wall tube CVD oven. Graphene on copper was spin-coated with PMMA (6% in anisole, Allresist GmbH, AR-P 662.06; 4000 rpm for 60 s, heated at 85°C for 10 minutes, then back-etched in oxygen plasma (0.30 mbar, 100 W, 2 minutes) and transferred on a cleaned wafer (sonication in acetone for 5 min, then rinsed with acetone, MilliQ and isopropanol, then treated with O_2 plasma (0.30 mbar, 100 W, 2 minutes), optionally with Au electrodes deposited beforehand. Au electrodes were fabricated on clean wafers by metal sputtering; first, a wafer was masked with aluminum foil with cutouts where the electrodes will be deposited. To assure adhesion of the gold to the wafer, a layer of chromium (5 nm) was deposited, after which 75 nm of gold was deposited. Wafers with Au electrodes were cleaned in the same way as bare wafers (see above) prior to graphene transfer.

Graphene was transferred using PMMA-assisted the transfer method by etching copper with an ammonium persulfate solution (0.2 M in MilliQ) and rinsing the PMMA-graphene film by transferring it in three MilliQ baths consecutively, after which this film was transferred on the wafer by fishing the floating film from below. Next, water was allowed to gently evaporate at 45°C; when water was evaporated, the coated wafer was heated at 150°C for 15 minutes. After successful transfer, the PMMA layer was removed by immersing the wafer in acetone for 10 minutes, then rinsing gently with acetone, ethanol and isopropyl alcohol, and blowing the wafer dry with pressurized air. In the case of wafers with Au electrodes, the electrodes were connected using electrically conductive silver epoxy (Gentec, EPOTEK EJ2189-LV) to copper wires. The wafer was heated to 150°C for 15 minutes to cure the conductive epoxy.

Graphene on silicon wafer was patterned with μ -contact printing. A PDMS stamp with the pattern was coated with a PMMA solution (6 wt% in anisole) using spin coating (15 seconds, 4000 rpm, acceleration 500 rpm/s), after which the stamp was pressed on a wafer on which graphene was transferred (PMMA-assisted) and exposed beforehand. After successful printing of the polymeric mask, excess graphene was removed through standard oxygen plasma cleaning. Finally, the polymeric mask was removed by immersion in acetone for 10 minutes and the wafer with exposed

patterned graphene was rinsed with acetone, ethanol and isopropyl alcohol and blown dry with pressurized air.

Oxygen plasma was generated using a capacitively coupled plasma system with radio-frequency of 40 kHz and 200 W power from Diener electronic (Femto), employed at room temperature. Spin coating was using with a POLOS SPIN150i tabletop spin coater. Optical images were obtained using a Leica DM2700 M Brightfield microscope fitted with Leica MC120 HD camera. AFM images were recorded on a JPK Nanowizard Ultra. Raman spectra were recorded on a Witec Alpha500 R Raman spectrometer using a 532 nm laser at low power (0.23 mW). EDX mapping was performed on an Apreo Scanning Electron Microscope (SEM). XPS spectra were recorded on a ThermoScientific K-Alpha spectrometer fitted with a monochromatic X-ray source. XRD spectra were recorded with a Bruker D8 Advance diffractometer using Cu K α radiation ($\lambda = 1.5406 \text{ \AA}$). Magnetic measurements were performed using a Quantum Design MPMS XL SQUID Magnetometer. Electrical characterization of devices was performed using Keithley Sourcemeters, models 2450 and 2400, in combination with Kickstart measuring software. Optical footage of a device inside the chamber was recorded using the optical camera equipped to the Raman microscope setup. Temperature cycling experiments were performed using a Linkam THMS600E microscope heating/cooling stage equipped on the Raman spectrometer in combination with LINK temperature control software. During temperature cycle experiments, the devices were electrically connected inside the heating/cooling stage. To prevent condensation, the chamber was purged with N₂ (N3.0) at the start each experiment, according to the manufacturer's protocol.

Supplementary Figures

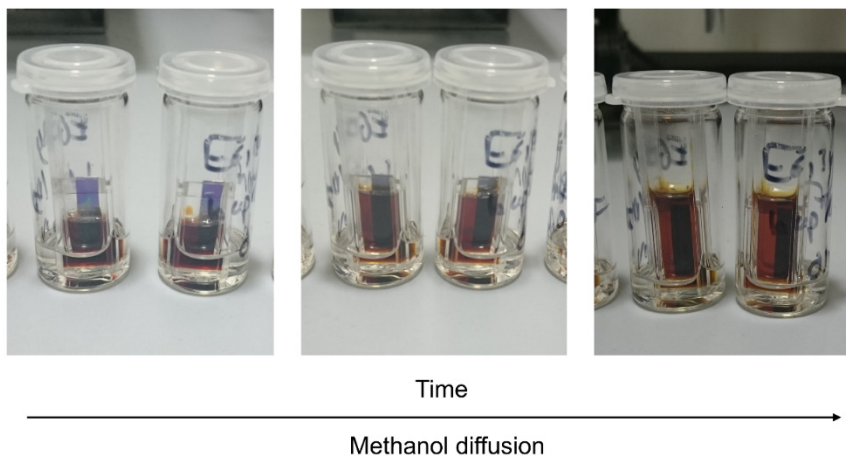


Figure S3.1: Photograph of a typical thin film growing experiment. Methanol diffused from the vial to the cuvette that is inside.

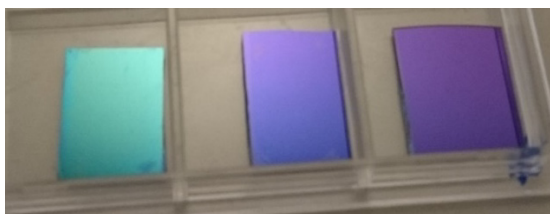


Figure S3.2: Camera images of wafer fully coated with thin film-coated graphene on wafer (left, blue-green, 5 days film growth), wafer fully coated with graphene (center, deep blue) and uncoated wafer (right, purple).

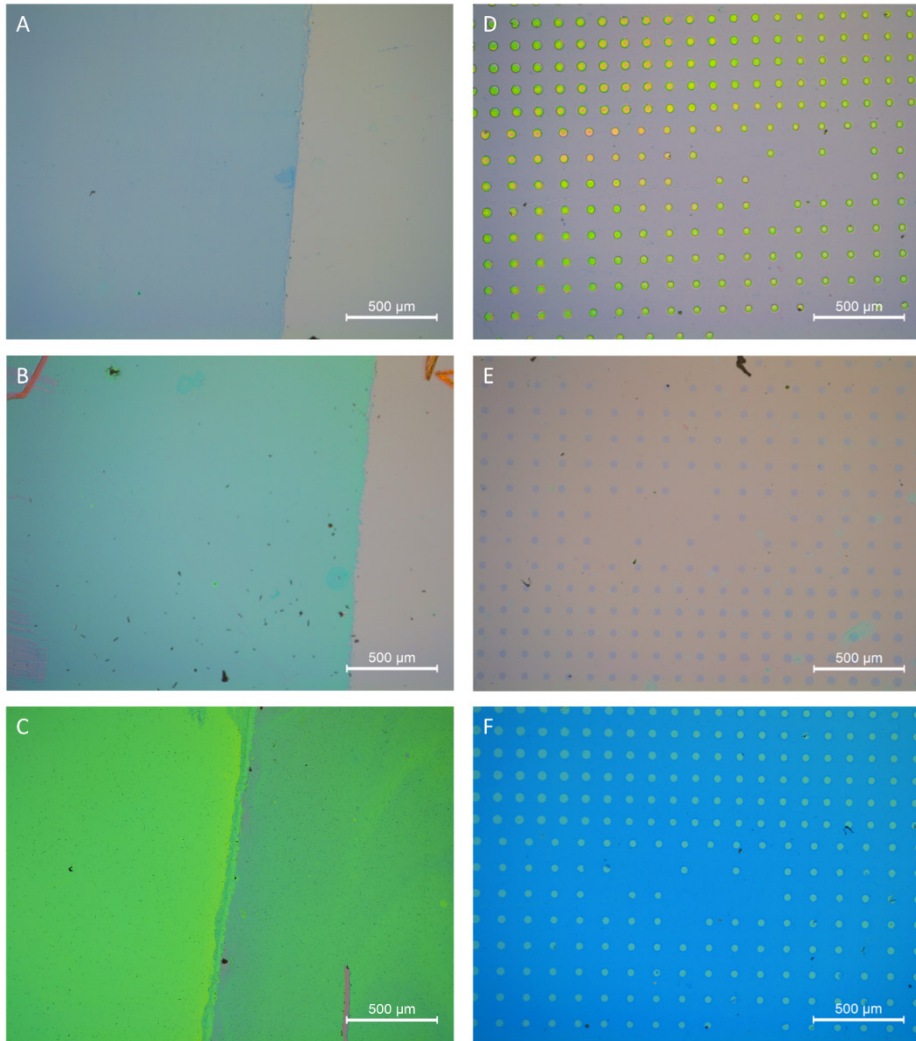


Figure S3.3: Optical microscopy images of 1 day, 2 day and 6 days of film formation (A-C) on graphene, always on the left side of the wafer. The scratch in C) reveals the wafer underneath the thin film, showing the thin film has deposited on the wafer itself as well. D-F) optical microscopy images of patterning and growing films on graphene, showing patterned PMMA mask on graphene (D), exposed graphene after oxygen plasma and removal of the polymer mask (E), and thin film grown on graphene (F, growth time = 6 days).

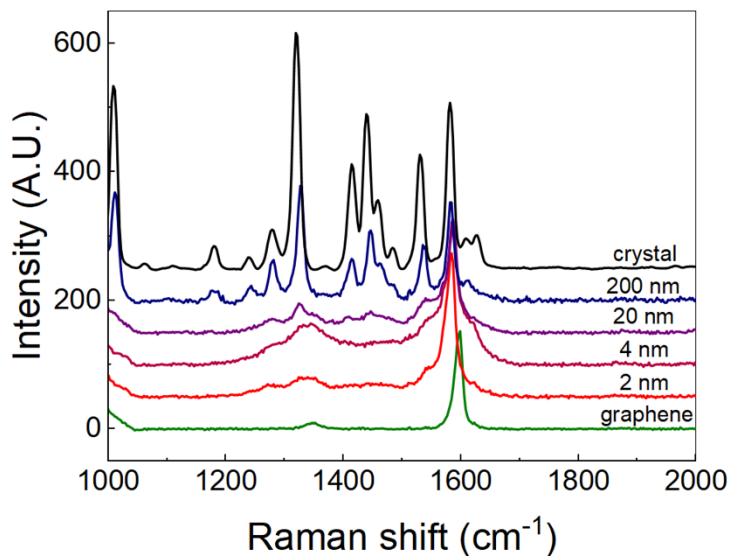


Figure S3.4: Raman spectrum (zoomed) of bare graphene on silicon wafer (green), graphene coated with thin films of $[\text{Fe}(\text{bapbpy})(\text{NCS})_2]$ with different thicknesses (red to blue), and single crystals of the HS phase of $[\text{Fe}(\text{bapbpy})(\text{NCS})_2]$ (black) at room temperature.

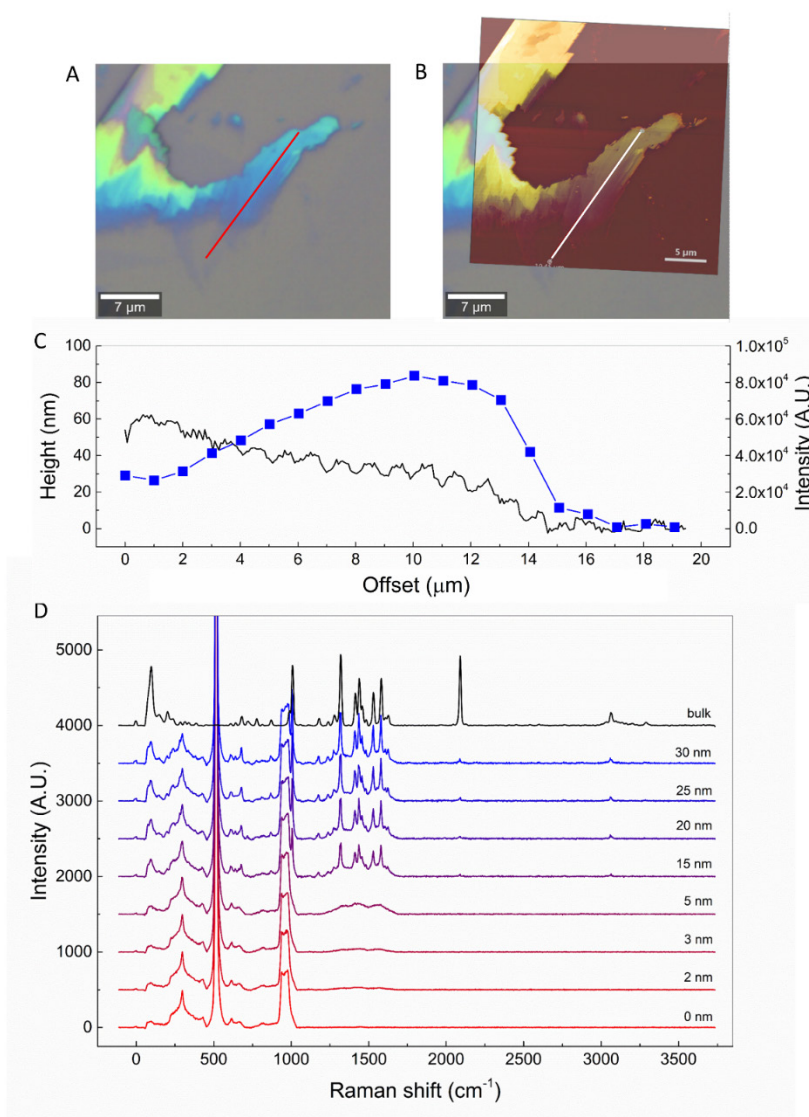


Figure S3.5: Raman spectroscopy of thin residue material from $[\text{Fe}(\text{bapbpy})(\text{NCS})_2]$ bulk crystal, damaged with sonication. A) Optical image of thin residue from bulk crystal. Red line indicates line across which Raman spectra were recorded. B) Overlay of optical image shown in A and AFM map of the area. C) Height profile across white line in AFM map (black), overlaying the line along which Raman spectra were recorded, and total peak area from Raman spectroscopy in the range of $1200\text{--}1700\text{ cm}^{-1}$ (blue squares). Lower Raman signal from 0 to $10\text{ }\mu\text{m}$ offset is due to out-of-focus measurement; focus is regained for 10 to $20\text{ }\mu\text{m}$ offset. D) Raman spectra of the thin residue at different thicknesses (red to blue) and Raman from an intact $[\text{Fe}(\text{bapbpy})(\text{NCS})_2]$ crystal (black). Peaks at from $0\text{--}1000\text{ cm}^{-1}$ at 0 nm are the background peaks from the silicon wafer.

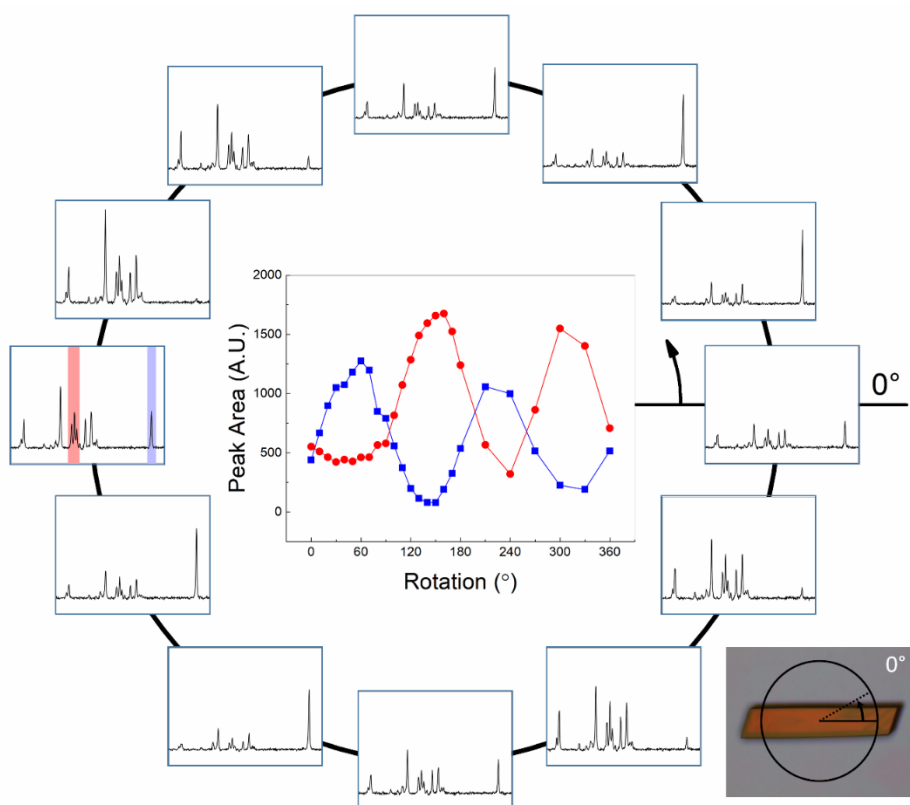


Figure S3.6: Raman spectroscopy of a single crystal of $[\text{Fe}(\text{babppy})(\text{NCS})_2]$ (optical image in the bottom right), rotated anticlockwise in the x,y plane. Individual spectra are displayed on the circle and are scaled equally; their location on the circle indicates the rotation. Red and blue areas at 180° indicate the areas that were integrated to obtain the peak area *vs.* rotation (center), where red corresponds to one of the babppy ligand peaks (integrated over $1375\text{-}1500\text{ cm}^{-1}$) and blue corresponds to the thiocyanate peak (integrated over $2050\text{-}2150\text{ cm}^{-1}$).

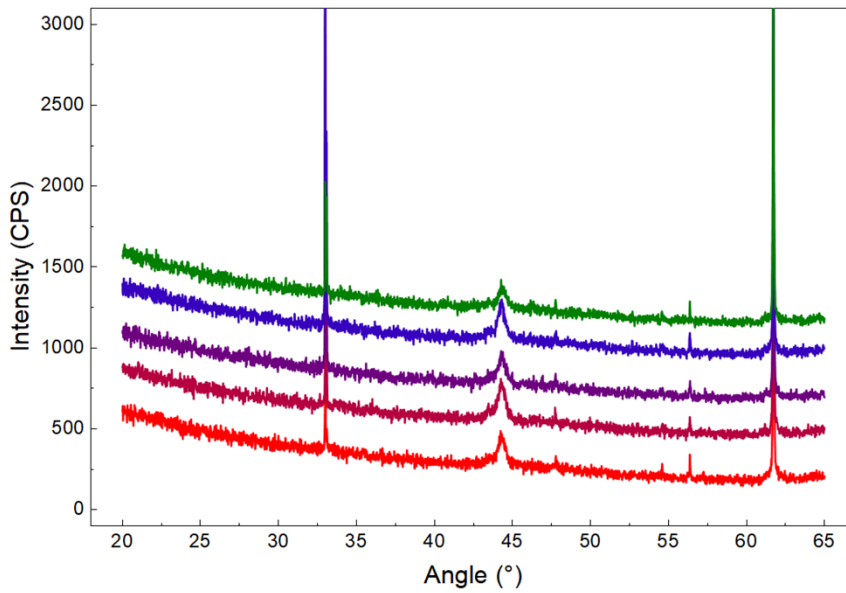


Figure S3.7: XRD spectra of thin films grown on graphene with different growing times on silicon wafer (red to blue: 0 days, 1 day, 2 days, 5 days) and clean silicon wafer (green).

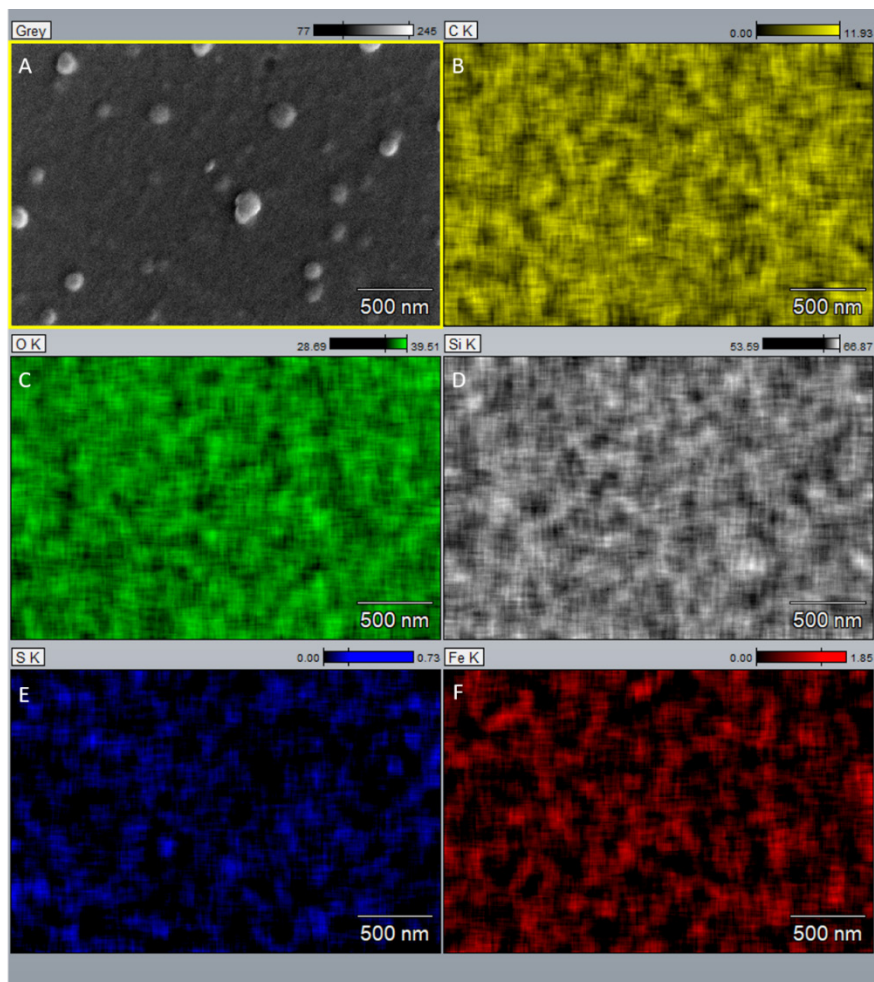


Figure S3.8: EDX analysis of a thin film on graphene. A) SEM image of a thin film on graphene, growth time was 5 days. EDX mapping of the elements carbon (B, yellow), oxygen (C, green), silicon (D, gray), sulfur (E, blue) and iron (F, red).

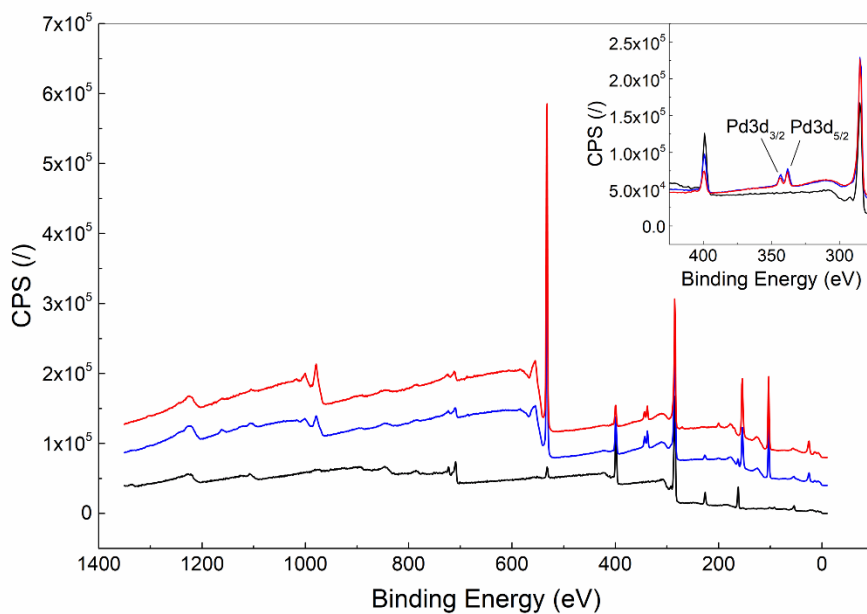


Figure S3.9: XPS spectra of thin film on graphene (growth time 3 days) grown under nitrogen (blue) and under normoxic atmosphere (red), and $[\text{Fe}(\text{bapbpy})(\text{NCS})_2]$ bulk material which was ground under nitrogen atmosphere (black). Notably, we found that a palladium contamination, likely originating from the ligand synthesis was transferred to the thin films, indicated by a clear doublet in the XPS spectrum of each examined film (338.0 eV and 342.9 eV, see inset).

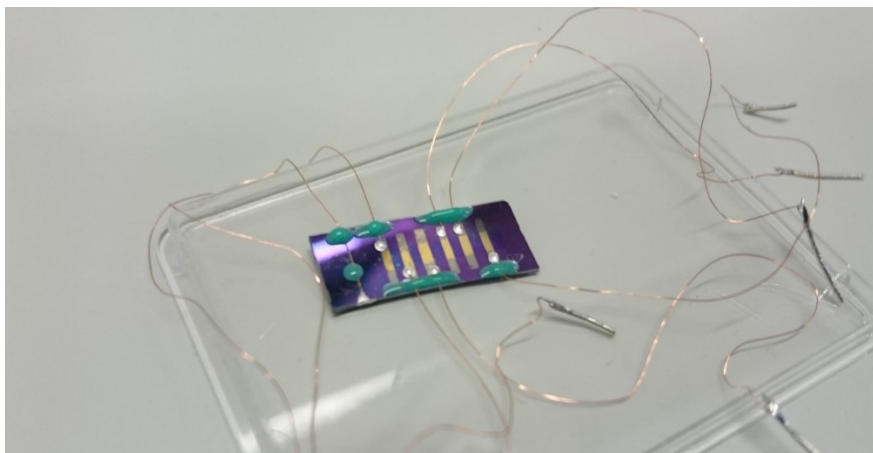


Figure S3.10: Optical image of a GFET coated with a chemically grown thin film, growth time is 2 days.

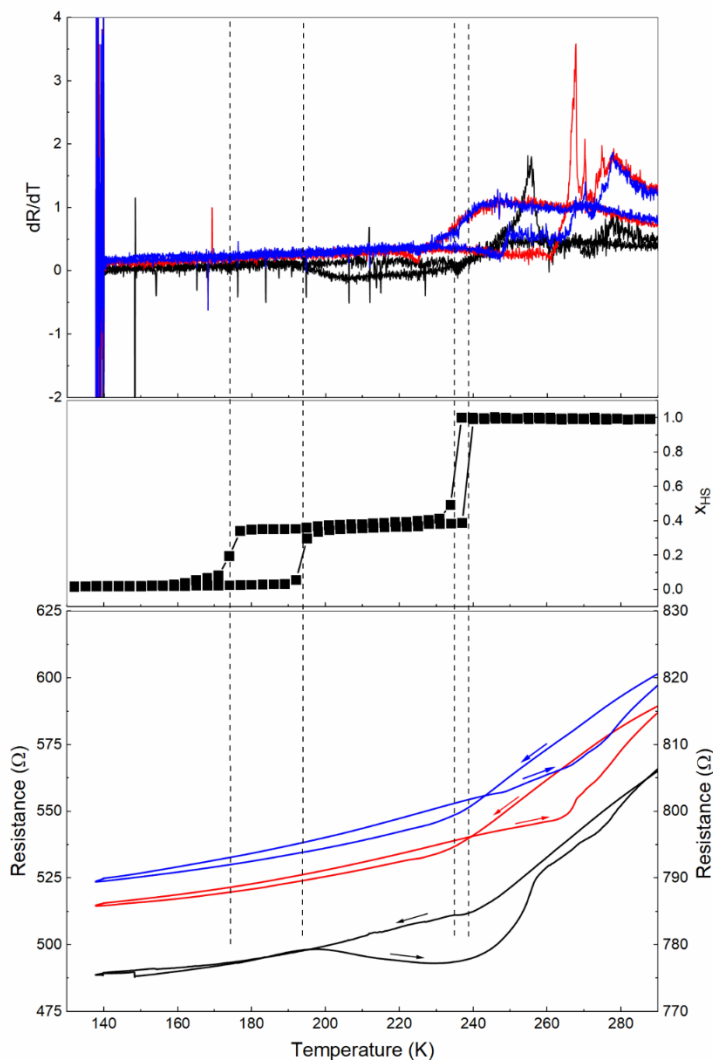


Figure S3.11: dR/dT and resistance *vs.* temperature for GFETs coated with a chemically grown thin film, growth time either 0, 1 day or 2 days (black; right axis R , red and blue; left axis R , respectively), based on $[\text{Fe}(\text{bapbpy})(\text{NCS})_2]$. Current I_{AF} was set to $100 \mu\text{A}$. Gate voltage was set to 0 V . Temperature was cycled at 2 Kmin^{-1} . Mole fraction of high spin molecules (obtained from $\chi_m T$ measurements using SQUID magnetometry, as was previously reported^[1]) in single crystals of $[\text{Fe}(\text{bapbpy})(\text{NCS})_2]$ is shown above (black squares); spin crossover transition temperatures are indicated by dashed lines.

References and notes

- [1] S. Bonnet, M. A. Siegler, J. S. Costa, G. Molnar, A. Bousseksou, A. L. Spek, P. Gamez, J. Reedijk, *Chem. Commun.* **2008**, 0, 5619.
 [2] S. Zheng, M. A. Siegler, O. Roubeau, S. Bonnet, *Inorg. Chem.* **2014**, 53, 13162.

Appendix

Chapter 4

Materials and Methods

PMMA solutions were purchased from Allresist GmbH. All chemicals, including a solution of Nafion® 117 (~5% in lower aliphatic alcohols and water, 70160-25ML) and CAB (Mn ~30.000, 419052-250G) powder were obtained from Sigma Aldrich.

Oxygen plasma was generated using a capacitively coupled plasma system with radio-frequency of 40 kHz and 200 W power from Diener electronic (Femto), employed at room temperature. Spin coating was done with a POLOS SPIN150i tabletop spin coater. Electrical characterization of devices was performed using Keithley Sourcemeters model 2450 and 2400 in combination with Kickstart measuring software.

Experimental

PMMA-coated devices (MEAS & REF)

Sensors for manual injection were produced using solely benchtop techniques, without the need of a cleanroom. A silicon wafer of 10 x 20 mm (Prime grade, 285 nm SiO₂ on 0.5 mm Si, single side polished, Siebert Wafer GmbH) was cleaned by sonication in acetone for 5 min, then rinsed with acetone, water and 2-propanol. Next, the wafer was treated with oxygen plasma (0.30 mbar, 100 W, 2 min), after which the wafer was masked with masking tape (Semiconductor Wafer Tape SWT 20+, Nitto Europe N.V.) which had the electrodes shape cut out previously. A mask typically had 6 electrodes (A-F) parallel to each other precut, *i.e.* cutting was not done on the wafer to prevent scratching of the SiO₂ layer at the risk of gate leakage. Electrodes were produced by a chemical silver deposition method using a Tollens' reagent (an aqueous [Ag(NH₃)₂]⁺ solution). The silvering solutions (A and B) were prepared as follows:

A: To a solution of silver nitrate (0.1 M in water, 25 ml), a potassium hydroxide solution (0.8 M in water, 25 ml) was added, upon which a silver(I) oxide precipitation formed. An ammonia solution (30% in water, few drops) was added drop-wise while the suspension was stirred, until the precipitation was fully dissolved.

B: α -D(+)-glucose (0.24 g) was dissolved in 50 ml water, [α -D(+)-glucose] = 0.58 M.

To produce metallic silver for the electrodes, solutions A and B were mixed in a ratio of 1:1, and pipetted to the target substrate immediately after mixing (covering the cutouts in the masking tape). The mixture, which quickly became dark brown and later gained a metallic shine at its surface, was left for 15 minutes at room temperature on the substrate. Afterwards, the silvering solution was removed, the wafer was rinsed with MilliQ water, and the mask was removed. The wafer then was sonicated for 5 minutes in acetone, then rinsed with acetone, water and 2-propanol and blown dry with pressurized nitrogen to remove any unattached silver particles.

Monolayer graphene on copper foil (synthesized in-house using a hot-wall CVD oven) was spin-coated with a PMMA solution in anisole (6wt% in anisole, Allresist GmbH., AR-P 662.06; 4000 rpm for 60 s), heated at 85 °C for 10 min, and back-etched with oxygen plasma (0.30 mbar, 100 W, 2 min). PMMA-coated graphene on copper was cut to size (3 x 10 mm) and placed floating (Cu-side down) on a bath of an aqueous ammonium persulfate solution (0.2 M); when copper was fully etched, the

PMMA-coated graphene sheet was rinsed by transferring to three MilliQ water baths, then back-fished with the silicon wafer, the graphene sheet stretching across the silver electrodes. Excess water was removed, and the wafer was heated to 150 °C for 15 min. Importantly, the PMMA layer was not removed from graphene.

Using a silver-based electrically conductive epoxy resin (Gentec, EPOTEK EJ2189-LV), copper wires were attached to the silver electrodes and a gate wire was installed to the silicon back side of the wafer, and the wafer was heated to 150 °C to cure the epoxy, which completed the device. Importantly, we chose to produce devices with six electrodes, to eliminate contact resistance by applying the current on electrodes A and F, while measuring the potential between electrodes B & C and D & E; by installing 4 inner electrodes, two transistors could be measured simultaneously to perform the measurements (MEAS, V_{BC}) and (REF, V_{DE}) at the same time.

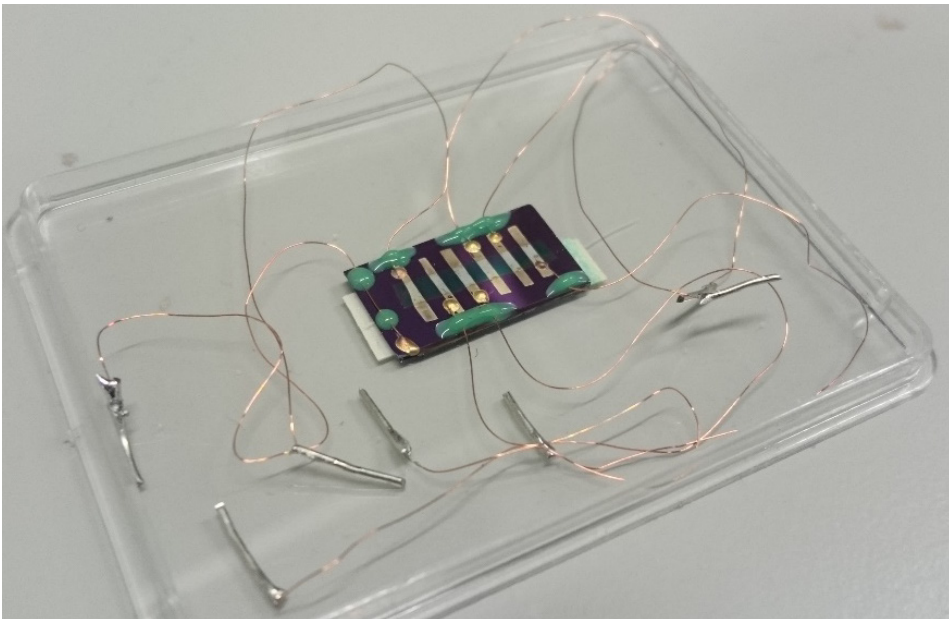


Figure S4.1: Optical photograph of a finished device.

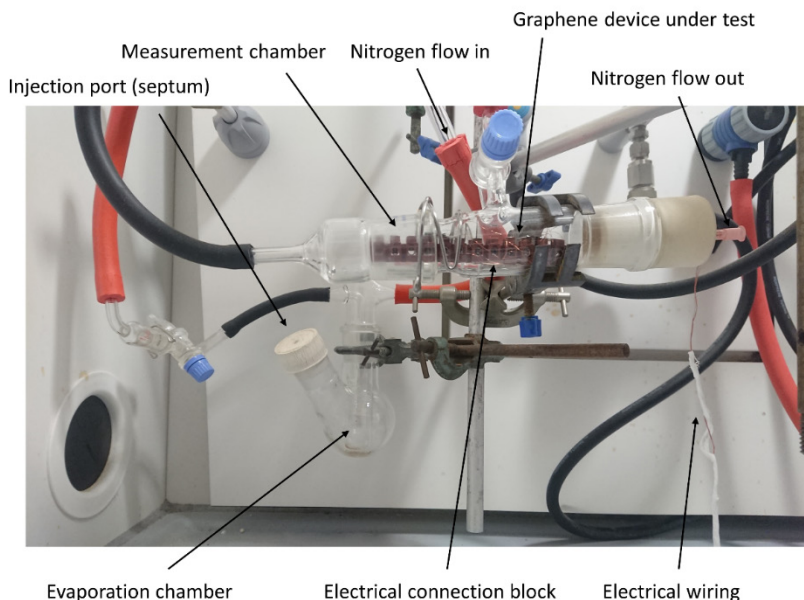


Figure S4.2: Measurement setup for PMMA-coated graphene devices, manual injection.

Table S4.1: List of compounds that were introduced to PMMA-coated graphene devices and numerical values for Peak area A_{norm} (average of 4 manual injections, 10 μl per injection) and standard deviations σ for PMMA-coated and bare GFETs.

#	compound	PMMA coated graphene		Bare graphene	
		A_{norm}	σ	A_{norm}	σ
1	water	25.18137	55.62705	7.43952	184.66897
2	methanol	73.71028	10.41363	14.21854	110.68771
3	ethanol	8.59934	3.1569	-121.21068	119.97978
4	n-propanol	5.11393	1.20193	62.97931	183.2412
5	i-propanol	11.70176	1.64195	-315.91891	353.11323
6	acetone	15.13339	2.31694	16.81714	154.4035
7	acetonitrile	-20.13984	5.10512	-78.87085	323.05426
8	pentane	0.35825	1.31289	116.39586	85.36589
9	diethyl ether	1.21561	1.91517	33.72192	126.32813
10	thiophene	4.37813	0.99344	-16.49915	373.43897
11	pyrrole	1.74565	0.36542	-203.30179	220.24747
12	pyridine	15.24397	2.01433	973.78835	1139.8853
13	toluene	1.98895	0.19504	134.65172	120.8377
14	anisole	2.1327	0.39652	408.22482	875.3277
15	benzonitrile	1.22257	0.48289	-269.6316	263.27598

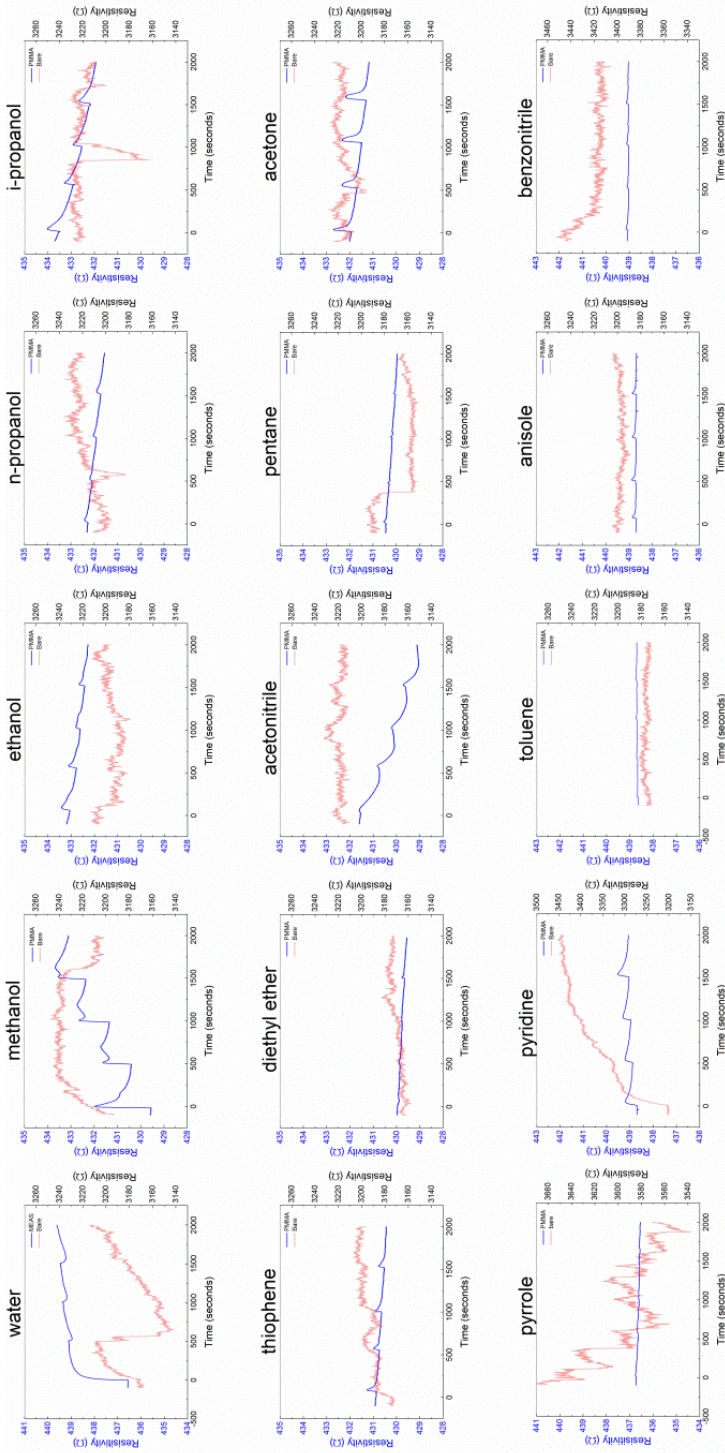


Figure S4.3: Resistance ρ vs. time for graphene-based sensors with a PMMA coating (blue) and without polymer coating (red). Each panel shows a different chemical vapour injection series (4x for each compound). Injections were performed manually with Hamilton gas-tight syringes. The volume of each injection was 10 μ l, injections were performed with intervals of 500 s. Resistance was measured continuously throughout the experiments.

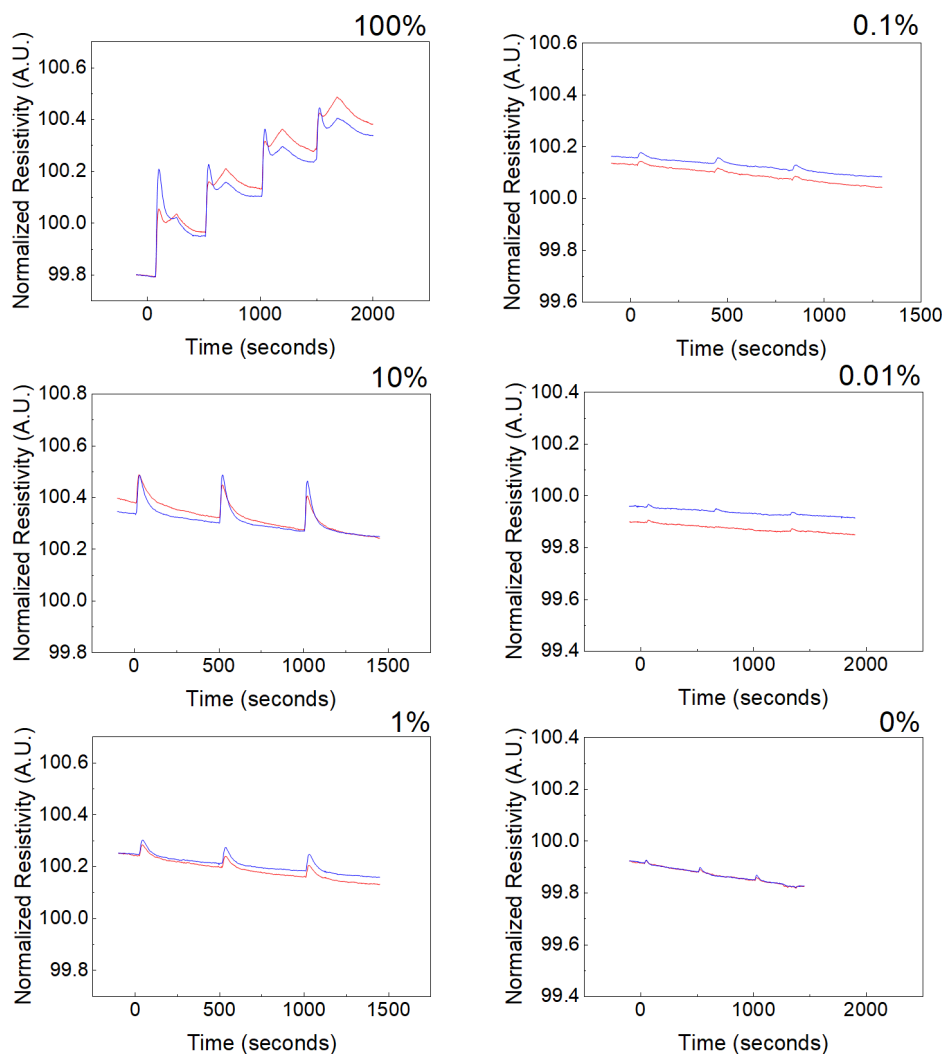


Figure S4.4: Normalized resistivity ρ_{norm} vs. time for PMMA-coated graphene sensor. Solutions of methanol in diethyl ether were injected, indicated in v%, 10 μ l per injection, with time intervals of 500 s. Percentages are indicated in the top right of each panel. Peak area A_{norm} (average of 4 data points for 100% methanol and 3 data points for other concentrations for duplicate MEAS, V_{BC} and REF, V_{DE} (red and blue, respectively)).

Fabrication of Chemical fingerprint (CF) arrays

CF arrays were fabricated with three different individual sensors, denoted CF sensors, combined in a single chamber for simultaneous measurement. CF sensors were fabricated with daughter chips that were obtained from a mother chip. The active components of the CF sensors in the CF array were polymer-coated graphene sheets.

To obtain polymer-coated graphene, monolayer graphene on copper (2x2 cm) grown in house in a hot-wall CVD oven was spin-coated with a 6wt% PMMA solution in anisole, 6wt% CAB solution in anisole, or 5wt% Nafion® 117 solution in aliphatic alcohols (4000 rpm, 500 rpm/s acceleration, 1 minute), heated to 85 °C for 10 min, then etched with O₂ plasma (0.30 mbar, 2 min, 100 W). Notably, all steps described below are the same for PMMA, Nafion® 117 and CAB coated graphene.

To fabricate a mother chip, first of all a silicon wafer chip (30 x 10 mm) was cleaned by sonication in acetone for 5 min. Next, the wafer was rinsed with acetone, MilliQ water and 2-propanol, blown dry with pressurized nitrogen and cleaned with O₂ plasma (Figure S4.5, I). A wafer tape mask with two electrodes cut out (3 mm in width and 20 mm in length, running parallel to the long sides the wafer and separated from each other by 2 mm, II) was applied directly after the plasma treatment for optimal adhesion. A mixture of silvering solution A and B, as described above (“PMMA-coated devices (MEAS & REF)”) was placed on the masked wafer; after 15 min at room temperature, the silvering solution was removed and the wafer was rinsed with water. Next, the mask was removed and the wafer was sonicated for 5 minutes in acetone to remove any unattached silver particles, then the wafer was rinsed with acetone, MilliQ water and 2-propanol and blown dry with pressurized nitrogen (III). A polymer-graphene film (4 x 20 mm) on copper was etched with an ammonium persulfate solution (0.2 M), the film was rinsed thrice with MilliQ water by transferring it into successive MilliQ baths, and transferred over the silver electrodes. Importantly, the silver epoxy electrodes were not completely covered by the polymer-graphene film; exposed silver was required for electrical connection later on. After transferring the films, wafers were kept at 45 °C to allow slow evaporation of water from underneath the film; once dry, the wafer was heated to 150 °C for 15 min and cooled to room temperature to obtain a mother chip (IV).

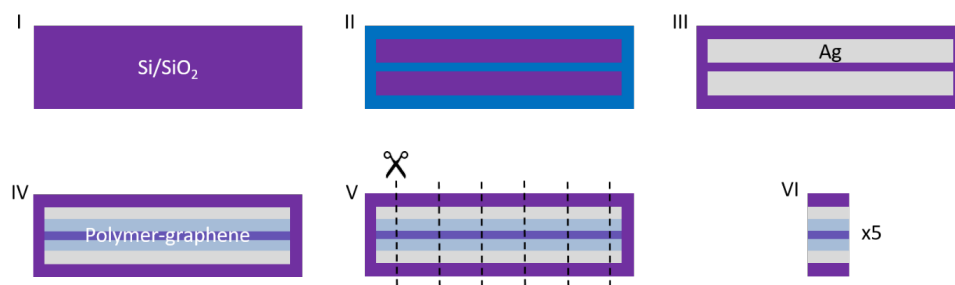


Figure S4.5: Schematic representation of daughter chip fabrication from a mother chip. A long silicon chip (approx. 30x10 mm) was cleaned and treated with O₂ plasma (I), then masked, leaving the electrode areas exposed (II). A silvering solution was placed on the wafer, which deposits metallic silver at the exposed areas, leaving the electrodes after removal of the mask and cleaning (III). Next, graphene was transferred using polymer-assisted transfer (IV). After drying and heating, the wafer was cut by introducing defects in the edge of the wafer and applying pressure (V), giving daughter chips (approx. 3x10 mm) that could be processed into CF sensors (VI).

Daughter chips were obtained by making a scratch on the mother chip and carefully breaking the wafer by applying pressure gently, while not touching the graphene or the silver electrodes (Figure S4.5, V) to obtain a daughter chip which were about 2 to 3 mm wide (VI). CF sensors for the CF array were produced from these daughter chips. Daughter chips could be coated with a PMMA, Nafion® 117 or CAB film; the fabrication process from daughter chip to CF sensor was the same for all

polymers. First, copper wires were taped to a glass slide, three in total. Next, a daughter chip was placed on top of these wires, and the chip was glued in place with Reprorubber epoxy resin (Figure S4.6, I). The copper wires were cut 1 mm away from the edge of the chip and bent towards the chip surface (II). Fresh epoxy resin was then placed at the side of the chip where the wires were bent up to fix them in place (IIIa); the epoxy was still fluid at this point, allowing it to flow under the chip, to fix the wires also at the bottom of the device (IIIb, seen from below). Short heating at 80 °C was applied to cure the epoxy once it completely covered the bottom of the chip. After, excess epoxy resin was removed with a razor blade, as close as possible to the edges of the chip, taking care that the wires were not cut (IV), and any epoxy traces were removed from the wires (V). Next, two wires were connected to the silver electrodes and one gate wire was connected to the silicon back side of the device using a silver-based conductive epoxy resin (VI). Notably, the insulating layer on the wires was not removed beforehand; the bare copper that was exposed by cutting was sufficient for electrical connection. The silver epoxy was cured at 150 °C for 15 min. After cooling to room temperature, the device was carefully removed from the glass slide (VII) to obtain the CF sensor that could be installed in a CF array.

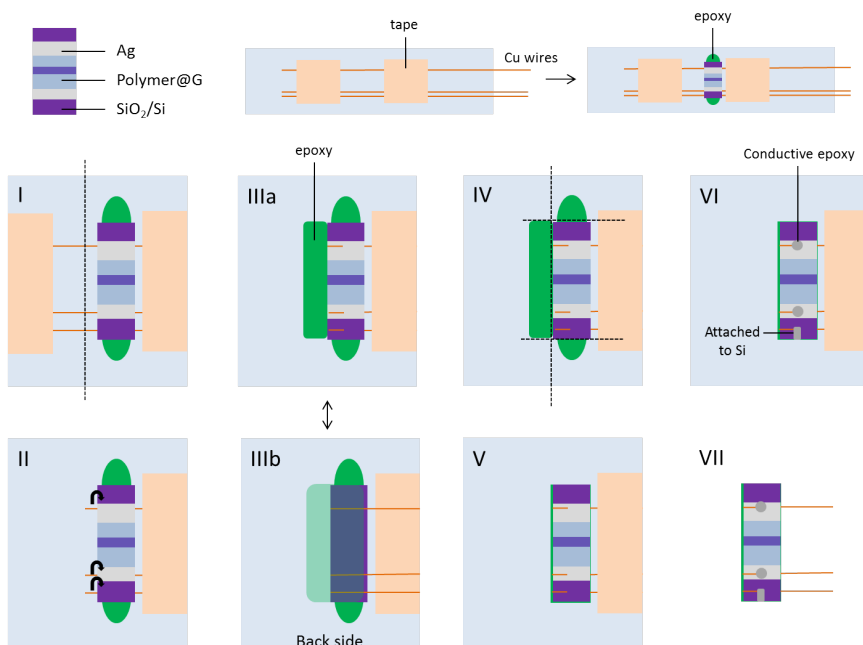


Figure S4.6: Schematic representation of fabrication, step by step, of CF sensors from daughter chips. First, a daughter chip was mounted on a glass slide, which had 3 copper wires taped to it. The daughter chip was placed on the wires and glued to the glass slide with epoxy resin. The wires were cut 1 mm away from the edge of the chip using a razor blade (I; top view), and bent upwards, with two wire ends over the electrodes of the chip and one close to the edge of the chip (II). The bent wires were fixed in position with epoxy resin (IIIa), allowing the resin to flow under the chip (IIIb, seen from below). Excess epoxy was removed with a razor blade (IV), as close as possible to the edges of the chip without damaging the wires (V). Next, the wires were connected to the electrodes (2x) and to the back side of the wafer (1x) using a silver-based conductive epoxy (VI). Finally, the device was removed carefully from the glass slide to obtain the finished CF sensor (VII).

Caps for the CF arrays were produced before installing the CF sensors in a CF array (see Figure S4.7). First of all, the needle (BD microlance™ 3, 18G, 1.2x40 mm, I) from a disposable needle was extracted from the needle base (II), then a separate needle (BD microlance™ 3, 23 G, 0.6x30 mm) was placed in the hole of the needle base (III). The needle base was then filled with Reprorubber epoxy resin while standing upright (IV). After curing at room temperature, the needle was extracted; this left a hole in the epoxy resin (V) through which the cut ends of a GC column (i.d. 0.54 mm, o.d. 0.8 mm) could be inserted to connect the sensor to the GC system (IV).

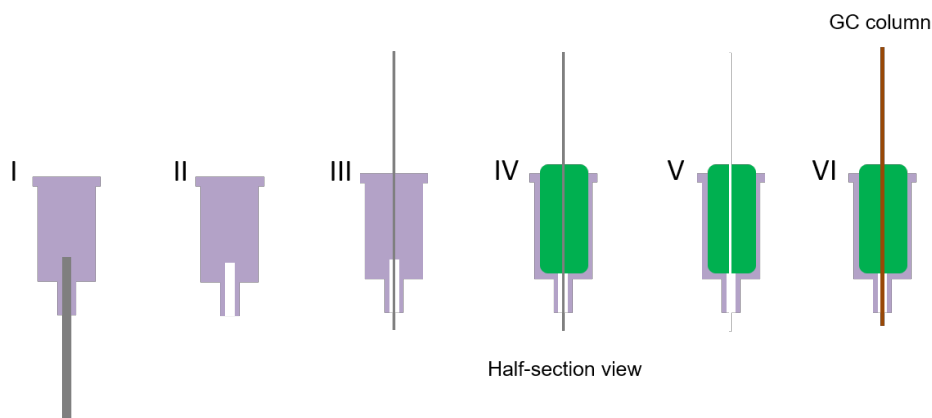


Figure S4.7: Schematic representation of fabrication of CF array caps for integration in a GC system. From a disposable needle (I) the needle was removed (II). Next, a second, thinner needle was placed in the hole that was created (III). Epoxy resin was poured in the needle base (IV), and after the epoxy was cured, the thin needle was extracted to leave a hole in the epoxy (V) through which a GC column fits (VI).

To construct the CF arrays, first of all a PTFE tube (4 cm, i.d. 3 mm, o.d. 3.5 mm) was inserted in a silicone tube (8 cm, o.d. 3 mm, o.d. = 4 mm, see Figure S4.8, I). The silicone tube was required for flexibility and for good adhesion of epoxy resins, while the PTFE tube was required for chemical inertness and structural strength. A CF sensor was inserted inside the PTFE tube with their wires run through the two tube walls using a needle (II). This was repeated twice, so three CF sensors with different polymer coatings on graphene (PMMA, Nafion® 117 and CAB) were lined up next to each other inside the PTFE tube (III). Next, the silicone tube was cut to size to fit the sensor caps, which were put into place with Reprorubber epoxy resin (acting as glue and lubricant for their insertion); at the same time the wire holes in the tube were coated with epoxy resin (IV). Next, a thermoplastic sleeve was placed over the silicone tube wall, with the wires running through a hole in this sleeve; the sleeve was then heated shortly with a heat gun to shrink the sleeve to complete the CF array (V). The CF array could be inserted in the GC column by inserting the cut GC column ends through the holes in the sensor caps; this yielded a gas-tight connection as flexible epoxy pushes on the column (the column is wider than the hole in the sensor cap (VI). Wires were connected to an electrical plug for easy connection to the electrical measurement equipment (see Figure S4.9 and Figure S4.10).

Appendix – Chapter 4

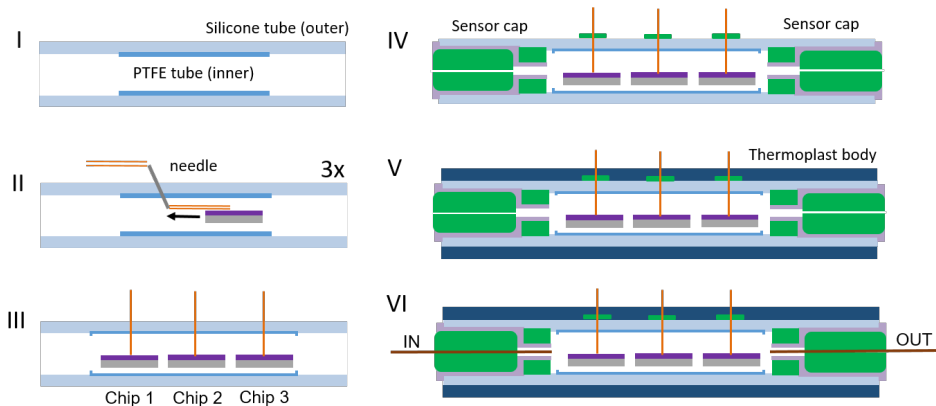


Figure S4.8: Schematic representation of final assembly of a CF array. A PTFE tube was inserted in a silicone tube, leaving about 2 cm of silicone tube on each end (I). CF sensors were inserted in the PTFE tube and their wires were run through the walls of the tubes with a needle (II). Three CF sensors were lined up in the PTFE tube and the tube ends of the silicon tube were cut to fit the sensor caps (III). Sensor caps were installed and fixed with epoxy resin, and the wire holes were patched with epoxy resin (IV). A thermoplastic sleeve was placed around the silicone tube and fixed in place by shrinking using a heat gun (V). The CF array was installed in the GC column by inserting the cut column ends through the sensor caps (VI).

To install the CF arrays in the GC setup (Varian CP3800 Gas Chromatograph, “Svetlana”, equipped with auto-injection module Varian CP-8400 Autosampler, “Vladimir”) for auto-sampling, the column of the GC (i.d. = 0.54 mm, o.d. = 0.8 mm) was cut ~30 cm away from the injection port of the GC system, creating two ends which could be inserted in the CF array caps (see Figure S4.8, VI). Sliding the column ends into the sensor caps provided a gas-tight connection. Helium was used as a carrier gas at 6 ml/min throughout all experiments; sensors were operated at 30 °C. The temperature of the injection port was 300 °C to ensure complete evaporation of the injected sample. Samples were injected in 1 μ l per injection, with a split ratio of 1:40 (*i.e.* one out of 40 parts of the injected volume was introduced to the GC column; the remainder was discarded).

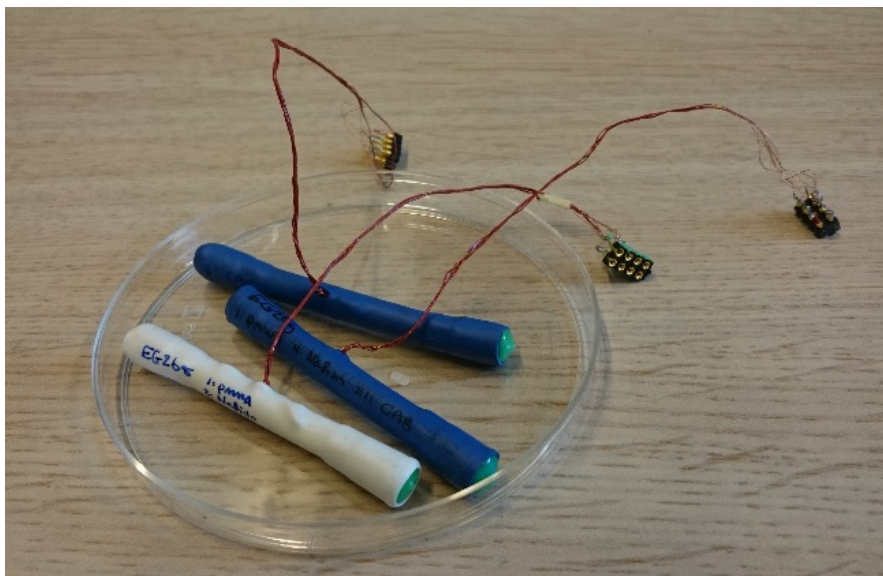


Figure S4.9: Photograph of finished CF arrays. Each tube contains three CF sensors, the wires of which were combined into one electrical plug.

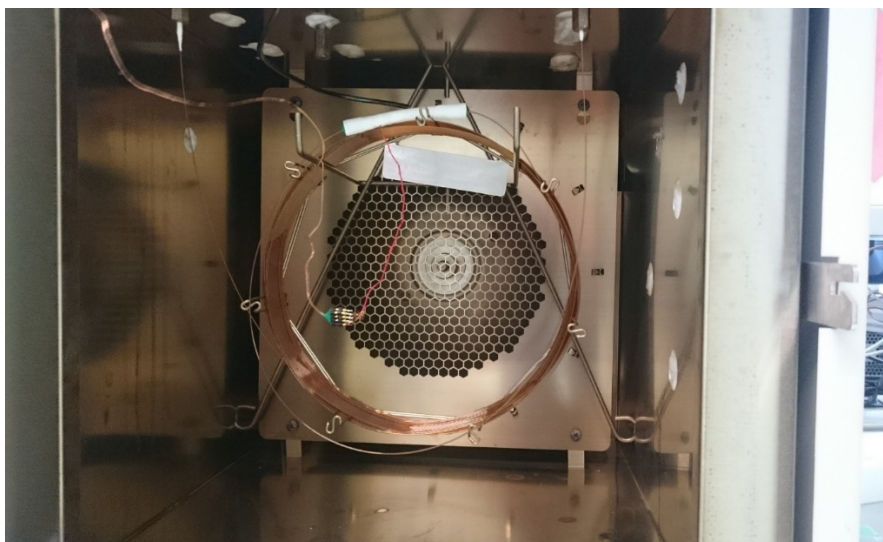


Figure S4.10: A CF array connected inside the oven of the GC system. The sensor is the white tube close to the ceiling of the GC oven; it was connected to the GC column through insertion of the cut ends of the GC column in the sensor caps. The device was electrically connected to the electrical measurement equipment through the plug that was connected to the red wire.

Table S4.2: List of compounds that were introduced to CF arrays.

#	Compound name	#	Compound name
1	acetone	22	2,4-pentadione
2	pentane	23	cyclopentane
3	diethyl ether	24	1-pentene
4	dichloromethane	25	1-pentyne
5	chloroform	26	2-methyl-2-butanol
6	ethyl acetate	27	ethyl acrylate
7	thiophene	28	4-pentenoic acid
8	toluene	29	1,4-dioxane
9	acetonitrile	30	cyclopentanone
10	methanol	31	3-methyl-1-butanol
11	ethanol	32	1-chlorobutane
12	n-propanol	33	1,5-dichloropentane
13	i-propanol	34	1-chlorohexane
14	tetrahydrofuran	35	1-bromobutane
15	diethyl ketone	36	1,4-dibromobutane
16	triethylamine ¹	37	1,2-dibromoethane
17	pyrrolidine ¹	38	1,3-dibromopropane
18	piperidine ¹	39	2,2,2-trifluoroethanol
19	pyridine ¹	40	1,1,1,3,3,3-hexafluoroisopropanol
20	isobutyraldehyde	41	ethyl formate
21	butylaldehyde	42	nitromethane

¹: 10v% in pentane

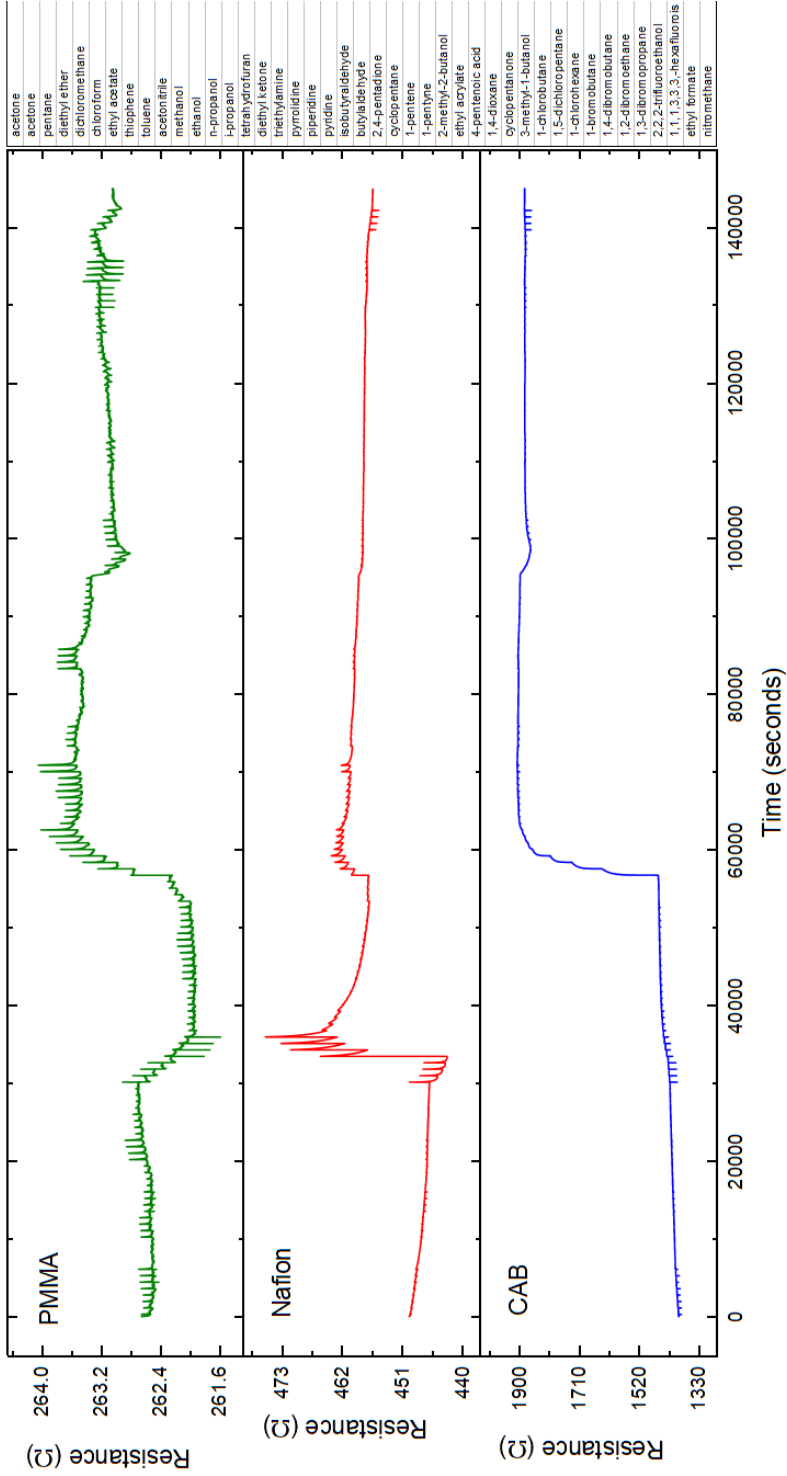


Figure S4.11: Resistance vs. time measurement for CF array 1. The compound injection sequence list is shown on the right, each compound was injected in series of 4 (acetone: 2x4 injections). Time is set to 0 at the first injection of acetone of the second acetone injection series.

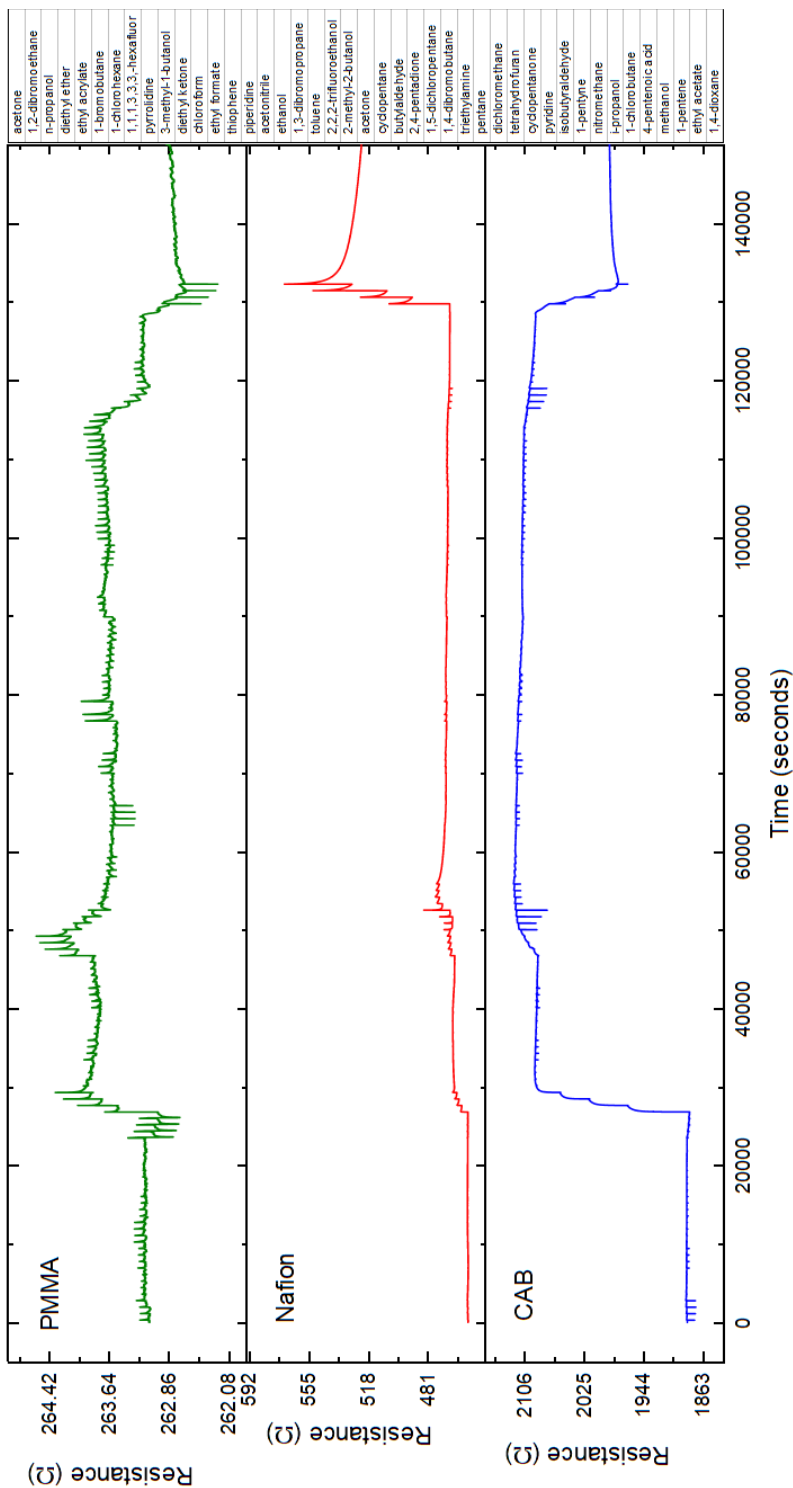


Figure S4.12: Resistance vs. time measurement #2 on CF array 1 (polymer coatings are PMMA, Nafion® 117 and CAB, from top to bottom), the sequence of the injected species was randomized (except for the first entry, acetone). Compound injection sequence list is the same for all runs depicted, as shown on the right. Time is set to 0 seconds at first injection of acetone.

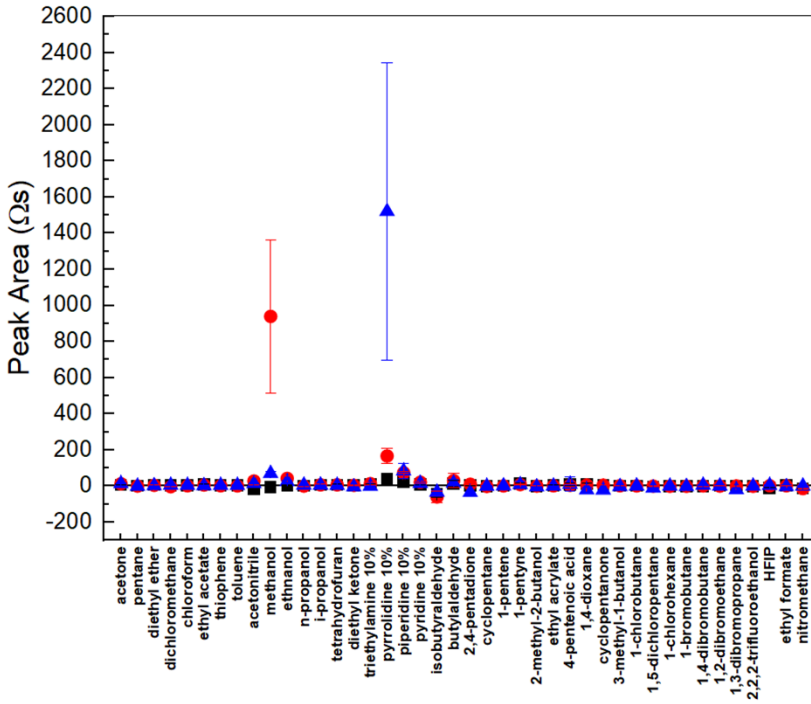


Figure S4.13: Peak area A_{norm} for chemical species, measured with CF array 1 (polymer coatings are PMMA, Nafion® 117 and CAB; black, red and blue, respectively). Peak area values are averages of 4 data points, except for acetone, which is an average of 6 data points.

Appendix – Chapter 4

Table S4.3: Numerical values for Peak area A_{norm} and standard deviations σ for CF array 1.

compound	PMMA		Nafion® 117		CAB	
	A_{norm}	σ	A_{norm}	σ	A_{norm}	σ
acetone	7.43896	2.78083	12.85827	3.03308	13.56756	0.66049
pentane ¹	1.07157	1.59823	0.41179	1.7257	-0.95157	1.24433
diethyl ether	7.01327	1.32845	4.94156	0.58798	2.15557	1.31364
dichloromethane	3.21905	1.39995	-3.12683	1.30346	4.36031	1.05728
chloroform	3.04386	2.22261	1.76379	1.51299	4.15439	2.62203
ethyl acetate	8.06609	1.16468	6.05993	1.46613	3.24944	1.74872
thiophene	4.54848	2.12179	1.79831	1.06159	4.04566	1.86002
toluene	2.91373	0.59207	1.67848	0.9511	3.54632	0.87343
acetonitrile	-15.1550	1.57902	28.92859	22.92587	13.14771	3.15161
methanol	-5.89378	3.07934	940.4069	423.6901	70.07013	9.2039
ethanol	1.77951	1.81184	43.20043	10.62601	24.47243	4.76745
n-propanol	2.42132	1.90014	0.23445	1.19124	5.97178	3.15219
i-propanol	7.43182	2.04388	7.32022	2.2044	5.70373	3.05182
tetrahydrofuran	7.6041	1.75653	7.48819	1.15154	3.57344	0.83428
diethyl ketone	5.3962	1.70443	4.32261	2.25637	-3.74829	1.70143
triethylamine 10% ^{1,2}	11.15849	2.15681	14.171	5.54386	-1.09646	1.78713
pyrrolidine 10% ²	40.54849	17.1272	167.7044	41.94557	1521.101	822.8834
piperidine 10% ²	25.19245	1.37007	73.69224	5.17681	83.54433	42.26122
pyridine 10% ²	9.40047	2.39664	22.08471	5.74916	14.99033	4.91891
isobutyraldehyde	-45.4707	17.35695	-59.1565	32.13924	-33.27751	11.4527
butylaldehyde ¹	14.04684	16.48295	31.50854	39.45431	16.51676	17.14666
2,4-pentadione	4.12845	1.98539	10.39429	4.29677	-35.46874	2.66765
cyclopentane	-1.50131	2.32989	-1.20635	2.41638	-1.21685	3.50804
1-pentene ¹	1.19036	2.11041	1.56157	1.55258	1.36114	1.26083
1-pentyne	13.98718	1.64323	9.28235	0.30478	8.08785	16.18646
2-methyl-2-butanol	0.63576	0.7438	0.6625	0.98742	-4.20456	1.56585
ethyl acrylate	2.77418	2.14237	1.76381	2.08929	0.52544	1.65388
4-pentenoic acid	8.96748	7.2974	4.3811	7.43171	9.64439	39.46284
1,4-dioxane	11.78946	5.4758	6.6345	1.18759	-21.3708	13.91718
cyclopentanone	5.33705	0.58355	5.65125	0.95392	-21.90836	1.2401
3-methyl-1-butanol	0.89499	0.96357	1.99293	1.34636	-2.30345	1.40885
1-chlorobutane	1.25859	0.91327	0.96833	0.8763	0.23461	0.8994
1,5-dichloropentane	-2.06434	2.27153	0.56876	2.15016	-10.60375	2.62628
1-chlorohexane ¹	0.67071	1.10135	-0.53106	1.01667	-0.0196	1.4552
1-bromobutane	-0.20781	1.81974	-0.40501	1.08789	-2.19186	1.55078
1,4-dibromobutane ¹	-0.40439	1.93878	1.37309	2.55367	4.82274	1.78403
1,2-dibromoethane ¹	2.0484	1.45638	0.74157	1.46897	0.34492	5.04421
1,3-dibromopropane ¹	-0.38169	2.14108	1.11345	2.53223	-19.77203	5.15564
2,2,2-trifluoroethanol	-1.22238	1.72534	-0.18561	0.87915	-0.24363	0.75251
HFIP ²	-9.59605	1.16899	1.73615	1.04815	4.15998	1.14245
ethyl formate	3.37347	1.65042	1.91783	1.57161	-3.1243	11.38078
nitromethane	-12.4171	0.94583	-13.03708	2.38556	0.54424	1.51129

¹: did not comply with machine learning criterion.

²: 10v% in pentane.

³: HFIP = 1,1,1,3,3,3,-hexafluoroisopropanol.

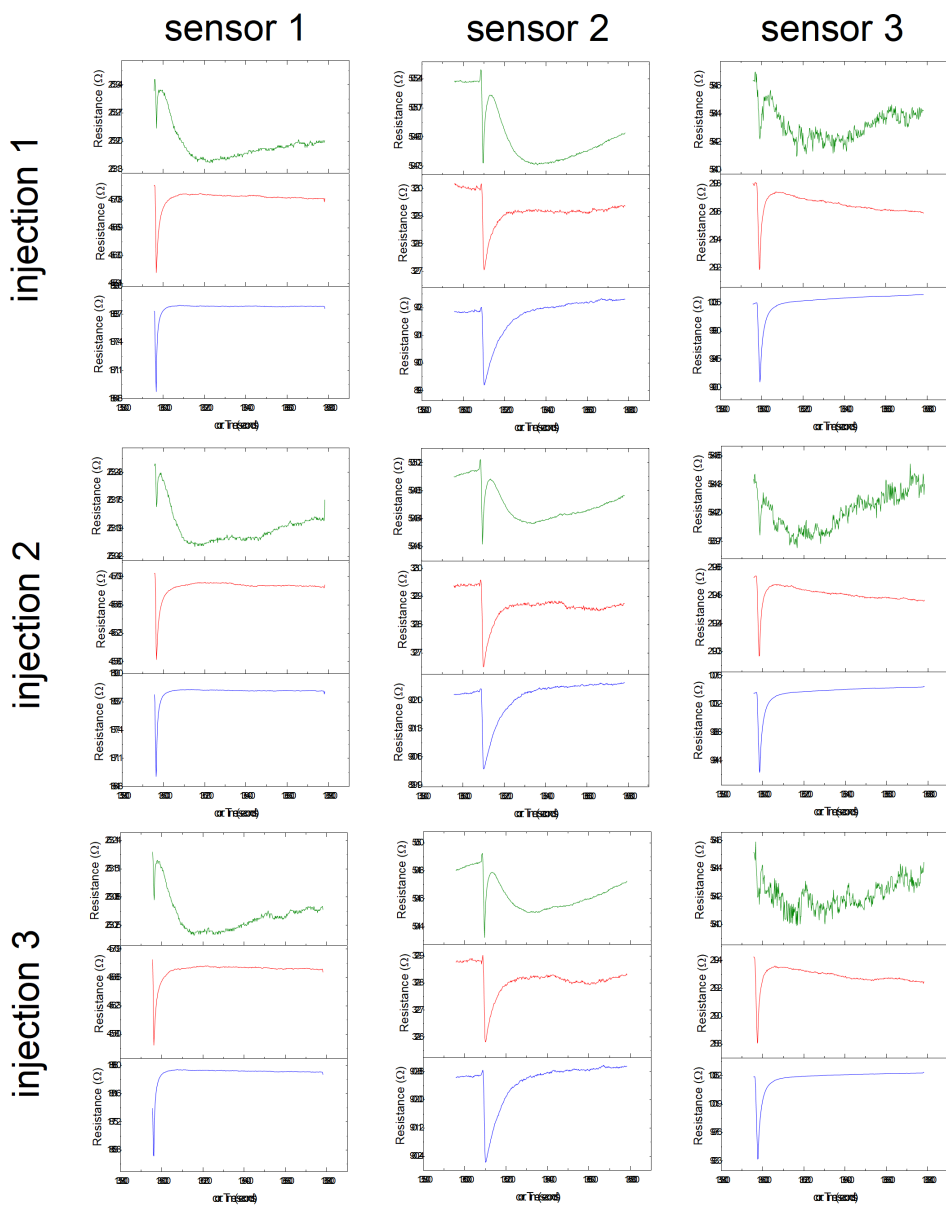


Figure S4.14: Resistance *vs.* time of different CF arrays 1, 2 and 3 to sequential injections of nitromethane (injections 1 to 3). PMMA-coated sensors is indicated in green, Nafion® 117-coated sensors in red and CAB-coated sensors in blue.

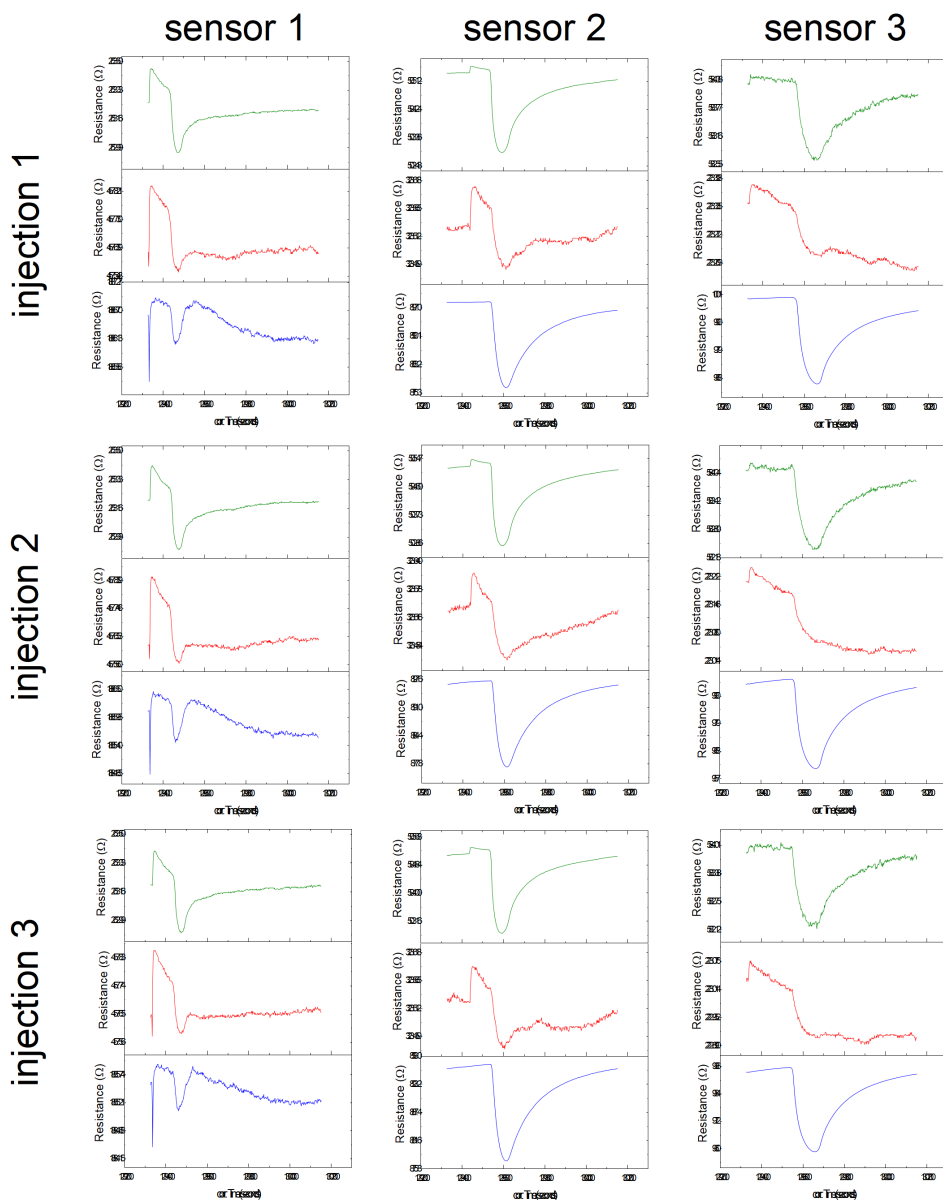


Figure S4.15: Resistance *vs.* time of CF arrays 1, 2 and 3 to sequential injections of 1,1,1,3,3,3-hexafluoroisopropanol (HFIP, injections 1 to 3). PMMA-coated sensors is indicated in green, Nafion® 117-coated sensors in red and CAB-coated sensors in blue.

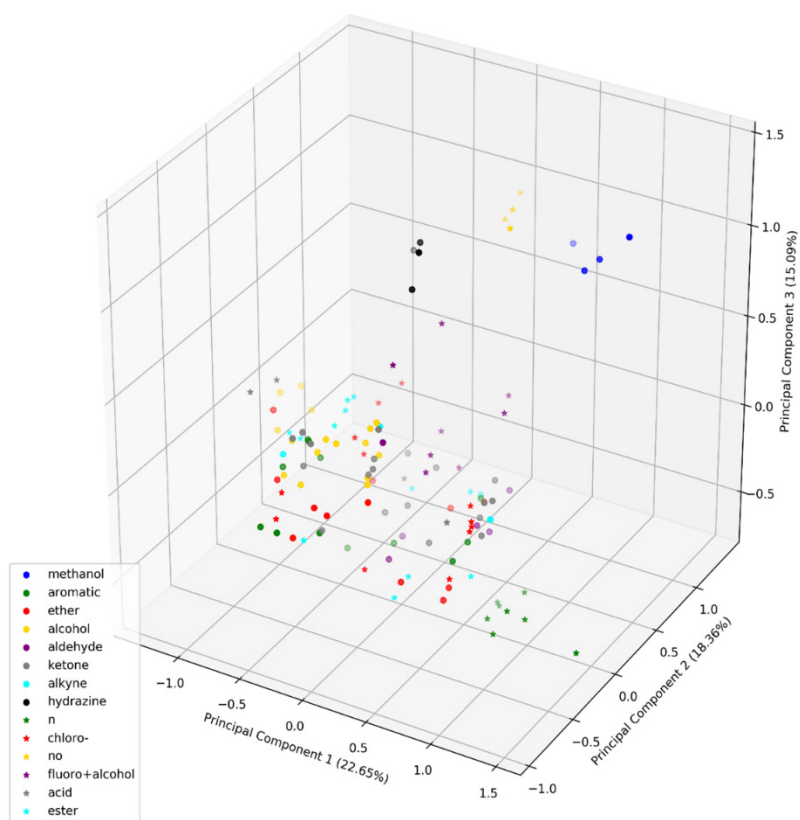


Figure S4.16: Distribution of samples in 3D plot with the first three components of principle component analysis (PCA). The plot was colored and shaped based on which family the compounds belong.

Appendix

Chapter 5

Materials and Methods

All chemicals were purchased from Sigma Aldrich and used without further purification. $[\text{Ru}(\text{tpy})(\text{biq})\text{Cl}]\text{Cl}$ was kindly provided by Dr. Lucien Lameijer.

Regular printing paper (Xerox, 80 gr/m², A4) was cut to pieces of 20 × 40 mm. Each piece was soaked with a solution of cellulose acetate butyrate (CAB) in ethyl acetate (30 mg/ml), creating a hydrophilic channel (2 to 3 mm wide) in the center of the paper. After taping the paper with the channel to a microscope slide for support, four electrodes running parallel to the hydrophilic channel, with the inner electrode close to the edges of the channel, were fabricated with conductive silver epoxy (Gentec, EPOTEK EJ2189-LV). The epoxy was cured at 150 °C for 15 minutes. Next, a piece of PMMA-coated graphene (grown by chemical vapor deposition (CVD), monolayer on copper foil; grown in-house in a CVD tube oven), spin-coated with PMMA (6% in anisole, Allresist GmbH., AR-P 662.06; 4000 rpm for 60 s, heated at 85 °C for 10 min, then back-etched in oxygen plasma (0.30 mbar, 100 W, 2 min) was cut to size (2 × 15 mm). The copper underneath the graphene was etched with an ammonium persulfate solution (0.2 M in MilliQ) and the PMMA-graphene film was rinsed by transferring the sheet in three MilliQ baths consecutively, then transferred on the paper, over the electrodes, by fishing the floating film from below. Water was allowed to evaporate at 80 °C, and once dry, the paper was heated for 150 °C for 15 min. Copper wires were placed and fixed to the paper substrate with epoxy resin (Reprorubber Thin Pour) and after curing the epoxy (5 min at 60 °C) the wires were electrically connected to the electrodes on the paper substrate with conductive silver epoxy. The device was heated to 150 °C for 15 min to cure the silver epoxy. Next, a piece of copper foil was cut to size (2 × 10 mm), and a small cut (3 mm) was created in the paper, in the hydrophilic area, perpendicular to the electrodes, away from the graphene. The copper foil was inserted in this cut, to end up underneath the paper supporting the graphene sheet, parallel to the hydrophilic channel. The copper foil was electrically connected to a copper wire with silver epoxy (curing at 150 °C for 15 min) to provide the device with a gate electrode, finishing the device. For wetting the devices, a simple reservoir was made by cutting a plastic syringe and fitting a plastic pipetting tip in the nozzle; the liquid was loaded in the pipetting tip which touched the device on the hydrophilic channel.

Oxygen plasma was generated using a capacitively coupled plasma system with radio-frequency of 40 kHz and 200 W power from Diener electronic (Femto), employed at room temperature. Spin coating was done with a POLOS SPIN150i tabletop spin coater. Optical images were obtained using a Leica DM2700 M Brightfield microscope fitted with Leica MC120 HD camera. Electrical characterization of devices was performed inside a closed steel box (with BNC connectors) using a Keithley Sourcemeter model 2450 and 2400 in combination with Kickstart measuring software. The gate voltage was supplied using a Keithley Sourcemeter (model 2450) as well; both Sourcemeters were earthed on the same point. Green light irradiation (530 nm) was done using a high-power LED (Roithner Lasertechnik, H2A1-H530) operated at 350 mA with optical power $P = 8.15$ mW, which was installed in the lid of the measurement box (~3 cm away from the GFET on paper device).

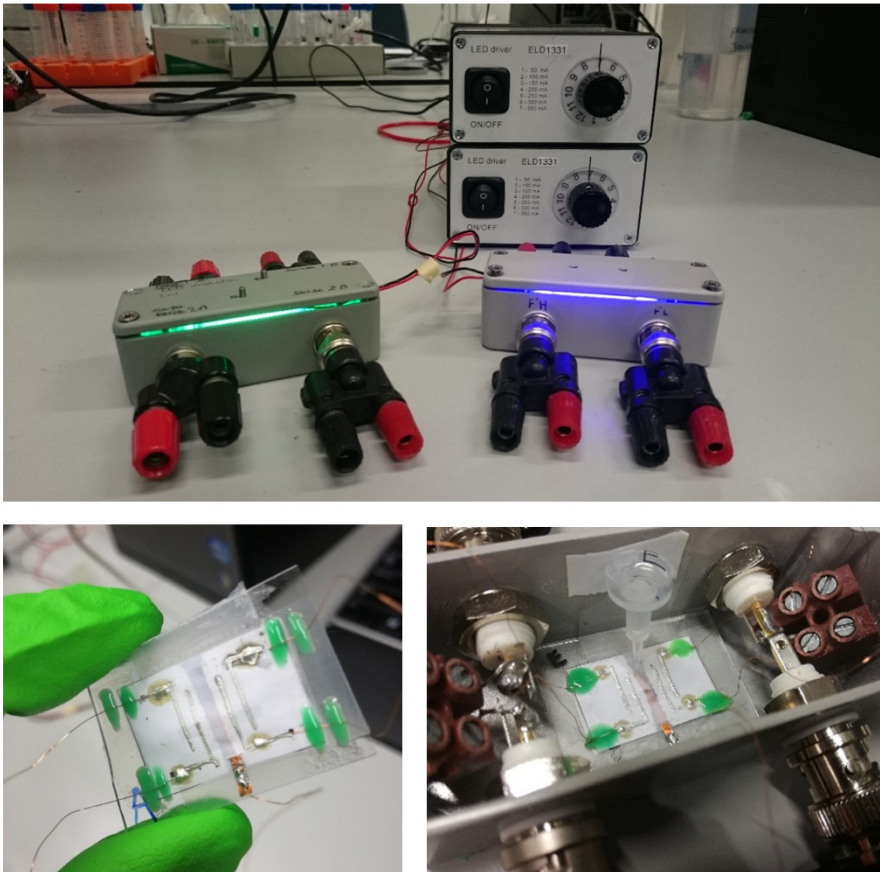


Figure S5.1: Photographs of the measurement setup (top, two setups are shown here with a green and blue LED), a finished GFET on paper (bottom left, without liquid reservoir), and a device installed in the measurement box, with the reservoir (bottom right).

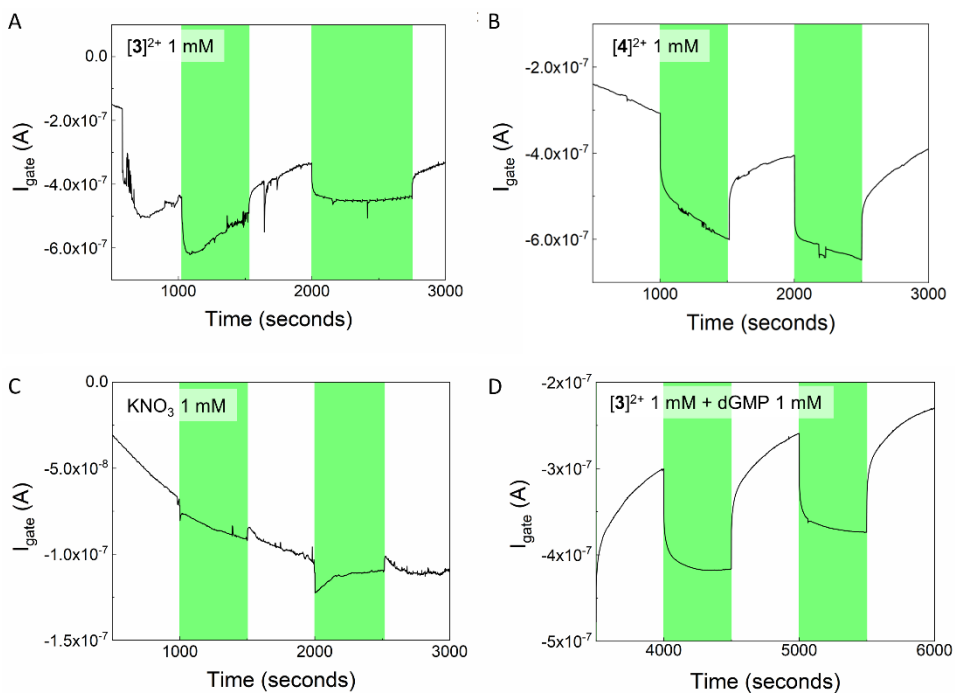


Figure S5.2: Leak current I_{gate} vs. time in the dark (white regions) and under irradiation conditions (green regions, 530 nm, $P = 8.15$ mW) for GFETs on paper wetted with A) a solution containing $[3]^{2+}$ made from $[1]Cl$ (1 mM) in water, B) $[4]Cl_2$ (1 mM) in water, C) KNO_3 (1 M) in water, and D) a solution containing $[3]^{2+}$ (1 mM) and dGMP (1 mM). R was measured between electrodes B and C , while a potential was applied on A and D , $V_{AD} = 250$ mV.

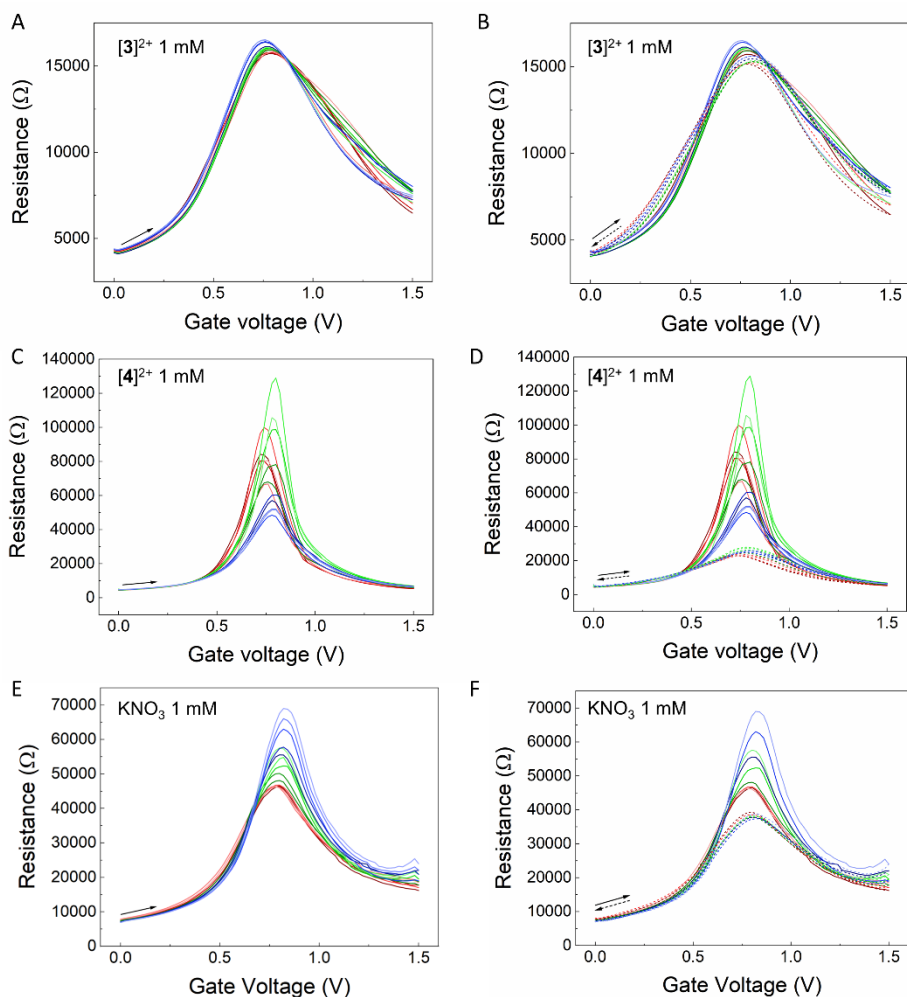


Figure S5.3: R vs. V_{gate} during forward sweeps (0 – 1.5 V) and overlay of forward (solid lines) and backward sweeps (dashed lines) for devices wetted with [1]Cl (hydrolyzed into $[3]^{2+}$, 1 mM, A-B), $[4]\text{Cl}_2$ (1 mM, C-D), or KNO_3 (1 mM, E-F). Starting in the dark (state I, red lines), a typical device was irradiated with green light (530 nm, $P = 8.15$ mW, state II, green lines), back to dark (state III, blue lines). After 10 dark stabilization cycles, 5 V_{gate} cycles were recorded for each state between 0 and 1.5 V, which are shown as their corresponding dark to light colors (dark to light red lines for state I, etc.), solid/dashed line indicates forward/backward sweep, respectively, with a sweeping rate of 0.02 V s^{-1} . R was measured between electrodes B and C, while a potential was applied on A and D, $V_{AD} = 250$ mV.

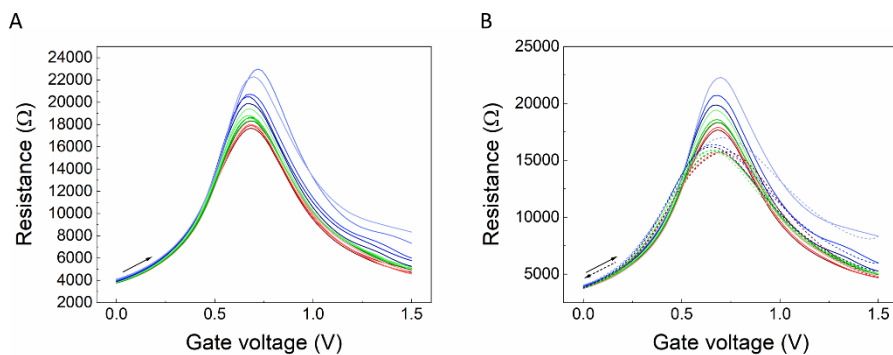


Figure S5.4: R vs. V_{gate} during forward sweeps (0 – 1.5 V, A) and overlay (B) of forward (solid lines) and backward sweeps (dashed lines) for devices wetted with $[3]^{2+}$ (1mM) + dGMP (1 mM). Starting in the dark (state I, red), the device was irradiated with green light (530 nm, $P = 8.15$ mW, state II, green line), back to dark (state III, blue line). After 10 dark stabilization cycles, 5 V_{gate} cycles were recorded for each state between 0 and 1.5 V, which are shown as their corresponding dark to light colors (dark to light red for state I, etc.), solid/dashed line indicates forward/backward sweep, varied at 0.02 V s^{-1} . R was measured between electrodes B and C , while a potential was applied on A and D , $V_{AD} = 250$ mV.

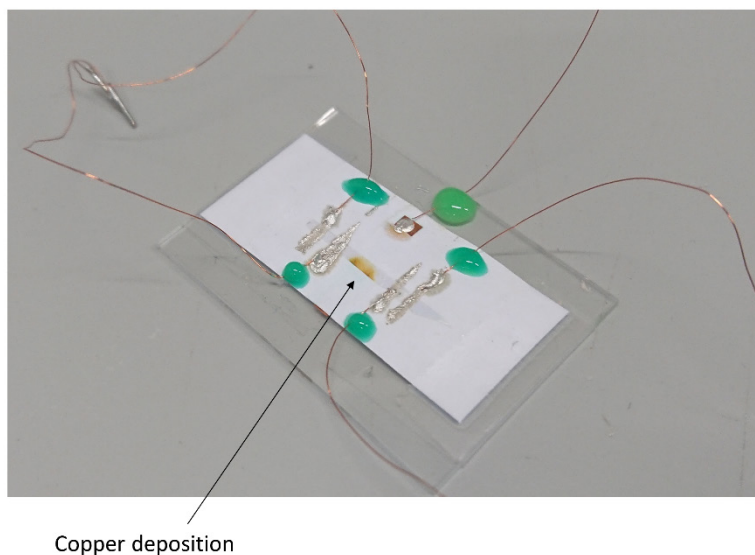


Figure S5.5: Deposition of solid copper on graphene for a GFET on paper that was wetted with KNO_3 (1 mM) and used in a gate cycling experiment (0 – 1.5 V, 15 cycles; cycle 1 to 5 and 10 to 15 in the dark, and cycle 6 to 10 under green light irradiation, 530 nm, $P = 8.15$ mW).

Appendix
Chapter 6

Materials and methods

All chemicals were purchased from Sigma Aldrich and used without further purification. λ -DNA (from *E. coli* bacteriophage λ , 48502 base pairs) was purchased at Sigma Aldrich (D9780-1MG, USA). When required, solvents were dried over activated molecular sieves (4 Å) and deoxygenated by nitrogen bubbling. Reactions were performed under inert nitrogen atmosphere using standard Schlenk techniques. $[\text{Ru}(\text{tpy})(\text{biq})\text{Cl}]\text{Cl}$, compound **[1]Cl**, was prepared according to a previously reported method.^[1] $[\text{Ru}(\text{tpy})(\text{biq})(\text{OH}_2)]^{2+}$, compound **[2]²⁺**, was obtained by dissolving **[1]Cl** in water.

Silicon nitride chips with a 30 nm thick membrane were used for nanopore drilling with dielectric breakdown by applying a potential between the *cis* and *trans* chamber that were filled with electrolyte solution (1 M KCl). The potential was applied with a pulse generator while measuring the resistance between the *cis* and *trans* chamber. When the resistance between the chambers dropped strongly, the hole was created and the potential over the membrane was removed and the nanopore could be used for DNA detection. All experiments were done in 1 M KCl buffered with 10 mM Tris and 1 mM EDTA. λ -DNA (10 ng/ μL), was introduced in the *cis* chamber of the nanopore device, which moved to the *trans* chamber through the nanopore, driven by an electrostatic potential of -100 mV. Analysis of the ion current traces was done with Transalyzer software.^[2]

Photochemistry

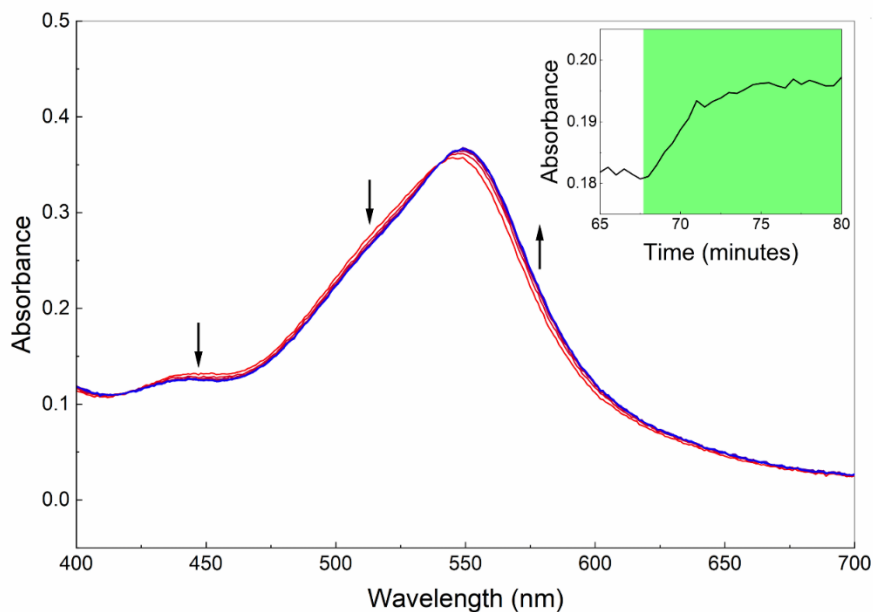


Figure S6.1: UV-vis spectra of 50 μM [1]Cl + 250 μM dGMP at 37 $^{\circ}\text{C}$. Solution was kept in the dark (red), then irradiation was started (530 nm) and spectra were recorded every 2 minutes, until the conversion was complete (blue). Inset: evolution of the absorbance at 580 nm, either in the dark (white region) or upon irradiation with 530 nm light (green region, photon flux = $1.36 \times 10^{-7} \text{ mol}\cdot\text{s}^{-1}$).

References and notes

- [1] L. N. Lameijer, D. Ernst, S. L. Hopkins, M. S. Meijer, S. H. C. Askes, S. E. Le Dévédec, S. Bonnet, *Angew. Chem., Int. Ed.* **2017**, *56*, 11549.
 [2] C. Plesa, C. Dekker, *Nanotechnology* **2015**, *26*, 084003.

Appendix
Chapter 7

Materials and methods

All chemicals were purchased from Sigma Aldrich and used without further purification. $[\text{Ru}(\text{tpy})(\text{biq})\text{Cl}]\text{Cl}$ was prepared according to a previously reported method.^[1] If required, solvents were dried over activated molecular sieves (4 Å) and deoxygenated by nitrogen bubbling. Reactions were performed under inert nitrogen atmosphere using standard Schlenk techniques.

Synthesis

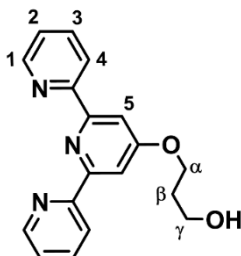
4'-(3-hydroxypropoxy)-2,2':6',2''-terpyridine (2)

Compound **2** was prepared according to a modified literature procedure.^[2] In a round bottom flask under nitrogen atmosphere, 1,3-propanediol (1.4 ml, 21 mmol) was dissolved in dry DMSO (25 ml). While the solution was stirred, powdered KOH (1.0 g, 18 mmol) was added and the mixture was heated up to 60 °C for 10 min. 4'-Chloro-terpyridine (0.96 g, 3.6 mmol) was added and the temperature was maintained at 60 °C. After 5 h, the mixture was cooled down to RT and diluted with ice cold water (50 ml). The pH was adjusted to 6 with 1 M HCl solution. The compound was extracted with ethyl acetate (3 x 25 ml) and the combined organic layer was washed with water and brine (both 3 x 25 ml) to remove DMSO. The organic layer was dried over MgSO_4 and the solvent was evaporated to obtain compound **2** as a white solid (824 mg, 2.64 mmol, 75%).

Analysis corresponded to the published data. For information:

¹H NMR (400 MHz, chloroform-*d*): δ (ppm) 8.68 (d, $J = 4.8, 1.8, 0.9$ Hz, 2H, 4), 8.61 (d, $J = 7.9, 1.1$ Hz, 2H, 1), 8.03 (s, 2H, 5), 7.86 (t, $J = 7.7, 1.8$ Hz, 2H, 3), 7.34 (t, $J = 7.5, 4.8, 1.2$ Hz, 2H, 2), 4.41 (t, $J = 6.1$ Hz, 2H, α), 3.89 (t, $J = 5.9$ Hz, 2H, γ), 2.12 (p, $J = 6.0$ Hz, 2H, β).

LC-MS (MeOH): m/z (calc) 308.2 (308.14, $[\text{2}+\text{H}]^+$), 637.2 (637.25, $[\text{2}\times\text{2}+\text{Na}]^+$).



3-([2,2':6',2''-terpyridin]-4'-yloxy)propyl-4-(pyren-1-yl)butanoate (3)

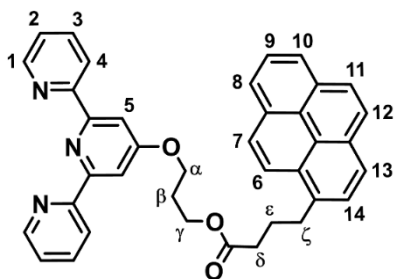
Compound **3** was prepared using a modified literature procedure.^[3] A mixture of 1-pyrenebutyric acid (616 mg, 2.14 mmol), **2** (590 mg, 1.92 mmol) and 4-(dimethylamino)pyridine (DMAP, 233 mg, 1.91 mmol) in anhydrous DCM (6 ml) was cooled to 0 °C and dicyclohexylcarbodiimide (DCC, 540 mg, 2.62 mmol) in anhydrous DCM (6 ml) was added. The reaction mixture was first stirred for 10 min at 0 °C, then overnight at room temperature. The precipitated dicyclohexylurea was removed by filtration over Celite. The filtrate was washed with water (3x 10 ml) and saturated NaHCO_3 aqueous

solution (3 x 10 ml). The organic layer was dried over anhydrous MgSO₄ and filtrated. The filtrate was evaporated by rotary evaporation. The product was then crystallized from chloroform, using methanol as a counter-solvent, to give compound **3** as an off-white solid (494 mg, 0.86 mmol, 45%).

¹H NMR (500 MHz, chloroform-*d*): δ (ppm) 8.66 (d, *J* = 4.8, 2H, 4), 8.57 (d, *J* = 7.9, 2H, 1), 8.26 (d, *J* = 9.2 Hz, 1H, 13), 8.13 (m, 2H, 8 + 10), 8.09 – 8.03 (m, 2H, 7 + 14), 8.03 (s, 2H, 5), 7.99 (s, 2H, 11 + 12), 7.96 (t, *J* = 7.6 Hz, 1H, 9), 7.84 – 7.78 (m, 3H, 2 + 6), 7.29 (t, *J* = 7.5 Hz, 2H, 3), 4.35 – 4.27 (m, 4H, α + γ), 3.36 (t, *J* = 7.7 Hz, 2H, δ), 2.48 (t, *J* = 7.2 Hz, 2H, ζ), 2.24 – 2.14 (m, 4H, β + ε).

¹³C NMR (126 MHz, chloroform-*d*): δ (ppm) 173.5 (C_q), 167.1 (C_q), 157.2 (C_q), 156.1 (C_q), 149.1 (4), 136.8 (2), 135.7 (C_q), 131.5 (C_q), 132.0 (C_q), 130.0 (C_q), 128.8 (C_q), 127.6 (11), 127.7 + 127.5 (6 + 7), 126.8 (12), 125.9 (9), 125.1 (C_q), 125.1 (C_q), 124.9 + 124.9 + 124.9 (8, 10, 14), 123.9 (3), 123.4 (13), 121.4 (1), 107.4 (5), 64.6 (α) + 61.0 (γ), 33.9 (δ), 32.8 (ζ), 28.5 (β), 26.8 (ε).

LC-MS (acetone): *m/z* (calc.) 578.0 (578.24, [3 + H]⁺), 600.1 (600.23, [3 + Na]⁺).

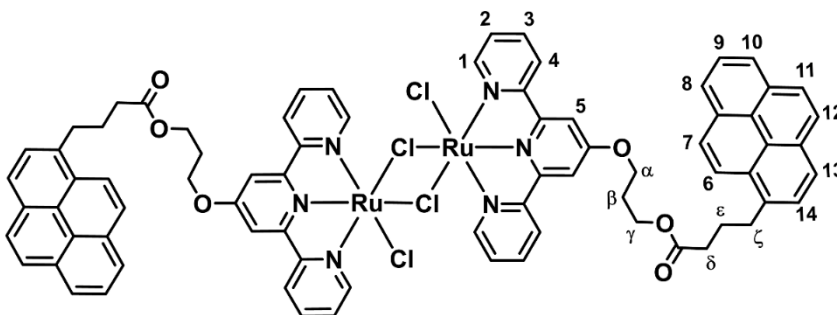


Ruthenium dimer [Ru(3)Cl₂]₂ ([4])

Compound [4] was prepared using an adapted literature procedure.^[4] In a 3-neck round-bottom flask equipped with dropping funnel and nitrogen flow, [Ru₂Cl₂(*p*-cymene)₂] (55 mg, 0.090 mmol) was dissolved in deoxygenated DCM (5 ml). A solution of **3** (100 mg, 0.17 mmol) in deoxygenated DCM (5 ml) was transferred to the dropping funnel, and added to the mixture over 60 min at RT. Next, the reaction mixture was filtered through a Whatman membrane filter (0.2 μm pore size) and [4] was obtained as a purple solid (91 mg, 0.061 mmol, 68%).

¹H NMR (500 MHz, DMSO-*d*₆): δ (ppm) 9.36 (d, *J* = 5.4 Hz, 4H, 4), 8.61 (d, *J* = 8.2 Hz, 4H, 1), 8.40 (d, *J* = 9.3 Hz, 2H, 13), 8.35 (s, 4H, 5), 8.26 (d, *J* = 7.6 Hz, 4H, 8, 10), 8.21 (d, *J* = 4.3 Hz, 2H, 14), 8.19 (d, *J* = 2.8 Hz, 2H, 7), 8.11 (d, *J* = 0.6 Hz, 4H, 11+12), 8.04 (t, *J* = 7.6 Hz, 2H, 9), 7.96 – 7.91 (m, 6H, 2 + 6), 7.49 (t, *J* = 7.3 Hz, 4H, 3), 4.50 (t, *J* = 6.2 Hz, 4H, α), 4.31 (t, *J* = 6.3 Hz, 4H, γ), 3.37 (t, *J* = 8.3 Hz, 4H, δ), 2.52 (m, overlap with DMSO peak, ζ), 2.22 (p, *J* = 6.2 Hz, 4H, β), 2.07 (p, *J* = 7.5 Hz, 4H, ε).

LC-MS (MeOH): *m/z* (calc.) 792.1 (792.63, [(Ru(3)Cl(DMSO))₂]²⁺), 870.1 (870.14, [Ru(3)Cl(DMSO)₂]⁺).



[Ru(biq)(3)Cl]Cl ([5]Cl)

[5]Cl was prepared using a modified literature procedure.^[1] Dimer [4] (90 mg, 0.060 mmol) was dissolved in deoxygenated ethylene glycol (0.75 ml) and 2,2'-biquinoline (33 mg, 0.13 mmol) was added. The mixture was heated up to 180 °C under a nitrogen atmosphere. After 2.5 h, the reaction mixture was diluted with ethanol (1.5 ml), and filtered over Celite to remove insoluble impurities. Ethanol was removed by rotary evaporation and Et₂O was added (25 ml) to the residue, resulting in a precipitate which was washed with Et₂O (3 x 25 ml) and filtered with a Whatman membrane filter (0.2 μm pore size). The obtained dark purple/blue solid was dissolved in methanol (5 ml) and a precipitation was formed by adding diethyl ether (50 ml), which after filtration, washing with ether (3 x 25 ml) and drying yielded [5]Cl (86 mg, 0.085 mmol, 71%).

¹H NMR (500 MHz, chloroform-*d*): δ 9.67 (d, *J* = 8.7 Hz, 1H, 15), 8.86 (d, *J* = 8.8 Hz, 1H, 20), 8.67 (d, *J* = 8.8 Hz, 1H, 19), 8.57 (d, *J* = 8.8 Hz, 1H, 21), 8.52 (d, *J* = 8.1 Hz, 2H, 4), 8.31 (d, *J* = 9.2 Hz, 1H, 14), 8.26 (s, 2H, 5), 8.14-8.10 (m, 2H, 8, 10), 8.10-8.04 (m, 4H, 18, 7, 13, 22), 7.98 (s, 2H, 11, 12), 7.95 (t, *J* = 7.6 Hz, 1H, 9), 7.86 (d, *J* = 7.8 Hz, 1H, 6), 7.81 (t, *J* = 8.7 Hz, 1H, 16), 7.77 (t, *J* = 8.0 Hz, 1H, 17), 7.68 (t, *J* = 7.8 Hz, 2H, 3), 7.63 – 7.57 (m, 3H, 1, 23), 7.30 (t, *J* = 8.0 Hz, 1H, 24), 7.20 (t, *J* = 8.7 Hz, 1H, 25), 7.05 (t, *J* = 6.8 Hz, 2H, 2), 6.79 (d, *J* = 8.9 Hz, 1H, 26), 4.71 (t, *J* = 5.9 Hz, 2H, α), 4.39 (t, *J* = 6.7 Hz, 2H, γ), 3.40 (t, *J* = 7.4 Hz, 2H, δ), 2.53 (t, *J* = 7.4 Hz, 2H, ζ), 2.30 (p, *J* = 6.1 Hz, 2H, β), 2.21 (p, *J* = 7.6 Hz, 2H, ε).

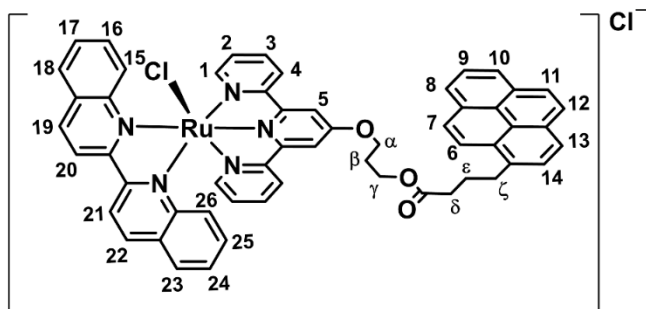
¹³C NMR (126 MHz, chloroform-*d*): δ 173.6 (C_q), 166.2 (C_q), 161.3 (C_q), 159.4 (C_q), 158.8 (C_q), 158.4 (C_q), 152.2 (C_q), 152.1 (1), 151.5 (C_q), 137.8 (19), 137.2 (3), 136.1 (22), 135.8 (C_q), 131.4 (C_q), 131.1 (16), 131.0 (25), 130.9 (C_q), 130.9 (15), 130.0 (C_q), 129.4 (17), 129.2 (23), 128.9 (C_q), 128.8 (C_q), 128.5 (18+24), 128.1 (C_q), 127.5 (7), 127.4 (6), 126.7 (11 + 12), 126.6 (2), 125.9 (9), 125.1 (C_q), 125.0 (C_q), 124.9 - 124.8 (8, 10, 13), 124.5 (4), 124.0 (26), 123.4 (14), 120.6 (21), 120.3 (22), 110.9 (5), 67.5 (α), 61.1 (γ), 33.9 (δ), 32.8 (ζ), 28.4 (β), 26.9 (ε).

LC-MS (MeOH): *m/z* (calc.) 970.3 (970.21, [5]⁺), 488.2 (488.14, [5 - Cl + MeCN]²⁺), 700.2 (700.11, [5 - 1-pyrenebutyric acid]⁺), 741.2 (741.13, [5 - 1-pyrenebutyric acid + MeCN]⁺).

HRMS (MeOH): *m/z* (calc.) 970.20924 (970.20979, [5]⁺), 467.62056 (467.62025, [5 - Cl]²⁺), 488.13395 (488.13359, [5 - Cl + MeCN]²⁺).

UV-vis: $\lambda_{max} = 577 \text{ nm}$, $\epsilon = 9400 \pm 500 \text{ M}^{-1}\text{cm}^{-1}$ in pure methanol.

Elem. Anal: Calcd (%). for [5]Cl: C, 66.86; H, 4.31; N, 6.96. Found: C, 66.81; H, 4.43; N, 6.92.



[Ru(biq)(3)(STF-31)](PF₆)₂ ([1](PF₆)₂)

[1](PF₆)₂ was prepared according to a modified literature procedure.^[1] [5]Cl (103 mg, 0.10 mmol) was dissolved in deoxygenated acetone/water 1:1 (15 ml) and STF-31 (83 mg, 0.20 mmol) was added. AgPF₆ was dissolved in deoxygenated acetone/water 1:1 (62 mg/ml) and 1.0 ml of this solution was added (0.25 mmol) to the reaction mixture. The mixture was heated to 50 °C under nitrogen, in the dark. After 3 h, the reaction mixture was filtered over Celite; the filter was flushed with acetone (3x 25 ml) to collect the product. Acetone was evaporated by rotary evaporation and the remaining water was decanted. The purple solid on the flask wall was washed with milliQ water (3 x 25 ml) and dried *in vacuo*. The crude mixture was separated on a silica column (acetone, then increase to acetone + 1% KPF₆ (sat.) with steps of + 0.25% KPF₆). The purple band with R_f = 0.31 in acetone + 2% KPF₆ (sat.) was collected and the solvent was rotary evaporated, then the solid was washed with MilliQ (3 x 25 ml) and dried *in vacuo* to obtain [1](PF₆)₂ as a dark purple solid (134 mg, 0.081 mmol, 81%).

¹H NMR (500 MHz, acetone-*d*₆): δ 9.56 (s, 1H, N1), 9.24 (d, $J = 9.0 \text{ Hz}$, 1H, 20), 9.11 (d, $J = 9.0 \text{ Hz}$, 1H, 19), 9.00 (d, $J = 8.9 \text{ Hz}$, 1H, 21), 8.98 (d, $J = 2.3 \text{ Hz}$, 1H, 27), 8.94 (d, $J = 8.1 \text{ Hz}$, 1H, 4A), 8.78 (s, 1H, 5A), 8.52 (m, 2H, 22 + 4B), 8.44 (s, 1H, 5B), 8.42 (d, $J = 8.2 \text{ Hz}$, 1H, 15), 8.38-8.33 (m, 2H, 14 + 1A), 8.21 (d, $J = 7.7 \text{ Hz}$, 1H, 10), 8.17 (t, $J = 7.7 \text{ Hz}$, 1H, 3A), 8.16 – 8.13 (m, 2H, 8 + 1B), 8.11 (d, $J = 9.3 \text{ Hz}$, 1H, 13), 8.07 (d, $J = 7.7 \text{ Hz}$, 1H, 7), 8.06 (d, $J = 8.7 \text{ Hz}$, 1H, 11), 8.03- 7.96 (m, 3H, 12, 9, 3B), 7.86 (m, 2H, 23, 6), 7.81 – 7.74 (m, 3H, 33, 16), 7.73 – 7.67 (m, 3H, 31, 28), 7.62 (d, $J = 5.6 \text{ Hz}$, 1H, 30), 7.58 (d, $J = 8.8 \text{ Hz}$, 2H, 34), 7.55 (7, $J = 6.6 \text{ Hz}$, 1H, 2A), 7.51 (m, 2H, 18 + 2B), 7.47 – 7.41 (m, 3H, 24 + 32), 7.41 – 7.35 (m, 2H, 17, 25), 7.07 – 6.99 (m, 2H, 26 + N2), 6.97 (t, $J = 7.1 \text{ Hz}$, 1H, 29), 4.70 (t, $J = 6.2 \text{ Hz}$, 2H, α), 4.39 (t, $J = 6.2 \text{ Hz}$, 2H, γ), 4.19 (d, $J = 6.6 \text{ Hz}$, 2H, η), 3.38 (t, $J = 7.6 \text{ Hz}$, 2H, δ), 2.52 (t, $J = 7.2 \text{ Hz}$, 2H, ζ), 2.35 (p, $J = 6.2 \text{ Hz}$, 2H, β), 2.13 (p, $J = 8.5 \text{ Hz}$, 2H, ϵ), 1.32 (s, 9H, θ).

¹³C NMR (126 MHz, acetone-*d*₆): δ 173.7 (C_q), 168.0 (C_q), 166.3 (C_q), 161.6 (C_q), 160.6 (C_q), 159.9 (C_q), 159.4 (C_q), 159.2 (C_q), 156.8 (C_q), 155.3 (1A), 153.7 (1B), 151.9 (C_q), 151.1 (C_q), 148.5 (30), 143.8 (C_q), 142.9 (27), 140.1 (19), 139.8 (3B), 139.6 (3A), 139.4 (22), 139.1 (C_q), 138.7 (C_q), 137.1 (C_q), 133.5 (C_q), 132.4 (25), 132.3 (C_q), 132.0 (17), 131.8 (C_q), 131.2 (C_q), 130.9 (15), 130.8 (C_q), 130.4 (23), 130.0 (16), 129.6 (24+2B), 129.5 (C_q), 129.4 (2A), 129.3 (28), 128.7 (32), 128.5 (31), 128.4 (6), 128.4 (12), 128.2 (13), 127.6 (33), 127.6 (18), 127.6 (11), 126.9 (9), 126.9 (34), 126.6 (4A), 126.6 (29), 125.9 (10), 125.8 (7), 125.7 (8), 125.7 (C_q), 125.4

Appendix – Chapter 7

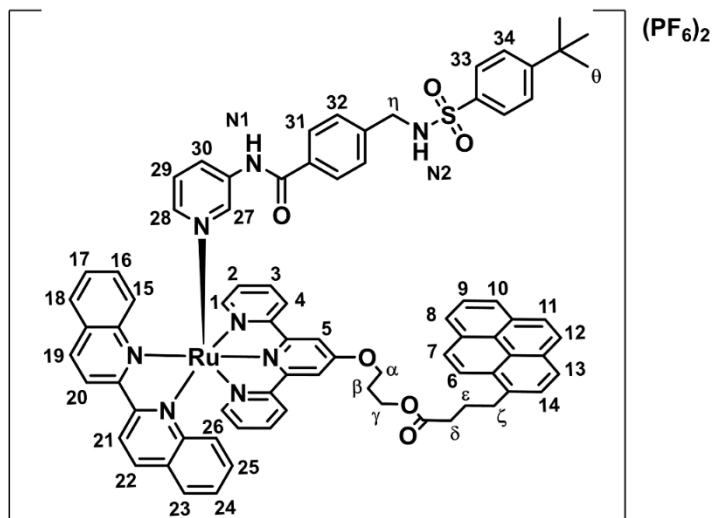
(4B), 124.8 (26), 124.3 (14), 122.3 (20), 122.1 (21), 113.3 (5A), 112.6 (5B), 67.9 (α), 61.4 (γ), 47.1 (η), 34.2 (ζ), 33.2 (δ), 31.3 (θ), 29.1 (β), 27.8 (ϵ).

LC-MS (MeOH): m/z (calc.) 679.1 (679.3, [1]²⁺), 1357.6 (1357.6, [1-H]⁺), 1503.6 (1503.6, [1+PF₆]⁺).

HRMS (MeOH): m/z (calc.) 679.20118 (679.20163, [1]²⁺).

UV-vis: λ_{max} = 537 nm, ϵ = 10700 \pm 500 M⁻¹cm⁻¹ in pure methanol.

Elem. Anal: Calcd (%). for [1](PF₆)₂: C, 57.56; H, 4.16; N, 6.80. Found: C, 57.06; H, 4.22; N, 6.73.



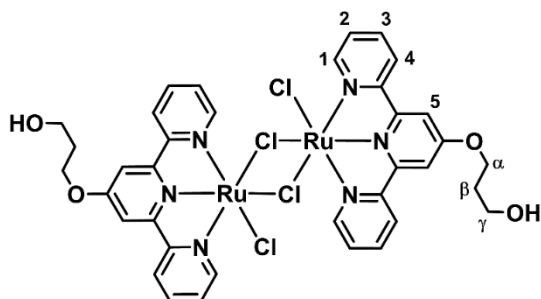
Ruthenium dimer [Ru(2)Cl₂]₂ ([6])

Compound [6] was prepared according to a modified literature procedure.^[4] In a 3-neck round bottom flask equipped with drop funnel and nitrogen flow, [Ru₂Cl₂(*p*-cymene)] (431 mg, 0.70 mmol) was dissolved in deoxygenated DCM (25 ml). A solution of 2 (430 mg, 1.4 mmol) in deoxygenated DCM (25 ml) was transferred to the drop funnel, and added to the mixture over 60 minutes at RT. Once a dark purple color was obtained, the reaction mixture was filtered through a membrane filter and [6] was obtained as a purple solid (620 mg, 0.65 mmol, 92%).

¹H NMR (400 MHz, DMSO-*d*₆): δ (ppm) 9.35 (d, J = 5.4 Hz, 4H, 4), 8.63 (d, J = 6.1 Hz, 4H, 1), 8.35 (s, 4H, 5), 7.96 (t, J = 7.8 Hz, 4H, 2), 7.49 (t, J = 7.3 Hz, 4H, 3), 4.73 (t, J = 5.1 Hz, 2H, OH), 4.50 (t, J = 6.3 Hz, 4H, α), 3.67 (q, J = 5.9 Hz, 4H, γ), 2.03 (p, J = 6.2 Hz, 4H, β).

¹³C NMR (101 MHz, DMSO-*d*₆): δ (ppm) 166.4 (C_q), 159.0 (C_q), 157.6 (C_q), 156.0 (4), 136.7 (2), 126.3 (3), 123.3 (1), 108.8 (5), 66.7 (α), 57.1 (γ), 31.9 (β).

LCMS (MeOH): m/z (calc.) 599.9 (600.03 [Ru(2)Cl(DMSO)₂]⁺).



[Ru(biq)(2)Cl]Cl ([7]Cl)

[7]Cl was prepared according to a modified literature procedure.^[1] Dimer [6] (540 mg, 0.56 mmol) was dissolved in deoxygenated ethylene glycol (7 ml) and 2,2'-biquinoline (292 mg, 1.14 mmol) was added. The mixture was heated up to 180 °C under a nitrogen atmosphere. After 2.5 h, the reaction mixture was diluted with ethanol (10 ml), and filtered over Celite to remove insoluble impurities. Ethanol was removed by rotary evaporation and the crude was purified over an alumina oxide column (DCM, gradual increase to 92:8 DCM/MeOH) to remove ethylene glycol. The obtained dark purple/blue solid was dried *in vacuo* to yield [7]Cl (250 mg, 0.34 mmol, 30%).

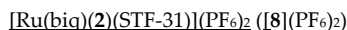
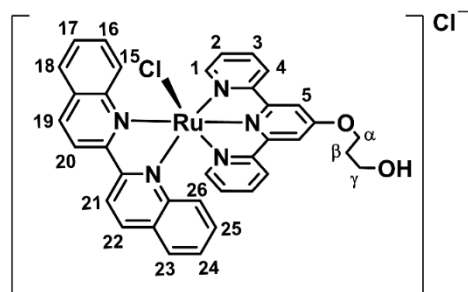
¹H NMR (400 MHz, methanol-*d*₄): δ (ppm) 9.60 (d, *J* = 0.9 Hz, 1H, 15), 8.91 (d, *J* = 8.9 Hz, 1H, 20), 8.83 (d, *J* = 8.3 Hz, 1H, 19), 8.62 (d, *J* = 8.8 Hz, 1H, 21), 8.45 (d, *J* = 8.1 Hz, 2H, 4), 8.28 (s, 2H, 5), 8.25 (d, 8.2 Hz, 1H, 18), 8.19 (d, 1H, 22), 7.89 – 7.74 (m, 7H, 3, 16, 16, 23, 1), 7.43 (t, *J* = 8.1 Hz, 1H, 24), 7.30 – 7.23 (m, 3H, 25, 2), 6.89 (d, *J* = 8.9 Hz, 1H, 26), 4.56 (t, *J* = 6.2 Hz, 2H, α), 3.88 (t, *J* = 6.1 Hz, 2H, γ), 2.19 (p, *J* = 6.2 Hz, 2H, β).

¹³C NMR (101 MHz, methanol-*d*₄): δ 168.1 (C_q), 163.4 (C_q), 160.9 (C_q), 160.5 (C_q), 160.3 (C_q), 154.0 (1), 153.4 (C_q), 152.7 (C_q), 139.6 (19), 138.7 (3), 137.3 (22), 132.0 (16), 131.7 (25), 130.6 (C_q), 130.4 (23), 130.4 (17), 129.9 (18), 129.7 (C_q), 129.6 (24), 128.2 (2), 125.1 (4, 26), 121.7 (21, 22), 111.9 (5), 70.5 (α), 62.3 (γ), 32.7 (β).

LCMS (MeOH): *m/z* (calc.) 700.7 (700.1, [7]⁺), 352.2 (353.1, [7 – Cl + MeCN]²⁺).

HRMS (MeOH): *m/z* (calc.) 700.10414 (700.10485, [7]⁺), 353.08095 (353.08105, [7 – Cl + MeCN]²⁺), 332.56763 (332.56774, [7 – Cl]²⁺).

UV-vis: λ_{max} = 577 nm, ε = 9200 ± 200 M⁻¹·cm⁻¹ in pure methanol.



[8](PF₆)₂ was prepared according to a modified literature procedure.^[1] [7]Cl (50 mg, 0.07 mmol) was dissolved in deoxygenated acetone/water 1:1 (7 ml) and STF-31 (43 mg, 0.14 mmol) was added. AgPF₆ was dissolved in deoxygenated acetone/water 1:1 (212 mg/ml) and 100 μL of this solution (0.08 mmol AgPF₆) was added to the reaction mixture. The mixture was heated to 50 °C under nitrogen, in the dark. After 3 h, the reaction mixture was filtered over Celite; the filter was flushed with acetone (3 x 25 ml) to collect the product. Acetone was rotary evaporated and the remaining water was decanted. The purple solid on the flask wall was washed with MilliQ water (3 x 25 ml) and dried *in vacuo*. The crude was separated on a silica column (acetone, then increase to acetone + 0.5% KPF₆ (sat.) with steps of + 0.25% KPF₆). The purple band with R_f = 0.16 in acetone + 2% KPF₆ (sat.) was collected and the solvent was evaporated, then washed with MilliQ (3 x 25 ml) and dried *in vacuo* to obtain [8](PF₆)₂ as a dark purple solid (4 mg, 0.003 mmol, 4%).

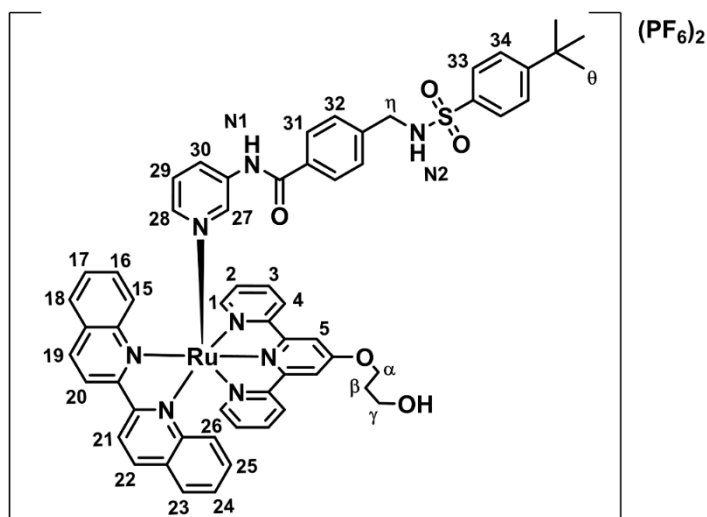
¹H NMR (500 MHz, acetone-*d*₆) δ 9.65 (s, 1H, N1), 9.25 (d, *J* = 8.9 Hz, 1H, 20), 9.12 (d, *J* = 8.8 Hz, 1H, 19), 9.05 – 8.97 (m, 3H, 21, 27, 4A), 8.79 (s, 1H, 5A), 8.61-8.56 (m, 2H, 22, 4B), 8.46 – 8.40 (m, 2H, 5B, 15), 8.37 (d, *J* = 5.6 Hz, 1H, 1A), 8.23 (t, *J* = 7.8 Hz, 1H, 3A), 8.16 (d, *J* = 5.5 Hz, 1H, 1B), 8.06 (t, *J* = 7.9 Hz, 1H, 3B), 7.99 (d, *J* = 8.1 Hz, 1H, 23), 7.82 – 7.76 (m, 4H, 16, 28, 33), 7.73 (d, *J* = 8.1 Hz, 2H, 31), 7.66 (d, *J* = 5.7 Hz, 1H, 30), 7.63 – 7.50 (m, 5H, 34, 24, 18, 2A, 2B), 7.50 – 7.40 (m, 4H, 25, 32, 17), 7.11 – 7.01 (m, 3H, 26, N2, 29), 4.69 (t, *J* = 6.4 Hz, 2H, α), 4.20 (d, *J* = 6.6 Hz, 2H, η), 3.88 (t, *J* = 5.0 Hz, 1H, OH), 3.83 (q, *J* = 5.6 Hz, 2H, γ), 2.18 (p, *J* = 6.3 Hz, 2H, β), 1.34 (s, 9H, θ).

¹³C NMR (126 MHz, acetone-*d*₆) δ 168.2 (C_q), 166.4 (C_q), 161.6 (C_q), 160.6 (C_q), 156.8 (C_q), 155.4 (1A), 153.7 (1B), 152.0 (C_q), 151.1 (C_q), 148.6 (30), 143.8 (C_q), 142.9 (27), 140.0 (19), 139.8 (3A), 139.6 (3B), 139.4 (22), 139.1 (C_q), 138.7 (C_q), 133.5 (C_q), 132.5 (17), 132.0 (25), 131.1 (C_q), 130.9 (15), 130.5 (23), 130.0 (16), 129.7 (28), 129.6 (C_q), 129.6 (2A + 2B), 129.3 (24), 128.7 (32), 128.5 (31), 127.6 (33+18), 126.9 (34), 126.7 (4A) 126.6 (29), 125.3 (4B), 124.9 (26), 122.3 (20), 122.1 (21), 113.2 (5A), 112.6 (5B), 68.3 (α), 58.5 (γ), 47.1 (η), 32.8 (θ).

LC-MS (MeOH): *m/z* (calc.) 544.0 (544.1, [8]²⁺), 1087.6 (1087.3, [8-H]⁺), 1233.6 (1233.2, [8+PF₆]⁺).

HRMS (MeOH): *m/z* (calc.) 544.14840 (544.14895, [8]²⁺).

UV-vis: λ_{max} = 538 nm, ε = 9000 ± 600 M⁻¹cm⁻¹ in pure methanol.



Photochemistry

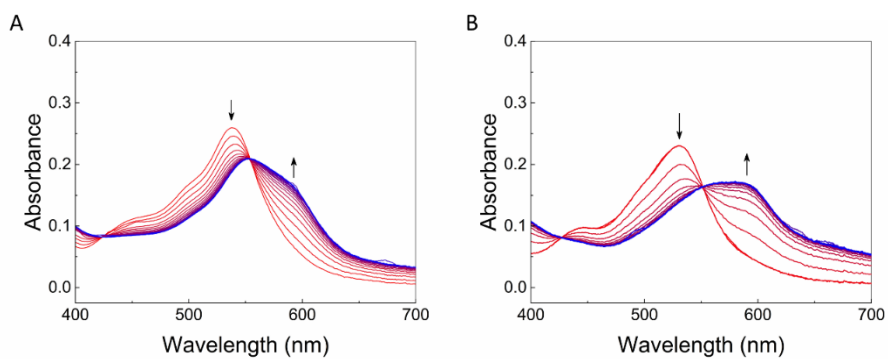


Figure S7.1: Evolution of the absorption spectrum of a solution of **[8](PF₆)₂** and **[9](PF₆)₂** (respectively A and B, 25 μ M) in methanol upon irradiation with 530 nm light (photon flux = 1.36×10^{-7} mol·s⁻¹). Spectra shown between $t = 0$ minutes (red spectrum) and $t = 10$ minutes (blue spectrum). Spectra were recorded under air, every 30 seconds. Temperature: 298 K.

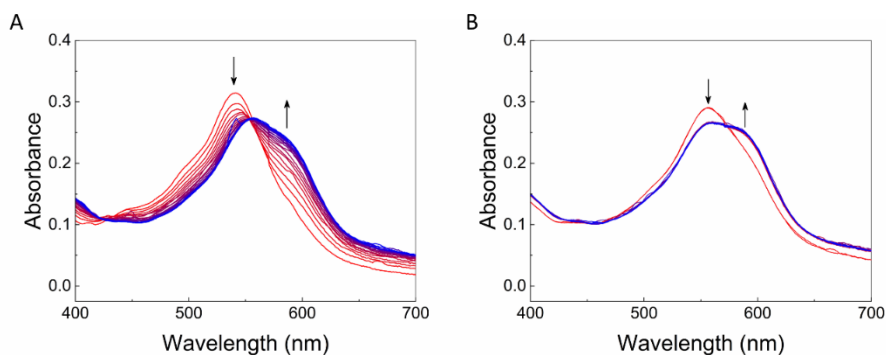


Figure S7.2: Evolution of absorbance for a solution of [1](PF₆)₂ (25 μM) in methanol/water (95:5) upon 1st (A) and 2nd (B) irradiation with 530 nm light (photon flux = 1.36 × 10⁻⁷ mol·s⁻¹). Spectra shown between t = 0 minutes (red spectrum) and t = 10 minutes (blue spectrum). Spectra were recorded under air, every 30 seconds. Temperature: 298 K.

2D luminescence plots

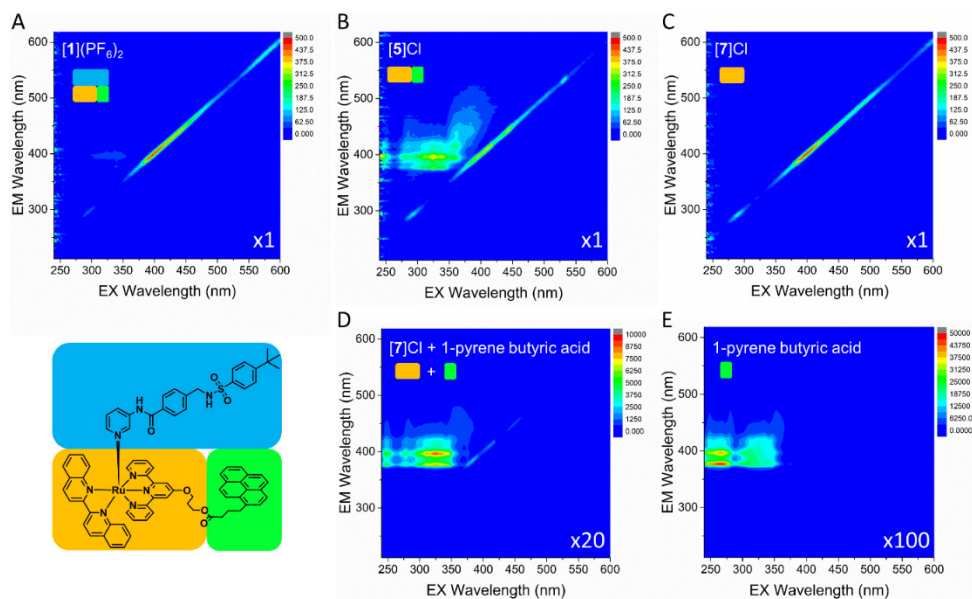


Figure S7.3: 2D Luminescence plots of [1](PF₆)₂, [5]Cl, [7]Cl, [7]Cl + 1-pyrene butyric acid and 1-pyrene butyric acid (respectively A-E, 50 μM) in methanol. Compounds are schematically represented by the components of the intact complex as orange, green and blue boxes. Excitation (EX) wavelength is plotted on the x-axis and emission (EM) wavelength on the y-axis. Rainbow color scale shows relative fluorescence intensity, with red for high emission and blue for no emission. Scale multiplier is indicated by the number in the bottom right of each panel. Detections at EX = EM are due to scattering of the excitation laser by the solutions.

Förster distance and FRET efficiency

The Förster distance R_0 in Å, at which 50% of the fluorescence of the donor (here: 1-pyrenebutyric acid) is quenched by the acceptor (here: [8](PF₆)₂) was calculated using Eq. 1:^[5]

$$R_0 = 9.78 \times 10^3 (k^2 n^{-4} \varphi_D J_{DA})^{1/6} \quad (\text{Eq. 1})$$

Where k^2 is the orientation factor ($k^2 = 2/3$), n is the refractive index of the solution ($n = 1.33$ for methanol), and φ_D is the emission quantum yield from the donor ($\varphi_D = 0.067$ for 1-pyrenebutyric acid in methanol^[6]). Using Eq. 2, we calculated J_{DA} in M⁻¹cm³, *i.e.* the spectral overlap of $F_D(\lambda)$, which is the emission intensity of the donor at wavelength λ , with the total area of the emission spectrum normalized to 1 (dimensionless), and ε_A in M⁻¹cm⁻¹, which is the extinction coefficient of the acceptor, multiplied by λ^4 (with λ in cm). For a plot of J_{DA} vs. λ , see Figure S7.4A.

$$J_{DA} = \int F_D(\lambda) \varepsilon_A(\lambda) \lambda^4 d\lambda \quad (\text{Eq. 2})$$

For J_{DA} we found a value of 1.61×10^{-14} M⁻¹cm³, giving $R_0 = 24.4$ Å for the pair 1-pyrenebutyric acid/[8](PF₆)₂. We calculated the FRET efficiency φ_{FRET} using Eq. 3:^[5]

$$\varphi_{FRET} = 1/(1 + (r/R_0)^6) \quad (\text{Eq. 3})$$

Using $r = 20$ Å (see Figure S7.4B), we found that $\varphi_{FRET} = 0.77$ for the donor/acceptor pair 1-pyrenebutyric acid/[8](PF₆)₂ in methanol.

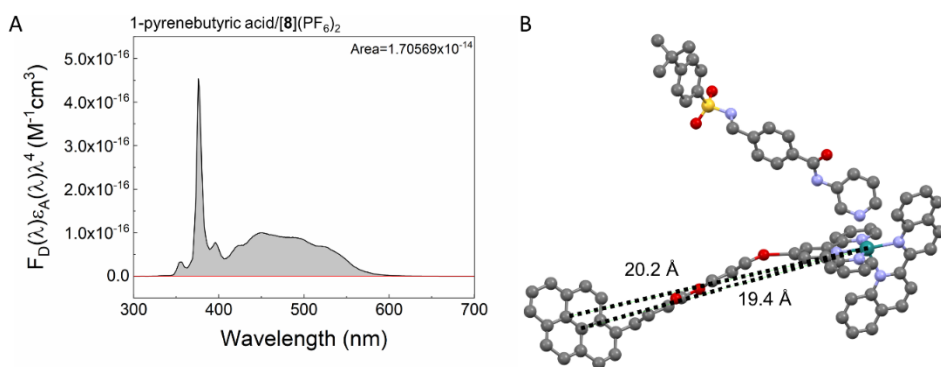


Figure S7.4: A) Spectral overlap ($F_D(\lambda)\varepsilon_A(\lambda)\lambda^4$) of the emission intensity, total area normalized to 1, ($F_D(\lambda)$) of the donor 1-pyrenebutyric acid, and the extinction coefficient of the acceptor [7]Cl ε_A , multiplied by λ^4 , vs. the wavelength (λ). B) Yasara simulation of [1]²⁺, the Ru-pyrene distance r (from the ruthenium ion to the center carbon atoms of the pyrene moiety) is indicated by the dashed lines; r was found to be 20 Å.

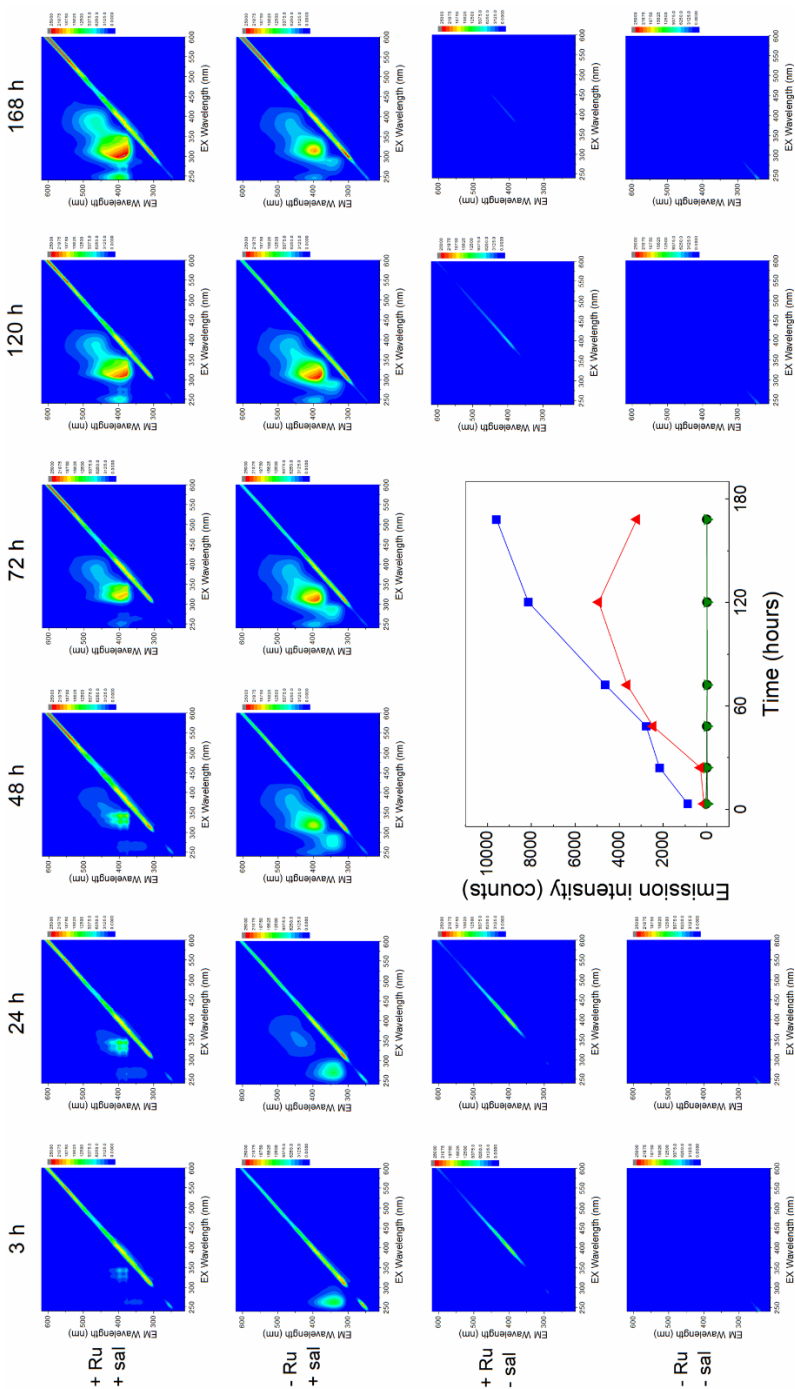


Figure S7.5: 2D emission spectra for [5]Cl degradation by saliva. Plus (+) or minus (–) on the far left indicates if the complex (Ru) and/or saliva (sal) are present in the sample ($[Ru]_{stock} = 1 \text{ mM}$, $Ru/saliva = 1:19$, when Ru or sal were not in the sample, they were replaced by MilliQ water). Color scale is the same for each panel (blue to red: 0 to 25000). Inset: emission intensity vs. time; excited at 354 nm, for +Ru/+sal (blue), –Ru/+sal (red), +Ru/–sal (black) and –Ru/–sal (green). Samples were incubated at 37 °C under stirring between measurements. Samples were centrifuged before measuring, emission was measured of the supernatant.

References

- [1] L. N. Lameijer, D. Ernst, S. L. Hopkins, M. S. Meijer, S. H. C. Askes, S. E. Le Dévédec, S. Bonnet, *Angew. Chem., Int. Ed.* **2017**, *56*, 11549.
- [2] U. Sampath, W. C. Putnam, T. A. Osiek, S. Touami, J. Xie, D. Cohen, A. Cagnolini, P. Droege, D. Klug, C. L. Barnes, A. Modak, J. K. Bashkin, S. S. Jurisson, *J. Chem. Soc., Dalton Trans.* **1999**, 2049.
- [3] M. A. Furrer, F. Schmitt, M. Wiederkehr, L. Juillerat-Jeanerret, B. Therrien, *Dalton Trans.* **2012**, *41*, 7201.
- [4] D. C. Marelius, S. Bhagan, D. J. Charboneau, K. M. Schroeder, J. M. Kamdar, A. R. McGettigan, B. J. Freeman, C. E. Moore, A. L. Rheingold, A. L. Cooksy, D. K. Smith, J. J. Paul, E. T. Papish, D. B. Grotjahn, *Eur. J. Inorg. Chem.* **2014**, *2014*, 676.
- [5] A. Bahreman, J.-A. Cuello-Garibo, S. Bonnet, *Dalton Trans.* **2014**, *43*, 4494.
- [6] Y. Matsushita, M. Tsukiori, T. Suzuki, I. Moriguchi, *J. Pharm. Sci.* **1986**, *75*, 193.

Samenvatting, conclusies en vooruitzichten

Moleculair en Nano-Designs met IJzer, Ruthenium en
Koolstof: Hybride Structuren voor Sensoren

Samenvatting

Algemene inleiding (H 1)

Meten en detecteren ligt aan de basis van de moderne gezondheidszorg en hierdoor is er een grote vraag naar steeds gevoeliger sensoren. Grafeen is een 2D halfgeleidermateriaal bestaande uit koolstofatomen en is zeer geschikt als basis voor zulke sensoren vanwege zijn elektronische eigenschappen. Echter, voor sensoren gebaseerd op grafeen moet de grafeenlaag gefunctionaliseerd worden met moleculen die hun omgeving aanvoelen. De eigenschappen van deze moleculen veranderen als ze reageren met een bindingspartner en deze veranderingen worden gedetecteerd door grafeen, dat gevoelig is voor veranderende dipoolmomenten nabij het oppervlak. Als gevolg hiervan veranderen de elektronische eigenschappen van grafeen, wat we eenvoudig kunnen zien aan de elektrische weerstand.

Metaalcomplexen kunnen deze rol van functioneel molecuul op een sensor vervullen. Door de ligandomgeving van het metaalion te veranderen en door de toegankelijkheid van meerdere ladingstoestanden van het metaalion zelf kunnen de eigenschappen van metaalcomplexen aangepast worden. Hierdoor kunnen metaalcomplexen zeer divers chemisch gedrag vertonen, wat ze interessant maakt als functioneel molecuul voor sensoren. IJzer(II) complexen kunnen bijvoorbeeld spinovergangen ondergaan, wat een herschikking van elektronen is in de d^6 -configuratie, van een hoogspintoestand naar een laagspintoestand en vice versa. Wanneer deze herschikking plaatsvindt, veranderen de chemische en fysische eigenschappen van zowel het molecuul als het bulkmateriaal. Dit moleculaire spinschakeleffect is technologisch interessant, maar het technologisch implementeren van deze materialen is lastig, omdat ze niet elektrisch geleidend zijn. Met strategieën uit de nanotechnologie zijn er methoden gevonden om het spinschakelgedrag te lezen op de nanoschaal. Echter, dit spinschakelgedrag wordt aangetast door het verkleinen van deze materialen naar de nanoschaal.

Rutheniumpolypyridylcomplexen kunnen veranderen onder invloed van licht, wat bijvoorbeeld kan resulteren in isomerisatie of liganduitwisseling: dit is ook een vorm van moleculair schakelen. Bovendien kunnen zij interacties aangaan met bijvoorbeeld DNA. Deze interacties kunnen worden gebruikt voor *bio-imaging* en detectie, aangezien de fotofysische eigenschappen van de complexen veranderen als zij aan een bindingspartner binden: ze kunnen bijvoorbeeld licht

uit gaan stralen. Het binden van rutheniumcomplexen aan nucleotiden kan nuttig zijn om detectie te verbeteren, bijvoorbeeld door specifieke nucleotiden van een label te voorzien. Rutheniumcomplexen zijn daarom interessant als moleculaire sonde en als label voor detectie.

Contactloze spinovergangsdetectie door middel van chemo-elektrisch gaten van grafeen (H 2)

In hoofdstuk 2 is beschreven hoe grafeen spinovergangen in een elektrisch isolerend materiaal met spinovergangseigenschappen kan detecteren. Hiervoor zijn grafeen-veldeffecttransistoren (GVETs) gefabriceerd op eenkristallen van het spinovergangskomplex $[\text{Fe}(\text{bapbpy})(\text{NCS})_2]$, waarbij het grafeen en het eenkristal van elkaar werden gescheiden door een isolerende polymeerlaag. Wanneer de GVETs werden afgekoeld of opgewarmd om de spinovergang op te laten treden, waren deze spinovergangen goed te zien door een sterke kleurverandering van het kristal. Tegelijkertijd met de kleurverandering veranderde de weerstand abrupt. De faseovergangen in het spinovergangskristal konden dus elektrisch worden waargenomen door middel van grafeen-veldeffecttransistoren.

De dikte van de polymeerlaag bleek een cruciale rol te spelen in het detectiemechanisme van spinovergangen door de GVETs, dat twee effecten omvat. Ten eerste speelden mechanische effecten (uitzetting en krimp van het kristal tijdens de faseovergangen in het spinovergangskristal) een kleine rol in de weerstandsveranderingen van grafeen. Deze mechanische effecten waren vooral sterk tijdens de allereerste faseovergang, zo bleek uit een analyse van de 2D piek van grafeen met behulp van Raman-spectroscopie. Dit kwam overeen met de uitzonderlijk grote weerstandsverandering tijdens de allereerste faseovergang. De mechanische effecten werden voor een groot deel opgevangen door de dikste polymeerlaag (0.5 μm).

Ten tweede speelde de elektrostatische potentiaal van het spinovergangskristal een grote rol in de weerstandsveranderingen tijdens faseovergangen. De moleculen zijn sterk geordend in het eenkristal, en hun dipolen zijn allemaal hetzelfde geïntendeerd, wat het kristal een elektrostatische potentiaal geeft. Wanneer een spinfaseovergang optreedt, veranderen al deze dipolen tegelijkertijd binnen een aantal seconden, en daarmee ook de elektrostatische potentiaal van het kristal. Het grafeen, dat dichtbij het spinovergangskristal is, voelt dat de elektrostatische potentiaal is veranderd. Dit is een nieuwe manier om

te detecteren met grafeen, die we “chemo-elektrisch gaten” hebben genoemd. Dit chemo-elektrisch gaten kan worden gebruikt voor de integratie van moleculaire materialen (materialen waarvan de eigenschappen veranderen door moleculaire veranderingen) in bijvoorbeeld sensoren en apparaten voor dataopslag.

Dunne films van het spinovergangskomplex [Fe(bapbpy)(NCS)₂] die selectief gegroeid zijn op grafeen (H 3)

Vervolgend op hoofdstuk 2 wordt in hoofdstuk 3 beschreven hoe het spinovergangsmateriaal [Fe(bapbpy)(NCS)₂] kan worden verkleind naar dunne films. We zagen dat een dunne film van dit metaalcomplex neersloeg wanneer methanol langzaam diffundeerde in een oplossing van dit complex. De dunne films groeiden met een sterke voorkeur op grafeen op siliciumwafers ten opzichte van schone siliciumwafers met een oppervlak van SiO₂, op zowel centimeter- als micrometerschaal. De dunne films groeiden met een gelijkmatige dikte, die met enkele nanometers per dag toenam. Raman-spectroscopie liet zien dat vooral de relatief dikke films (meer dan 20 nm) een grote chemische gelijkenis vertoonden met het bulkmateriaal. Bovendien lieten Raman en XRD zien dat de films amorf zijn. Ten slotte zagen we met XPS dat een deel van de Fe(II) ionen in de films geoxideerd waren naar Fe(III); de mate van oxidatie leek af te hangen van de manier van zuurstofbescherming tijdens het vormen van de film.

Het meten van de spinovergangseigenschappen van deze films was uitdagend. Monsters werden geanalyseerd met SQUID magnetometrie, maar het weinige materiaal van de film en het sterke achtergrondsignaal van de siliciumwafer zelf maakte het interpreteren van de resultaten lastig. Voor een van de vier monster konden we een omkeerbare overgang waarnemen, wat lijkt te betekenen dat deze film spinovergangsactief was; we kunnen hierover echter geen harde conclusies trekken. In hoeverre de oxidatie van de ijzerionen in de dunne films de spinovergangseigenschappen van de dunne films beïnvloedt blijft een belangrijke onderzoeksvraag.

De dunne films konden ook groeien op grafeen-veldeffecttransistoren (GVETs), met opnieuw een voorkeur voor het groeien op het grafeen. Echter, alleen hele dunne films konden worden verkregen, omdat de goudelektrodes van de GVET werden geëet door de dunnefilmoplossing. Hierdoor konden de GVETs slechts een gelimiteerde tijd aan de dunnefilmoplossing worden blootgesteld. Ondanks deze beperking konden functionele GVETs worden gemaakt. Deze GVETs

werden afgekoeld naar 150 K en weer opgewarmd naar kamertemperatuur om spinovergangen te initiëren. Er werden echter geen weerstandsveranderingen waargenomen die kunnen duiden op een spinovergang. Al met al hebben we geen sterke bewijzen gevonden dat de films spinovergangsactief zijn.

Grafeen met een polymeercoating als sensoren: simultane detectie levert de chemische vingerafdrukken op van chemische dampen (H 4)

In hoofdstuk 4 beschrijven we een sensor gebaseerd op grafeen die niet gefunctionaliseerd was met een molecuul of materiaal dat een specifieke interactie aangaat met een bindingspartner. Deze sensoren, gefabriceerd op standaard siliciumwafers en simpelweg gefunctionaliseerd met het overdrachtspolymeer poly-(methylmethacrylaat) (PMMA, 300 nm), werden blootgesteld aan 15 verschillende chemische dampen die met een stikstofstroom naar de meetkamer werden gedragen. Weerstandsveranderingen werden waargenomen voor de meeste dampen en waren zeer reproduceerbaar. De piekintensiteit was verschillend voor de verschillende dampen, wat laat zien dat de sensoren deze dampen konden onderscheiden.

Het vermogen om te onderscheiden tussen dampen werd verder bestudeerd door de respons van de sensoren op mengsels te bepalen. Door de respons te meten van de sensoren wanneer zij werden blootgesteld aan mengsels van methanol in diethylether, waarvan de concentratie van methanol varieerde, konden we inschatten dat de detectielimiet van de PMMA-gecoate sensoren voor methanol 6 ppm was. Bovendien konden de sensoren gebruikt worden om de componenten van binaire mengsels te kwantificeren; er werden goede lineaire relaties gevonden tussen de piekintensiteit en het percentage methanol in ethanol, en tussen de piekbreedte van de respons en het percentage water in ethanol.

Deze resultaten lieten de potentie zien van de PMMA-gecoate sensoren, echter de sensoren waren weinig selectief en konden daarom niet worden gebruikt voor herkenning van specifieke verbindingen. Om de sensoren alsnog te kunnen gebruiken voor herkenning, hebben we sensorreeksen gemaakt, elk gecoat met een ander overdrachtspolymeer (PMMA, Nafion® 117, en cellulose acetaat butyraat (CAB)). De sensorreeks werd in een kleine buis geplaatst die kon worden geïntegreerd in een gaschromatografieopstelling, wat het mogelijk maakte om automatische injectie te gebruiken voor continue bemonstering. Op deze manier werd de chemische vingerafdruk bepaald van in totaal 42 verschillende

chemische dampen. Deze vingerafdruk was het resultaat van de combinatie van de respons van de drie verschillende sensoren, die tegelijkertijd aan dezelfde damp waren blootgesteld. Met behulp van algoritmes konden de data van de chemische vingerafdruksensoren worden gebruikt voor klassificatie en identificatie van de dampen waarbij een nauwkeurigheid van 92% werd bereikt. De chemische vingerafdrukken van de sensorreeksen konden dus worden gebruikt voor stofherkenning met een hoge betrouwbaarheid.

Een monolaag van grafeen op papier als monitoringsplatform voor een lichtreactie (H 5)

In hoofdstuk 5 wordt een nieuwe funderingslaag (substraat) voor sensoren op basis van grafeen geïntroduceerd: alledaags papier. Het gebruik van papier als substraat heeft als voordeel dat vloeibare monsters (waterige oplossingen) in het papier kunnen worden opgenomen, waardoor de analyten in het monster eenvoudig bij het grafeenoppervlak kunnen komen, waar de detectie plaatsvindt. We hebben deze sensoren blootgesteld aan oplossingen met daarin het fotoreactieve rutheniumcomplex $[\text{Ru}(\text{tpy})(\text{biq})(\text{OH}_2)]^{2+}$, het rutheniumcomplex $[\text{Ru}(\text{bpy})_3]\text{Cl}_2$ (een goed elektronoverdrachtsagens dat geen fotosubstitutie ondergaat), of KNO_3 . Wanneer de weerstand van de grafeenlaag werd gemonitord, zagen we tot onze verrassing dat alle sensoren op licht reageerden, onafhankelijk van wat er in de oplossing zat.

We hebben deze sensoren elektrisch gekarakteriseerd door te 'gaten', oftewel door de elektrische *gate*-potentiaal onder de grafeenlaag te veranderen, om de relatie van deze potentiaal met de weerstand van het grafeen te onderzoeken. We hebben hierbij de potentiaal veranderd tussen 0 en 1.5 V, en zagen de Dirac-piek, typisch voor grafeen, bij alle sensoren. De Dirac-piek verschoof niet wanneer de sensoren werden blootgesteld aan de bovengenoemde oplossingen. Er werd vervolgens een ligand toegevoegd aan een oplossing van het fotoreactieve complex $[\text{Ru}(\text{tpy})(\text{biq})(\text{OH}_2)]^{2+}$ om een mogelijk detecteerbare fotoreactie uit te kunnen voeren. In het donker coördineert het ligand 2-deoxyguanosine monofosfaat (dGMP) aan het rutheniumcomplex, terwijl dit ligand dissocieert onder invloed van zichtbaar licht. Wanneer we de sensoren die blootgesteld waren aan deze oplossing van complex en ligand met licht bestraalden, konden we een kleine verschuiving zien in de Dirac-piek, wat erop leek te duiden dat de grafeenlaag inderdaad de chemische reactie in het papier kon detecteren.

Tegelijkertijd zagen we ook dat er een stroom liep van de *gate*-elektrode naar de grafeenlaag terwijl we de *gate*-potentiaal veranderden. Er onstonden pieken in de grafiek van de *gate*-stroom als functie van de *gate*-potentiaal, wat erop duidde dat er elektrochemische processen aan de gang waren. De exacte toedracht van deze elektrochemische processen, mogelijk de oxidatie en reductie van de rutheniumcomplexen, kon echter niet worden achterhaald. De vraag of de grafeenlaag inderdaad de (foto)chemische reactie kon detecteren is dus nog niet definitief beantwoord, aangezien deze elektrochemische processen de interpretatie van de resultaten zeer lastig maakt. Verder onderzoek is nodig om de processen in deze sensoren volledig te begrijpen en om grafeen op papier verder te ontwikkelen als een detectieplatform.

Het verlagen van de DNA-doorgangssnelheid in nanoporiën door het labelen van DNA met fotolabiele rutheniumcomplexen (CH 6)

In hoofdstuk 6 wordt een andere vorm van detecteren met nanotechnologie op basis van grafeen beschreven. In een DNA-sensor gebaseerd op een nanoporie stromen er ionen tussen twee compartimenten oftewel 'kamers', die gescheiden zijn door een membraan met daarin deze nanoporie. Deze 'ionenstroom' kunnen we elektrisch meten door een elektrische potentiaal aan te leggen tussen de twee kamers. In een van de twee kamers zit DNA, dat door een elektrisch potentiaalverschil tussen de kamers naar de andere kamer toe wordt getrokken. Terwijl de DNA-streng door de porie gaat, wordt de ionenstroom gedeeltelijk geblokkeerd, omdat het aanwezige DNA de porie vernauwt. Door fluctuaties in de ionenstroom nauwkeurig te analyseren kan, in theorie althans, worden bepaald welke DNA-basen er in de porie aanwezig zijn. Echter, voor nanoporiën in vaste membranen is de hoge snelheid waarmee het DNA door de porie gaat een probleem, waardoor dit type membranen nog niet gebruikt kan worden om de volgorde van DNA-basen te bepalen.

In een poging om het DNA af te remmen in de nanoporie van een DNA-sensor, hebben we een poging ondernomen om rutheniumcomplexen te laten binden aan het DNA, die onder invloed van licht weer van het DNA kunnen worden verwijderd. Wanneer deze complexen aan het DNA gebonden zijn, zou het DNA meer frictie moeten ervaren door de toegevoegde massa, wat de bewegingssnelheid verlaagt, terwijl door het schijnen van licht de snelheid weer omhoog kan worden gebracht door die massa weer te verwijderen. Op deze manier kan de snelheid van DNA worden gestuurd met licht.

Door middel van UV-Vis spectroscopie vonden we dat het rutheniumcomplex $[\text{Ru}(\text{tpy})(\text{biq})\text{Cl}]\text{Cl}$, dat in waterige oplossingen hydrolyseert naar $[\text{Ru}(\text{tpy})(\text{biq})(\text{OH}_2)]^{2+}$, bindt aan DNA en specifiek aan het nucleotide dGMP. Voor de andere nucleobasen, dAMP, dTMP en dCMP, vonden we geen interactie met het rutheniumcomplex. Het complex werd gemengd met DNA, zodat het complex aan het DNA kon binden. Hierna werd het DNA met het gebonden complex door een nanoporie geloodst met een diameter van 40 nm, in een siliciumnitridemembraan van 30 nm dik. De doorgangssnelheid van het DNA door de porie werd niet verlaagd door de aanwezigheid van het rutheniumcomplex, maar de blokkering van de ionenstroom was wel hoger. Dit liet zien dat de rutheniumcomplexen meereisden met het DNA, door de porie heen. Met het rutheniumcomplex was de blokkade van de ionische stroom dus wel groter, maar de doorgangssnelheid van de DNA-streng was niet significant verlaagd; waarschijnlijk bood het toegevoegde complex niet genoeg frictie. Verder onderzoek moet uitwijzen of de rutheniumcomplexen aan het oppervlak van een membraan kunnen worden vastgemaakt om zo de benodigde extra frictie te verkrijgen en de doorgangssnelheid van het DNA te verlagen. Bovendien moet worden onderzocht wat het effect is van zichtbaar licht op de doorgangssnelheid van DNA door een nanoporie in een ruthenium-gemodificeerd membraan.

$[\text{Ru}(\mathbf{3})(\text{biq})(\text{STF-31})]^{2+}$: een 'lock-and-kill' antikanker PACT-agens (CH 7)

In hoofdstuk 7 beschrijven we een molecuul dat zelf als een sensor kan dienen, zonder dat deze geïntegreerd hoeft te worden in een elektronisch apparaat. We hebben een rutheniumcomplex ontworpen en gesynthetiseerd dat een dubbele rol kan spelen in antikanker-lichttherapie, ook wel bekend als fotoactiveerbare chemotherapie (PACT, van het Engelse *photoactivated chemotherapy*). We veronderstelden dat het complex $[\text{Ru}(\mathbf{3})(\text{biq})(\text{STF-31})](\text{PF}_6)_2$ ($\mathbf{3}$ = 3-([2,2':6',2''-terpyridin]-4'-yloxy)propyl-4-(pyren-1-yl)butanoaat), biq = 2,2'-biquinoline, en STF-31 = 4-((4-*t*-butyl)fenylsulfonamido)methyl)-*N*-(pyridin-3-yl)benzamide) kan worden gebruikt om door middel van een lichtsignaal te laten zien dat het complex is opgenomen door een cel. Deze informatie kan buitengewoon handig zijn omdat het laat zien waar de prodrug (het nog niet geactiveerde medicijn) zich bevindt in de patient. Hierdoor kan er mogelijk beter worden bepaald waar de patient behandeld moet worden met licht om cellen selectief te doden. Wanneer het rutheniumcomplex wordt beschenen, laat het een NAMPT-eiwit inhibitor los in de cel, waardoor de functie van dit eiwit geblokkeerd wordt en de cel sterft.

Het gesyntheseerde rutheniumcomplex bleek inderdaad fotoreactief: het STF-31 ligand – de inhibitor – werd losgelaten onder invloed van groen licht. Kinetische studies lieten zien dat de pyreengroep, die aan het tridentaalligand vastzit, de kwantumopbrengst van de fotoexpulsie van STF-31 niet verlaagde, maar de etherverbinding aan het tridentaalligand wel. De aanwezigheid van de pyreengroep had dus geen effect op de kwantumopbrengst. Bovendien lieten fluorescentiestudies zien dat de pyreengroep, die gebonden zat via een esterverbinding in ligand **3**, niet fluorescent was wanneer deze gebonden zat aan het rutheniumcomplex. Wanneer de esterverbinding werd verbroken onder invloed van esterase-activiteit, werd de fluorescentie van de pyreengroep hersteld. We verwachten dat deze esterverbinding in levende cellen ook eenvoudig wordt verbroken door intracellulaire processen, maar niet in de bloedsomloop, waar geen esterases zijn. Het breken van de esterverbinding leidt tot fluorescentie, en cellen die de prodrug hebben opgenomen zouden dus moeten oplichten ten opzichte van cellen die de prodrug niet hebben opgenomen.

In de nabije toekomst moet confocale microscopie uitwijzen of cellen die het complex hebben opgenomen inderdaad fluorescent worden. Bovendien moet de giftigheid van het complex in kankercellen zowel in het donker als na beschijning met licht worden bestudeerd door middel van *in vitro* cytotoxiciteitstesten, om te bepalen of dit complex inderdaad dodelijker is voor cellen nadat het met licht bestraald is.

Conclusies & Vooruitzichten

Algemene conclusies

We hebben laten zien dat grafeen en metaalcomplexen waardevolle gereedschappen zijn voor het ontwerpen en maken van elektronische en moleculaire sensoren. De verschillende eigenschappen van deze materialen konden worden gebruikt voor verschillende sensorplatforms. De mogelijkheden om dit soort platforms te ontwerpen lijken eindeloos. We hebben sensoren op basis van grafeen gemaakt op conventionele substraten (siliciumwafers), maar ook op onorthodoxe substraten, waaronder eenkristallen van een ijzercomplex met spinovergangseigenschappen, die slechts enkele honderden micrometers groot zijn, en alledaags papier. We konden sensoren maken die gebruik maken van de specifieke eigenschappen van deze substraten: faseovergangen in het spinovergangskristal konden contactloos worden gedetecteerd dankzij de

elektrostatische potentiaal van het kristal, die veranderde tijdens de faseovergang. Bovendien konden we, door papier als substraat te gebruiken, direct analyten in waterige oplossingen naar het grensvlak van het papier en de grafeenlaag brengen. Tegelijkertijd konden we deze apparaten efficiënt *gaten*, zodat we de elektronische eigenschappen van het grafeen nauwkeurig konden bestuderen. De mogelijkheid om grafeen op diverse substraten te plaatsen met behulp van een overdrachtspolymeer, maakt daarom dat grafeen een heel geschikt materiaal is voor de constructie van sensoren op functionele substraten.

Bovendien bleek dat het coaten van grafeen een gedegen strategie was voor het fabriceren van sensoren. Dunne films van het spinovergangscoplex groeiden specifiek op grafeen, zelfs op grafeen-veldeffecttransistors; we konden echter geen spinovergangen in de dunne film detecteren met deze transistors. De overdrachtspolymeren bleken zeer geschikt voor het maken van sensoren, doordat ze een cruciale rol speelden in de bescherming van het grafeen wanneer dit grafeen op het eenkristal of op papier was geplaatst. Het overdrachtspolymeer kon zelfs een sensor gevoelig maken in het geval van dampsensoren gebaseerd op grafeen: door sensorreeksen met verschillende polymeercoatings te maken kon een hoge selectiviteit worden gehaald voor een groot aantal verbindingen. Sterker, het intact laten van de overdrachtspolymeer is mogelijk het ontwerpprincipe geweest dat het meest gunstig was voor de sensoren die gerapporteerd zijn in dit proefschrift.

Tegelijkertijd hebben we ook onderzocht of rutheniumcomplexen gebruikt kunnen worden voor het verbeteren van DNA-sensoren en voor het maken van moleculaire sensoren. Rutheniumpolypyridylcomplexen konden binden aan DNA. Door een dergelijk rutheniumcomplex te binden aan DNA werd de detectie van dit DNA door een sensor op basis van een nanoporie verbeterd: door het labelen van DNA met het rutheniumcomplex was de signaalsterkte van een DNA-passage door de nanoporie sterker, en het signaal dus beter waarneembaar. Ook kon een rutheniumcomplex de lichtemissie van een fluorescent label, pyreen, uitdoven wanneer dit label aan het rutheniumcomplex was gebonden via een esterverbinding. Wanneer de pyreengroep was losgemaakt van het complex door het verbreken van de esterverbinding door esteraseactiviteit, werd de lichtemissie van het pyreenlabel weer hersteld. Hiermee kan dit complex mogelijk laten zien waar het is opgenomen in cellen en weefsels door de cellen die het complex hebben opgenomen op te laten lichten. Tegelijkertijd is dit complex een

lichtactiveerbare antikankerprodrug: de oplichtende cellen kunnen simpelweg gedood worden door ze met zichtbaar licht te beschijnen. De fotofysische eigenschappen van rutheniumcomplexen kunnen dus zeer behulpzaam zijn om sensortechnieken te verbeteren en om moleculaire sensors te ontwerpen.

Uiteindelijk bleek de strategie van het combineren van metaalcomplexen met grafeen zeer succesvol. We hebben slechts een zeer klein aantal metaalcomplexen gebruikt: de chemische diversiteit van metaalcomplexen en de grote variatie van sensoren op basis van grafeen maakt dat we alleen de top van de ijsberg hebben waargenomen. Door nanomaterialen zoals grafeen te combineren met metaalcomplexen, kunnen hybride structuren gemaakt worden die niet alleen voor sensoren, maar voor bijna elk type elektronische hardware (transistors, actuatoren, geheugenchips, etc.) nuttig kunnen zijn.

Vooruitzichten

De beschreven principes in dit proefschrift bieden ruimte voor verder onderzoek. De lijnen die hier zijn gepresenteerd kunnen worden voortgezet in meerdere richtingen, waaraan verschillende onderzoeksroutes kunnen worden gekoppeld.

Het gebruik van schakelbare substraten, zoals de spinovergangskristallen, voor grafeen-veldeffecttransistoren kan twee richtingen opgaan. Ten eerste kunnen andere typen kristallen worden gebruikt in plaats van het spinovergangskristal. Kristallen van ruthenium-DMSO-complexen die in een ander isomeer veranderen wanneer de kristallen worden beschenen met licht, zijn bijvoorbeeld interessante vervangers.^[1] Op die manier kan er met licht in plaats van temperatuur worden geschakeld. Bovendien kunnen eenkristallen van gasgevoelige metaal-organische raamwerken (MOFs, van het Engelse *metal-organic framework*) ook de plaats innemen van de schakelbare kristallen. Zo kunnen sensoren worden gemaakt die een gas kunnen detecteren door de faseovergang in het MOF-kristal te registeren, die op zijn beurt wordt veroorzaakt door de aanwezigheid van dat gas.^[2] Ten tweede zouden ook nanosensoren gemaakt kunnen worden op een enkel eenkristal, bijvoorbeeld met behulp van (elektronenstraal) lithografie.^[3] De kristallen die we hebben gebruikt waren honderden micrometers groot, wat genoeg ruimte geeft om een veelvoud van nanosensoren te maken op één kristal. Bovendien kan in het spinovergangskristal zelf ook met een laser gesneden of “geschreven” worden,^[4] waarmee kleine spinovergangsactieve domeinen kunnen worden gemaakt, die mogelijk individueel activeerbaar zijn. Deze kleine

domeinen, in combinatie met nanosensoren, kunnen leiden tot een grote verzameling van schakelgevoelige sensoren op een enkel kristal, wat nuttig kan zijn voor dataopslag.

Verdere studie van de dunne films gebaseerd op het complex $[\text{Fe}(\text{bapbpy})(\text{NCS})_2]$ zou dezelfde richting op kunnen gaan. Omdat de films selectief groeien op grafeen, zouden standaardtechnieken kunnen worden gebruikt om elektronische transistors van grafeen te ontwerpen en fabriceren, waarbij het grafeen selectief gecoat kan worden met de dunne film. Mogelijke applicaties van dit soort transistors zijn dataopslag, maar ook sensoren, aangezien de moleculen in de dunne film waarschijnlijk gevoelig zijn voor hun omgeving.^[5]

De chemische vingerafdruksensor is een voorbeeld van een grafeentransistor die werkt als sensor door middel van een dunne coating, een polymeerlaag in dit geval. De vingerafdruksensoren die beschreven zijn in dit proefschrift zijn 1^e generatie prototypes: verdere ontwikkeling zou gefocust moeten zijn op het produceren van data van hoge kwaliteit om die te gebruiken om verbindingen betrouwbaar te kunnen identificeren met behulp van algoritmes.^[6] De resultaten van de 1^e generatie prototypes zijn bemoedigend; het is echter een uitdaging om afwijkingen tussen verschillende sensoren te verminderen. Idealiter reageert iedere sensor hetzelfde, waardoor het mogelijk wordt om één geoptimaliseerd algoritme te bouwen voor alle sensoren om de betrouwbaarheid te maximaliseren. Uiteindelijk zouden deze chemische vingerafdruksensoren gebruikt kunnen worden in de kliniek als ademanalyseapparaat voor screening en diagnose.

Ook hebben we grafeen op papier onderzocht als sensorplatform. Dit platform heeft nog niet zijn volledige potentieel bereikt, doordat het onderzoek werd bemoeilijkt door het bestaan van de elektrochemische processen die tegelijkertijd plaatsvonden. Enerzijds kan het bestuderen van deze processen helpen om te begrijpen wat er precies gebeurt tijdens de metingen, wat kan bijdragen aan de verdere ontwikkeling van dit sensorplatform. Anderzijds zou het gebruiken van strikt niet-electrochemisch actieve stoffen (binnen de *gate*-potentiaal van 0 tot 1.5 V) voor het bestuderen van deze sensoren nuttig kunnen zijn, omdat dit een vereenvoudigde blik kan bieden op de processen die spelen in de grafeensensoren op papier.

Verder hebben we laten zien dat rutheniumcomplexen nuttig kunnen zijn om DNA te labelen, zodat het DNA beter gedetecteerd kan worden in DNA-sensoren

op basis van een nanoporie. Hierin hebben we slechts een start gemaakt. In een voortzetting van dit onderzoek is het cruciaal dat het effect van licht op de doorgang van ruthenium-gelabelde DNA wordt bestudeerd. De fotoreactiviteit van het rutheniumcomplex kan worden gebruikt om de binding van het complex aan DNA te manipuleren. Wanneer er bovendien gebruikt wordt gemaakt van complexen die verankerd zijn aan het oppervlak van het membraan waar de porie in zit, kan het complex het DNA mogelijk afremmen. Met licht kan dan de mate van binding van de complexen aan DNA worden bepaald, waarmee dus de snelheid van het DNA kan worden gestuurd. Een dergelijk complex met ankergroep is al beschreven in hoofdstuk 7; de pyrengroep kan worden gebruikt om het complex te binden aan een grafeenmembraan.

Het complex dat is beschreven in hoofdstuk 7 kan uiteraard ook verder worden bestudeerd als een antikanker PACT-agens. We hebben aangetoond dat de fluorescentie van de pyrengroep toeneemt door het verbreken van de esterverbinding tussen pyreen en ruthenium. Een belangrijke vervolgstap is nu om te bestuderen of levende cellen oplichten wanneer ze het complex opnemen en de esterverbinding verbreken. Verder moet de cytotoxiciteit van het complex in zowel het donker als onder zichtbaar licht worden bestudeerd. Het slecht in water oplosbare complex kan waarschijnlijk gedragen worden door liposomen, aangezien het complex amfifiel is, om de toedoeing van de prodrug te verbeteren.^[7] Uiteindelijk zou dit complex een effectief PACT-agens kunnen zijn, die eerst laat zien in welke cellen de stof zich bevindt (waarbij tumorcellen mogelijk eerder oplichten door een verhoogd metabolisme), zodat deze cellen door het beschijnen met licht selectief gedood kunnen worden.

Referenties

- [1] J. J. Rack, J. R. Winkler, H. B. Gray, *J. Am. Chem. Soc.* **2001**, *123*, 2432; J. J. Rack, A. A. Rachford, A. M. Shelker, *Inorg. Chem.* **2003**, *42*, 7357.
- [2] D. E. Jaramillo, D. A. Reed, H. Z. H. Jiang, J. Oktawiec, M. W. Mara, A. C. Forse, D. J. Lussier, R. A. Murphy, M. Cunningham, V. Colombo, D. K. Shuh, J. A. Reimer, J. R. Long, *Nat. Mater.* **2020**, *19*, 517; D. A. Reed, B. K. Keitz, J. Oktawiec, J. A. Mason, T. Runčevski, D. J. Xiao, L. E. Darago, V. Crocellà, S. Bordiga, J. R. Long, *Nature* **2017**, *550*, 96.
- [3] G. J. Dolan, *Appl. Phys. Lett.* **1977**, *31*, 337.
- [4] S. Bedoui, M. Lopes, S. Zheng, S. Bonnet, G. Molnár, A. Bousseksou, *Adv. Mater.* **2012**, *24*, 2475.
- [5] K. Senthil Kumar, M. Ruben, *Coord. Chem. Rev.* **2017**, *346*, 176.
- [6] T. Hayasaka, A. Lin, V. C. Copa, L. P. Lopez, R. A. Loberternos, L. I. M. Ballesteros, Y. Kubota, Y. Liu, A. A. Salvador, L. Lin, *Microsyst. Nanoeng.* **2020**, *6*, 50.
- [7] J. Shen, H.-C. Kim, J. Wolfram, C. Mu, W. Zhang, H. Liu, Y. Xie, J. Mai, H. Zhang, Z. Li, M. Guevara, Z.-W. Mao, H. Shen, *Nano Lett.* **2017**, *17*, 2913.

List of publications

Published:

W. Fu, L. Jiang, E. P. van Geest, L. M. C. Lima, G. F. Schneider, *Adv. Mater.* **2017**, 29, 1603610

E.P. van Geest, K. Shakouri, W. Fu, V. Robert, V. Tudor, S. Bonnet, G. F. Schneider, *Adv. Mater.* **2020**, 32, 1903575

In preparation:

E.P. van Geest, P. van Deursen, L. Wu, N. Puthuval Prasad, T. de Haas, J.P. Hofmann, G.F. Schneider and S. Bonnet, *Large-area thin films of the spin crossover complex [Fe(bapbpy)(NCS)2] grown selectively on graphene*. In preparation for publication.

E.P. van Geest, H. de Bruijn, X. Liu, G. van Westen, S. Bonnet, and G.F. Schneider, *Polymer coated graphene-based gas sensors: chemical fingerprinting by simultaneous sensing*. In preparation for publication. Patent application filed.

E.P. van Geest, J. de Ruiter, D. van den Bos, C. Blet, J. van Ruitenbeek, G.F. Schneider and S. Bonnet. *Monitoring a ruthenium-based photoreaction with graphene on paper*. In preparation for publication.

E.P. van Geest, R. Versloot, S. Popal, P. van Deursen, L. Lameijer, S. Bonnet and G.F. Schneider. *Reducing the translocation speed of DNA in solid-state nanopores by photo-labile ruthenium complex decoration*. In preparation for publication.

E.P. van Geest, N. Salitra, S. Popal, R. Vadde, C. Van de Griend, G.F. Schneider and S. Bonnet. *[Ru(3)(biq)(STF-31)]²⁺: A lock-and-kill anticancer PACT agent*. In preparation for publication.

R. Vadde, E.P. van Geest, W. Verbeet, *Metal complexes as anticancer drugs: intracellular targets and analytical techniques to detect metal-protein interactions*. In preparation for publication.

Curriculum Vitae

Erik Pieter van Geest was born on the 23rd of March in 1991 in Naaldwijk, The Netherlands. He attended the high school ISW Tiendweg in Naaldwijk, where he received his degree with the specialization 'Natuur en Techniek' in 2009. In the same year, he started studying Molecular Science and Technology at Leiden University and TU Delft, with the Chemistry specialization. He received his BSc degree in 2012 with a thesis entitled "*Synthesis of palladium N-heterocyclic carbene complexes towards palladium-imido compounds*", after completing an internship (18 EC) at the MCBIM group. He started the MSc Chemistry at Leiden University in the same year. In 2014 he obtained his MSc degree with a major thesis entitled "Liposomes functionalized with ruthenium: towards a tumor-targeted, light-controlled anticancer drug" (40 EC) describing the results of research performed within the MCBIM group, followed by a minor thesis entitled "*An alternative synthetic route towards Akardite II*" (35 EC) describing the research performed at TNO in the Energetic Materials department.

Between 2014 and 2016 he worked at TNO, in the Energetic Materials department. In 2016, he started a PhD programme under the co-supervision of Prof. Dr. Sylvestre Bonnet and Dr. Gregory Schneider, at the interface between the MCBIM and SBC research groups. The results of this PhD research are described in this thesis, and were in parts presented as poster and oral presentations at the NWO CHAINS conference in Veldhoven (2017, 2018), at the 2017 Chem2DMat conference in Strasbourg (poster), and at the 2019 Nanotech France conference in Paris (oral). He had a supervisory role in the NWO-funded Team Slow-motion, which competed in the TOP-sector Chemie research competition Finals in 2018. As part of his PhD programme, he attended several events from the HRSMC, including the Physical methods in Inorganic Chemistry (PhMIC) course in 2017, the Advanced Metal Organic Chemistry and Catalysis (AMOCC) summer school in 2018 and Photophysics, Photochemistry and Photobiology (PPP) in 2019. Finally, he attended the Leiden University Graduate School courses on Time Management, How to be a Scientist, Communication in Science and Effective Communication.

Acknowledgements

First, and most of all, I want to thank all staff and students from the MCBIM and SBC groups. Within and outside working hours, I really enjoyed your company as the years flew by. Especially my fellow members of the First Office (Lucien, Sven, Andrea, Corjan, Valeriia), of the Coffee Crew, most notably Hans, and of the “Pirates of Huigsloot” Andrea and Imma, thanks for the good times we have spent. Discussions both in formal and informal settings always gave me new inspiration and a drive to continue, even if results were lacking. Lucien, Pauline, Roderick, and Sorraya, thanks for everything we achieved with Team Slow-Motion. Being involved in a research competition is an experience that all brought us to a higher level. What starts as an idea in a forgotten night at Lemmy’s, really turned out to be a fruitful project with great results in a very limited time.

Most projects would not have progressed as much as they did without the help of collaborators. Khosrow, I still owe you a bottle of wine, thanks for all the work on chapter 2. Jan Philipp, Gabor, and Aurelian, thanks for the help with the measurements on the thin films for chapter 3 and Wim, thanks for the help with μ -contact printing. Xuhan and Gerard, thanks for the data analysis of chapter 4 that truly showed the potential of the CF sensors. Jan, thanks for the deep discussions we have had about the GFETs on paper from chapter 5. From the physics department, thank you Douwe and Federica, for making me accustomed to the amazing machines and setups that I have used.

I would like to thank the students that contributed to this thesis; their time and work significantly pushed the projects they were involved in forward. Reinout Ubbink and Ted de Haas contributed to chapter 3. Camille Blet, Daan van den Bos, and Jonathan de Ruiter contributed to chapter 5. Roderick Versloot and Sorraya Popal, as part of Team Slow-Motion contributed largely to chapter 6. Nadiya Salitra contributed to chapter 7. Lastly, Benjamin Oudot and Simon Chen contributed projects that sadly did not make it to this thesis. I’d like to thank all of you for the time spent, discussions that we had and the many things we learned from each other. I really enjoyed being your supervisor.

I'd like to give special thanks to Prof. dr. E. Bouwman, for all the time she put in reading this thesis and providing very useful feedback. Thanks a lot Lies, I really appreciate this.

Of course, I want to thank my own supervisors. Les Frenchies Sylvestre and Gregory, thank you for making my PhD very much fit for me, with lots of room to explore, a lot of freedom, and the occasional critical view on my various projects. I've enjoyed all the discussions we have had, whether scientific or not, and all the fun we had. Je m'apelle un croissant et non de jus plus maintenant! Merci, merci, merci. All the best for the future, and I'm sure I'll see you around.

Lastly, I'd like to thank my family and friends for their company, support and the time we have shared, which kept me going during my entire PhD. In the end, you helped me to keep my mind fresh and my enthusiasm up. Man, man, man, many thanks.